

12. SITE 1219¹

Shipboard Scientific Party²

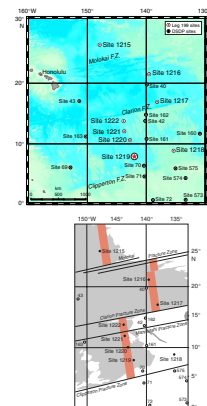
BACKGROUND AND OBJECTIVES

Site 1219 (7°48.019'N, 142°00.940'W; 5063 meters below sea level [mbsl]; Fig. F1) is the southernmost site to be drilled on the 56-Ma transect during Leg 199 and is situated ~3° to the north of the Clipperton Fracture Zone on abyssal hill topography. The age of basement at Site 1219 was poorly constrained prior to Leg 199 because little reliable magnetic anomaly data are available between the Clipperton and Clarion Fracture Zones (Cande et al., 1989). At the outset of Leg 199, based on one interpretation of the location of magnetic Anomaly C25r (~57 Ma) (Petronotis et al., 1994), previous drilling, and assumed spreading rates, we estimated the age of basement at Site 1219 to be ~55 Ma. Site 1219 is the only site to be drilled during Leg 199 that features all of the seismic horizons identified for a Paleogene equatorial seismic stratigraphy (Lyle et al., this volume), and an estimate of sediment thickness at Site 1219 prior to drilling (based upon the seismic reflection profile; Fig. F2) was 270–290 meters below seafloor (mbsf), depending on which reflection was chosen as basement.

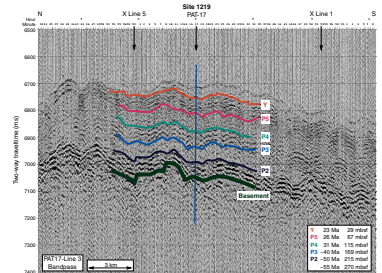
Based upon a fixed hotspot model (Gripp and Gordon, 1990, for 0- to 5-Ma Pacific hotspot rotation pole; Engebretson et al., 1985, for older poles), Site 1219 should have been within 2° of the equator between 40 and 21 Ma and should have crossed the equator at 29 Ma. Thus, the sediments should record equatorial conditions from the late middle Eocene to the early Miocene. In addition, Site 1219 should provide an analog for Site 1218, except that it is on older deeper crust.

Site 1219 will be used to study near-equatorial ocean circulation from the late Paleocene to the late Eocene including deepwater flow and sea-surface properties. Sediment records from this site will help to define the carbonate compensation depth (CCD) and lysocline during the Eocene–Oligocene transition and near the Oligocene/Miocene (O/M) boundary. Based on the results from a site survey piston core (EW3709-

F1. Site location map, p. 42.



F2. Seismic reflection profile, p. 43.



¹Examples of how to reference the whole or part of this volume.
²Shipboard Scientific Party addresses.

12PC; Lyle, 2000) taken a few kilometers to the southwest, we anticipated that Site 1219 passed below the CCD in the early Miocene. The basement at Site 1219 should have formed in the Southern Hemisphere, and changes in magnetic inclination at this site will be important to define the position of the equator in the early Eocene.

SUMMARY

Site 1219 (7°48.01'N, 142°00.94'W) is the southernmost site drilled during Leg 199. It is situated on the 56-Ma transect ~3° north of the Clipperton Fracture Zone and is located at a water depth of 5063 m on abyssal hill topography. The age of basement at Site 1219 was poorly constrained prior to Leg 199 because little reliable magnetic anomaly data are available between the Clipperton and Clarion Fracture Zones (Cande et al., 1989). At the outset of Leg 199, based on one interpretation of the location of magnetic Anomaly An25r (~57 Ma) (Petronotis et al., 1994), previous drilling, and assumed spreading rates, we estimated the age of basement at Site 1219 to be ~55 Ma. Site 1219 is the only site drilled during Leg 199 that features all of the seismic horizons identified for a Paleogene equatorial seismic stratigraphy (Lyle et al., this volume).

Based upon a fixed hotspot model (Gripp and Gordon, 1990, for the 0- to 5-Ma Pacific hotspot rotation pole; Engebretson et al., 1985, for older poles), Site 1219 should have been within 2° south of the equator between 40 and 21 Ma and should have crossed the equator at 29 Ma. Thus the sediments should record equatorial conditions from the late middle Eocene–early Miocene. In addition, Site 1219 should provide an analog for Site 1218, except that it is on older, deeper crust.

Two holes were drilled at Site 1219. Hole 1219A was a remarkable operations success. We advanced to ~225 mbsf using Ocean Drilling Program's (ODP's) advanced piston corer (APC) technology, thereby achieving one of our high-priority objectives by recovering sediments suitable for whole-core magnetostratigraphy below the lower Oligocene (including the Eocene/Oligocene [E/O] boundary). Basement was reached at ~250 mbsf, shortly after switching to extended core barrel (XCB) coring. A full suite of downhole logs was obtained to the base of Hole 1219A, and the data are of high quality. In addition to these downhole logs, multisensor track (MST) data from the uppermost Eocene to the lowermost Miocene interval in this hole bore a striking resemblance to those recovered from Site 1218, so much that it was possible to correlate between Sites 1218 and 1219 (which are separated by 7° of longitude and 1° latitude, or ~800 km) to a submeter scale.

In contrast to Hole 1219A, Hole 1219B was terminated when an APC core jammed in the bottom-hole assembly (BHA) at the depth of the E/O boundary (~155 mbsf). In light of these difficulties in Hole 1219B and the successes of both Hole 1219A and Site 1218, the shipboard party made a collective decision to abandon Site 1219 earlier than planned in order to target additional and more complete programs at forthcoming sites having early and middle Eocene objectives.

Holes 1219A and 1219B can be spliced to form a continuous section to 130 meters composite depth (mcd) (~30 Ma) with two apparent gaps at ~90 and ~100 mcd. Excellent correlations between Site 1218 and 1219 allow us to estimate the properties of the unrecovered intervals, whereas correlations between logging data and the cores can be used to estimate the size of core gaps deeper in the sedimentary section. Sedi-

mentation rates over the Oligocene interval were ~16% slower than at Site 1218, based upon the site-to-site correlation.

The sediment column at Site 1219 has a strong resemblance to that of Site 1218. Thirty meters of clay (lithologic Unit I) overlies Oligocene–lower Miocene nannofossil ooze (Unit II; 30–151 mbsf). Strong cyclic variations in nannofossil content are apparent in both the upper and lower parts of Unit II. An abrupt change in lithology from nannofossil ooze to radiolarian clay and clayey radiolarian ooze occurs at 151 mbsf within the E/O boundary interval. The lithologic change marks the upper boundary of lithologic Unit III: an upper and middle Eocene unit composed of radiolarian ooze and radiolarian clay, becoming radiolarite, chert, and zeolitic clay at the base. A short section in Unit III within polarity Chron C18r (40.1–41.3 Ma) contains alternating diatom and nannofossil ooze. Below the cherty, clay-rich section at the base of Unit III are the chalks of lithologic Unit IV (234–243 mbsf; ~53–54.8 Ma). The oldest sediments above basalt are slightly younger than the Paleocene/Eocene (P/E) boundary.

Natural remanent magnetization (NRM) intensity of the sediments at Site 1219 is relatively strong, and the magnetic overprint from drilling can be mostly removed by alternating-field (AF) demagnetization. An excellent record of magnetic reversals was made for the entire APC-cored sediment section (0–223 mbsf), from Pleistocene Chron C1n to early middle Eocene Chron C20r (43.8–46.3 Ma). This remarkably clean magnetic reversal stratigraphy allows us to calibrate biostratigraphic events and to develop detailed sedimentation-rate curves downhole to lower middle Eocene sediments. Inclination patterns in discrete samples show that at least the lower part of the sedimentary section was located in the Southern Hemisphere during deposition. The mean inclination depicts a time-averaged paleolatitude of 1.6°S for the site, but this result is preliminary and will require further testing. The paleolatitude inferred from the inclination is consistent with the expected latitudes as calculated from both paleomagnetic pole positions and those based upon a fixed hotspot model.

Nannofossils are present to abundant in the Oligocene–middle Miocene sediments (~151–10 mbsf) but absent from upper Eocene sediments. Nannofossils reappear briefly in polarity Chron C17r (~38.3 Ma) in the middle Eocene, disappear, and then reappear and are present between the middle of polarity Chron C18r to the base of C20n (~40.5–43.8 Ma) and are found in the chalk in the lower Eocene interval. Planktonic foraminifers are present in the lower Miocene–Oligocene sediments and in the lower Eocene chalks. Preservation quality and abundance are highest in the lower Miocene (Zones M4–M2) and the middle part of the Oligocene (Zones P20 and P21). Benthic foraminifers are consistently present and well preserved through the Miocene and Oligocene at Site 1219 but are scarce and very poorly preserved through much of the Eocene sections. Radiolarians were found in all cores except the deepest one (Core 199-1219A-27X), which recovered chalk over basalt basement.

The magnitude of the downhole calcium concentration increase and magnesium and potassium concentration decrease in pore waters at Site 1219 is the greatest seen at all sites during Leg 199. This pattern is consistent with the extensive alteration (e.g., chlorite formation) of basement rocks observed here. Depth gradients of pore water alkalinity, pH, sulfate, and ammonium reflect the small amount of organic matter degradation occurring in these sediments, whereas the chlorinity profile may reflect the diffusion of the more saline Pacific Bottom Water of the

last glacial maximum into the sediments. Bulk-sediment geochemical analyses from Site 1219 reflect the shifts in lithology back and forth between sediments dominated by silica and carbonate. Clay-rich units are high in Ti and Al but are also high in Fe and Mn, presumably reflecting the deposition of authigenic ferromanganese oxyhydroxides. Physical properties of the sediments also primarily reflect lithology. The carbonate sediments are higher in density, lower in porosity, and lower in magnetic susceptibility (MS) than the clay or radiolarian ooze lithologies. This is true even on a fine scale (see Fig. F29 and “Physical Properties,” p. 28). The radiolarian ooze has higher compressional wave velocity than the carbonates despite having higher average porosity.

Highlights

Magnetic Reversal Stratigraphy

The clean record of magnetic reversal history for Site 1219 (for the entire APC-cored sediment section; 0-223 mbsf) from the Pleistocene down to Chron C20r (43.8–46.3 Ma) is remarkable for a tropical site and, together with the superb cyclostratigraphic correlations to Site 1218 (see “MST Correlation to Site 1218,” p. 4), will provide invaluable time control for shore-based high-resolution paleoceanographic studies.

MST Correlation to Site 1218

The MST data from Site 1219 bear a striking resemblance to those recovered from Site 1218 from the middle Eocene–lowermost Miocene interval. The excellent match in these data sets between the two sites made it possible to align both records on a common (Site 1218 mcd) depth scale. The two records show such high quality correlation (down to the submeter scale) that successful a priori prediction of biostratigraphic zones and magnetic reversals was possible at Site 1219. The mapping from Site 1219 mcd to Site 1218 mcd results in relative sedimentation rates at Site 1218 that are ~16% higher than at Site 1219 over the Oligocene interval. The remarkable fidelity of the correlation between these two sites, separated by more than 1° of latitude and 7° of longitude (~800 km), suggests that drilling results from these two sites are representative of large-scale paleoceanographic-forcing functions in the late Paleogene eastern equatorial Pacific Ocean. We anticipate that the continuously cored sediments from Site 1218 with supplementary control from correlative sediments in Site 1219 will provide a paleoceanographic reference section for the late Paleogene tropical Pacific Ocean.

Oligocene–Miocene Transition

Calcareous nannofossils suggest a placement of the O/M boundary ~55 mcd within polarity Subchron C6Cn.2r at Site 1219, where the range of *Sphenolithus delphix* was observed. On the Cande and Kent (1995) timescale, an age estimate of 24.28 ± 0.05 Ma is obtained for the base of *S. delphix* at Site 1219. Conversion to the orbitally tuned timescale of Shackleton et al. (2000) by subtracting 0.9 m.y. from the Cande and Kent (1995) timescale estimate gives an age of 23.38 Ma for the base of *S. delphix*. This value is 0.14 m.y. older than the orbitally tuned estimate for this datum derived from the eastern South Atlantic (Deep

Sea Drilling Project [DSDP] Site 522) and the western equatorial Atlantic (Sites 926, 928, and 929) (Shackleton et al., 2000). Yet, the calibration of the *S. delphix* event to the geomagnetic polarity record is remarkably consistent in Subchron C6Cn.2 from the South Atlantic Ocean to the Mediterranean region (Raffi, 1999) and to the tropical Pacific Ocean (Site 1219).

Eocene–Oligocene Transition

The Eocene–Oligocene transition at Site 1219 is associated with an abrupt lithological change from radiolarian clays below to nannofossil ooze above. This transition is similar to but sharper than that observed at Site 1218, presumably reflecting higher rates of carbonate dissolution at Site 1219 (the contemporaneous paleowater depth is ~400 m deeper at Site 1219 than Site 1218). Together with drilling results from Site 1217, this finding offers exciting prospects for shore-based investigation of the first Pacific Ocean depth and latitudinal transect across this important paleoceanographic boundary.

Eocene Sediments

The Eocene sediments at Site 1219 are dominated by radiolarian oozes from the period between ~45 Ma and the E/O boundary. Nevertheless, there are intervals of carbonate within the section, most notably at ~40.5 Ma but also at ~38.3 and ~43.5 Ma. These carbonate units can be detected by density, reflectivity, velocity, and light absorption spectroscopy (LAS) mineralogy as well as by chemical analyses and microscopic examination of the sediments. The 40.5- and 38-Ma events are also found at Site 1218, but the oldest of these events is older than the base of the sediment column at Site 1218.

The lower–middle Eocene interval is represented by cherty sediments that were not recovered by drilling. This is one of five sites on the 56-Ma transect where we encountered cherts in roughly the same interval. Immediately below the cherts at Site 1219 are zeolitic clays barren of microfossils, suggesting that the chertified interval was deposited slowly. The uppermost lower Eocene chalk in contact with the zeolitic clay has an age of ~53 Ma (nannofossil Subzone CP9b), whereas the lowermost radiolarian ooze above the cherty interval is dated as ~46 Ma. Thus, the average sedimentation rate over the 10-m-thick cherty interval could be as low as 1.4 m/m.y. The interval has been condensed by diagenesis, but an estimate of the bulk mass accumulation rate (MAR) using sediment density measured by downhole logging (~2 g/cm³) is about half that of the sediments immediately above it.

The lower Eocene chinks were poorly recovered but appear to be typical basal carbonate-rich sediments. There is little evidence of hydrothermal sediments within the chinks.

OPERATIONS

Transit to Site 1219 (PAT-17C)

The 398-nmi voyage to proposed Site PAT-17C was accomplished in 36.0 hr at an average speed of 11.1 kt. After the vessel slowed to 5 kt at 0100 hr on 23 November, 2001 a short 3.5-kHz survey was made from east to west across the site. Upon conclusion of the 1-hr survey, the ves-

sel came about and returned to site as the thrusters were lowered and the dynamic positioning system (DPS) was activated. The Global Positioning System receiver interface to the DPS was employed to situate the vessel over the coordinates of the new location by 0200 hr. A beacon was deployed at 0300 hr. The corrected precision depth recorder (PDR) depth was 5084.4 meters below rig floor (mbrf).

Hole 1219A

After the drill string was deployed to a depth of 5071 mbrf, the driller further lowered the bit until the heave compensator appeared to activate, suggesting contact with a firm seafloor. The contact was at a bit depth of ~5075 mbrf. Hole 1219A was then spudded with the APC at 1200 hr on 23 November with the bit at 5071.0 mbrf. The seafloor depth indicated by the recovery of the initial core was 5074.5 mbrf. This depth was 9.9 m shallower than the PDR depth.

Hole 1219A was deepened to 224.5 mbsf with the APC before the XCB was deployed to accomplish the deeper objectives of the hole. Orientation began with Core 3H. All 24 piston cores were fully stroked events, but six core barrels (Cores 18H and 20H–24H) could not be pulled free of the sediment even with 80,000 lb of overpull. The core barrels had to be drilled over to release them from the sediment. The active heave compensator was engaged during drill-over operations for the majority of these cores. The average recovery in the APC section was 103.7% (Table T1).

XCB coring (Cores 25X–27X) deepened the hole from 244.5 to 250.8 mbsf. A small sample of basalt was obtained in the last core, confirming basement contact. XCB coring advanced 26.3 m and recovered 7.67 m (29.2%). The total recovery of Hole 1219B was 240.41 m, which represents 95.9% of the cored interval (Table T1).

Downhole Measurements, Hole 1219A

To prepare the hole for logging, the drill string was pulled to 80.5 mbsf and then lowered back to 250.8 mbsf. The hole was then displaced with 100 bbl of 8.9 lb/gal sepiolite mud, and the bit was placed at the logging depth of 83.3 mbsf. Logging then began at 1530 hr on 25 November.

The triple combo configuration with the multisensor spectral gamma ray tool (MGT) was deployed first. Two passes were made with the triple combo tool in Schlumberger mode followed by two passes in Lamont mode for MGT data acquisition. The triple combo configuration was followed by two passes of the Formation Microscanner-sonic (FMS-sonic) tool string. In all, six passes were made with no bridges encountered, and the bottom of the hole was reached on all passes. Logging operations were completed by 1200 hr on 26 November (see “[Downhole Measurements](#),” p. 33, for details of the logging operations).

Hole 1219B

After logging operations were completed, the bit was pulled free of the seafloor at 1230 hr on 26 November, and the vessel was offset 20 m north of Hole 1219A. Hole 1219B was spudded with the APC at 1330 hr on 26 November. In order to obtain a good stratigraphic overlap with results from the first hole, Hole 1219B was drilled to 21 mbsf before piston coring was initiated. The plan for this hole was to deepen it with

APC/XCB coring to ~240 mbsf. This depth objective was thwarted when the core barrel containing Core 16H could not be retrieved with the wireline. The piston core was fully stroked and was pulled free of the sediment with a moderate amount of overpull (60,000 lb). However, the core barrel jammed in the BHA and could not be recovered in a routine manner. The Kinley Cutter was used to sever the wireline, after which the drill string and BHA with the core barrel and Tensor tool, were recovered.

In light of the operational difficulties in Hole 1219B and the successes of both Hole 1219A and Site 1218, the shipboard party made a collective decision to abandon Site 1219 earlier than planned. This decision was made in order to target additional and more complete programs at forthcoming sites having lower and middle Eocene objectives. The vessel departed for the next site (PAT-9D) at 0445 hr on 27 November.

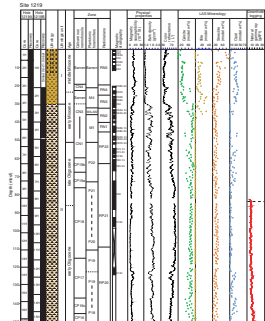
Sixteen piston cores were recovered at Hole 1219B with orientation starting on Core 1H. Heat flow measurements were obtained at 49.5 mbsf (Core 4H), 78.0 mbsf (Core 7H), and 116.0 mbsf (Core 11H). The average recovery in the Hole 1219B cores was 101.1% (Table T1).

LITHOSTRATIGRAPHY

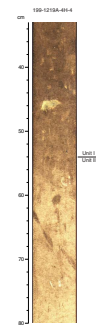
The 286.1 m of sediment recovered at Site 1219 consists primarily of radiolarian and nannofossil ooze with varying clay contents in a sequence similar to Site 1218 and DSDP Site 162. Lithologic descriptions are primarily based on sediments from Hole 1219A. The Neogene is represented by 30 m of radiolarian clay and radiolarian ooze. About 120 m of nannofossil ooze, with variable radiolarian and clay content, comprises the lower Miocene and Oligocene sections at this site. A 95-m-thick Eocene section contains a diverse array of sediments including radiolarian and zeolitic clays, radiolarian and diatom oozes, and nannofossil oozes and cherts. Chert was encountered near the base of the Eocene section. Minor components throughout the sequence include diatoms, foraminifers, iron oxides, and zeolites. Other minor to trace components include fish teeth, sponge spicules, silicoflagellates, and volcanic glass.

The sequence is divided into five major lithologic units (Fig. F3). With the exception of the Unit I/II contact, all unit boundaries are sharp lithologic transitions (Figs. F4, F5, F6, F7). Physical properties data support our interpretation of lithologic units and subunits (see “Physical Properties,” p. 28). Unit I extends from 0 to 30.0 mbsf (Hole 1219B: 21.0–29.2 mbsf) and consists primarily of radiolarian clay grading to radiolarian ooze that is late Miocene–Holocene in age. Alternations of nannofossil ooze with radiolarians and clay are present in the basal portion of Unit I. These variations are expressed as decimeter-scale, light–dark color cycles. Unit II, lower Oligocene–lower Miocene nannofossil oozes, begins at 30.0 mbsf and extends to 150.8 mbsf (Hole 1219B: 29.2–154.5 mbsf). The upper and basal portions of Unit II contain significant clay and radiolarian components, which are also expressed as decimeter- to meter-scale color cycles. Subunit IIIA (Hole 1219A: 150.8–224.5 mbsf; Hole 1219B: 154.5–158.0 mbsf) begins at the lithologic transition associated with the E/O boundary and grades from a radiolarian clay to a radiolarian ooze. Approximately 10 m of radiolarite and chert, underlain by a zeolitic clay, comprises Subunit IIIB (Hole 1219A: 224.5–234.2 mbsf). Core recovery in the cherty interval of Sub-

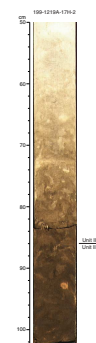
F3. Core recovery, corresponding lithologic units, and age, Holes 1219A and 1219B, p. 44.



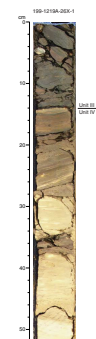
F4. Unit I–II transition, p. 46.



F5. Unit II–III transition, p. 47.



F6. Unit III–IV transition, p. 48.



unit IIIB was poor. Unit IV spans the interval from 234.2 to 244.8 mbsf and contains extensively recrystallized nanofossil chalk and calcareous chalk that is early Eocene in age. The basal portion of Unit IV contains 20–30 cm of extensively altered chalk and basalt. Unit V consists of a fine-grained phaneritic basalt.

Unit I

Intervals: 199-1219A-1H-1, 0 cm, through 4H-4, 54 cm, and 199-1219B-1H-1 through 2H-6, 82 cm
 Depths: 0.0–30.0 mbsf (Hole 1219A) and 21.0–29.2 mbsf (Hole 1219B)
 Age: Holocene to early Miocene
 Lithology: radiolarian clay and radiolarian ooze

The upper 14.6 m of Unit I consists of alternating radiolarian clay, clay with radiolarians, and clayey radiolarian ooze with the radiolarian fraction decreasing downhole. This is also expressed as a decrease in lightness (L^*) and an increase in the red/blue (680 nm/420 nm; a^*/b^*) ratios in spectral reflectance (Fig. F8). Lithologic alternations are seen as half-meter to meter-scale, light–dark cycles. Clay layers range from dark yellowish brown (10YR 4/4) to very dark grayish brown (10YR 3/2) in color, whereas ooze intervals range from yellowish brown (10YR 5/4) to dark gray (7.5YR 3/2). Mottles are abundant in the clayey radiolarian ooze, common in the other lithologies, and tend to be light yellowish brown (10YR 6/4). Contacts between interbeds tend to be gradational and overprinted by bioturbation. Diatoms and iron oxides are minor components (up to 10%). Trace amounts (<5%) of silicoflagellates and volcanic glass are present throughout.

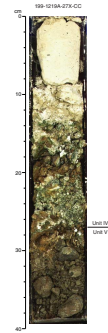
Below 14.6 mbsf, the biogenic fraction is dominant, and the principal lithology is radiolarian ooze. Color ranges from very dark brown (7.5YR 2.5/2) to dark brown (7.5YR 3/2) and lightens downcore, reflecting a relative decrease in the clay and an increase in the nanofossil component. Mottles are common in the radiolarian ooze. Contacts are gradational and heavily bioturbated. Diatoms, sponge spicules, and iron oxides are minor components, and foraminifers and volcanic glass are present in trace amounts.

Decimeter-scale alternations of nanofossil ooze with radiolarians and clay and nanofossil radiolarian ooze are present between 19 and 24 mbsf. These minor lithologies exhibit a marked increase in lightness and a decrease in the red/blue spectral ratio and range from yellowish brown (10YR 5/4) to dark brown (7.5YR 3/3) in color. Mottles are abundant and tend to be very pale brown (10YR 7/4) to yellowish brown (10YR 5/4).

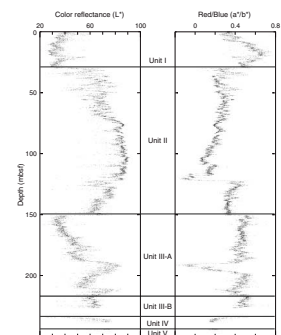
Unit II

Intervals: 199-1219A-4H-4, 54 cm, through 17H-2, 86 cm, and 199-1219B-2H-6, 82 cm, through 16H-1, 45 cm
 Depths: 30.0–150.8 mbsf (Hole 1219A) and 29.2–154.5 mbsf (Hole 1219B)
 Age: early Oligocene to early Miocene
 Lithology: nanofossil ooze and nanofossil ooze with radiolarians and clay

F7. Unit IV–V transition, p. 49.



F8. Lightness and red/blue spectral data, p. 50.



The dominant lithology in Unit II is nannofossil ooze, with significant siliceous components in the upper (radiolarians) and basal (radiolarians and clay) portions. Clay and radiolarian contents (as estimated from smear slides) generally remain below 20% and 30%, respectively. From ~30.0 to 77.5 mbsf, this unit contains alternations of nannofossil radiolarian ooze, nannofossil ooze with radiolarians, and nannofossil ooze with the radiolarian fraction decreasing downhole. These variations are expressed as decimeter- to meter-scale, light–dark color cycles. A decrease in the amplitude of these color cycles is present below ~50.0 mbsf (Fig. F8). The layers of nannofossil radiolarian ooze range from brown (10YR 5/3) to yellowish brown (10YR 5/4) and contain abundant mottles. Intervals of nannofossil ooze with radiolarians range from light gray (10YR 7/2) to very pale brown (10YR 8/2, 10YR 8/3) and are slightly mottled. The nannofossil ooze layers range from very pale brown (10YR 7/3) to pale brown (10YR 6/3) and are homogeneous. Contacts between interbeds are gradational and overprinted by bioturbation. Iron oxides, diatoms, and siliceous sponge spicules are a minor component. Zeolites and silicoflagellates are present in trace amounts. Granule-sized concretions and burrow molds are common from 44.0 to 53.7 mbsf, and calcite needles are a minor component (up to 10%) from 53.5 to 63.0 mbsf. Black (N1) concretions, also granule sized, are present infrequently from 63 to 72.5 mbsf. X-ray diffraction results are inconclusive about the mineralogy of the concretions, burrow molds, and nodules but do indicate that these features are not pyrite or manganese oxides.

From 77.5 to 122.8 mbsf, Unit II consists of nannofossil ooze. Below ~123 mbsf, nannofossil ooze alternates with nannofossil ooze with clay and nannofossil ooze with radiolarians. Faint decimeter- to meter-scale color cycles are present throughout this lithology. Nannofossil ooze ranges from very pale brown (10YR 8/3, 10YR 8/2, and 10YR 8/4) to white (10YR 8/1) and pink (7.5YR 8/3, 7.5YR 8/4). Nannofossil ooze with clay ranges from pink (7.5YR 8/4) to reddish yellow (7.5YR 6/6) and light gray (10YR 7/2). Nannofossil ooze with radiolarians is light gray (10YR 7/2). Lithologic cycles are expressed in the lightness and red/blue spectral data and are of smaller amplitude than in the overlying lithologies (Fig. F8). Mottles are rare to common and range from pink (7.5YR 8/3) to very pale brown (10YR 8/3) in color. *Zoophycos* is the only recognizable trace fossil. Black (N1) spots containing iron and manganese oxides are also common. Radiolarians and foraminifers are minor components, and iron oxides, zeolites, volcanic glass, sponge spicules, and diatoms are present in trace amounts.

The base of Unit II represents the lithologic transition associated with the E/O boundary (Figs. F5, F9) and is marked by a 24-cm-thick interval of nannofossil ooze with clay and radiolarians that is distinguished by a yellowish brown (10YR 5/4) color (interval 199-1219A-17H-2, 63–87 cm). Coring disturbance obscured this transition in Hole 1219B. Several fish teeth fragments are found near the base of this layer (Hole 1219A interval).

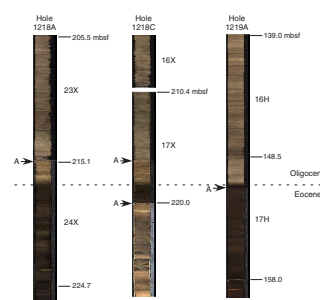
Unit III

Intervals: 199-1219A-17H-2, 86 cm, through 26X-1, 14 cm, and 199-1219B-16H-1, 45 cm, through 16H-6

Depths: 150.8 to 234.2 mbsf (Hole 1219A) and 154.5–158.0 mbsf (base of hole) (Hole 1219B)

Age: middle to late Eocene

F9. Cores from the upper Eocene–lower Oligocene, p. 51.



Lithology: radiolarian clay, radiolarian ooze, radiolarite, chert, and zeolitic clay

The dominant lithology in Unit III is radiolarian ooze, with a significant clay component in the upper and basal portions (up to 50%).

Subunit IIIA

Intervals: 199-1219A-17H-2, 86 cm, through 24H-CC, 24 cm, and 199-1219B-16H-1, 45 cm, through 16H-6

Depths: 150.8–224.5 mbsf (Hole 1219A) and 154.5–158.0 (base of hole) (Hole 1219B)

Age: middle to late Eocene

Lithology: radiolarian clay and radiolarian ooze

Between 150.8 and 224.5 mbsf, the principal lithologies are radiolarian clay, clayey radiolarian ooze, and radiolarian ooze. Clay content gradually decreases and color lightens downhole, but below 188.6 mbsf, sediments are more clay rich and become darker in color. Sediments range from very dark brown (10YR 2/2) to dark yellowish brown (10YR 3/4, 10YR 4/4). Compositional variations are expressed in the lightness and red/blue spectral data and are similar in amplitude to cycles in the base of Unit II. Mottles are common and range from strong brown (7.5YR 5/6) to reddish yellow (7.5YR 6/6) to black (10YR 2/1) in color. Some mottles contain minor amounts of pyrite and radiolarian ooze with volcanic glass. Contacts are gradational and are obscured by bioturbation. Diatoms are a minor component, and nannofossils and sponge spicules are minor to trace components. Iron oxides, volcanic glass, foraminifers, and fish teeth are present in trace amounts. Aggregates of manganese oxide minerals are found occasionally, and porcellanite and pyrite concretions are present in the basal section of the radiolarian ooze.

Between 176.0 and 224.5 mbsf, decimeter- to meter-scale intervals of radiolarian ooze with nannofossils alternate with radiolarian ooze. Layers of this minor lithology range from pink (7.5YR 8/4) to light yellowish brown (10YR 6/4) and very pale brown (10YR 7/4). Contacts are gradational and are obscured by bioturbation.

Several minor lithologies are present between 188.2 and 196.0 mbsf (interval 199-1219A-21H-2, 25 cm, through 21H-CC, 24 cm). This interval contains 2.9 m of diatom ooze underlain by 2.7 m of nannofossil ooze, 20 cm of radiolarian ooze, 1.7 m of nannofossil ooze, and 30 cm of diatom ooze. Components of radiolarians, diatoms, nannofossils, and clay are present in each of these oozes (0%–20%). The diatom ooze grades from very pale brown (10YR 8/4) to light greenish gray (5GY 8/1). Nannofossil ooze ranges from light greenish gray (5GY 8/1) to bluish white (5B 9/1). Radiolarian ooze is light gray (5YR 7/2). The basal nannofossil ooze and diatom ooze are very pale brown (10YR 8/1 and 10YR 8/2). Interbeds are clearly demarcated in the lightness and red/blue spectral data (Fig. F8). Mottles are common throughout these lithologies.

Several normal faults with minor offsets (<10 cm) are present within the radiolarian ooze, between 173.0 and 181.0 mbsf (intervals 199-1219A-19H-4, 75–105 cm; 19H-6, 52–81 cm; and 20H-3, 67–102 cm). Faults are high angle (~70°) and ~30 cm in length. Along the fault plane, there is a 1-mm-thick layer that is slightly darker than surround-

ing sediment, which may represent microfault gouge or authigenic precipitates.

Subunit IIIB

Interval: 199-1219A-25H-1, 0 cm, through 26X-1, 14 cm
Depth: 224.5–234.2 mbsf (Hole 1219A)
Age: middle Eocene
Lithology: radiolarite, chert, and zeolitic clay

Sediments below 224.5 mbsf were cored with the XCB system. Radiolarite and chert are the dominant lithologies in Subunit IIIB between 224.5 and 234.2 mbsf. Radiolarite ranges from reddish yellow (7.5YR 8/6) to pink (7.5YR 8/4) and is homogeneous. Chert is present from 226.8 to 234.2 mbsf (interval 199-1219A-25X-CC, 26 cm, through 26X-1, 14 cm). The chert and surrounding sediments were poorly recovered. Chert is brown (7.5YR 4/3) to black (7.5YR 2/1). The base of Unit III is marked by a 14-cm-thick layer of black (10YR 2/1) zeolitic clay with iron oxides, chert fragments, and trace amounts of nannofossils (interval 199-1219A-26X-1, 0–14 cm).

Unit IV

Interval: 199-1219A-26X-1, 14 cm, through 27X-CC, 27 cm
Depth: 234.2–244.8 mbsf
Age: early Eocene
Lithology: calcareous chalk

The dominant lithologies in Unit IV are calcareous chalk and calcareous chalk with clay. A brown (10YR 3/3) nannofossil chalk with clay comprises the upper 34 cm of this unit (interval 199-1219A-26X-1, 14–48 cm). Recrystallized calcareous chalk grades from light gray (10YR 7/3) to pale yellow (2.5Y 8/2). Examination of the calcareous chalk in smear slides indicates that nannofossils were the likely source of carbonate. Horizontal streaks and layers are common throughout the chalk and probably represent collapsed burrows. Small low-angle (30°–60°) normal faults are present between 235.1 and 236.7 mbsf (Sections 199-1219A-26X-1, 97, 100, and 104 cm, and interval 26X-2, 97–106 cm). The chalk is biscuitied and brecciated by XCB drilling disturbance.

Fragments of chloritized basalt and chalk comprise the basal 14 cm of Unit IV (interval 199-1219A-27X-CC, 13–27 cm), where the chalk dominating Unit IV overlies the basalt of Unit V. This lithology contains glassy, highly weathered basalt and is highly fragmented. Color ranges from grayish green (5GY 4/6) to brown (10YR 4/3).

Unit V

Interval: 199-1219A-27X-CC, 27 cm, to base of hole
Depth: 244.8–250.8 mbsf
Age: early Eocene
Lithology: basalt

The base of Core 199-1219A-27X contains weathered fine-grained phaneritic basalt. Millimeter-scale calcite veins are present within the basalt.

Discussion/Summary

At Site 1219, early Eocene seafloor basalt is overlain by 245 m of biogenic sediments and pelagic clays. Four sedimentary units and a basal basalt unit are identified and can be correlated to lithologic Units I–V at Site 1218 (Fig. F10) (see “Lithostratigraphy,” p. 7, in the “Site 1218” chapter) and Units 162-1 to 162-8 at DSDP Site 162 (van Andel et al., 1973).

Sediments present in the basal few centimeters of Subunit IIIA and in Subunit IIIB and Unit IV have experienced compaction and lithification with depth as indicated by the presence of porcellanite, chert, radiolarite, and chalk. Strongly flattened burrows in the chalk recovered in Unit IV indicate considerable compaction prior to cementation. The green to gray colors in Core 199-1219A-21H and the presence of pyrite indicates that low redox conditions prevailed after deposition. A zeolitic clay bed marking the top of the basal carbonate chalk at this site and Site 162 probably represents an interval of rapid dissolution, a hiatus, and/or altered volcanic ash. Unlike Sites 1217 and 1218, dolomite was not found in the basal carbonate chalk.

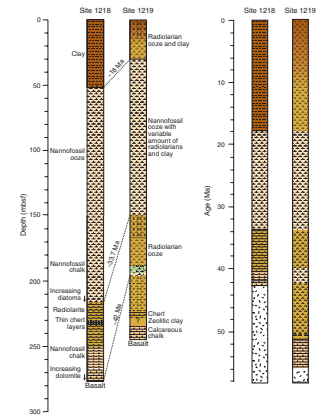
Nannofossil and calcareous chinks dominate the lower Eocene section and are capped by a zeolitic clay at ODP Site 1219 and DSDP Site 162. A transition to radiolarian ooze deposition occurred at 52 Ma. Long-term deposition of radiolarian ooze during the middle and late Eocene was interrupted from 42 to 40 Ma, and nannofossil ooze was deposited at all three sites. Nannofossils and radiolarians dominate at Site 1218 and DSDP Site 162, whereas diatoms are more common at Site 1219. Whether this represents regional differences in sedimentation regimes associated with the position of the site relative to the paleoequatorial productivity zone or differences in preservation (or recovery) between sites resulting in lithologic “alias” remains to be seen. All sites may have experienced episodes of diatom ooze deposition from 42 to 40 Ma, but this may not be represented at DSDP Site 162 because of recrystallization of surrounding nannofossil ooze and formation of chalk.

Siliceous sediments dominate the Paleogene section until the E/O boundary. Unlike at Site 1218, the E/O boundary section at Site 1219 was recovered using ODP’s APC technology (Figs. F5, F9) and a record of whole-core magnetostratigraphy was produced as a result (see “Paleomagnetism,” p. 21). A concentration of fish teeth is present in the E/O boundary section in 1219A, probably as part of a large fecal pellet. The transition to nannofossil-rich sediments at Site 1219 is seen at other sites in the region and probably represents a deepening of the CCD (van Andel et al., 1975).

Nannofossil ooze was deposited throughout the region during the Oligocene and into the early Miocene. Variations in clay and radiolarian content are expressed as light–dark color cycles and are evident in color reflectance and physical properties data (Fig. F8). Amplitude of lightness (L^*), red/blue spectral ratio (a^*/b^*), and gamma ray attenuation (GRA) bulk density data increases above ~50 mbsf, which corresponds to the O/M boundary. This change in amplitude is not seen in the MS data.

The O/M boundary section recovered at Site 1219, although similar to the record from Site 1218, is condensed. The Neogene section at this site, as at Site 1218 and DSDP Site 162, contains a transition from nannofossil ooze to noncarbonate deposition at ~18 Ma. However, Unit I at Site 1219 is dominated by a radiolarian biosiliceous component,

F10. Lithologic columns, Sites 1218 and 1219, p. 52.



whereas at Sites 1218 and 162 this interval is represented by an eolian component.

BIOSTRATIGRAPHY

A total of 250 m of middle Miocene–lower Eocene sediments and basalt. Calcareous and siliceous microfossils provide a well-defined biostratigraphy in the Miocene and Oligocene (Fig. F11A). Preservation of calcareous microfossils varies considerably through the section, and most assemblages are affected by some degree of dissolution. Planktonic foraminifers and calcareous nannofossils are absent from upper Eocene and upper middle Eocene strata, where stratigraphic subdivision is provided by radiolarian zonation and magnetostratigraphy. Weathered basalt is present below chalk assigned to the upper part of planktonic foraminifer Zone P5 and calcareous nannofossil Subzone CP8b. The volcanic basement is therefore slightly younger than the P/E boundary (~55 Ma) in contrast to the 56-Ma crust expected for this location.

The biostratigraphic results are summarized in Figure F11 and Tables T2, T3, T4, T5, T6, and T7.

Calcareous Nannofossils

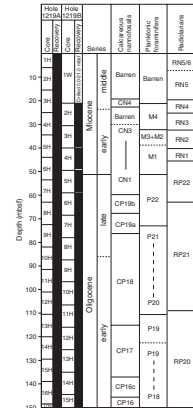
Detailed correlation between Holes 1219A and 1219B was achieved using MST data (see “Composite Depths,” p. 22). This report is, therefore, focused on the biostratigraphy of Hole 1219A. Depth positions and age estimates of biostratigraphic marker events are shown in Table T2.

Cores 199-1219A-1H and 2H are barren of calcareous nannofossils. Below this barren interval, assemblages show poor to moderate preservation. The first downhole occurrence of nannofossils is observed in Section 199-1219A-3H-3, containing a middle Miocene assemblage in which all components except discoasters are completely dissolved. The lower Miocene and Oligocene assemblages contain the best-preserved assemblages. But even these relatively well preserved assemblages are partially altered by dissolution. The Eocene carbonate-bearing sediments show poorly preserved nannofossil assemblages, often with abundant fragments of placoliths. Several barren intervals are observed within the Eocene that severely decreased the number of datums, thus reducing the biostratigraphic resolution. Abundant moderately to poorly preserved assemblages characterized the lowermost Eocene calcareous nannofossil assemblages in Cores 199-1219A-26X and 27X (Zones NP11, NP10, and NP9).

Miocene

Only middle Miocene discoasters are preserved in Sample 199-1219A-3H-3, 92 cm. Several samples in Section 199-1219A-3H-4 contain assemblages mainly consisting of *Discoaster* spp., such as *Discoaster deflandrei*, *Discoaster exilis*, *Discoaster musicus*, *Discoaster signus*, and *Discoaster variabilis*. Other assemblage components include poorly preserved specimens of abundant *Cyclicargolitus floridanus*, common *Coccolithus pelagicus*, and rare *Coronocyclus nitescens*, *Sphenolithus abies*, and *Sphenolithus heteromorphus*, placing Section 199-1219A-3H-4 in Zone NN5 or Zone NN4 (CN4/CN3). The upper half of Core 199-1219A-4H is barren. Nannofossils are present from Sample 199-1219A-4H-4, 90 cm,

F11. Lithologic columns showing the major units plotted vs. depth and age, p. 53.



and downcore. Rare *Discoaster druggii*, abundant *D. deflandrei*, rare *Triquetrorhabdulus carinatus*, and few *Orthorhabdus serratus* are present in Sample 199-1219A-4H-4, 140 cm, together with other typical lower Miocene species.

O/M Boundary

The calcareous nannofossils suggest a placement of the O/M boundary in Section 199-1219A-6H-6, where the range of *S. delphix* was observed. The first occurrence of this species is between Samples 199-1219A-6H-6, 120 cm, and 6H-7, 20 cm (56.97 ± 0.25 mcd) and correlates to Subchron C6Cn.2r (see “Paleomagnetism,” p. 21). On the Cande and Kent (1995) timescale, an age estimate of 24.28 ± 0.05 Ma is obtained for the base of *S. delphix* at Site 1219. Conversion to the orbitally tuned timescale of Shackleton et al. (2000), by subtracting 0.9 m.y. from the Cande and Kent (1995) timescale estimate, yields an age of 23.38 Ma for the base of *S. delphix*. This value is 0.14 m.y. older than the Shackleton et al. (2000) tuned estimate for this datum, which was derived from the eastern South Atlantic (DSDP Site 522) and the western equatorial Atlantic (ODP Sites 926, 928, and 929). Yet the calibration of *S. delphix* event to the geomagnetic polarity timescale is remarkably consistent in upper Subchron C6Cn.2r from the South Atlantic Ocean to the Mediterranean region (Raffi, 1999) and to the tropical Pacific Ocean (Site 1219).

Oligocene

The interval between the top of *Sphenolithus ciproensis* and the top of the abundance peak of *Cyclicargolithus abisectus* defines the *C. abisectus* subzone in Bukry’s (1973) zonal scheme (CN1a) (Okada and Bukry, 1980). *S. ciproensis* has its last occurrence above the abundance peak of *C. abisectus* in Hole 1219A. This is consistent with results obtained from Site 1218 indicating that Subzone CN1a is obsolete in this part of the tropical Pacific Ocean. Bukry (1973) used the top of *Dictyococcites bisectus* as an alternative marker for the base of Subzone CN1a. In Hole 1218A, this event is present 21.5 mbsf below the last occurrence of abundant *C. abisectus* in Subzone CP19a. This stratigraphic interval corresponds to a time interval of ~1.3 m.y. The distance between the top of abundant *C. abisectus* and the top of *D. bisectus* is even wider in Hole 1219A (46.1 m), where the latter event is present in lower Zone CP18, ~4.5 m.y. prior to the disappearance of *C. abisectus*. Taking into account the relatively short geographic distance between Sites 1218 and 1219 (~700 nmi but within 1° of latitude), the time transgressiveness exhibited by *D. bisectus* suggests that its stratigraphic distribution is influenced by a still unknown paleoecological factor. *D. bisectus* is, therefore, not suitable for recognition of the base of Subzone CN1a in the tropical Pacific Ocean.

The top and base of *S. ciproensis* and *Sphenolithus distentus*, respectively, are used for subdivision of a good portion of the Oligocene: the top of CP19b, the base of CP19b (base of NP25), the base of CP19a (base of NP24), and the base of CP18 (base of NP25 and base of NP24). These two species are consistently rare members of the Oligocene assemblages at the Leg 199 sites. They are also small (generally 3–5 µm high and 1–2 µm wide), making them difficult to observe in smear slides with dense concentrations of nannofossils. Thus, the low abundance and small size

of these biostratigraphic markers hinders accurate determination of their critical evolutionary transitions.

In Hole 1219A, we also determined that the last occurrence of *Sphenolithus pseudoradians* seems to have a distinct abundance decline preceding its extinction. The extinction occurs in Section 199-1219A-12H-5, in lower Zone CP18. *S. distentus* evolves just after a bloomlike occurrence of another sphenolith species, *Sphenolithus moriformis*. This bloomlike occurrence of *S. moriformis* was observed in Sample 199-1219A-13H-4, 80 cm. Core 199-1219A-13H also holds the first down-hole presence of the helicolith *Helicosphaera compacta*.

D. bisectus exhibits highly variable abundances in Core 199-1219A-15H, from absence in Sample 199-1219A-15H-6, 10 cm, to bloomlike abundances in Sections 199-1219A-15H-3 and 15H-4. *Reticulofenestra umbilicus* has its last occurrence (NP22/23 and CP16c/CP17 boundaries) in the upper part of Section 199-1219A-15H-6. *Ericsonia formosa* has its last occurrence (NP21/NP22 and CP16b/CP16c boundaries) in Section 199-1219A-16H-5. Section 199-1219A-17H-2 shows another bloomlike occurrence of *Dictyococcites* spp., including exceptionally large (>15 µm) specimens of *D. bisectus*.

Core 199-1219A-17H contains a change in lithology and color, reflecting a shift in the position of the Paleogene CCD. This change occurs within Zone NP21 (CP16a+b) above the extinction of the final Eocene discoasters, which is consistent with the results from Site 1218. Cores 199-1219A-18H and most of 19H are barren of calcareous nanofossils. An interval from Samples 199-1219A-19H-7, 5 cm, through 20H-2, 135 cm, contains nanofossils. Only discoasters are preserved in these two end-member samples, but intervening samples contain a more diverse assemblage, consisting of *Chiasmolithus grandis*, *C. pelagicus*, *Coccolithus eopelagicus*, *Dictyococcites hesslandii*, *D. bisectus*, *Dictyococcites barbadiensis*, *Dictyococcites nodifer*, *Dictyococcites saipanensis*, *Dictyococcites tanii*, *Reticulofenestra dictyoda*, *R. umbilicus*, and *S. moriformis*. The co-occurrence of *C. grandis* and *D. bisectus* places this assemblage in Zone NP17 (CP14b).

Another barren interval exists from Samples 199-1219A-20H-3, 90 cm, to 21H-2, 30 cm. Sections 199-1219A-21H-3 through 21H-7 contain middle Eocene assemblages. *Dictyococcites* spp. are no longer members of these assemblages that contain *Discoaster binodosus*. The first occurrence of *R. umbilicus* defines the CP13/CP14a boundary. This boundary is observed in Section 199-1219A-22H-3 using a minimum size of 14 µm for *R. umbilicus*. The top of *Nannotetrina* spp. is observed in Sample 199-1219A-22H-CC, which also contains *Discoaster bifax*, *D. binodosus*, *Discoaster gemmifer*, *Discoaster septemradiatus*, *Discoaster wemmelensis*, *Pseudotriquetrorhabdulus inversus*, among other middle Eocene taxa. Bukry (1973) used the evolutionary appearance of both *R. umbilicus* and *D. bifax* for recognition of the base of Subzone CP14a. At Site 1219, *D. bifax* evolves before *R. umbilicus* when applying the 14-µm minimum size concept for *R. umbilicus*.

The total range of *Nannotetrina fulgens* is used for recognition of Zone NP15 (CP13). A few well-developed specimens of this species are observed in lowermost Core 199-1219A-23H and uppermost Core 24H. The lowermost nanofossil-bearing sample here is 199-1219A-24H-4, 100 cm, holding only a sparse discoaster assemblage, including *D. gemmifer*, *D. mirus*, *D. septemradiatus*, and four- to six-rayed *Discoaster strictus*. This sample is also characterized by obvious *Discoaster subbloedensis* in the absence of *Nannotetrina* spp., suggesting a position not far from the NP14/NP15 (CP12b/CP13a) boundary.

The interval from Section 199-1219A-24H-2 to uppermost 26X-1 is barren of calcareous nannofossils.

Sample 199-1219A-26X-1, 40 cm, contains an odd, virtually monospecific assemblage consisting of abundant *Tribra-chiatus orthostylus*, together with a few *D. binodosus*, *Discoaster diastypus*, and *Discoaster multi-radiatus*, placing this sample in Zone NP11 (CP9b). The NP10/NP11 (CP9a/CP9b) boundary is observed shortly below, in Section 199-1219A-26X-1. The degree of recrystallization of the *Rhomboaster-Tibra-chiatus* lineage increases downhole, preventing recognition of the base of *Tribra-chiatus bramlettei* and the NP9/NP10 (CP8b/CP9a) boundary. Yet, *Tribra-chiatus contortus* is recognized down to Sample 199-1219A-26X-2, 11 cm, indicating a position within the upper half of Zone NP10. Samples 199-1219A-26X-CC through 27X-CC contain a fairly diverse lowermost Eocene assemblage, including *Chiasmolithus bidens*, *Cruciplacolithus tenuis*, *D. multiradiatus*, *Neochiastozygus junctus*, *Placozygus sigmoides*, *Prinsius bisulcus*, *Sphenolithus primus*, and *Toweius pertusus*. Members of the genus *Fasciculithus* were not observed in any of the samples investigated from the two lowermost cores, indicating a position in upper NP9 (CP8b), which is still within the lowermost Eocene, for Sample 199-1219A-27X-CC.

Planktonic Foraminifers

The initial two cores of radiolarian ooze and clay (lithologic Unit I) were barren of planktonic foraminifers, but, starting in Core 199-1219A-3H, the nannofossil-radiolarian ooze and clay contained planktonic foraminifers of Miocene age. A record of lower Miocene–lower Oligocene planktonic foraminifers was obtained between Cores 199-1219A-3H and 17H (32–150 mbsf). Abundance levels and preservation quality fluctuate considerably during this interval, with preservation optima in the lower Miocene (Zones M4–M2) and the middle part of the Oligocene (Zones P20–P21) when, presumably, the CCD was deepest. The O/M boundary is well resolved in Hole 1219A at ~51 mbsf. In terms of preservation and species abundance, the Miocene and Oligocene assemblages are very similar to those found at Site 1218, although the genus *Catapsydra* is less common at Site 1219 than at Site 1218. Preservation deteriorates greatly in the lower Oligocene, and the radiolarian oozes of the Eocene–Oligocene through middle Eocene are completely devoid of planktonic foraminifers. Planktonic foraminifers become abundant again in the lower Eocene calcareous chalk overlying basement. This chalk contains poorly to moderately well preserved assemblages, which are assigned to Subzones P6b to upper P5, indicating a younger age (<55.0 Ma) for the crust at this site than was previously estimated by magnetic seafloor anomaly patterns and hotspot reference backtracking. Planktonic foraminifer distributions are listed in Tables T3 and T4. Datum levels of planktonic foraminifers are given in Table T5 and are illustrated in Figure F11.

Planktonic foraminifers can be used to delineate a short lower Miocene sequence. The youngest samples (199-1219A-3H-4, 103–108 cm, through 3H-CC) contain rare specimens of *Globoquadrina venezuelana*, species belonging to the *Globoquadrina tapuriensis-dehiscens* group, *Paragloborotalia mayeri*, *Paragloborotalia nana*, and *Globoquadrina prasaepis*. Preservation improves slightly in Samples 199-1219A-3H-CC and 4H-4, 136–140 cm. Also present in these samples are *Dentoglobigerina altispira*, *Dentoglobigerina galavisi*, *Dentoglobigerina yeguaensis*, *Globoquadrina dehiscens*, and *Globoquadrina rohri*. Based on the absence of *Catapsydrax dis-*

similis, which is less susceptible to dissolution than most species, these samples are assigned to Zone M4 or younger parts of the Miocene. The first downhole occurrence of *C. dissimilis ciproensis* is in Sample 199-1219A-4H-5, 115–120 cm. The subsequent interval, between this sample and 5H-1, 50–55 cm, consistently contains *C. dissimilis* in the absence of *Paragloborotalia kugleri* and is thus assigned to the zonal range M2–M3. The boundary between these zones could not be differentiated because of the absence of *Globigerinatella insueta*.

The highest occurrence of *P. kugleri* is present in Sample 199-1219A-5H-4, 130–135 cm (40.3 mbsf), and defines the top of Subzone M1b. Samples from this interval (Samples 199-1219A-5H-4, 130–135 cm, to 6H-6, 63–65 cm) contain relatively diverse, moderately well preserved planktonic foraminifers. As in the younger samples, species in the *Globoquadrina tripartita* and *G. dehiscens* group are common, with large inflated forms of *G. sellii* and *Globoquadrina tapuriensis* being distinctive elements. *D. altispira* and *Dentoglobigerina globulosa* are also found frequently. Notably rare from the Site 1219 assemblages, as at Site 1218, are representatives of the *Globigerinoides primordius* and *Globigerinoides triloba* groups. The extremely rare occurrence and poor preservation of both species in the Miocene at Site 1218 suggest high susceptibility to dissolution.

The O/M boundary is recognized between Samples 199-1219A-6H-5, 5–7 cm, and 6H-6, 63–65 cm (~51 mbsf), based upon the rare occurrence of *P. kugleri*. This datum could also be drawn slightly lower (between Samples 199-1219A-6H-6, 63–65 cm, and 6H-CC; ~53 mbsf) based on the occurrence of a single corroded specimen of *P. kugleri*. The 2-m difference in the placement of the biostratigraphic datum is significant because this event at Site 1219 could be moved from Subchron C6Cn.2r to Chron C6Cr, a difference of ~0.5 Ma in the Cande and Kent (1995) timescale. It will be necessary to conduct much more detailed counts of the distribution of *P. kugleri* to determine its true first occurrence relative to the Site 1219 magnetostratigraphy. However, we note that the placement of the first occurrence datum of *P. kugleri* in the middle of Subchron C6Cn.2r agrees closely with the similar correlation at Site 1218.

Berggren et al. (1995) calibrated the appearance of *P. kugleri* to the base of Subchron C6Cn.2n from Atlantic Ocean DSDP sites. The internal consistency of the position of the base of *P. kugleri* and the calcareous nannofossil species *S. delphix* relative to the geomagnetic polarity record appears to suggest that both events in the Pacific are consistent within ~140 k.y. or less of the same events in the Atlantic (see “**Calcareous Nannofossils**,” p. 13).

Planktonic foraminifer preservation declines in the upper Oligocene compared to the basal Miocene but then improves again just below the Zone P21b/P22 boundary (~73.3 mbsf). Overall species diversity of planktonic foraminifers reaches its highest level (19 species) in the middle of Zone P21b, attesting to the moderate to good preservation of both thin-walled and small-sized species that are ordinarily absent from most other samples at Site 1219. However, even the best-preserved samples still show fragmentation in the <63- μ m fraction and corrosion of the walls of dissolution-prone species. The highest occurrence of *Paragloborotalia opima opima* (marker for the top of Subchron P21b) is very well defined because this species is very abundant just before its extinction level. Accessory species within Subzone P21b include *Dentoglobigerina pseudocontinua*, *D. yeguaensis*, and tenuitellids such as *Tenuitella clemenciae* and *Tenuitella angustiumbilitata*. Species that range across the

Zone P21b/P22 boundary include *G. tapuriensis*, *G. tripartita*, *G. prasaepis*, and *Globorotaloides suteri*. *C. dissimilis ciproensis* first becomes a regular constituent below the Zone P21b/P22 boundary at Site 1219, in contrast to its abundance throughout the Miocene and Oligocene at Site 1218.

We are unable to differentiate Zones P21 or P20 owing to the absence of either *Globigerina angulituralis* or *Chiloguembelina cubensis* at Site 1219. However, the highest occurrence of *Turborotalia ampliapertura* is present in Sample 199-1219A-12H-CC, 24–30 cm (111.10 mbsf), and identifies the top of Zone P19. A distinct drop in planktonic foraminifer abundance, preservation state, and species richness occurs at ~106 mbsf in Core 199-1219A-17H and renders the last occurrence of *T. ampliapertura* as a potentially unreliable datum level. Species typical of Zone P19 include dissolution-resistant taxa such as *C. dissimilis ciproensis*, *G. suteri*, *P. nana*, and *P. opima opima*.

The first occurrence of *P. opima opima* could not be determined reliably at Site 1219, owing to intervals of rarity or complete absence of planktonic foraminifers between Samples 199-1219A-14H-2, 53–58 cm (122 mbsf), and 15H-3, 100–105 cm (133.5 mbsf). Single specimens of *C. dissimilis*, *Catapsydrax unicavus*, and occasional *Subbotina euapertura* typify these dissolved assemblages. Planktonic foraminifers are completely absent between Sample 199-1219A-17H-2, 104–106 cm (roughly the level of the E/O boundary according to calcareous nannofossil stratigraphy and magnetostratigraphy), and the top of Core 26X.

The chalk encountered in Cores 199-1219A-26X and 27X contains a moderately to poorly preserved assemblage of lower Eocene planktonic foraminifers. The presence of *Morozovella formosa* in Sample 199-1219A-26X-CC, 21–24 cm, in the absence of *Morozovella aragonensis*, suggests that the sample belongs to Subzone P6b. *M. formosa* was not found in shallower samples from Core 26X, but the continued absence of *M. aragonensis* and the abundance of *Morozovella gracilis*, *Morozovella subbotinae*, *Acarinina soldadoensis*, *Acarinina quetra*, and *Acarinina coalingensis* is typical of Subzone P6b assemblages at other Leg 199 sites.

Sample 199-1219A-27X-1, 19–21 cm, contains *Morozovella oclusa* and *Morozovella acuta*, both species that become extinct at the top of Zone P5 (~54.7 Ma). We do not find the zone marker for the upper boundary of Zone P5, *Morozovella velascoensis*, but we do find several species that make their first appearance at or above the P/E boundary, including *Pseudohastigerina wilcoxensis* and *Chiloguembelina wilcoxensis*, both of which also occur in Section 199-1219A-27X-CC. In as much that the bottom of Section 199-1219A-27X-CC recovered weathered basalt, it appears that the seafloor age is very close to, but slightly younger than, the P/E boundary (~55 Ma) and belongs to the middle of Chron C24r, rather than the expected Chron C25n.

Benthic Foraminifers

Benthic foraminifers are consistently present through the Miocene and Oligocene cores at Site 1219 but are scarce and very poorly preserved through much of the Eocene section. Foraminiferal assemblages consisting of only agglutinated foraminifers are present in Samples 199-1219A-1H-CC through 3H-CC, 17H-CC, 18H-CC, and 24X-CC. The walls of agglutinated forms are well preserved in Samples 199-1219A-1H-CC through 3H-CC but often became fragmented during the sample treatment. Calcareous foraminifers are moderately well preserved in Samples 199-1219A-4H-CC and -5H-CC, but preservation improves rap-

idly in most of the Miocene and Oligocene. Samples 199-1219A-6H-CC through 16H-CC are well preserved. Preservation of both calcareous and agglutinated foraminifers deteriorates through Eocene Samples 199-1219A-17H-CC through 19H-CC, 21H-CC, 23H-CC through 24H-CC, 26X-CC, and 27X-CC, with most assemblages very poorly preserved. Benthic foraminifers are barren in Samples 199-1219A-20H-CC, 22H-CC, and 25X-CC. The distribution of benthic foraminifers is reported in Table T6.

Miocene benthic assemblages are characterized by *Siphonodosaria abyssorum*, *Oridorsalis umbonatus*, *Globocassidulina* spp., *Cibicidoides* spp., *Pleurostomella* spp., and *Gyroidinoides* spp., all of which are common in bathyal and abyssal depths. *Nuttallides umbonifer* is rare, but it is consistently present in Miocene Samples 199-1219A-5H-CC and 6H-CC. This species indicates the influences of carbonate-corrosive Antarctic Bottom Water at this site. *Epistominella exigua* occurs in low abundance in Samples 199-1219A-5H-CC and 6H-CC. The presence of this species indicates a supply of phytodetritus into the deep sea (Nomura, 1995).

Oligocene benthic assemblages are characterized by *O. umbonatus*, *Cibicidoides* spp., *Globocassidulina* spp., *Pullenia* spp., and various nodosulids and dentalinids. Large specimens of *O. umbonatus*, *Cibicidoides grimsdalei*, and *Cibicidoides eocaenus* are found in Samples 199-1219A-7H-CC through 16H-CC. Both of the *Cibicidoides* species indicate bathyal to abyssal paleodepths (van Morkhoven et al., 1986). *N. umbonifer* is rare in Samples 199-1219A-7H-CC through 10H-CC but becomes more common in 10H-CC. The latter sample also contains a number of thin-walled taxa such as *Chilostomella* sp. and *Francesita advena*. *Astrononion echolsi* is found in Sample 199-1219-16H-CC, which is a long-ranging (upper Paleogene–Neogene) species and of little stratigraphic use. It is reported to be particularly common in the Antarctic region (Nomura, 1995). The co-occurrence of *A. echolsi* and *N. umbonifer* in Sample 199-1219A-16H-CC indicates the influence of Antarctic Bottom Water at this site in the early Oligocene (Nomura, 1995).

Eocene benthic foraminifers are strongly affected by diagenetic changes, with the test walls of benthic foraminifers often showing the signs of chemical etching. Rare calcareous foraminifers are found in Samples 199-1219A-19H-CC, 21H-CC, and 23H-CC and are also affected by diagenesis.

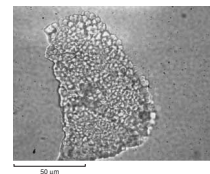
In order to examine foraminiferal preservation in more detail, test walls of several species in Sample 199-1219A-5H-CC were observed with a polarizing microscope. Observations reveal that the radial texture of *E. exigua* has been lost and that microscopic crystals have grown on the test surface to give a granular appearance (Fig. F12). The granular texture of *O. umbonatus* and *Globocassidulina* sp. has also been destroyed by calcite overgrowth on the walls.

Radiolarians

Radiolarians are present in all recovered material except for the deepest core (199-1219A-27X). Preservation and abundances are poor and rare in the first core but are generally good to very good and common to abundant in all other material. The sediments range in age from middle Miocene (Zone RN5) to middle Eocene (Zone RP12).

Core 199-1219A-1H and the upper part of 2H contain a mixed assemblage of species found in Zones RN5 and RN6. However, the samples from Sample 199-1219A-2H-CC and 3H-3, 45–47 cm, can be assigned to

F12. Photomicrograph of the radial wall texture of *Epistominella exigua*, p. 55.



middle Miocene Zone RN5 as shown by the evolutionary transition of *Dorcadospyris dentata* to *D. alata*. Zone RN4 in the lower Miocene extends to the base of Core 199-1219A-3H, and Zone RN3 is found in Samples 199-1219A-4H-1, 90–92 cm, to 4H-5, 46–48 cm. The boundary between Zones RN4 and RN3 is better defined in Hole 1219B between Samples 199-1219B-2H-2, 45–47 cm, and 2H-3, 45–47 cm. The boundary between Zones RN2 and RN1 is between Samples 199-1219A-5H-4, 45–47 cm, and 5H-5, 45–47 cm.

For radiolarian biostratigraphy, the first occurrence of *Cryptocapsella tetrapera*, which defines the boundary between Zones RN1 and RP22, serves as a good approximation to the O/M boundary (Sanfilippo and Nigrini, 1995). In Hole 1219A, this boundary lies between Samples 199-1219A-6H-1, 45–47 cm (which is also rich in diatoms), and 6H-2, 45–47 cm. As expected, the radiolarian zonal boundary lies somewhat above the first occurrence of *S. delphix* (between Samples 199-1219A-6H-6, 120 cm, and 6H-7, 20 cm [Subchron C6Cn.2r]) and the first occurrence of *P. kugleri* (between intervals 199-1219A-6H-5, 5–7 cm, and 6H-6, 63–65 cm [Subchron C6Cn.2r], or between Samples 199-1219A-6H-6, 63–65 cm, and 6H-CC [Subchron C6Cn.2r]). In Hole 1219A, the boundary between Zones RN1 and RP22 lies at the base of Subchron 6CBn.2n, which is in reasonably good agreement with the Chron C6Br level found in Hole 1218A. The boundary between Zones RP22 and RP21 lies between Samples 199-1219A-7H-CC and 8H-1, 43–45 cm, but is better constrained in Hole 1219B between Samples 199-1219B-6H-2, 46–48 cm, and 6H-3, 46–48 cm.

The boundary between the upper Oligocene Zone RP21 and late Oligocene Zone RP20 is formally defined as the evolutionary transition from *Tricerospyris tricerus* to *Dorcadospyris ateuchus*. However, in Hole 1219A, it was found that these species are rather rare near their transition, and so the first occurrence of *Theocyrtis annosa* is used instead, placing the boundary between Samples 199-1219A-12H-6, 45–47 cm, and 12H-7, 45–47 cm. Zone RP20 extends to Sample 199-1219A-17H-4, 15–17 cm. Most of the lower Oligocene samples are rich in diatoms.

Zone RP19 crosses the E/O boundary and is present in a relatively short sequence between Samples 199-1219A-17H-5, 32–34 cm, and 17H-CC. The boundary between Zones RP19 and RP18 could not be further constrained by material from Hole 1219B. Zone RP18 is also relatively short extending only to Sample 199-1219A-18H-3, 45–47 cm. Zone RP17 crosses the middle–upper Eocene transition and is present between Samples 199-1219A-18H-4, 45–47 cm, and 19H-4, 45–47 cm. The rest of the recovered material lies within the middle Eocene. Zone RP16 lies between Samples 199-1219A-19H-5, 45–47 cm, and 20H-5, 45–47 cm; Zone RP15, between Samples 20H-6, 45–47 cm, and 22H-3, 46–48 cm; Zone RP14, between Samples 22H-4, 46–48 cm, and 23H-5, 45–47 cm; Zone RP13, between Samples 23H-6, 45–47 cm, and 24H-2, 45–47 cm; and Zone RP12 extends from Samples 24H-3, 45–47 cm, through 25X-CC. The base of Zone RP15 is rich in diatoms. All zonal boundaries from RN5 to RP12 (Sanfilippo and Nigrini, 1998) are recognized (Table T7) and could be placed between successive samples, usually from one core section to the next. First and/or last occurrences of seven species and one evolutionary transition, for which numerical ages have previously been determined in conjunction with paleomagnetic data (see Table T3, p. 61, in the “Explanatory Notes” chapter), could be placed within 1- to 2-m intervals.

PALEOMAGNETISM

A total of 39 cores from Holes 1219A and 1219B were measured on the shipboard pass-through cryogenic magnetometer. The NRM was measured at 5-cm intervals in each core section, followed by three to four steps of AF demagnetization up to a maximum peak field of 20 mT. XCB cores from Hole 1219A were not measured with the pass-through system because they are made up of short “biscuits” and the information obtained from a given core would not contribute any interpretable directional data. In addition to core measurements, numerous discrete samples were taken from Hole 1219A cores to conduct more detailed progressive demagnetization. Only a few core sections from Site 1219 were in poor condition, mostly because of drilling disturbance, and were not used for paleomagnetic study.

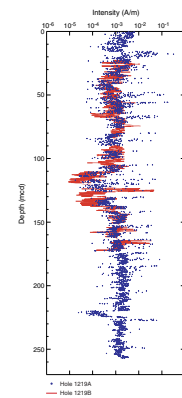
NRM intensities were in the order of 10^{-1} to 10^{-2} A/m and decreased to about 10^{-3} to 10^{-2} A/m after partial AF demagnetization (Fig. F13). Cores 199-1219A-12H and 199-1219B-10H and 11H had the weakest NRM intensity, dropping to $\sim 10^{-5}$ A/m after AF demagnetization, which is close to the noise level of the magnetometer. The drilling-induced overprint was mostly removed with AF demagnetization, typically disappearing by 10 mT. Some magnetic directions did not reach a stable point between 15 and 20 mT, and a large group of samples from Core 199-1219A-23H retained steep inclinations, suggesting that the characteristic remanent magnetization (ChRM) has not been fully isolated in these samples.

Discrete Sample Analysis

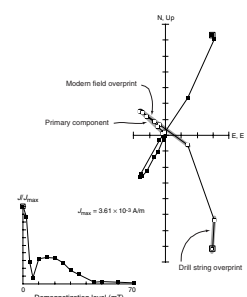
About 250 discrete samples (8-cm³ plastic cubes) were collected from Hole 1219A, and 125 of them were AF demagnetized. The aim of these measurements was to investigate the stability of the remanent magnetization and compute a more faithful ChRM direction based on progressive demagnetization instead of blanket demagnetization. About 60% of the discrete samples gave stable ChRM directions, and 40% showed erratic behavior during demagnetization. The average inclination of discrete samples from Cores 199-1219A-23H and 24H is 3.2° ($\alpha_{95} = 2.3^\circ$). Overall, declination and inclination patterns show that at least the lower part of the section was located in the Southern Hemisphere during deposition. The obtained mean inclination indicates a time-averaged paleolatitude of 1.6°S for the site, but this result is preliminary and will require further testing. The paleolatitude inferred from the inclination is consistent with the expected latitudes as calculated from both paleomagnetic pole positions (Petronotis et al., 1994) and those based upon a fixed hotspot model.

Using narrow demagnetization steps, it is possible to distinguish several soft components in some samples (Fig. F14). A very low coercivity component with a very steep downward direction, which is removed by 2 mT, is attributed to the drill string overprint. In addition, we found a second overprint, removed between 4 and 10 mT, which most likely represents a viscous component parallel to the present-day geomagnetic field. A mean inclination of this overprint component gives a value of 24° ($\alpha_{95} = 4^\circ$), which is statistically indistinguishable from the present-day magnetic inclination at the site ($\sim 20^\circ$). The mean paleolatitude (8°) measured from discrete samples from Cores 199-1219A-1H and 2H represents the mean latitude between the present

F13. Magnetization intensities after AF demagnetization, p. 56.



F14. Magnetically soft overprint used to reorient cores, p. 57.



and 5 Ma. This value is very close to the expected present-day value of 7.8° and increases our confidence on the reliability of the paleomagnetic directions in these sediments. Samples displaying such a clear present-day field overprint have been used to orient the uppermost two cores from Hole 1219A that were not oriented using the Tensor tool as well as those cores that had unsatisfactory orientations.

Magnetic Polarity Stratigraphy

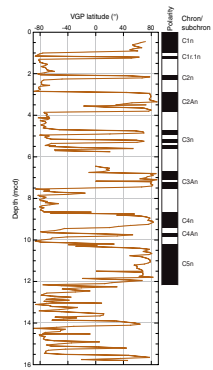
Data from only a few sections from Hole 1219A and 1219B had to be discarded because of core disturbance. For example, no reliable direction was obtained from Cores 199-1219A-12H and 199-1219B-10H and 11H because of the weak magnetic intensity; therefore, the polarity record in this interval has not been interpreted. Directions obtained from Core 199-1219A-18H show a distribution into several clusters corresponding to the different sections with an apparent clockwise rotation downcore. We suggest that this is a consequence of coring-induced internal deformation or some sort of unrecognized distortion that occurred during coring or handling of the core before cutting it. Thereafter, a rotation was applied to the magnetization directions in an attempt to recover the original orientation. The magnetization intensity (Fig. F13) shows many large spikes that often reflect spurious changes in the direction. This has to be taken into account in the interpretation of the directional results. The composite magnetic stratigraphy at Site 1219 spans the interval from the Pleistocene (C1n or Brunhes Chron) to the middle Eocene (Chron C20r).

The uppermost part of this stratigraphy obtained from Cores 199-1219A-1H and 2H, which were oriented using the inferred present geomagnetic field soft-component overprint, is shown in Figure F15. This record gives the only available age information for this part of the section. The oldest identified Chron, C20r, has only been partially recovered (Fig. F16B). The interval between 183 and 191 mcd, comprising Core 199-1219A-18H, does not show a clear pattern of magnetozones. Chron C15n was not unambiguously recognized, and hence, the results from this interval should be taken with caution. Chron C12r is clearly recognized, although quite noisy, perhaps because of the presence of cryptochrons. We are confident that we can also recognize Chron C13n, its lower boundary occurring at 176.3 mcd (Fig. F16). Paleontological events (for NP zones see “Calcareous Nannofossils,” p. 13, in “Biostratigraphy”) corroborate the presence of the E/O boundary at around the suggested C13n/C13r reversal. No data are available from 12 to 20 mcd and from 110 to 130 mcd because of weak magnetization or because the results were not interpretable. Some other intervals with no data reflect incomplete core recovery (see “Composite Depths,” p. 22).

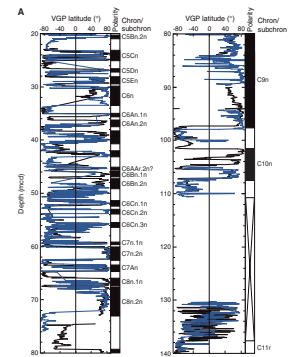
COMPOSITE DEPTHS

A composite section was constructed for the upper 173 mcd of Site 1219 using MST and color reflectance data to determine depth offsets between cores in Holes 1219A and 1219B (Figs. F17, F18, F19). In Hole 1219A, MS and color reflectance data were collected at 2-cm intervals, and GRA bulk density at 4-cm intervals down to Core 199-1219A-16H, below which GRA bulk density data were acquired at 2-cm intervals. GRA bulk density data were collected at 2-cm intervals throughout Hole 1219B. In Hole 1219A, P-wave velocity data were collected at 2-cm in-

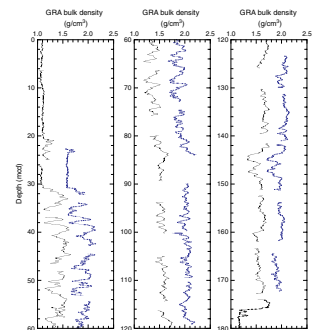
F15. Magnetostratigraphy of the upper 12 mcd, Hole 1219A, p. 58.



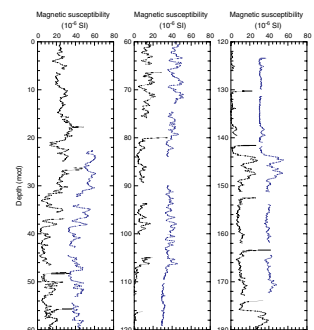
F16. Composite magnetic stratigraphy, p. 59.



F17. GRA bulk density plotted vs. composite depth, p. 61.



F18. MS plotted vs. composite depth, p. 62.

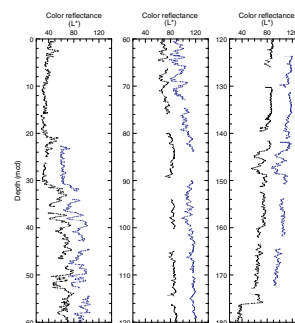


tervals through Core 199-1219A-24H. No *P*-wave data were collected in the XCB portion of Hole 1219A. Minolta color reflectance data were collected on cores from both holes at 2-cm intervals. Readings from the natural gamma ray (NGR) instrument showed only background radiation levels below ~30 mbsf. This component from the MST assemblage was only run on Hole 1219A cores. Disturbed intervals, as determined by visual inspection of split cores, are listed in Table T8. Data from these intervals were removed prior to correlation work. Table T9 lists the offsets that were applied to cores from each hole to create a composite depth record.

Cores from Site 1219 overlap and form a continuous sedimentary sequence down to ~130 mcd (base of Core 199-1219B-11H), with the exception of two apparent gaps at ~90 mcd between the base of Core 199-1219A-9H and the top of Core 199-1219B-8H and at ~100 mcd between the base of Core 199-1219A-10H and the top of Core 199-1219B-9H. Between 130 and 173 mcd, cores were placed into a composite depth framework, but a continuous section could not be constructed over this interval because gaps were aligned and it was not always possible to establish the true stratigraphic position of the cores. For example, Cores 199-1219A-14H and 199-1219B-13H can be correlated to each other but not to cores above or below. Figures F17 and F18 show that in this interval between 142 and 151 mcd the position of these cores is not constrained with respect to Hole 1219A or other intervals above or below in either hole. The first core from Hole 1219B recovered sediment from 23 mbsf and below, so there is no spliced record available for the interval covered by Cores 199-1219A-1H through 3H. However, this interval of predominantly red clay was recovered in the site survey piston Core EW9709-12PC (Lyle, 2000). There is a problematic interval at the base of Core 199-1219A-6H and the top of Core 7H, where paleomagnetic data from both holes imply that these two cores overlap by nearly 2 m. Although visual inspection of the top of Core 199-1219A-7H does not show any evidence for disturbance, the MST data for the top three sections of this core are strikingly different than equivalent intervals in Hole 1219B.

Following construction of the composite depth section for Site 1219, a single quasi-continuous spliced record was assembled for the aligned cores down to ~173 mcd by patching across core gaps with data from Holes 1219A and 1219B (Table T10; Fig. F20). Intervals having significant disturbance or distortion (see Table T8) were avoided. The Site 1219 splice can be used as a sampling guide to recover a nearly continuous single sedimentary sequence between 0 and 173 mcd, although individual cores below 132 mcd are merely appended to the core above and the true stratigraphic position of these cores is unconstrained. When utilizing this splice as a sampling guide, it is advisable to overlap a few decimeters from different holes when sampling in order to accommodate anticipated ongoing development of the depth scale. Stretching and compression of sedimentary features in aligned cores indicates distortion of the cored sequence. Because much of the distortion occurs within individual cores on depth scales of <9 m, it was not possible to align every feature in the MST and color reflectance records. However, at crossover points along the splice (Table T10), care was taken to align highly identifiable features from cores from each hole. Postcruise work will establish a detailed correlation between holes by establishing a revised meters composite depth scale that allows differential stretching and squeezing within cores, following Hagelberg et al. (1992).

F19. Color reflectance data plotted vs. composite depth, p. 63.

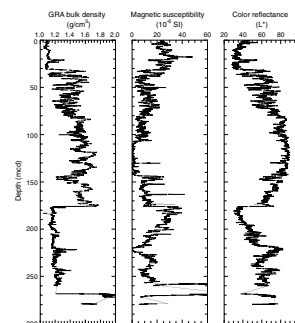


T8. Core disturbance intervals, p. 107.

T9. Composite depth offsets, p. 108.

T10. Splice tie points, p. 109.

F20. Spliced records of GRA bulk density, MS, and color reflectance parameter vs. composite depth, p. 64.



The MST data from Site 1219 bear a striking resemblance to those recovered from Site 1218 (see “**Composite Depths,**” p. 21, in the “Site 1218” chapter) from the uppermost Eocene–lowest Miocene interval. The excellent match between the two sites made it possible to align both records on a common (Site 1218 mcd) depth scale (Fig. F21). The two records show such correlation (down to the submeter scale) that a priori prediction of biostratigraphic zones and paleomagnetic reversals was possible at Site 1219. The correlation between the mcd scales from both sites will allow the postcruise evaluation of missing intervals from either site as well as the determination of core gaps in intervals from Site 1219 where no continuous overlap was achieved. The mapping from Site 1219 mcd to Site 1218 mcd (see bottom of Fig. F21) results in relative sedimentation rates at Site 1218 that are ~16% higher than Site 1219 over the Oligocene interval.

Downhole logging data were collected from Hole 1219A (see “**Downhole Measurements,**” p. 33), which will allow a detailed postcruise core to log correlation and integration. The detailed match between Site 1218 and 1219, established from the MST data, will also facilitate a detailed log-to-log correlation from both sites.

SEDIMENTATION AND ACCUMULATION RATES

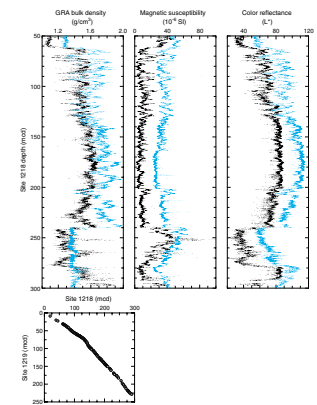
All the principal biostratigraphies, plus a good set of paleomagnetic reversals, are defined in Holes 1219A and 1219B (Tables T11, T12). Paleomagnetic reversals are used to calculate the average linear sedimentation rates (LSRs) for Site 1219 through most of the section. An unusually good set of magnetic reversals were obtained in the slowly accumulating near-surface sediments, and these extend through the section recovered by APC methods (Table T11). The age of the base of the hole is based on the top of the planktonic foraminifer *M. acuta* datum (54.25 Ma) (Table T12).

Calcareous nannofossils and radiolarians are present in the uppermost part of the section; however, reworking of the radiolarians make their biostratigraphic events less reliable (Fig. F22). The two uppermost nannofossil events lie close to the uppermost paleomagnetic reversal sequence. From the middle Miocene–middle Oligocene, all three fossil groups were useful in establishing age control. In most of the Eocene, both radiolarians and nannofossils are present (Fig. F22), although the occurrence of nannofossils is spotty through the radiolarian ooze of lithologic Unit III (see “**Biostratigraphy,**” p. 13).

The siliceous clays of lithologic Unit I (see “**Lithostratigraphy,**” p. 7) have an LSR of ~1 m/m.y. The LSR in the alternating siliceous and calcareous clays of lithologic Unit II reaches nearly 6 m/m.y. in the lower Miocene–upper Oligocene part of the section (Tables T11, T12; Fig. F22). Piston Core EW9709-12P (Lyle, 2000), taken in the survey area, can be correlated to the density records of Hole 1219A (Fig. F23). The lower part of the site survey piston core (from ~7 to 13 m) closely approximates variations in sediment density at Site 1219 (22–32 mcd; Fig. F23). This correlation is constrained by radiolarian events in both Site 1219 and piston Core EW9709-12P.

Through the remainder of the carbonate-rich Oligocene, the LSR is near 16 m/m.y. Below the E/O boundary, there is a sharp drop in LSRs along with the abrupt disappearance of carbonate from the sediments. A second maximum in LSRs of ~8.6 m/m.y. is present in the silica-rich middle Eocene radiolarian ooze of lithologic Unit III (Fig. F22). The LSR

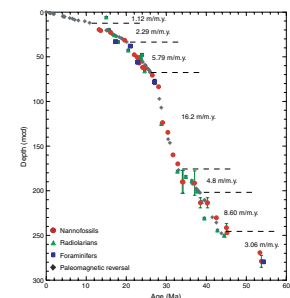
F21. Spliced records of Sites 1218 and 1219 GRA bulk density, MS and the color reflectance parameter vs. Site 1218 composite depth, p. 65.



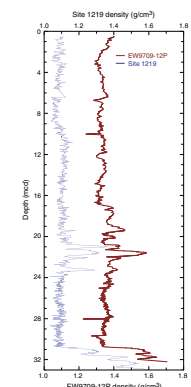
T11. Paleomagnetic events, p. 110.

T12. Nannofossil, foraminifer, and radiolarian events, p. 111.

F22. LSR and chronostratigraphic markers, p. 66.



F23. Density record of site survey piston Core EW9709-12P compared to density record of Site 1219, p. 67.



is low near the base of the middle Eocene near the appearance of the first significant chert layers (see “**Lithostratigraphy**,” p. 7).

LSR values may be combined with the dry bulk density (DBD) data from porosity measurements on individual samples (see “**Physical Properties**,” p. 28) (Table T17) to determine the bulk MARs of the sediments (Table T13). Sediment with an LSR of 1.0 cm/k.y. and a DBD of 1.0 g/cm³ will have a MAR value of 1.0 g/cm²/k.y. The observed values are rarely this high, so we report the data in milligrams per square centimeter per thousand years (mg/cm²/k.y.). MAR flux values are low in lithologic Unit I, generally <75 mg/cm²/k.y. (Fig. F24). Lithologic Unit II, dominated by calcareous material, accumulates at 500–1500 mg/cm²/k.y., with the maximum flux rates in the very light brown to white nannofossil ooze of early Oligocene age. Unit III, dominated by radiolarian ooze and radiolarite, has much lower MARs of ~200–400 mg/cm²/k.y. The basal chalk of lithologic Unit IV accumulated at rates of ~200–400 mg/cm²/k.y.

GEOCHEMISTRY

Interstitial Water Geochemistry

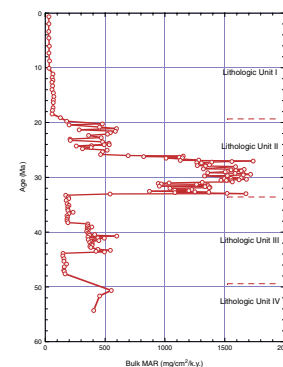
We collected interstitial waters from 11 samples in Hole 1219A at depths ranging from 2.95 to 200.45 mbsf, one sample every core for the first six cores and every third core thereafter (Table T14; Fig. F25). Samples were not obtained from the lowermost 40 m of Hole 1219A because the core designated for an interstitial water sample (Core 199-1219A-25X) recovered only chert and subsequent cores were short and possibly contaminated with seawater. Chemical gradients in the interstitial waters at Site 1219 primarily reflect the changing bottom-water salinity of Pacific deep waters through time, relatively limited organic matter diagenesis, dissolution of biogenic silica, and diffusive influence of reactions in the underlying basalt.

Chlorinity (as measured by titration) increases with depth, from values of ~552 mM at 2.95 mbsf to values of ~565 mM at 38.95 mbsf (Fig. F25). The lower than average seawater value of interstitial water at shallow sediment depth (2.95 mbsf) at this site is consistent with the chlorinity of modern Pacific Bottom Waters (~542 mM). Chlorinity increases to a middepth maximum of 565 mM at 38.95 mbsf. Sodium concentrations determined by charge balance were on average 2.6% higher than those measured by ion chromatograph (Table T14). Consistent with the pattern of the chlorinity values, sodium concentrations as determined by charge balance, increase from 481 mM at 2.95 mbsf to a maximum value of 494 mM at 38.95 mbsf and then decrease to 484 mM at 200.45 mbsf. Salinity, as measured by a handheld refractometer, slightly increases downhole from 35.0 at 2.95 mbsf to 35.5 at 200.45 mbsf.

Alkalinity, pH, and sulfate generally follow the same trend of a decrease to a mid-depth minimum and subsequently an increase to the deepest sample. Alkalinity decreases with depth in the uppermost 135 m, to 0.89 mM, and thereafter slightly increases with depth to ~1.06 mM at 200.45 mbsf. The pH also decreases with depth from 7.16 at 2.95 mbsf to 6.82 at 135.45 mbsf and then increases with depth to 7.24 at 200.45 mbsf. Sulfate concentrations are higher than 25 mM throughout the section, and ammonium is present in extremely low levels (<10 μM). Both indicate that the amount of labile organic matter available

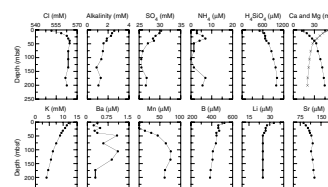
T13. Depths, ages, rates, and fluxes of sediments, p. 112.

F24. Bulk MARs of sediments, p. 68.



T14. Interstitial water data, p. 115.

F25. Interstitial water data, p. 69.



for oxidation is extremely low. Minima in sulfate and ammonium coincide at 105.45 mbsf.

Dissolved silica concentrations increase with depth, from ~500 μM at 2.95 mbsf to ~1000 μM at 200.45 mbsf. These high interstitial water silica values are consistent with dissolution of biogenic silica throughout the sediment.

The magnitude of the calcium concentration increase and magnesium concentration decrease with depth (2.95–200.45 mbsf) at Site 1219 is significantly greater than that seen at any other Leg 199 site (Sites 1215–1222). This pattern is consistent with alteration of basement rocks, with magnesium replacing calcium during the formation of chlorite. In addition, potassium concentrations show a profile similar to that of magnesium, presumably reflecting the uptake of potassium during basement alteration. These interstitial water profiles are consistent with the recovery of highly altered basalt at Site 1219, unlike at previous sites in the Leg 199 transect.

Strontium concentrations are similar to seawater (87 μM) at 2.95 mbsf, then slightly increase with depth to ~126 μM at 200.45 mbsf. This pattern likely reflects dissolution of the carbonate sediments that occurs between 50 and 150 mbsf, which is consistent with micropaleontological observations (see “[Calcareous Nannofossils](#),” p. 13, “[Planktonic Foraminifers](#),” p. 16, and “[Benthic Foraminifers](#),” p. 18, all in “[Biostratigraphy](#)”). Dissolved manganese concentrations are low (<1 μM) from the seafloor to 21.45 mbsf and then rapidly increase downhole (to 76.3 μM at 105.45 mbsf) before showing a subsequent decrease to 61.4 μM at 200.45 mbsf. This Mn profile is the exact opposite of that observed at Site 1218 where Mn values were high at shallow depths and decreased with depth. Lithium pore water values are slightly higher than that of seawater (33 μM) at 2.95 mbsf but decrease with depth to values of 25–26 μM between 38.95 and 200.95 mbsf, which is consistent with lithium uptake during low-temperature basalt alteration. Barium concentrations are low (≤ 1 μM), and boron concentrations range from 0.23 to 1.10 μM .

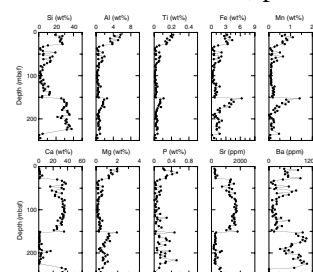
In summary, the pore water profiles from Site 1219 primarily reflect the record of changing deepwater chlorinity, little organic matter degradation, the dissolution of biogenic silica, the alteration of underlying basalt, and subsequent diffusion. The alkalinity, pH, sulfate, and ammonium profiles in the interstitial waters reflect the small amount of organic matter degradation occurring in these sediments. The silica interstitial water profile indicates dissolution of biogenic silica. Calcium, magnesium, potassium, and lithium profiles appear to be controlled by the alteration of basalt and subsequent diffusion to the sediment/water interface.

Solid-Phase Geochemistry

We collected bulk-sediment samples adjacent to the interval sampled for physical properties in every other section (see “[Physical Properties](#),” p. 28), resulting in a sampling resolution of approximately three per core from 2.23 to 244.38 mbsf in Hole 1219A (Table [T15](#); Fig. [F26](#)). We measured silicon (Si), aluminum (Al), titanium (Ti), iron (Fe), manganese (Mn), calcium (Ca), magnesium (Mg), phosphorus (P), strontium (Sr), and barium (Ba) concentrations in the sediment by inductively coupled plasma–atomic emission spectroscopy (ICP-AES). Bulk-sediment geochemistry primarily reflects the changing lithology of the sediments downhole from radiolarian ooze and clay (Unit I) to nanno-

[T15](#). Bulk-sediment data, p. 116.

[F26](#). Bulk-sediment data, p. 70.



fossil ooze (Unit II) to radiolarian ooze (Units III) to calcareous chalk (Unit IV) (Fig. F26).

Silicon at Site 1219 averages ~25 wt% between 2.23 and 27.23 mbsf (Unit I), decreasing to an average of 10 wt% in Unit II (30–150 mbsf). Throughout Unit III, silicon increases slightly from 26 wt% at 152.59 mbsf to 38 wt% at 223.35 mbsf. Silicon concentrations reach ~2 wt% near basement (Fig. F26).

Aluminum and titanium concentrations are highest in the clay and siliceous sediments (lithologic Units I and III) and lowest in the carbonate sediments (lithologic Units II and IV). Aluminum concentrations decrease downhole from ~6 to ~0.63 wt% between 2.23 and 150.35 mbsf and then increase to ~3 wt% at 152.59 mbsf. Farther downhole, aluminum concentrations decrease to an average of 0.6 wt% between 184.81 mbsf and basement. Titanium content decreases from ~0.3 to 0.1 wt% within Unit I, is very low (<0.07 wt%) throughout the carbonate sediments (Units II and IV), and is ~0.08 wt% at the top of Unit III, decreasing to 0.03 wt% at the base of Unit III decreasing toward basement.

Al/Ti ratios vary slightly downhole with the greatest variation (8.5–25) throughout Unit III (see Fig. F19, p. 70, in the “Leg 199 Summary” chapter). The average Al/Ti ratio is high relative to the Post-Archean Average Shale value of 16.7 (Taylor and McLennan, 1985). The Si/Ti ratio is higher in Unit III than in Unit I, possibly reflecting the increased biogenic component of the silicon in the radiolarian ooze relative to the clay (see Fig. F19, p. 70, in the “Leg 199 Summary” chapter).

Iron and manganese contents show similar trends to aluminum and titanium, with maximum values in Units I and III and values at or near 0 wt% in Unit II (Fig. F26). Iron varies on average between 1 and 3 wt% in Units I and III, with a maximum of 6.3 wt% at 152.59 mbsf at the top of Unit III, and between 0.2 and 2 wt% in Units II and IV. Manganese concentrations are ~0.2 wt% in Unit II and average ~0.5 wt% within Units I and III, with a maximum of 1.4 wt% at 152.59 mbsf (top of Unit III).

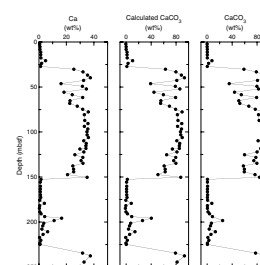
Calcium and strontium concentrations are highest in the carbonate-rich lithologies (Units II and IV). Calcium concentrations vary between 0.58 wt% at 2.23 mbsf (Unit I) and 37.4 wt% at 39.73 mbsf (Unit II). The variability in calcium (16–37 wt%) throughout Unit II reflects layers of clay-rich sediment within the nannofossil radiolarian ooze and can be seen as dark to light color cycles in the sediment (see “Unit II,” p. 8, in “Lithostratigraphy”). Strontium concentrations are lowest (~250 ppm) in the siliceous-rich lithologies (Units I and III) and highest (~1600 ppm in Unit II and 600 ppm in Unit IV) in the carbonate-rich lithologies (Units II and IV). Magnesium varies between 0.3 and 2 wt% in the siliceous units (I and III) and between 0.1 and 0.6 wt% in the carbonate-rich sediments.

Phosphorus concentrations are low (generally <0.5 wt% in siliceous and clay sediments and <0.2 wt% in carbonate sediments). Barium concentrations in Site 1219 sediments are highest in the siliceous sediments, varying between 4,500 and 10,000 ppm. Barium concentrations are lower (between 700 and 3000 ppm) throughout the nannofossil oozes and chalks (Units II and IV).

Calcium carbonate (CaCO₃) (in weight percent) was determined by coulometric methods for approximately three samples per core from 2.23 to 244.38 mbsf in Hole 1219A (Table T16; Fig. F27). CaCO₃ is low (≤1 wt%) in clay-rich Unit 1, high (~60–100 wt%) in Unit II (where carbonate defines the lithology), low to moderate (<1–40 wt%) in siliceous

T16. CaCO₃ and C_{org} data, p. 118.

F27. CaCO₃ and Ca data, p. 71.



Unit III, and high (up to 96 wt%) in Unit IV. CaCO_3 values calculated from Ca ICP-AES data and salt fraction data (in weight percent) yielded similar trends to CaCO_3 measured via coulometer, although absolute values differ by up to ~10% (see “Geochemistry,” p. 20, in the “Explanatory Notes” chapter). Organic carbon (C_{org}) (in weight percent) determined for one sample per core is uniformly low (<1 wt%) for the samples measured.

In summary, the bulk geochemistry of the sediments from Site 1219 reflects the shifts in lithology between sediments dominated by silica and carbonate.

PHYSICAL PROPERTIES

Physical properties at Site 1219 were measured on whole cores, split cores, and discrete samples. MST measurements (bulk density, MS, *P*-wave velocity, and NGR) and thermal conductivity comprised the whole-core measurements. Compressional wave velocity measurements on split cores and moisture and density (MAD) analyses on discrete core samples were made at a frequency of one per undisturbed section. LAS analyses were performed on the MAD samples as well as an additional one sample per section (located ~50 cm from the MAD sample). Three in situ temperature measurements were obtained using the Adara tool in Hole 1219B.

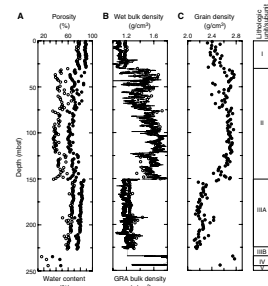
Density and Porosity

Two methods were used to evaluate the wet bulk density at Site 1219. GRA provided an estimate from whole cores. MAD samples gave a second, independent measure of wet bulk density, along with providing DBD, grain density, water content, and porosity from discrete samples (Table T17). In the radiolarian oozes and clays of lithologic Units I (0–30.0 mbsf) and III (150.6–234.2 mbsf), the MAD wet bulk density is consistently greater than GRA bulk density by 0.05–0.10 g/cm^3 (Fig. F28). Despite the offset, the two bulk density measures follow the same general trends. The agreement between the wet bulk density and GRA density is better in the nannofossil ooze of Unit II (30.0–150.6 mbsf), where the two data sets track each other through the alternating lithologies that are expressed as sediment color cycles. A comparison of the GRA density and the digital color image for Core 199-1219A-6H shows that the darker-colored, more radiolarian- and clay-rich intervals are less dense than the lighter-colored, more nannofossil-rich intervals (Fig. F29). Lithologic Unit IV (234.2–244.9 mbsf) was drilled with the XCB, and the limited data that are available display a fair correlation between the discrete sample and GRA densities. Crossplots of wet and DBD vs. interpolated GRA density (Fig. F30) show excellent correlation between the MAD and GRA data for sediments recovered with the APC.

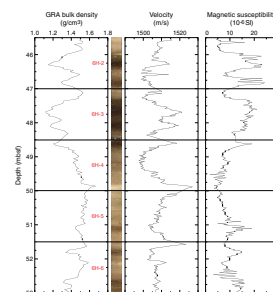
The MAD wet bulk density is nearly constant, with an average of 1.18 g/cm^3 in the uppermost 30 m of Hole 1219A. Density increases rapidly at the top of Unit II to 1.54 g/cm^3 at 33.25 mbsf. Between 30 and 77 mbsf, Unit II is characterized by highly variable wet bulk density, as a result of alternations between nannofossil ooze and nannofossil ooze with radiolarians and clay. Bulk density in this interval ranges from 1.23 to 1.72 g/cm^3 . From 77 to 121 mbsf, the variability in bulk density is less than that between 30 and 77 mbsf because the sediment is a

T17. Moisture and density measurements, p. 119.

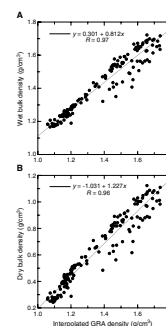
F28. MAD measurements, p. 72.



F29. GRA density, PWL velocity, and MS vs. color cycles, p. 73.



F30. Wet and dry bulk density plotted with GRA density, p. 74.



more uniform nannofossil ooze with high CaCO_3 content (see “**Solid-Phase Geochemistry**,” p. 26, in “Geochemistry”). The trend for the upper part of Unit II (from 30 to 120 mbsf) is a slight increase in density with depth, from $\sim 1.50 \text{ g/cm}^3$ near the top of the unit to 1.66 g/cm^3 at 120.75 mbsf. Below 121 mbsf, wet bulk density decreases sharply to 1.39 g/cm^3 and the variability of the density increases, which reflects greater abundance of clay and radiolarians in the sediment and alternating lithologies similar to the upper part of Unit II. The general trend for the whole unit is increasing wet bulk density with depth reflecting downhole compaction from increasing overburden. Wet bulk density decreases to 1.23 g/cm^3 at the top Unit III, followed by an overall slow increase in density with depth, to 1.31 g/cm^3 at 226.27 mbsf. There are two density maxima in the lower part of Unit III, with values of 1.43 and 1.39 g/cm^3 at 192.40 and 212.27 mbsf, respectively. The first maximum corresponds to a distinctive nannofossil ooze layer (see “**Unit III**,” p. 9, in “Lithostratigraphy”) and a calcite peak in the LAS analysis. The latter maxima coincides only with an LAS-analysis calcite peak. Wet bulk density increases significantly at the top of Unit IV, followed by a steady decrease in density to the base of the unit. The uppermost sample measured in Unit IV (Sample 199-1219A-26X-1, 42–44 cm) at 234.52 mbsf has a density of 2.16 g/cm^3 . Qualitatively, the appearance of sediments near the top of Core 199-1219A-26X suggests that they possess even higher densities than the sediment sampled. Wet bulk density decreases steadily toward the base of Unit IV, with a value of 1.81 g/cm^3 at 244.38 mbsf.

Variation in grain density corresponds well to the changes in lithology in Hole 1219A (Fig. F28). In Unit I, grain density ranges from 2.33 to 2.57 g/cm^3 and averages 2.45 g/cm^3 . The transition from predominantly siliceous to more calcareous sediments in Unit II is marked by an increase in the magnitude and variability of grain density in the upper part of Unit II. Between 30 and 77 mbsf the grain density ranges from 2.40 to 2.77 g/cm^3 and averages 2.63 g/cm^3 . The more calcareous interval between 77 and 121 mbsf displays relatively uniform grain density, which averages 2.70 g/cm^3 . In the lower part of Unit II, the transition to the radiolarian ooze and clay of Unit III is marked by greater variability and a decrease in grain density. The pattern of variable and decreasing grain density continues in Unit III. Grain density is 2.51 g/cm^3 at 151.45 mbsf, near the top of the unit, and 2.15 g/cm^3 at 226.27 mbsf, near the base of the unit. The average grain density for sediments in Unit III is 2.24 g/cm^3 . A significant increase in grain density to 2.77 g/cm^3 is present at the top of Unit IV, marking the change in lithology to nannofossil chalk. At the base of Unit IV, grain density is 2.54 g/cm^3 .

Porosity and water content vary inversely with wet bulk density (Fig. F28). The high porosity of the clay- and radiolarian-rich sediments of Units I and III are prominent features of the porosity profile. Average porosities for Units I and III are 89% and 80%, respectively. Porosity is nearly constant in Unit I. In Unit III, it decreases with depth, from 86% at 151.45 mbsf to 75% at 226.27 mbsf. In Unit II, porosity trends are similar to those of wet bulk density. Porosity is highly variable between 30 and 77 mbsf in association with the alternating lithologies, relatively uniform in the nannofossil ooze between 77 and 121 mbsf, and more variable and higher at the base of the unit, in the transition to Unit III. Overall, porosity decreases from 79% near the top of the Unit II to 60% at the base of the unit as a result of compaction. The contact between

Units III and IV is marked by a substantial decrease in porosity to 34%. At the base of Unit IV, porosity is 48%.

LAS

LAS studies were conducted on cores from Hole 1219A at a frequency of two samples per section (see [Vanden Berg and Jarrard](#), this volume, for a discussion of the LAS technique). Semiquantitative mineral concentrations were calculated from the collected spectra, assuming a four-component system: calcite, opal, smectite, and illite (Table [T18](#)). The results of the LAS analyses correlate well with the major lithologic boundaries (Fig. [F31](#)).

The radiolarian clay of lithologic Unit I shows clay contents of ~50%, with the dominant clay being smectite. The uppermost sample contains 47% illite and is followed by a drop in illite concentration to near 15%. This transition is believed to correlate with the illite–smectite transition seen at previous sites. Illite concentrations in the interval between 10 and 35 mbsf are higher than expected and may be the result of an increase in metal oxides, which darken the color of the sediment. Opal concentrations in the upper unit average 25% and are consistent with the lithologic description (see “[Unit I](#),” p. 8, in “[Lithostratigraphy](#)”). Calcite is overestimated in Unit I compared to the geochemical data (see “[Solid-Phase Geochemistry](#),” p. 26, in “[Geochemistry](#)”) for reasons unknown. Postcruise research will focus on better calibration of LAS mineralogical calculations.

The carbonate-rich lithologic Unit II has an expected increase in calcite values to ~80%, as well as a corresponding drop in clay content. The clay that is present is mainly smectite, which varies from a low of 0% to a high of ~25%. Between 50 and 75 mbsf, radiolarians increase in abundance, resulting in higher opal concentrations. Likewise, between 125 and 150 mbsf, opal concentrations again rise with increased radiolarian contents (see “[Unit II](#),” p. 8, in “[Lithostratigraphy](#)”). Percent silica data show the same trends as LAS percent opal in lithologic Unit II (see “[Solid-Phase Geochemistry](#),” p. 26, in “[Geochemistry](#)”).

The top of Unit III marks the lithologic transition associated with E/O boundary with a decrease in calcite (an average of 73% in Unit II to an average 17% in Unit III) and an increase in clay (an average of 19% in Unit II to an average of 29% in Unit III) and opal (an average of 7% in Unit II to an average of 53% in Unit III). Between 189 and 196 mbsf, calcite values again increase to an average of 33%, whereas clay and opal values decrease. This increase correlates with the layer of nannofossil ooze (see “[Unit III](#),” p. 9, in “[Lithostratigraphy](#)”). The clay in this interval is predominantly smectite, with concentrations averaging 29%.

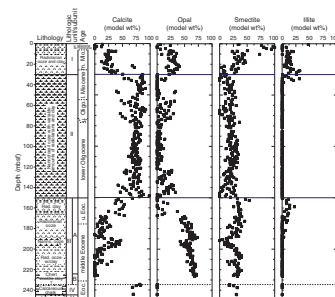
Lithologic Unit IV is a calcareous chalk and correlates with an increase in calcite concentrations to an average of 73%. Opal and illite concentrations are negligible in this unit, and smectite concentrations average 27%. These data correlate well with the percent silica and percent calcium concentrations (see “[Solid-Phase Geochemistry](#),” p. 26, in “[Geochemistry](#)”).

Compressional Wave Velocity

Compressional wave velocity was measured by the *P*-wave logger (PWL) on whole cores from Holes 1219A and 1219B and the insertion and contact probe systems on split cores from Hole 1219A (Table [T19](#)).

[T18](#). LAS-based mineralogy, p. 121.

[F31](#). LAS mineralogy determinations, p. 75.



[T19](#). Split-core velocity measurements, p. 124.

For XCB cores, cube samples were cut with the dual-bladed rock saw, allowing determination of velocities in the y- and z-directions with the contact probe system. The match between the whole-core and split-core measurements is relatively good for the insertion and contact probe systems, with only a few anomalous points (Fig. F32).

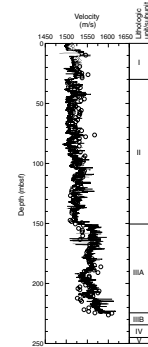
Downhole trends in velocity approximate changes in lithology and bulk properties. Velocity (transverse) increases slightly with depth in Unit I, from ~1500 m/s near the seafloor to 1524 m/s at ~30 mbsf. The sharp increase in density and decrease in porosity that occurs at the boundary between Units I and II is not seen in the velocity profile. Overall, there is a gradual increase in velocity with depth in Unit II. Small variations in velocity most likely reflect alternations in lithology and porosity (Fig. F29). Unit III is marked by a jump to higher velocity values, from an average of 1534 m/s in Unit II to an average of 1570 m/s in Unit III. Lower velocities at 192 and 210 mbsf correlate with regions of higher LAS calcite concentrations (Fig. F31). Below 212 mbsf, velocity continues to increase downhole. Velocities from Unit IV were determined on three cut samples and record much higher values compared to the rest of the hole, averaging 1901 m/s. These high velocities are consistent with the high densities and low porosities in this interval.

The lack of simple downhole velocity trends in Hole 1219A is partly explained by the crossplot of velocity and wet bulk density (Fig. F33). The nannofossil ooze of Unit II is characterized by a general increase in velocity with increasing density. The radiolarian clays of Units I and III differ from the calcareous sediment in their relationship with bulk density. In Units I and III, there is either no relation or a weak increase in velocity with decreasing density. This pattern results from the stiff sediment framework created by the shape of radiolarians and their interlocking spines. This stiffness produces a higher shear modulus and velocities higher than expected for the high porosity of the sediment. The difference in the trends of velocity with bulk density for the calcareous and siliceous sediments explains the lack of a prominent change in velocity at the boundary between radiolarian clay of Unit I and the nannofossil ooze of Unit II.

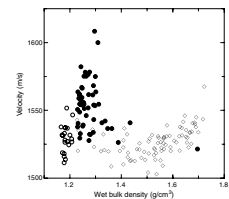
Inconsistencies in the relationship between velocity and bulk density also are present at the core scale (Fig. F29). Sections 199-1219A-6H-2 and 6H-3 contain dark-colored, clay- and radiolarian-rich intervals with low bulk density, high MS, and high velocity and light-colored, more calcareous intervals of higher density, lower susceptibility, and lower velocity. In Sections 199-1219A-6H-4 through 6H-6, the pattern is reversed, with light-colored intervals displaying higher velocity than the dark layers.

Velocity anisotropy was calculated from longitudinal (z-direction) and transverse (y-direction) measurements provided by the insertion probe system and the cut samples measured with the contact probe system (Table T19). The sediments of Hole 1219A are essentially isotropic and do not show effects of particle realignment that accompany compaction of clayey sediments. The anisotropy ranges from 1.0% to 1.5% and averages 1.3% for the insertion probe system (upper 18 m of Hole 1219A). Anisotropy also was determined on the three cut samples from below 234 mbsf, with an average of 1.7%.

F32. Compressional wave velocity, p. 76.



F33. Compressional wave velocity vs. wet bulk density, p. 77.



Thermal Conductivity and Temperature Measurements

Thermal conductivity was measured on the third section of all APC-recovered cores from Holes 1219A and 1219B (Table T20). The thermal conductivity shows a strong dependence on lithology (Fig. F34) and porosity (Fig. F35). The radiolarian oozes and clays of Units I and III display a nearly constant conductivity, which averages 0.73 W/(m·K). Thermal conductivity increases sharply to 0.93 W/(m·K) at the top of Unit II. Between 30 and 120 mbsf, conductivity values are scattered but display a general increase with depth, with a maximum of 1.22 W/(m·K). Thermal conductivity gradually decreases between 120 and 150 mbsf and sharply declines to 0.71 W/(m·K) at the top of Unit III. The expected inverse relationship between thermal conductivity and porosity is displayed by the nannofossil ooze of Unit II but is lacking for the radiolarian oozes and clays of Units I and III (Fig. F35). The lack of a relationship results from the high porosity of the sediment and the poor heat conduction in the biogenic silica that comprises the radiolarians.

In situ temperature measurements were taken using the Adara tool with three cores in Hole 1219B. Borehole temperatures range from 5.72°C at 49.50 mbsf to 9.34°C at 116.00 mbsf, with an average seafloor temperature of 1.45°C (Table T21; Fig. F36).

Heat flow at Site 1219 was determined according to the procedure of Pribnow et al. (2000). The laboratory-determined thermal conductivity was used to estimate in situ thermal conductivity (see “Heat Flow Calculation,” p. 28, in “Physical Properties” in the “Explanatory Notes” chapter). The thermal resistance was calculated assuming a constant conductivity for Unit I (0–30 mbsf) and a linear fit through conductivity values between 30 and 125 mbsf in Unit II (Fig. F36). Thermal resistance was estimated for the depths of the temperature measurements, and the heat flow was obtained from the inverse of the linear fit for the crossplot of temperature and thermal resistance (Fig. F36). The heat flow estimate for Site 1219 is 66 mW/m², which essentially is the same as the heat flow calculated for Site 1218 (67 mW/m²). The value of 66 mW/m² compares favorably to the heat flow of 62 mW/m² at the point (9°0.0′N, 163°48.2′W) in the global heat flow data set (Pollack et al., 1993) that is closest to Site 1219.

Natural Gamma Radiation

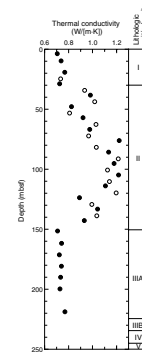
Natural gamma radiation was measured on all whole cores at Site 1219 (Fig. F37). The highest natural gamma radiation values occur in the clay-rich lithologic Unit I, where they decrease downcore from 68.7 counts per second (cps) at the seafloor to ~1.0 cps (near background levels) at 30 mbsf. Below 30 mbsf, values drop to zero in the carbonate-rich Unit II and remain at this level to a depth of 150 mbsf. There is a slight increase in natural gamma radiation values (average = 0.84 cps) in lithologic Unit III, which correlates with an increase in clay content over the E/O boundary.

MS

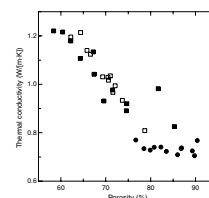
Whole-core MS measurements correlate well with the major differences in lithology and to changes in other bulk physical properties. MS values in Unit I, are relatively high, averaging 26×10^{-6} SI. The MS record (Fig. F38) contains significant variation that is not present in the

T20. Thermal conductivity, p. 126.

F34. Thermal conductivity, p. 78.

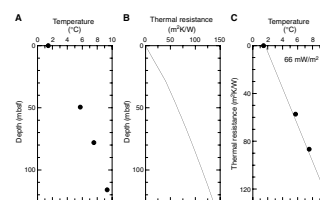


F35. Thermal conductivity plotted with porosity, p. 79.

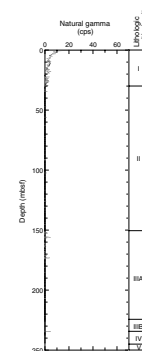


T21. In situ temperature, p. 127.

F36. Heat flow calculation, p. 80.



F37. Natural gamma radiation, p. 81.



more uniform GRA bulk density profile (Fig. F28), although there is a match between the general trends of both data sets.

A significant decrease in susceptibility marks the top of the carbonate-rich Unit II at 30 mbsf. MS values in the interval between 30 and 95 mbsf average 11×10^{-6} SI, and the variation that is present corresponds with alternations between nannofossil ooze (lower MS) and nannofossil ooze with radiolarian ooze and clay (higher MS) (Fig. F29). Between 95 and 122 mbsf, MS values decrease to an average of 8×10^{-6} SI, which suggests that this interval contains the greatest amounts of calcite. Other data sets (percent calcium, grain density, and porosity) show a thicker interval (between 70 and 122 mbsf) of high calcite content. MS values increase between 122 and 150 mbsf, averaging 12×10^{-6} SI, correlating to small increases in LAS clay and opal contents (Fig. F31).

An increase in susceptibility marks the boundary between Units II and III as the clay content increases. MS values then decrease downhole to near zero in the nannofossil ooze at 192 mbsf and increase below 195 mbsf as clay content increases. Lower MS values at 212 mbsf correlate with higher calcite concentrations present in the LAS mineralogy data (Fig. F31). The large spike at the bottom of Subunit IIIA most likely reflects the presence of a chert bed. Data from Subunit IIIB and Unit IV are not representative because of poor core condition.

DOWNHOLE MEASUREMENTS

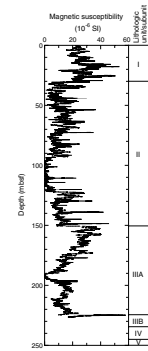
Logging Operations

Two logging runs (triple combo and FMS-sonic) (see Fig. F10, p. 55, in the “Explanatory Notes” chapter) were planned for Hole 1219A after basement was reached at 254 mbsf. In preparation for logging, the hole was conditioned with a wiper trip of the drill string (up to 75 mbsf and back to basement), and ~2 m of fill was flushed from the bottom of the hole. A breakdown of the chronology of logging operations is provided in Table T22, including some details of the tools used. The hole was then displaced with 100 barrels of 8.9 lb/gal sepiolite mud, and the bit was withdrawn to 82 mbsf in preparation for logging. Tool rig-up was begun at 0945 hr and completed by 1145 hr. The first tool was run to the bottom of the hole (5326 mbrf), and logging began at 1530 hr on 25 November. Seasoning of the new wireline (installed during port call) limited the maximum speed of run into and out of pipe to 6500 ft/hr (~2000 m/hr), leading to an ~60% increase in wireline time.

The classic triple combo configuration with the Lamont-Doherty Earth Observatory high-resolution MGT on top was run first, followed by the FMS-sonic tool string (see Fig. F10, p. 55, in the “Explanatory Notes” chapter). A total of six passes were made (providing ~170 m of logged section per pass) with no bridges encountered, and the bottom of the hole was reached on all passes (Fig. F39). The caliper log indicates that sections of the hole are enlarged ≥ 18 in (i.e., wider than the caliper extension) (Fig. F40).

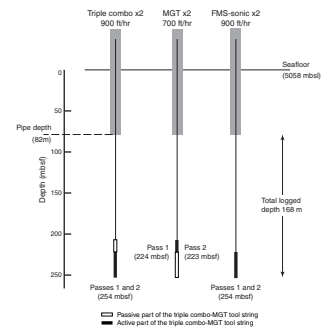
Upon completion of the second pass of the triple combo, control switched to the downhole measurements lab, and the tool string was again lowered to the bottom of the hole. The formation was then logged up hole for two passes, with the logging conducted in the “Lamont mode” for high-resolution MGT data acquisition. At the end of the second pass, the tool string was retrieved to the rig floor.

F38. Magnetic susceptibility, p. 82.

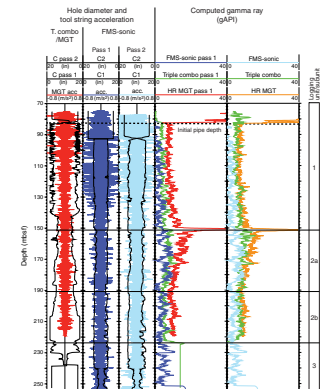


T22. Logging operations, Hole 1219A, p. 128.

F39. Logging operations, p. 83.



F40. Caliper, acceleration, and gamma ray logs, p. 84.



The FMS-sonic was rigged up and run to the bottom of the hole. The dipole shear sonic imager (DSI) was run in primary (compressional, [*P*-wave] and secondary [shear, *S*-wave]) modes, monopole and dipole shear modes and also in first motion detection (FMD) mode. As a result of the slowness of the formation and the large hole size, the *P*- and *S*-wave velocity logs are of low quality, but the FMD log appears to provide a better *P*-wave velocity (see below). The caliper readings from the FMS suggest that the hole conditions are better than those indicated by the triple combo caliper. The FMS-sonic tool string was then retrieved to the rig floor, and logging operations were completed by 1200 hr on 26 November. The weather was variable throughout logging operations, and heave conditions were good, typically <2 m. Consequently, the wireline heave compensator (WHC) experienced no problems during logging operations.

Data Quality

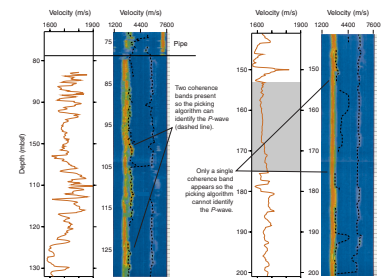
The triple combo caliper indicated that the hole conditions were good in the bottom 20 m of the borehole and from 206 to 146 mbsf, with widths <16 in (Fig. F40). The worst section of the hole is between 226 and 206 mbsf, with a hole diameter >18 in (beyond the maximum extension of the caliper arms). From 146 to 82 mbsf, the hole condition is variable, with a diameter of 16–18 in. The FMS caliper logs indicate that the hole is close to, but just below, the maximum (15 in) diameter of the FMS caliper arms (Fig. F40). On FMS-sonic pass 1, neither caliper extended beyond 14.1 in. On pass 2, hole conditions appear slightly different with caliper 2 extended to 15 in for 17 m of the hole. Close inspection of the caliper data, however, indicates that the caliper 2 (C2) curves (for both passes) are “overly smooth” (compared to C1 curves), suggesting poor contact with the borehole wall. Thus, the triple combo caliper data are thought to be reliable. The differences between the triple combo and FMS caliper logs may also result from an elliptically shaped borehole.

It appears that only one FMS caliper (C1) (each caliper has two pads) made good contact with the borehole wall for most of the log, which is indicated by the rugosity differences between C1 and C2 (Fig. F40). Despite the apparently poor hole conditions, the processed images are reasonably good for most of the borehole length on both passes. The slow sonic velocity of the sediments combined with the similarity in velocity between the drilling mud (typically 189 μs/ft) and the formation led to problems in processing DSI data. The wave labeling algorithm in the Schlumberger software could not differentiate between the fluid wave from the drilling mud and the compressional *P*-wave from the formation. Thus, for significant portions of the log the compressional *P*-wave remains unidentified (Fig. F41). In FMD mode, the wave labeling algorithm identifies the first good signal that it receives as the *P*-wave velocity of the formation. A comparison between the FMD data and core velocity measurements is presented in Figure F42.

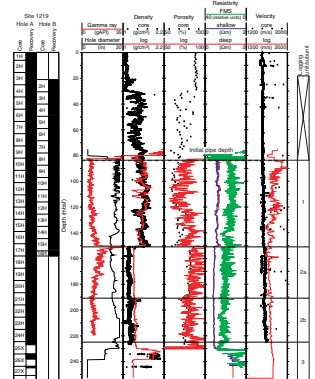
Computed gamma ray measurements from each pass show excellent correlation (Fig. F40), indicating the high quality of the data.

Continuous wavelet analysis provides an automatic localization of specific behavior, such as cyclic patterns or discontinuities, both in time and frequency (e.g., Torrence and Compo, 1998). In contrast to classical Fourier or windowed Fourier transform, which decompose the original signal on the basis of an infinite periodic function depending on a unique parameter (space frequency), the wavelet transform (WT)

F41. Example of the problem encountered in identifying *P*-waves, p. 85.



F42. Log and equivalent core physical properties, p. 86.

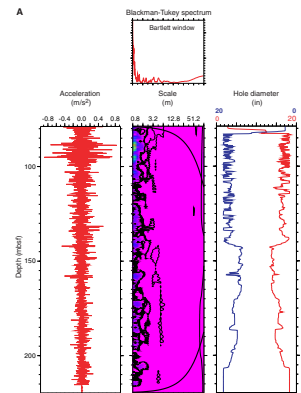


allows a “depth-scale” representation that depends on a scale parameter and a translation parameter. The accelerometer data integrate the effects of heave, borehole wall contact, and wireline stretch on the tool string, and WT of the acceleration data allows the multiscale components of the tool acceleration to be deciphered. This analysis provides a quality control check on the logging data. Figure F43 presents the analyses from one pass each of the MGT and FMS-sonic logging runs. The MGT pass displays a very smooth wavelet spectrum with the only significant frequency band operating at a depth scale of <1.6 m (Fig. F43A). This frequency band relates to the heave motion of the ship (despite the damping effect of the WHC). Thus, for the MGT passes the data quality can be assumed to be excellent. The wavelet spectrum from pass 2 of the FMS-sonic tool string is shown in Figure F43B. Visually, the acceleration data are more complex, and this is interpreted to reflect the greater degree of contact between the FMS-sonic tool string and the borehole wall than is the case for the triple combo. The four FMS pads and two DSI centralizers contact the borehole wall, resulting in greater frictional resistance during logging compared to the MGT, which only has one bow spring. The wavelet spectrum shows the same high-frequency heave component but also three lower-frequency bands operating at depth scales of around 4.5, 15, and 25 m, as seen in the Blackman-Tukey spectrum (Fig. F43B). The 25-m frequency is present downhole to a depth of ~200 mbsf, whereas the two shorter frequency bands only appear above 150 mbsf (i.e., in the carbonates). The FMS-sonic accelerometer data indicate good quality, with the longer frequency depth-scale cycles being interpreted to represent formation parameters.

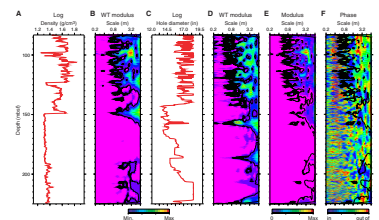
As mentioned above, the borehole width and wall rugosity (especially above 120 mbsf) may affect the quality of data from tools that require good tool-borehole wall contact (e.g., the hostile environment litho-density tool [HLDT]). The triple combo caliper indicates that the top of the borehole is especially rugose. The quality of these data was checked using WT analyses. The high-frequency range of the wavelet spectrum of both the density and the borehole wall are shown in Figure F44. The density displays no significant cyclicity in the formation below 150 mbsf (i.e., within the radiolarian ooze) but shows some cyclicity at a depth scale of ~8 m above (in the carbonates). The borehole-wall wavelet spectrum has no significant cyclicity operating at high frequencies, where borehole wall rugosity effects should be greatest. The cross-wavelet modulus spectrum shows no significant high-frequency cyclicity. The phase diagram perhaps sums up the data quality best. If data quality was being impaired it would be expected that, as the borehole wall widened, the density would decrease (i.e., greater influence of mud density) and the signals should be out of phase. However, the high-frequency spectrum shows that the borehole wall and density data are in phase, indicating no degradation of the data (Fig. F44F).

A similar analysis could be undertaken for the porosity data, but the relationship is not so simple (i.e., the two signals should be in phase whether they are degraded or nondegraded). However, given that the resolution of the porosity tool is less than the (unaffected) density tool’s resolution and that there is good correlation between the porosity log and core porosity measurements, the porosity log is believed to be of excellent quality (Fig. F42). As expected, core density is lower than that recorded by logging. The difference between log and core density is assumed to result from the porosity increase in the cores caused by elastic strain recovery following unloading. Nevertheless, the correlation be-

F43. MGT and FMS-sonic data quality, WT analysis, and caliper logs, p. 87.



F44. WT analyses of density and hole diameter logs, p. 89.



tween data sets is good, and the porosity logging data will thus provide the baseline for depth shifting and compressing the core-derived composite depth scale (see “[Composite Depths](#),” p. 22). Gamma ray levels are low throughout the formation, but passes show good repeatability (Fig. [F41](#)).

Logging Stratigraphy

Logging units were differentiated using a combination of gamma ray, density, porosity, resistivity, and velocity logs (Figs. [F40](#), [F42](#), [F45](#)) and the FMS static-normalized images. The formation is divided into three logging units: (1) an upper unit characterized by low gamma ray activity, porosity, and velocity, as well as high density and resistivity, with the density, porosity, and gamma ray logs displaying cyclicity at a number of depth scales; (2) a middle unit characterized by significantly higher gamma ray counts and porosities; and (3) a lower unit characterized by a zone of very high density and resistivity and higher-amplitude, lower-frequency gamma ray data. The middle unit is further subdivided into two subunits, based on an increase in density and a reduction in porosity and gamma ray counts.

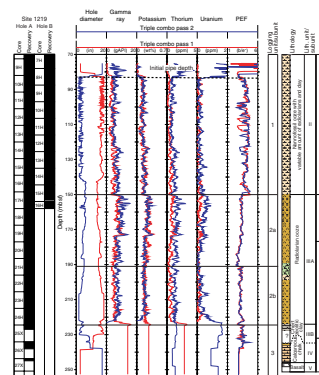
Logging Unit 1: Base of Pipe (82 mbsf) to 151 mbsf

Logging Unit 1 is characterized by low gamma ray counts, low porosity, and high density (Figs. [F42](#), [F45](#)). Density first increases then decreases downhole, most probably related to changes in carbonate levels (see “[Solid-Phase Geochemistry](#),” p. 26, in “[Geochemistry](#)”). The porosity log displays cyclicity at a number of depth scales. For example, porosity has a frequency of variation at a depth scale of ~15 m (Fig. [F42](#)). The high-resolution MGT gamma ray log shows cyclicity down to the submeter scale. As a result of the hole diameter effects upon the FMS log, the resolution of the images is impaired, and small scale cyclicity is not easily identified. This logging unit correlates with lithostratigraphic Unit II (nannofossil ooze) (see “[Unit II](#),” p. 8, in “[Lithostratigraphy](#)”).

Logging Unit 2: 151 to 224.3 mbsf

The upper boundary of logging Unit 2 is defined by a rapid change in gamma ray, density, resistivity, and porosity (Figs. [F40](#), [F42](#), [F45](#)). The gamma ray counts for this unit are consistently the highest for the whole formation. The density log shows a marked decrease across the boundary and also a shift to more stable conditions (Fig. [F42](#)). Cyclicity occurs at ~0.5- and 0.1-m depth scales in the enhanced high-resolution density logs. The porosity shows much greater fluctuation than the density, with cyclicity displayed at a number of depth scales (Fig. [F42](#)). Resistivity fluctuates little throughout this unit, although there is a very subtle decrease downhole to 190 mbsf followed by a similarly subtle increase to the bottom of the unit (Fig. [F42](#)). The photoelectric factor (PEF) provides a qualitative representation of mineralogical change occurring at the upper boundary of this unit. The PEF is generally used as an indicator of lithology with values toward six indicating carbonate and values toward one indicating silica (Rider, 1996). The PEF values of logging Unit 2 are clearly lower than for logging Unit 1 above (Fig. [F45](#)), and the mineralogy change identified in the log matches that found in the cores (see “[Solid-Phase Geochemistry](#),” p. 26, in

F45. Gamma ray, radioactivity, and PEF logs, p. 90.



“Geochemistry”). Logging Unit 2 is further subdivided into two subunits, with the boundary at 191 mbsf marked by a peak in density, minima in resistivity and porosity, and a shift in PEF (Figs. F42, F45). The boundary also marks the stabilization of gamma ray levels. Subunit 2a has high porosity and higher levels of gamma ray with greater variability (Figs. F42, F45). Subunit 2b has lower porosity and slightly higher density, but the amplitude and frequency of cyclicity appear little changed. PEF values increase at the top of Subunit 2b, indicating an increase in the carbonate content, which is substantiated by core measurements (see “Solid-Phase Geochemistry,” p. 26, in “Geochemistry”). Logging Unit 2 correlates with lithostratigraphic Subunit IIIA (radiolarian ooze) (see “Subunit IIIA,” p. 10, in “Lithostratigraphy”).

Logging Unit 3: 224.3 mbsf to Bottom Of Logging Formation

This unit only has density, resistivity, and NGT gamma ray logs (Table T22). The top of the unit is marked by an increase in both gamma ray levels and the amplitude of fluctuation, with a clear periodicity operating at an ~10-m depth scale (Fig. F40). Density increases gradually from the boundary down to a depth of 230 mbsf, where there is a massive increase in density (Fig. F42). This high-density region also appears as a zone of very high resistivity (Fig. F42) and is related to the occurrence of 15 chert bands (see “Subunit IIIB,” p. 11, in “Lithostratigraphy”). Figure F46 shows the FMS images from this part of the formation. A number of chert layers are visible as light-colored, high-resistivity bands. The log of microresistivity from a single button highlights this region (Fig. F42). This logging unit correlates with lithostratigraphic Subunits IIIB (chert zeolitic clay) and IV (calcareous chalk) (see “Subunit IIIB,” p. 11, in “Lithostratigraphy”).

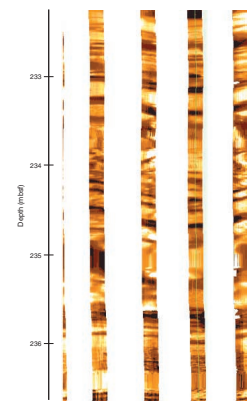
Discussion

Despite the borehole washout, the quality of the logging data appears good. The main objectives of acquisition of in situ, continuous, multiparameter logging data at this site were

1. To assess the physical, chemical, and structural characteristics of the formation, and to provide a baseline for depth matching the core-derived composite depth scale;
2. To perform cyclostratigraphic analysis of continuous Paleogene sequences;
3. To identify and characterize chert layers, which are usually poorly recovered in cores; and
4. To conduct a seismic integration (time-depth model and synthetic seismogram) allowing identification and dating of seismic reflectors at a regional scale.

The logging units described above correlate well with the designated lithostratigraphic units (see “Lithostratigraphy,” p. 7). The high-resistivity region in logging Unit 3 correlates with the chert-rich zeolitic clay (lithostratigraphic Subunit IIIB) and can be easily mapped on the FMS images. The uppermost chert layer is located at 233 mbsf and is 0.2 m thick (the thickest of all the bands). The entire high-resistivity region is composed of at least 15 bands, down to 237 mbsf. Between 239 and 243 mbsf, a large number of chert nodules are visible, with some chert bands

F46. Chert bands in FMS images, logging Unit 3, p. 91.

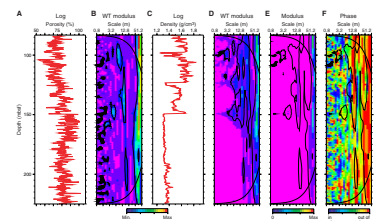


appearing again at 244 mbsf. Passing uphole into the Eocene section, the gamma ray counts increase significantly, indicating a higher quantity of clay in the formation. The Oligocene/Eocene boundary produces a very clear signal on most of the logs (Figs. F42, F43, F45). The PEF log provides a good approximation of the mineralogy changes occurring in the formation. The lower Oligocene nannofossil ooze is identified as a region with consistently low NGR activity, reflecting the low clay content of these sediments. However, the high-resolution MGT gamma ray data provide a detailed record of cyclicity in sedimentation down to the sub-meter level. The density data in logging Unit 1 show good agreement with the core data (Fig. F42). The porosity log generally covaries with the density log and displays cyclicity down to the meter scale.

The sonic velocity data in formations, such as those logged at this site, are invariably difficult to interpret because the velocity of the drilling mud is so close to that of the formation and the slowness of the formation reduces the quality of the return signal to the receivers (see “Synthetic Seismogram,” p. 36, in “Downhole Measurements” in the “Site 1218” chapter). The *P*-wave processing algorithm for the DSI tool has difficulty in resolving the *P*-wave of the formation from the fluid wave of the drilling mud (Fig. F41), leading to velocity data sets that are incomplete. As an experiment, an additional data collection mode (FMD) was run at this site. The wave-labeling algorithm used the first good signal it received this time and assumed this to be the formation *P*-wave. The results of this experiment are presented in Figure F41 and compare favorably with the core data. The FMS-sonic velocity data are shown along with the coherency plots of the stacked sonic waveforms, with the dashed lines representing algorithm-identified (*P* and *S*) waves (Fig. F41). Plotting the data, as shown in Figure F41, provides a method for qualitatively determining the data quality. The FMD data look good for the most part, except between 153 and 168 mbsf, where the coherency band is very narrow, indicating either mud velocity or equal mud/formation velocities. However, when compared to the density data (Fig. F44) and the core velocity data, the FMD data appear good. The use of the FMD mode, in conjunction with the *P* and *S* monopole mode, may prove to be a useful addition to the velocity measurements routinely made during ODP logging when investigating slow formations.

WT analyses were undertaken on the density and porosity logs from both passes of the triple combo (Fig. F47A, F47B). The porosity shows a dominant cyclicity through the formation at a depth scale of ~15 m (Fig. F47B). This frequency is most obvious in the nannofossil ooze (i.e., above 151 mbsf) but reappears downhole between 180 and 215 mbsf. As a first approximation, based on the LSRs calculated from the nannofossil, radiolarian, foraminifer, and paleomagnetic data (Fig. F22) (“Sedimentation and Accumulation Rates,” p. 24), this frequency relates to an ~1-m.y. cyclicity. A localized frequency depth scale of ~8 m, which is equivalent to a timescale of ~0.5 m.y., appears between 90 and 115 mbsf. The density wavelet spectrum shows a very similar pattern, with the 15-m periodicity less apparent below 150 mbsf and the 8-m periodicity significantly better developed (Fig. F47C, 47D). The cross-wavelet spectrum modulus shows the dominant depth-scale frequency to be the 15-m one (Fig. F47E). Finally, the phase diagram confirms the expected covarying relations of density and porosity at this frequency (i.e., out of phase) (Fig. F47F).

F47. WT analyses of porosity and density logs, p. 92.



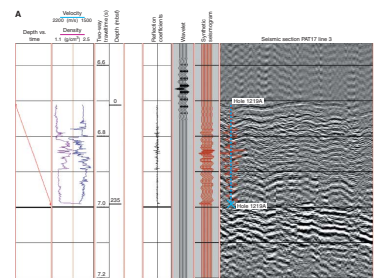
Synthetic Seismics

The aim of creating a synthetic seismogram is to provide a means of matching the reflections expected from the formation (measured physical properties from log and core sources) with those in the seismic data. This allows the seismic data to be interpreted in terms of the measured formation properties; for example, lithologic or chronologic boundaries can be picked out as specific seismic horizons. If a synthetic seismogram can be generated for a number of sites, these data provide the basis for producing a regional seismic stratigraphy.

The GRA density and PWL (whole core) velocity data sets were spliced onto the top of the FMD sonic log and HLDT density logging data in order to provide data for the entire formation. Because the core densities and velocities differ from the in situ measured logging data, a correction factor for the spliced section was computed (i.e., core data were corrected to in situ values). These full-depth data sets were then imported into the IESX module of the Schlumberger GeoQuest program Geoframe to calculate the synthetic seismograms. The impedance (velocity \times density) was calculated, and the impedance contrast between successive layers gave the reflection coefficient series. The source wavelet (obtained by extracting the seafloor reflection from the seismic data) was convolved with the reflection coefficient series to generate the synthetic seismogram (Fig. F48A).

The synthetic seismogram matched the seismic data well. The chert layers, which appear as a high-density and high-velocity region (Fig. F42), should be located at the base of the borehole and show up as a strong reflector. However, the first strong reflector appears 15 to 20 m lower in the section, suggesting that either the chert layers were discontinuous and the section cored was a very small patch higher than the main chert horizons, or the formation velocities are lower than those measured by the logging data. To check this latter possibility, the lower PWL velocities were used to calculate a second synthetic seismogram (Fig. F48B). The match between the synthetic seismogram and the seismic data is good. Generally it is expected that the in situ collected logging velocity data will better reflect the true formation velocity than the core velocity data (Mayer et al., 1985). Here, however, the opposite situation suggests that the FMD logging velocity measurements may have overestimated the true formation velocities, most likely as a result of problems with similarity in the mud and formation velocities.

F48. Synthetic seismograms derived from velocity and density, p. 93.



REFERENCES

- Berggren, W.A., Kent, D.V., Swisher, C.C. III, and Aubry, M.-P., 1995. A revised Cenozoic geochronology and chronostratigraphy. *In* Berggren, W.A., Kent, D.V., Aubry, M.-P., and Hardenbol, J. (Eds.), *Geochronology, Time Scales and Global Stratigraphic Correlation*. Spec. Publ.—Soc. Econ. Paleontol. Mineral., 54:129–212.
- Bukry, D., 1973. Low-latitude coccolith biostratigraphic zonation. *In* Edgar, N.T., Saunders, J.B., et al., *Init. Repts. DSDP*, 15: Washington (U.S. Govt. Printing Office), 685–703.
- Cande, S.C., and Kent, D.V., 1995. Revised calibration of the geomagnetic polarity timescale for the Late Cretaceous and Cenozoic. *J. Geophys. Res.*, 100:6093–6095.
- Cande, S.C., LaBrecque, J.L., Larson, R.L., Pitmann, W.C. III, Golovchenko, X., and Haxby, W.F., 1989. *Magnetic Lineations of the World's Ocean Basins*. AAPG Map Ser., 13.
- Engebretson, D.C., Cox, A., and Gordon, R.G., 1985. *Relative Motions Between Oceanic and Continental Plates in the Pacific Basin*. Spec. Pap.—Geol. Soc. Am., 206.
- Gripp, A.E., and Gordon, R.G., 1990. Current plate velocities relative to the hotspots incorporating the NUVEL-1 global plate motion model. *Geophys. Res. Lett.*, 17:1109–1112.
- Hagelberg, T., Shackleton, N., Pisias, N., and Shipboard Scientific Party, 1992. Development of composite depth sections for Sites 844 through 854. *In* Mayer, L., Pisias, N., Janecek, T., et al., *Proc. ODP, Init. Repts.*, 138 (Pt. 1): College Station, TX (Ocean Drilling Program), 79–85.
- Lyle, M., 2000. Data submission to ODP Pollution Prevention and Safety Panel: proposed drill sites for ODP Leg 198—a Paleogene equatorial APC transect. *BSU-CGISS Tech Rept.*, 2000-03.
- Mayer, L.A., Shipley, T.H., Theyer, F., and Wilkens, R.H., 1985. Seismic modelling and paleoceanography at Deep Sea Drilling Project Site 574. *Init. Repts. DSDP*, 85: Washington (U.S. Govt. Printing Office).
- Nomura, R., 1995. Paleogene to Neogene deep-sea paleoceanography in the eastern Indian Ocean: Benthic foraminifera from ODP Sites 747, 757, and 758. *Micropaleontology*, 41:251–290.
- Okada, H., and Bukry, D., 1980. Supplementary modification and introduction of code numbers to the low-latitude coccolith biostratigraphic zonation (Bukry, 1973; 1975). *Mar. Micropaleontol.*, 5:321–325.
- Petronotis, K.E., Gordon, R.G., and Acton, G.D., 1994. A 57 Ma Pacific plate paleomagnetic pole determined from a skewness analysis of crossings of marine magnetic Anomaly 25r. *Geophys. J. Int.*, 118:529–554.
- Pollack, H.N., Hurter, S.J., and Johnson, J.R., 1993. Heat flow from the earth's interior: analysis of the global data set. *Rev. Geophys.*, 31:267–280.
- Pribnow, D.F.C., Kinoshita, M., and Stein, C.A., 2000. Thermal data collection and heat flow recalculations for ODP Legs 101–180. Institute for Joint Geoscientific Research, GGA, Hanover, Germany, 0120432. Available from World Wide Web: <<http://www-odp.tamu.edu/publications/heatflow/>>. [Cited 2001-11-22]
- Raffi, I., 1999. Precision and accuracy of nannofossil biostratigraphic correlation. *Philos. Trans. R. Soc. London, Ser. A*, 357:1975–1994.
- Rider, M., 1996. *The Geological Interpretation of Well Logs* (2nd ed.): Caithness (Whittles Publishing).
- Sanfilippo, A., and Nigrini, C., 1995. Radiolarian stratigraphy across the Oligocene/Miocene transition. *Mar. Micropaleontology*, 24:239–285.
- Sanfilippo, A., and Nigrini, C., 1998. Code numbers for Cenozoic low latitude radiolarian biostratigraphic zones and GPTS conversion tables. *Mar. Micropaleontol.*, 33:109–156.

- Shackleton, N.J., Crowhurst, S.J., Weedon, G.P., and Laskar, J., 1999. Astronomical calibration of Oligocene–Miocene time. *Philos. Trans. R. Soc. London, Ser. A*, 357:1907–1929.
- Shackleton, N.J., Hall, M.A., Raffi, I., Tauxe, L., and Zachos, J., 2000. Astronomical calibration age for the Oligocene–Miocene boundary. *Geology*, 28:447–450.
- Taylor, S.R., and McLennan, S.M., 1985. *The Continental Crust: Its Composition and Evolution*: Oxford (Blackwell Scientific).
- Torrence, C., and Compo, G.P., 1998. A practical guide to wavelet analysis. *Bull. Am. Meteorol. Soc.*, 79:61–78.
- van Andel, T.H., Heath, G.R., et al., 1973. *Init. Repts. DSDP*, 16: Washington (U.S. Govt. Printing Office).
- van Andel, T.H., Heath, G.R., and Moore, T.C. Jr., 1975. *Cenozoic History and Paleooceanography of the Central Equatorial Pacific Ocean: A Regional Synthesis of Deep Sea Drilling Project Data*. Mem.—Geol. Soc. Am., 143.
- van Morkhoven, F.P.C.M., Berggren, W.A., and Edwards, A.S., 1986. *Cenozoic Cosmopolitan Deep-Water Benthic Foraminifera*. Bull. Cent. Rech. Explor.—Prod. Elf-Aquitaine, 11.

Figure F1. Location of Site 1219 in the Leg 199 transect. In the lower panel, gray shading = seafloor depths >5000 mbsl, red shading = approximate position of magnetic Anomaly C25, the nominal target crust of the 56-Ma transect. FZ = fracture zone.

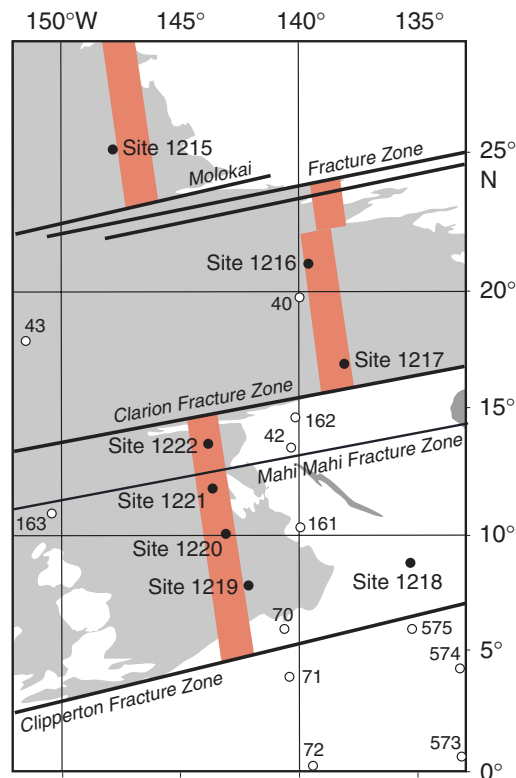
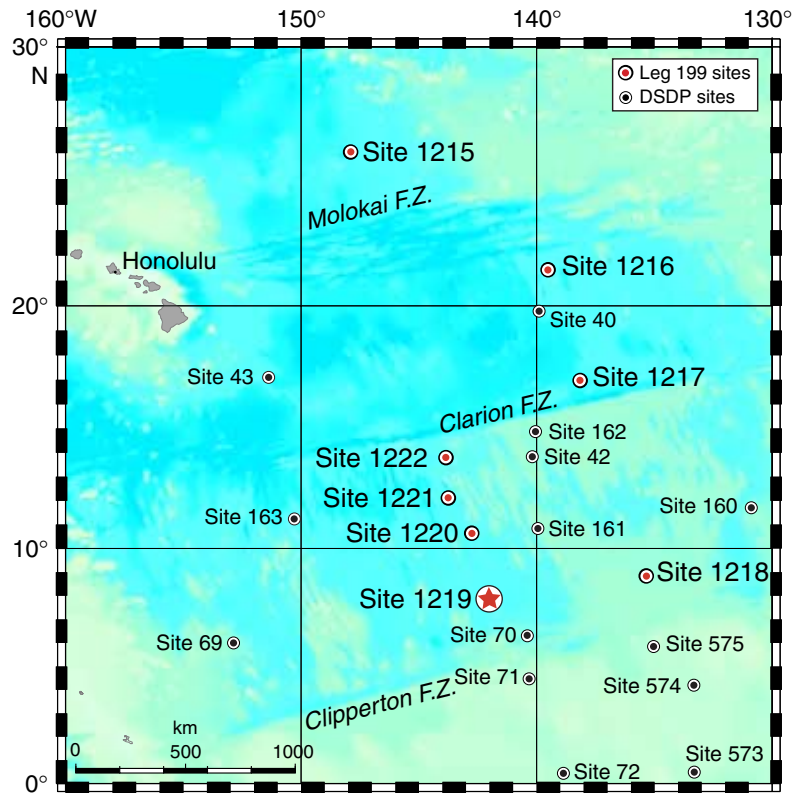


Figure F2. Seismic reflection profile across Site 1219. The sedimentary section is marked by a weakly reflective unit, ~38 ms two-way traveltime (TWT) below the seafloor, assumed to be clays. Below, between 38 and 219 ms TWT, are units bounded by the Y, P5, P4, and P3 seismic horizons (see [Lyle et al.](#), this volume) that we assigned to lower Miocene–upper Eocene sedimentary units.

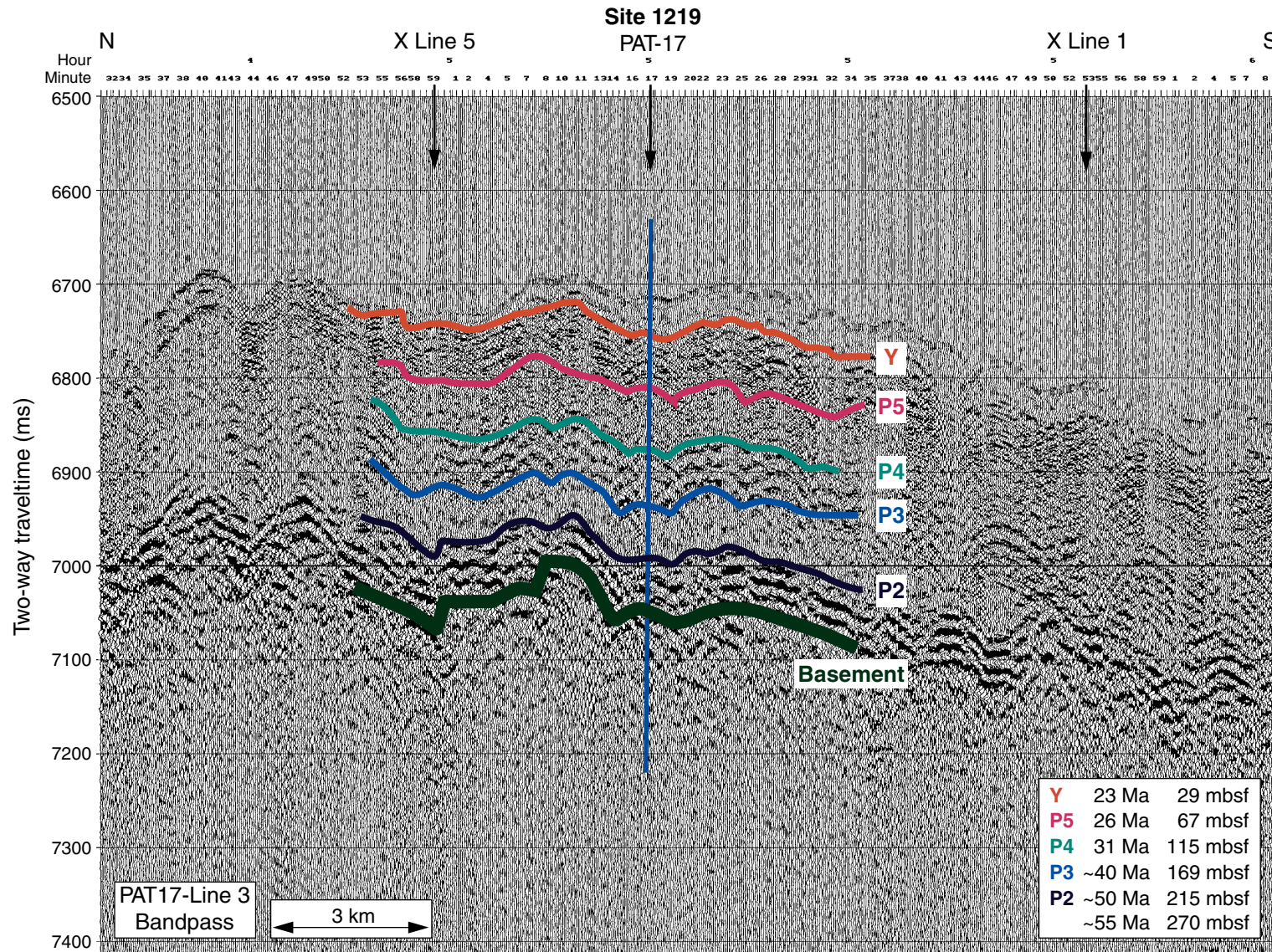


Figure F3 (continued).

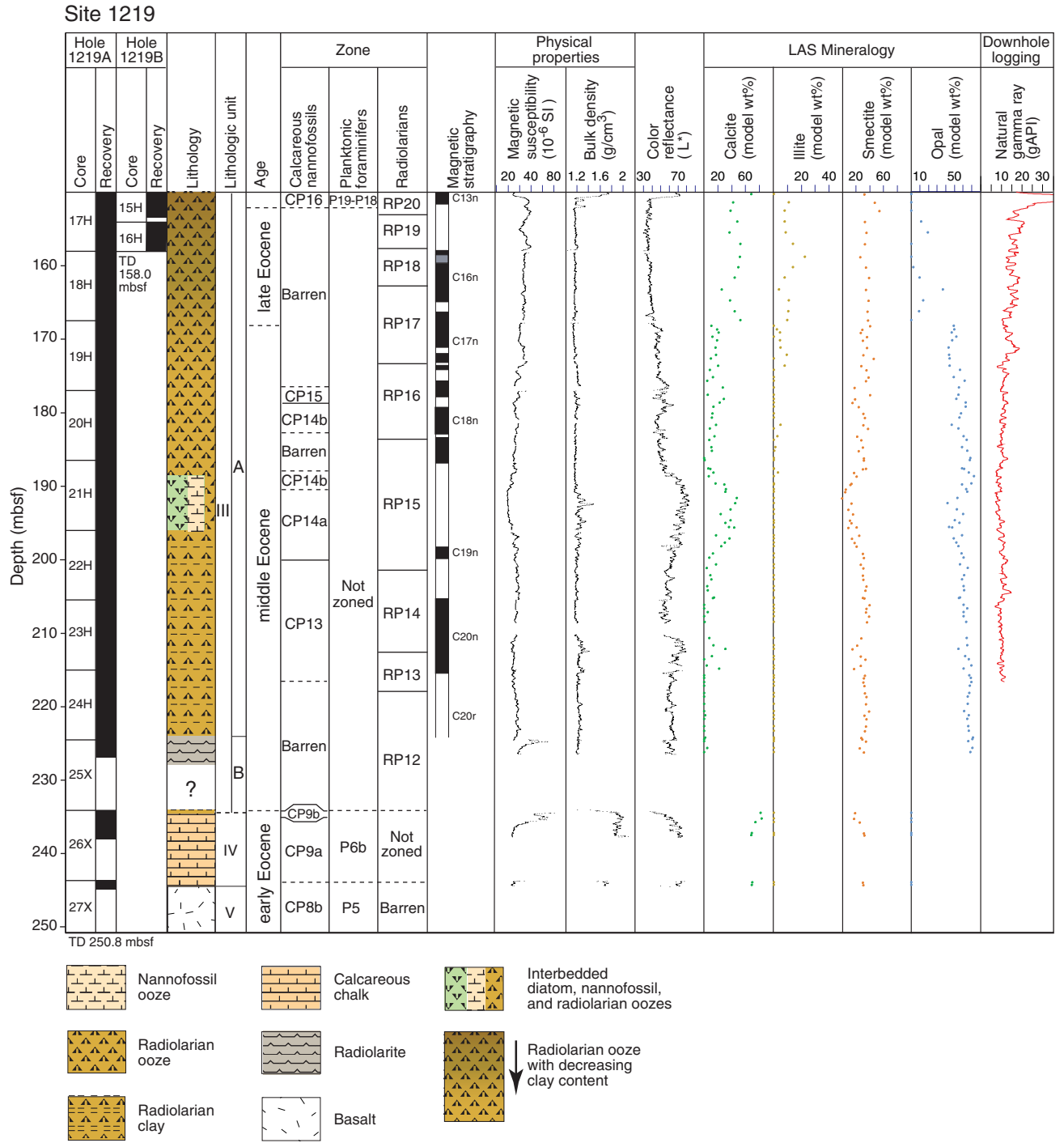


Figure F4. Close-up digital photograph of the Unit I–II transition (interval 199-1219A-4H-4, 34–80 cm).

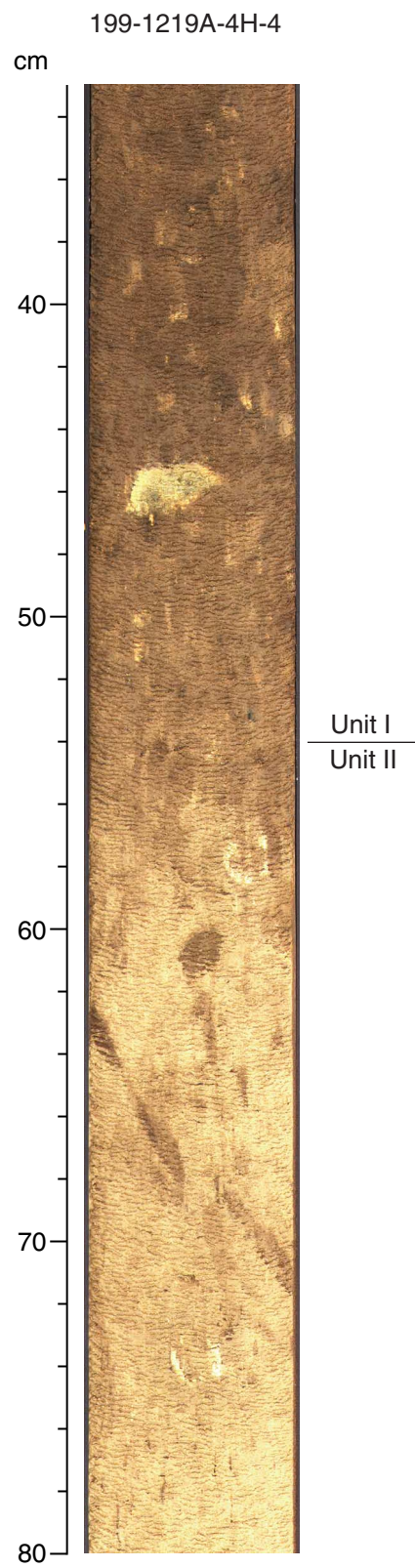


Figure F5. Close-up digital photograph of the Unit II–III transition (interval 199-1219A-17H-2, 50–102 cm).

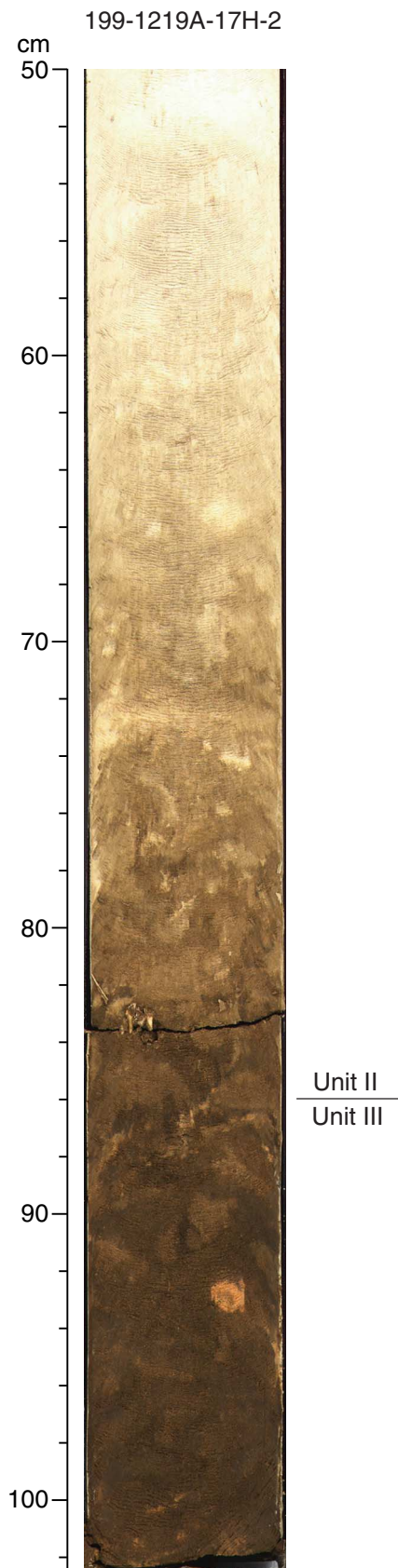


Figure F6. Close-up digital photograph of the Unit III–IV transition (interval 199-1219A-26X-1, 0–52 cm).

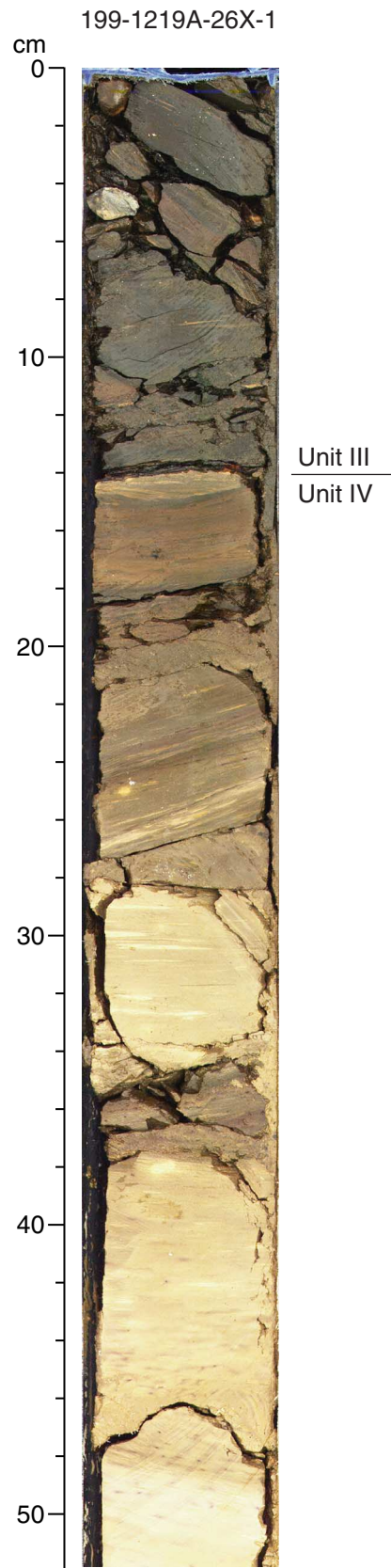


Figure F7. Close-up digital photograph of the Unit IV–V transition (interval 199-1219A-27X-CC, 0–39 cm).

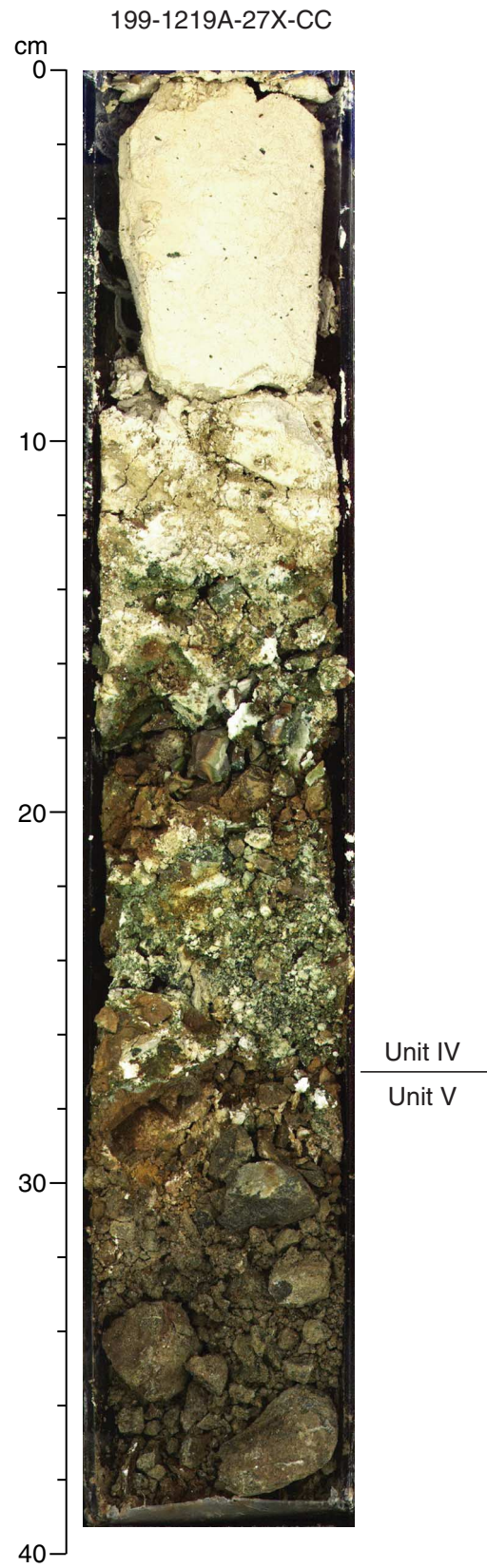


Figure F8. Color reflectance (L^*) and red/blue (a^*/b^*) spectral data from Hole 1219A. Color reflectance primarily records variations in clay and nannofossil content and, to a lesser degree, radiolarian content. Changes in red/blue spectral values can result from small changes in the amount organic matter and oxide minerals that are redox sensitive, with higher values generally corresponding to more oxygenated conditions. Cyclical variations in both parameters occur throughout the section, with a pronounced shift from high- to low-amplitude variations occurring at 50.0 mbsf.

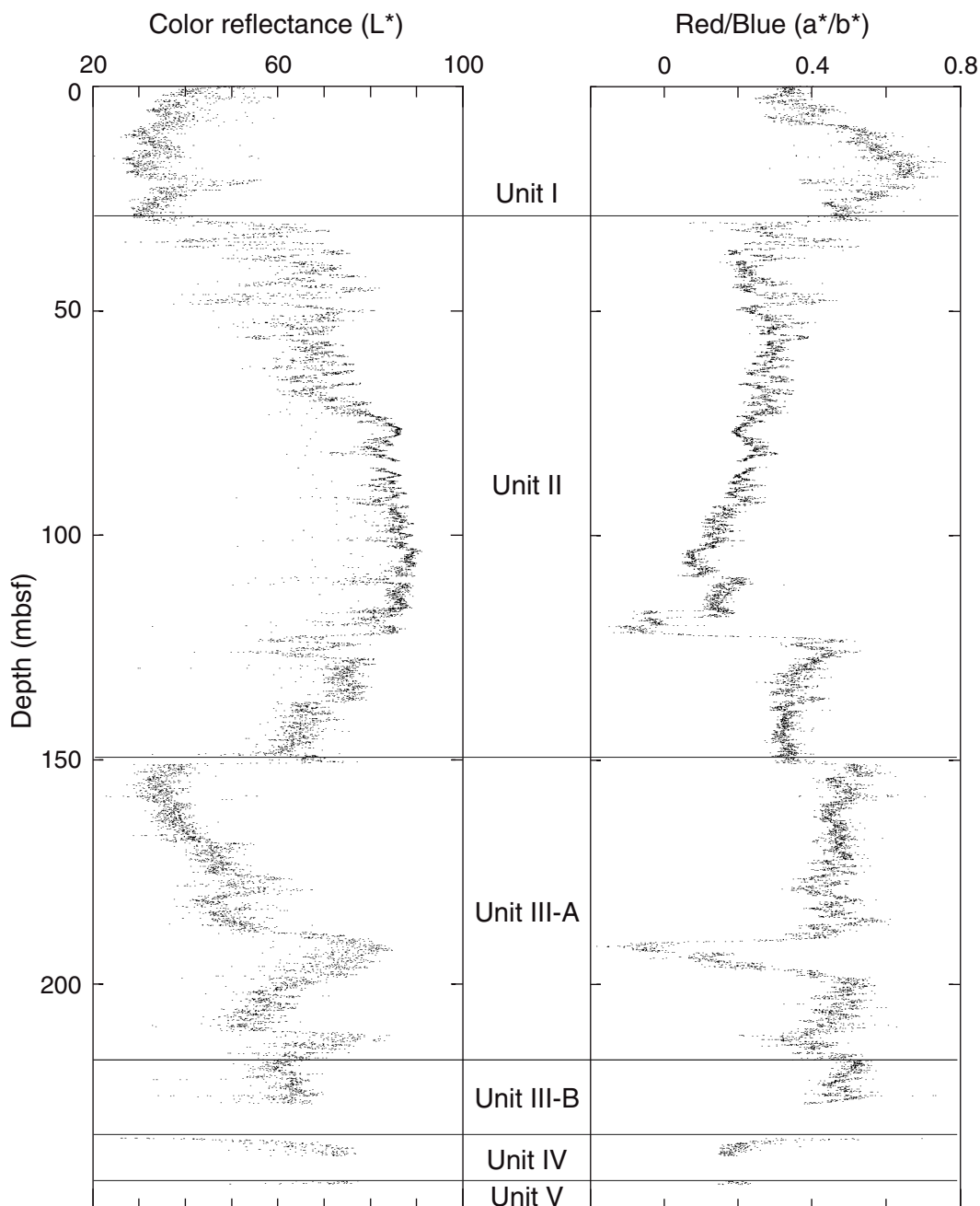


Figure F9. Composite digital photographs of cores from the upper Eocene–lower Oligocene in Holes 1218A, 1218C, and 1219A. A distinct color change is associated with the transition from radiolarian-ooze to nanofossil-ooze sedimentation at the E/O boundary. Aperture changes are denoted with an arrow and the letter A.

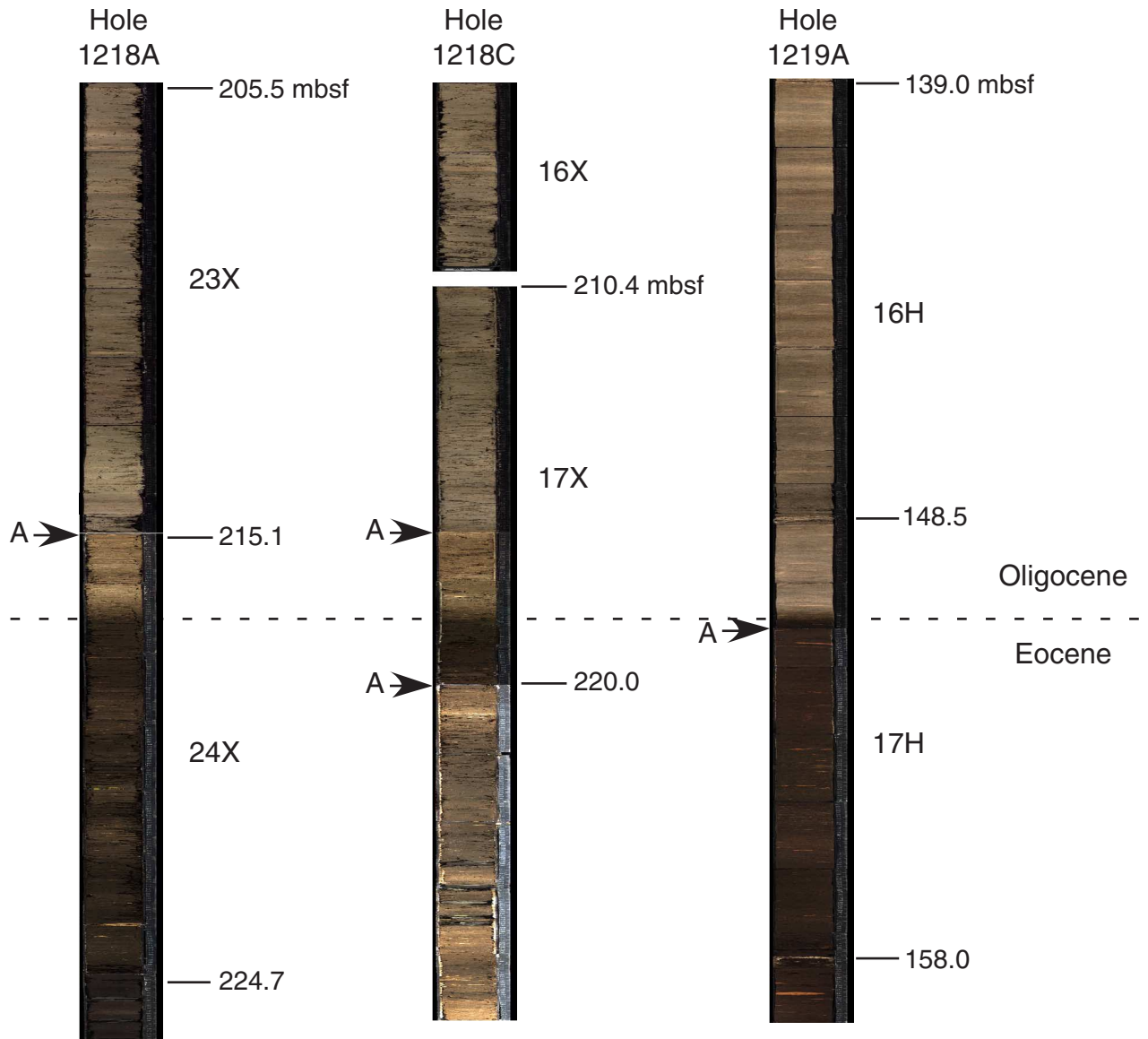


Figure F10. Lithologic columns showing the major units from Sites 1218 and 1219 plotted vs. depth and age.

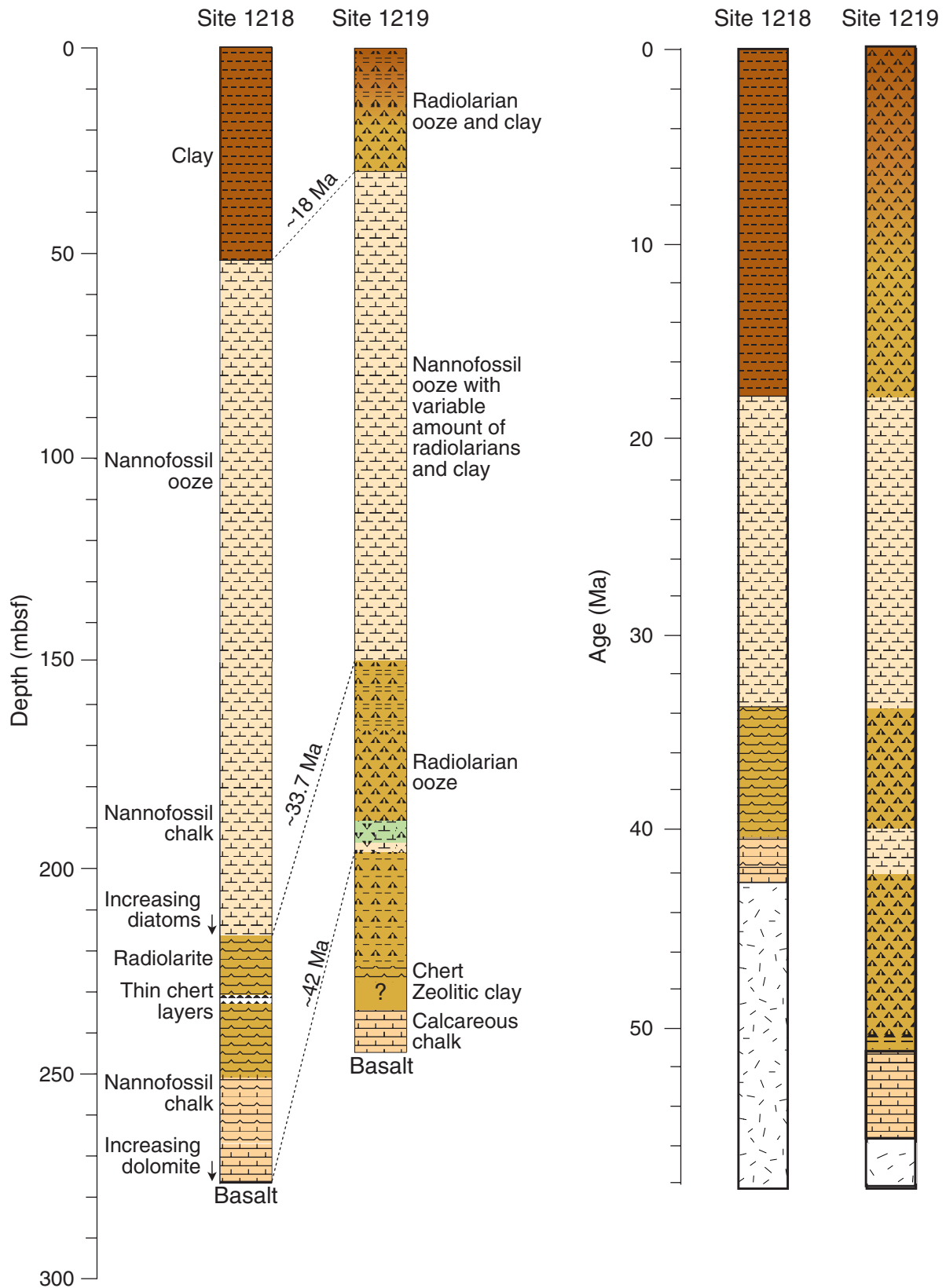


Figure F11. Biostratigraphic zonation for Site 1219. Horizontal dashed lines indicate that a boundary can only be approximated by available biostratigraphy. Vertical dashed lines show intervals where the absence of intervening zonal markers prevents further subdivision of the zonation. TD = total depth. (Continued on next page.)

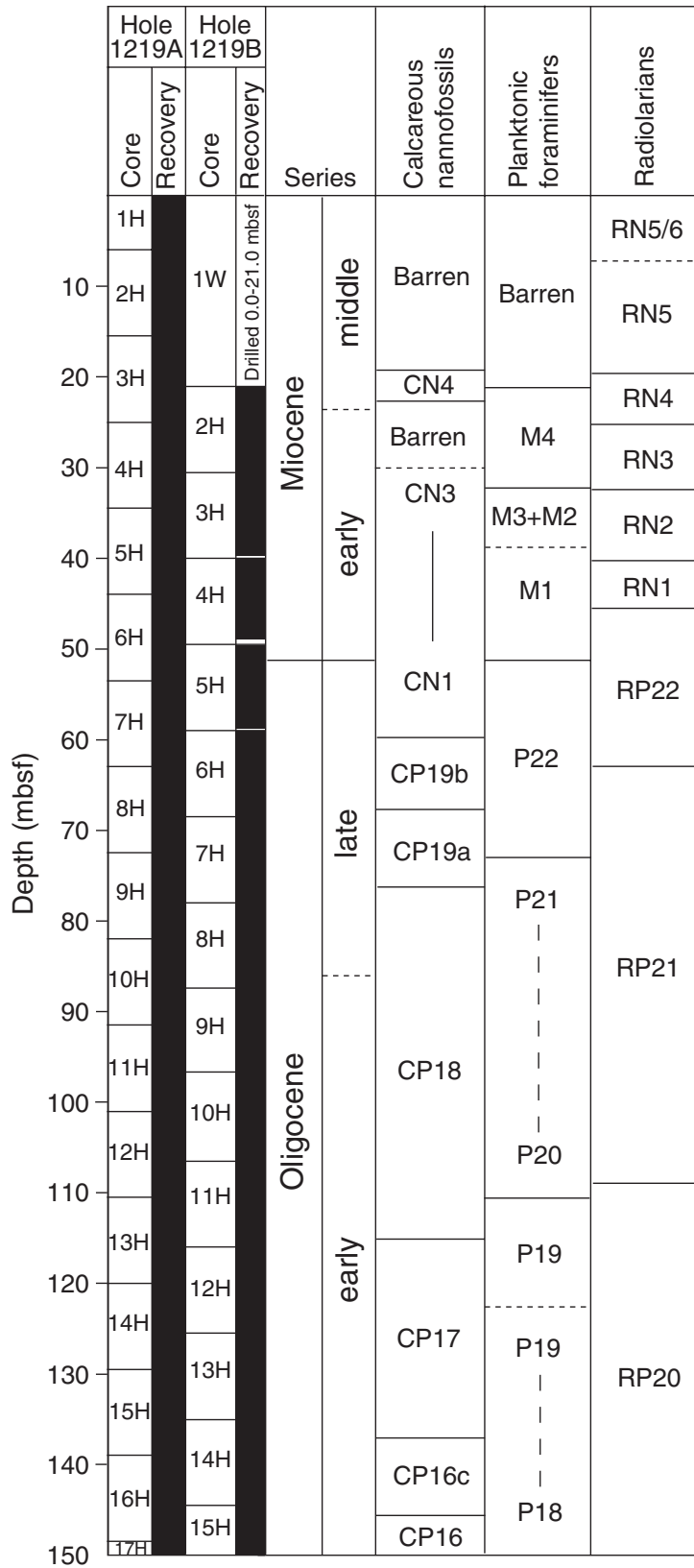


Figure F11 (continued).

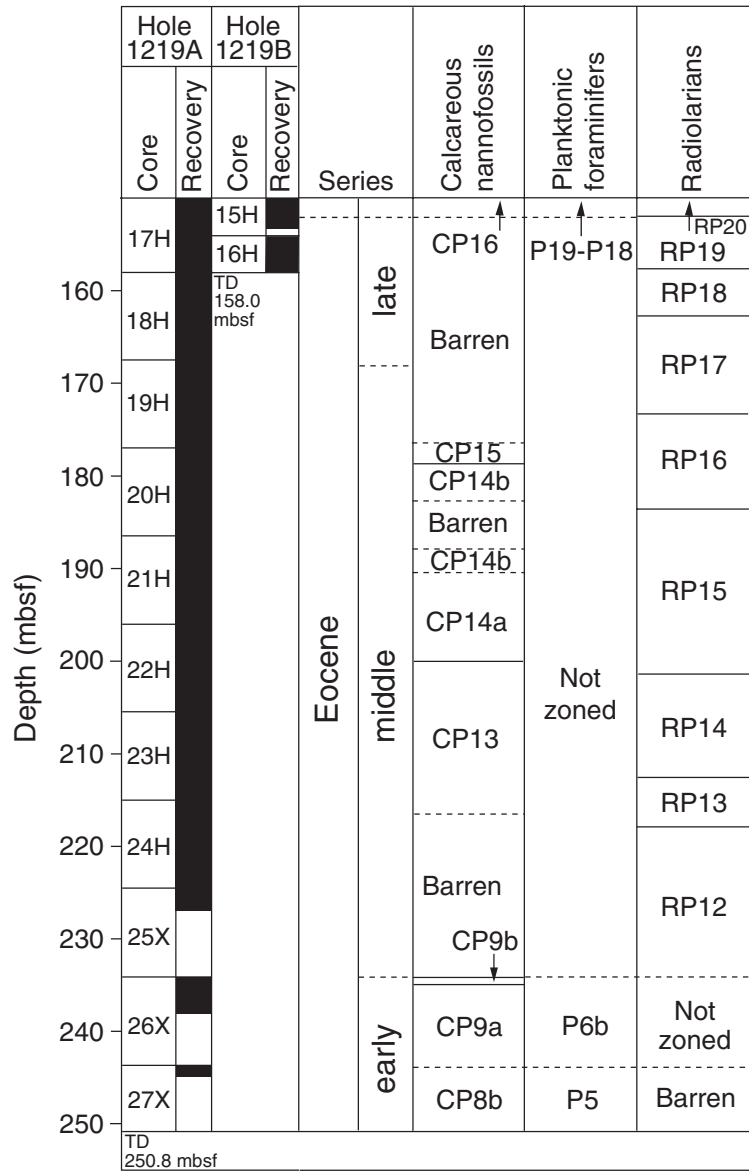
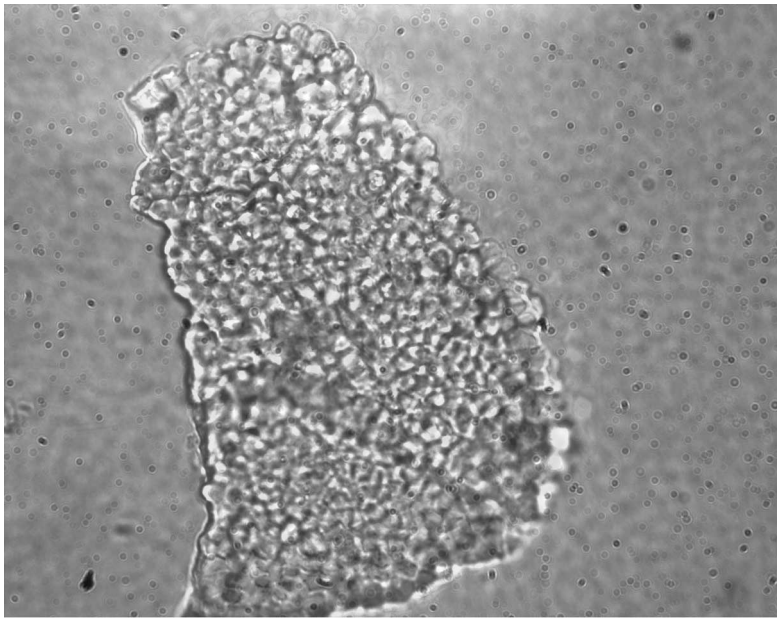


Figure F12. Photomicrograph (open nicol) of the radial wall texture of *Epistominella exigua*, showing secondary calcite overgrowth on wall surface. Scale bar = 50 μm .



50 μm

Figure F13. Archive-half magnetization intensities after AF demagnetization at a peak field of 20 mT from Holes 1219A and 1219B.

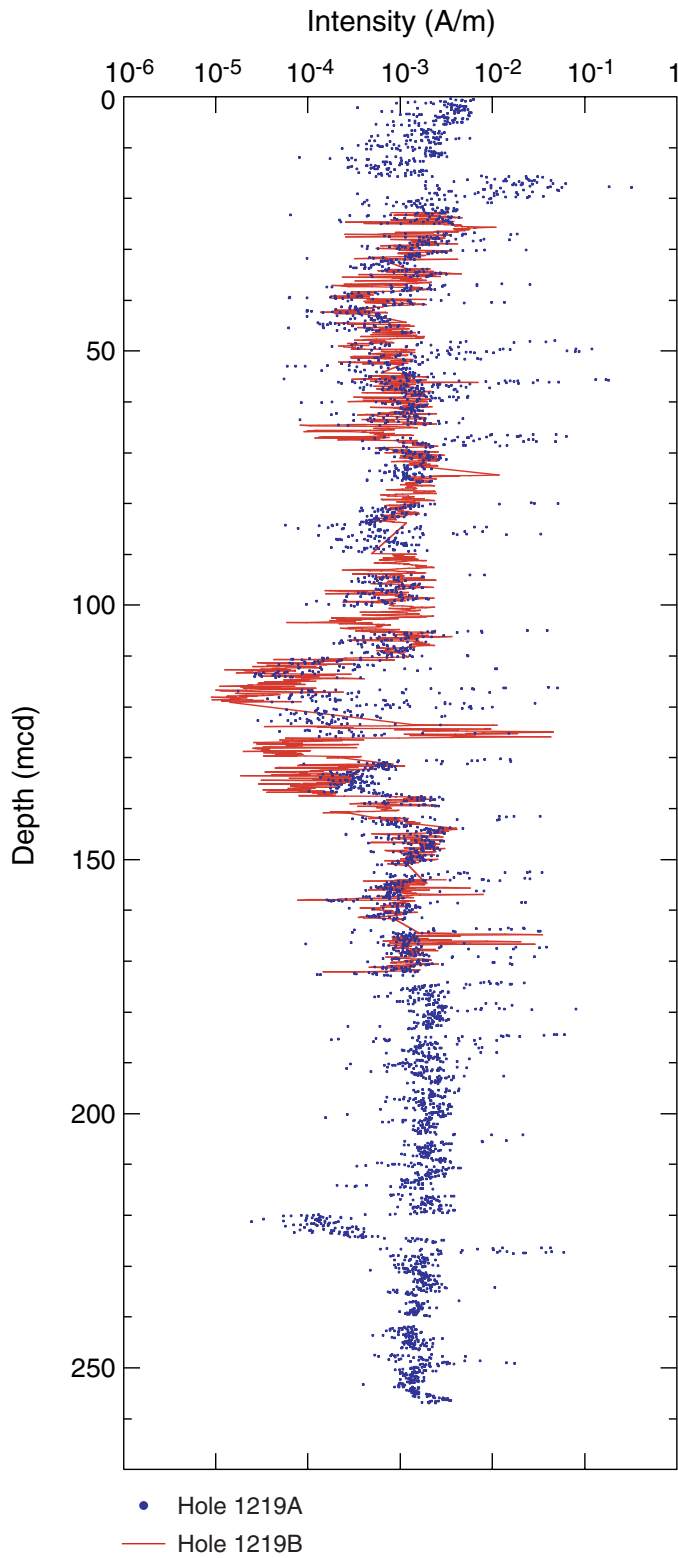


Figure F14. Zijdeveld plot for a typical sample showing the magnetically soft overprint that was used to reorient Cores 199-1219A-1H and 2H. The drilling-induced overprint was removed after the first demagnetization step. J = intensity.

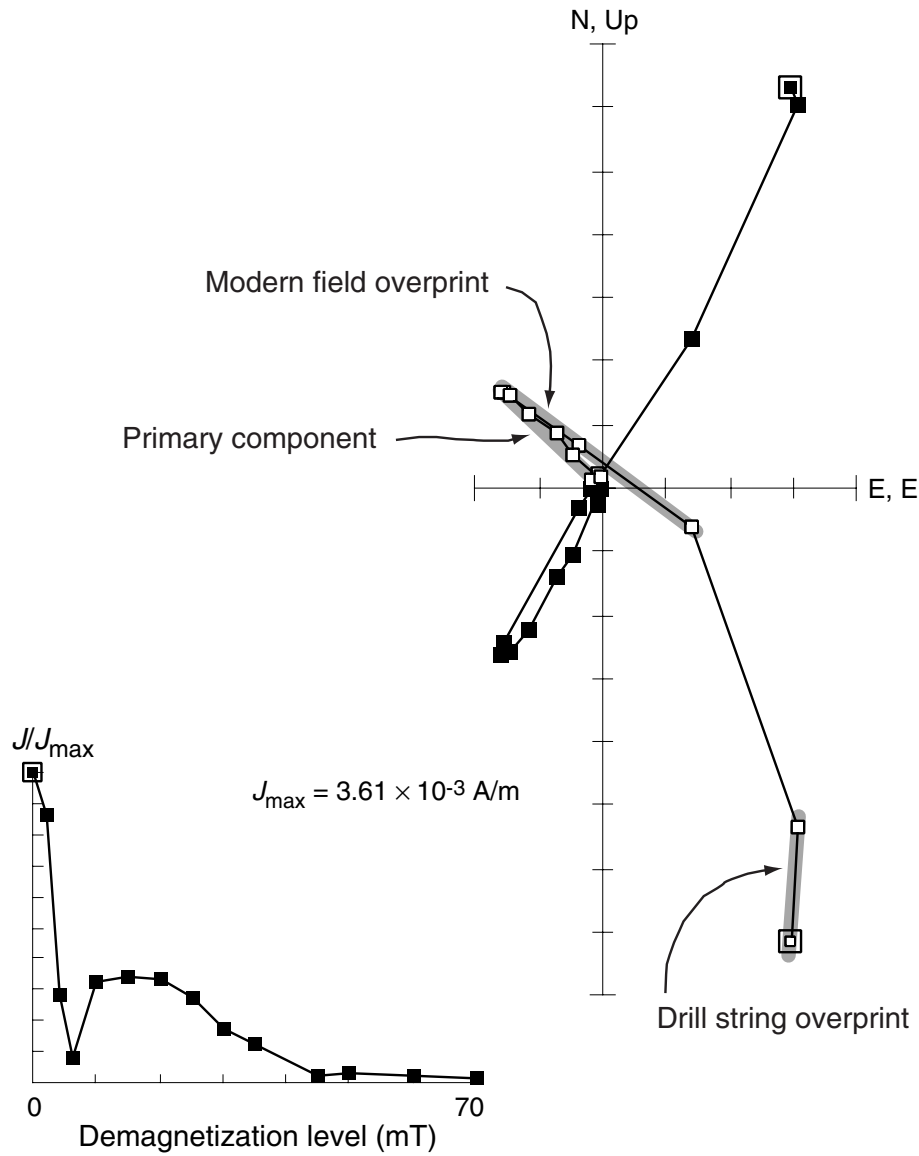


Figure F15. Magnetostratigraphy of the upper 12 mcd at Hole 1219A. To calculate virtual geomagnetic pole (VGP) latitudes, core declination was restored to magnetic north using the soft-overprint direction from discrete samples.

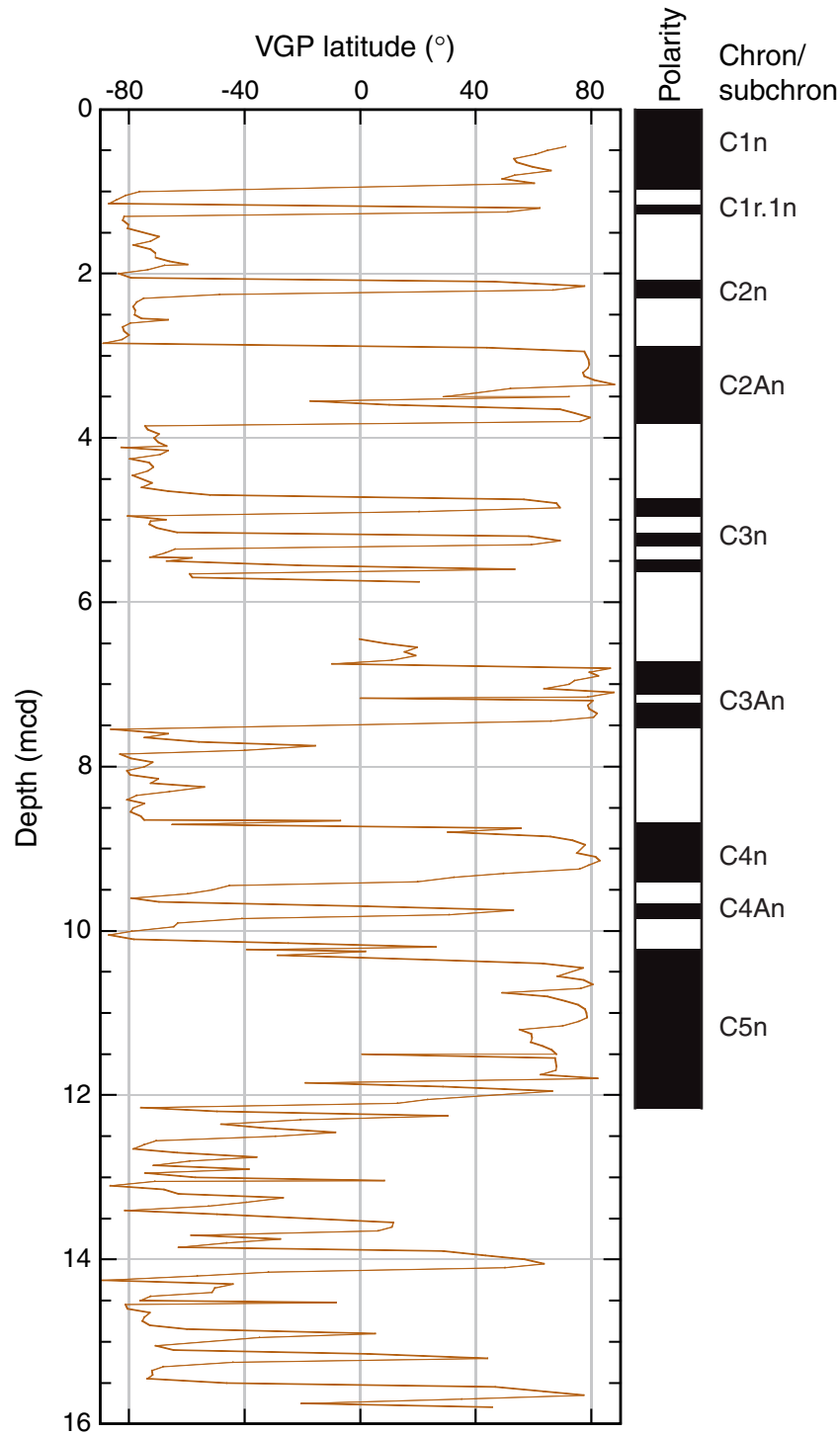


Figure F16. Composite magnetic stratigraphy at Site 1219 (blue line = Hole 1219A and black line = Hole 1219B). Virtual geomagnetic pole (VGP) latitudes were obtained after partial AF demagnetization of continuous measurements at a peak field of 20 mT. Polarity column shows interpreted zones of normal (black) and reversed (white) magnetization. Gray intervals indicate zones with an uncertain polarity interpretation. A. Miocene to early Oligocene, top 140 mcd. (Continued on next page.)

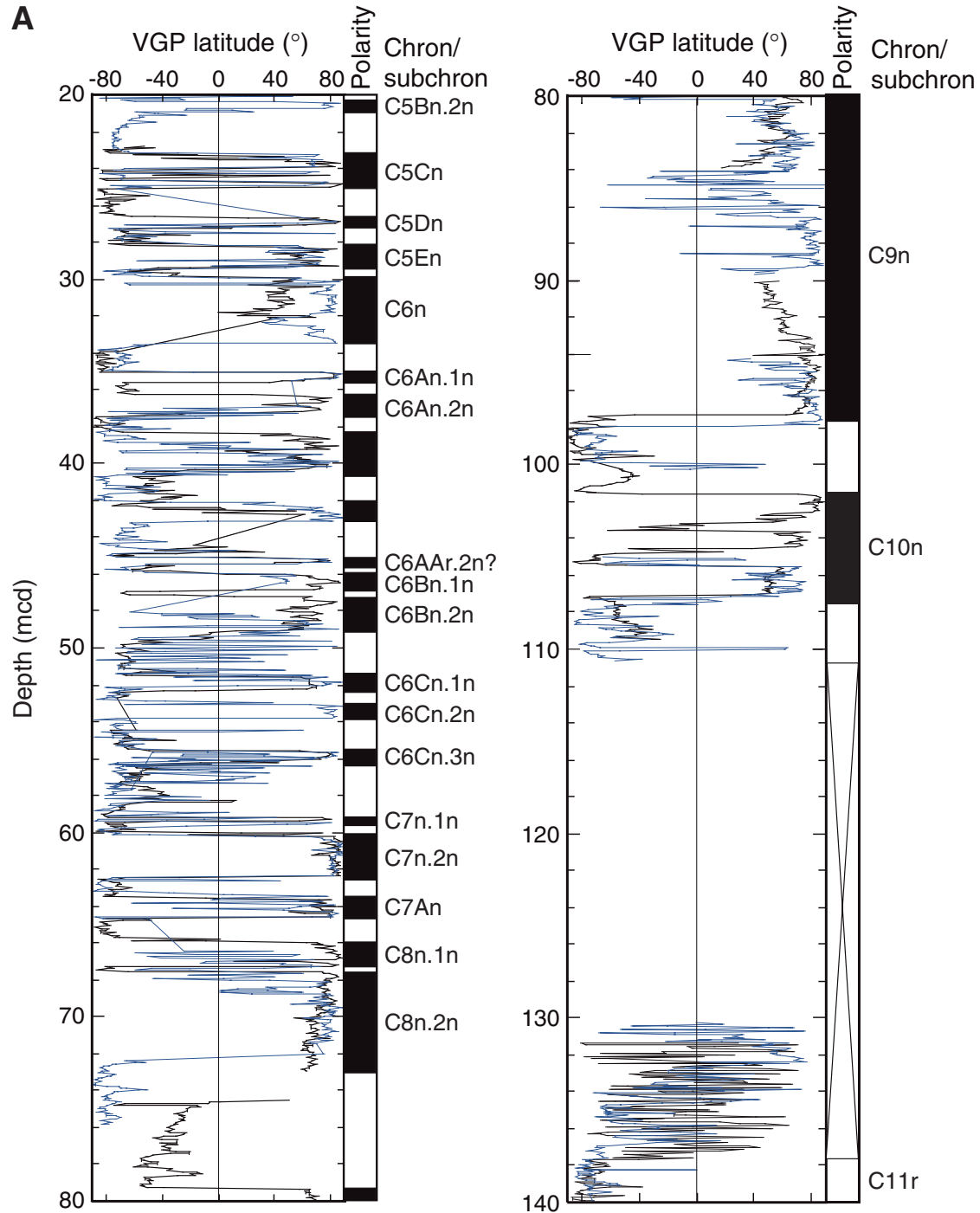


Figure F16 (continued). B. Early Oligocene–middle Eocene (bottom 120 mcd).

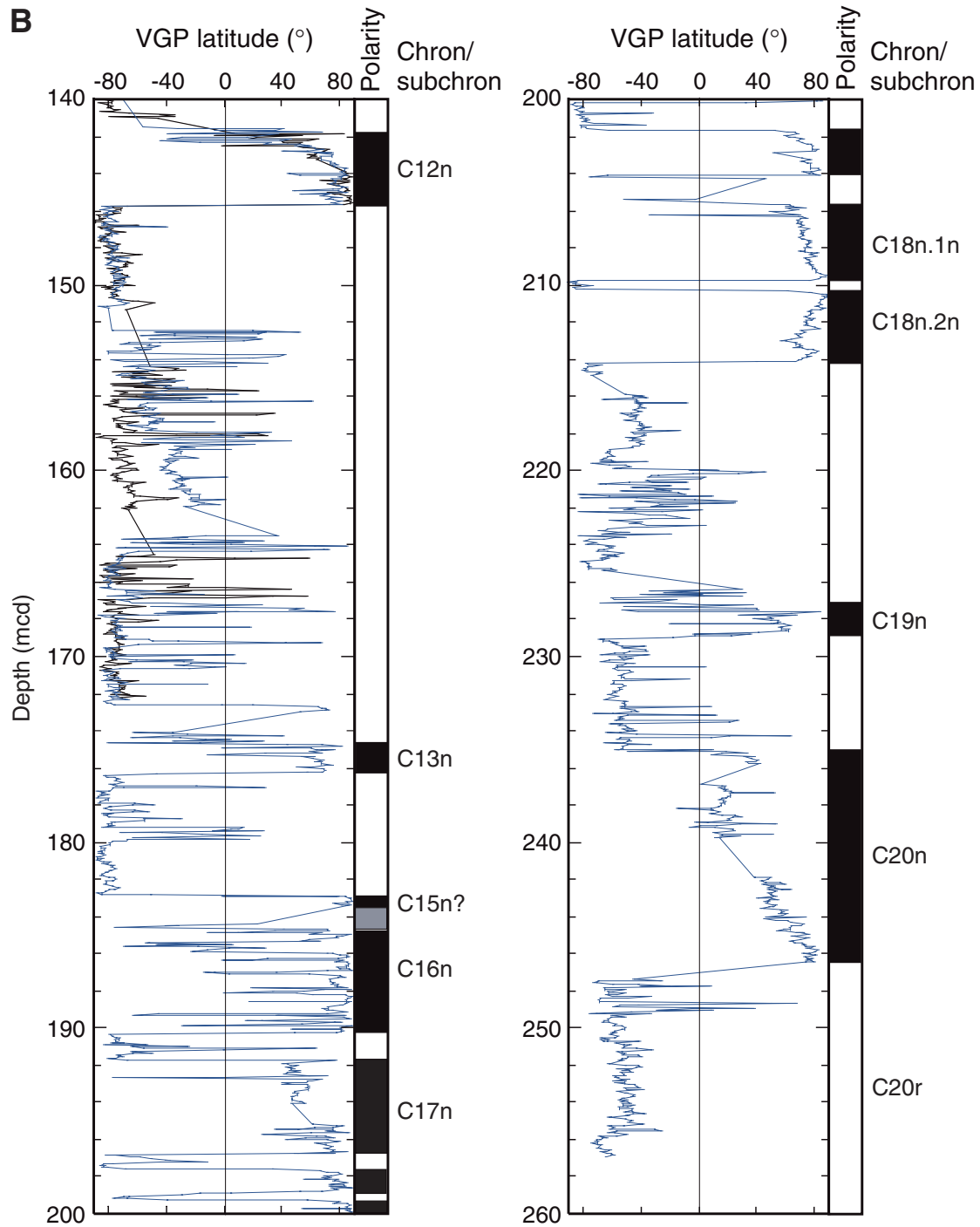


Figure F17. Gamma ray attenuation (GRA) bulk density data for Holes 1219A (leftmost curve in each panel) and 1219B plotted vs. composite depth. The data from Hole 1219B are offset by a constant for illustration purposes. All data sets are smoothed with a nine-point Gaussian filter. Intervals with obvious flow-in or drilling disturbance are removed from the data sets (see Table T8, p. 107).

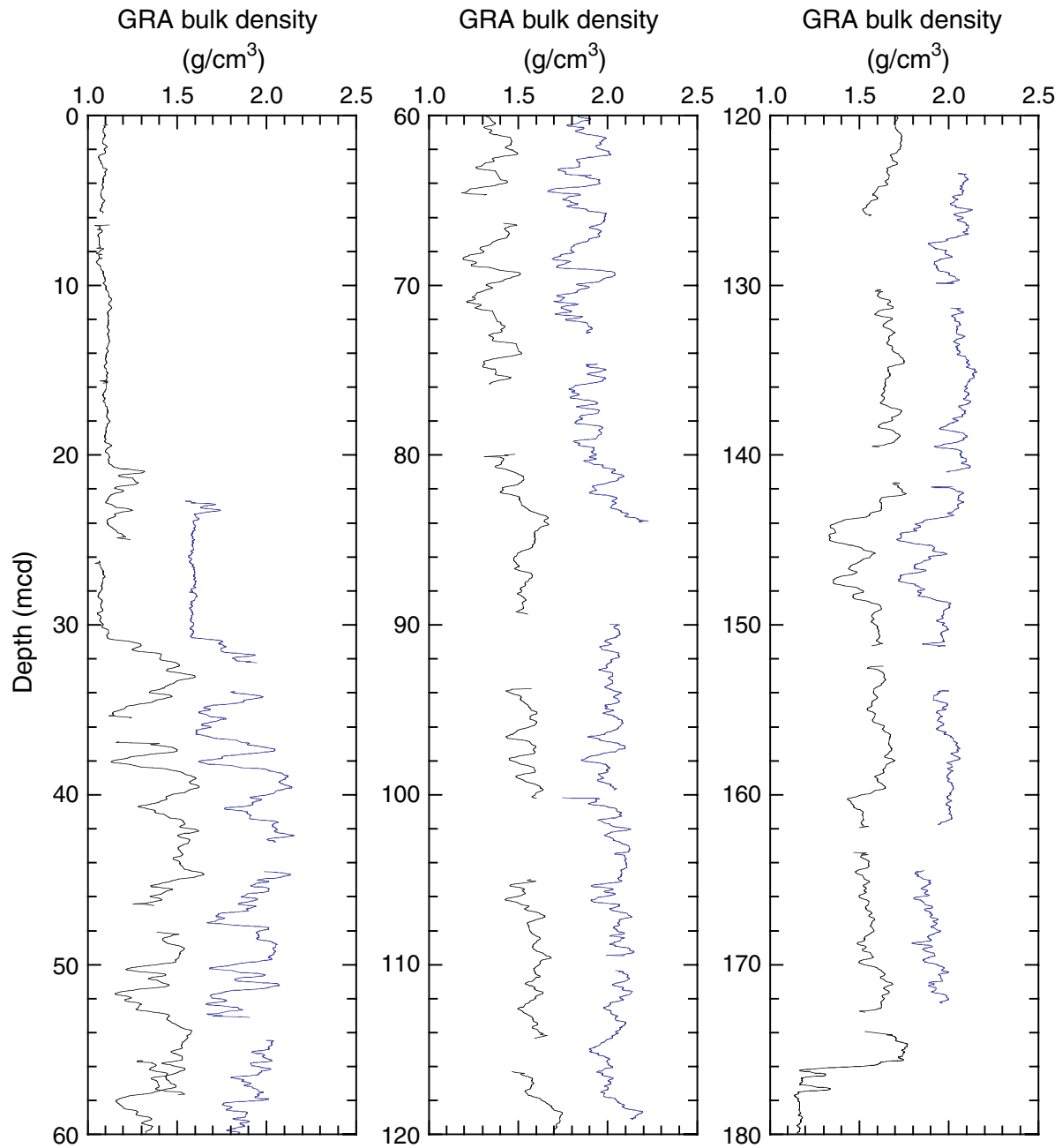


Figure F18. MS data for Holes 1219A (leftmost curve in each panel) and 1219B (rightmost curve in each panel) plotted vs. composite depth. The data from Hole 1219B are offset by a constant for illustration purposes. All data sets are smoothed with a nine-point Gaussian filter. Intervals with obvious flow-in or drilling disturbance are removed from the data sets (see Table T8, p. 107).

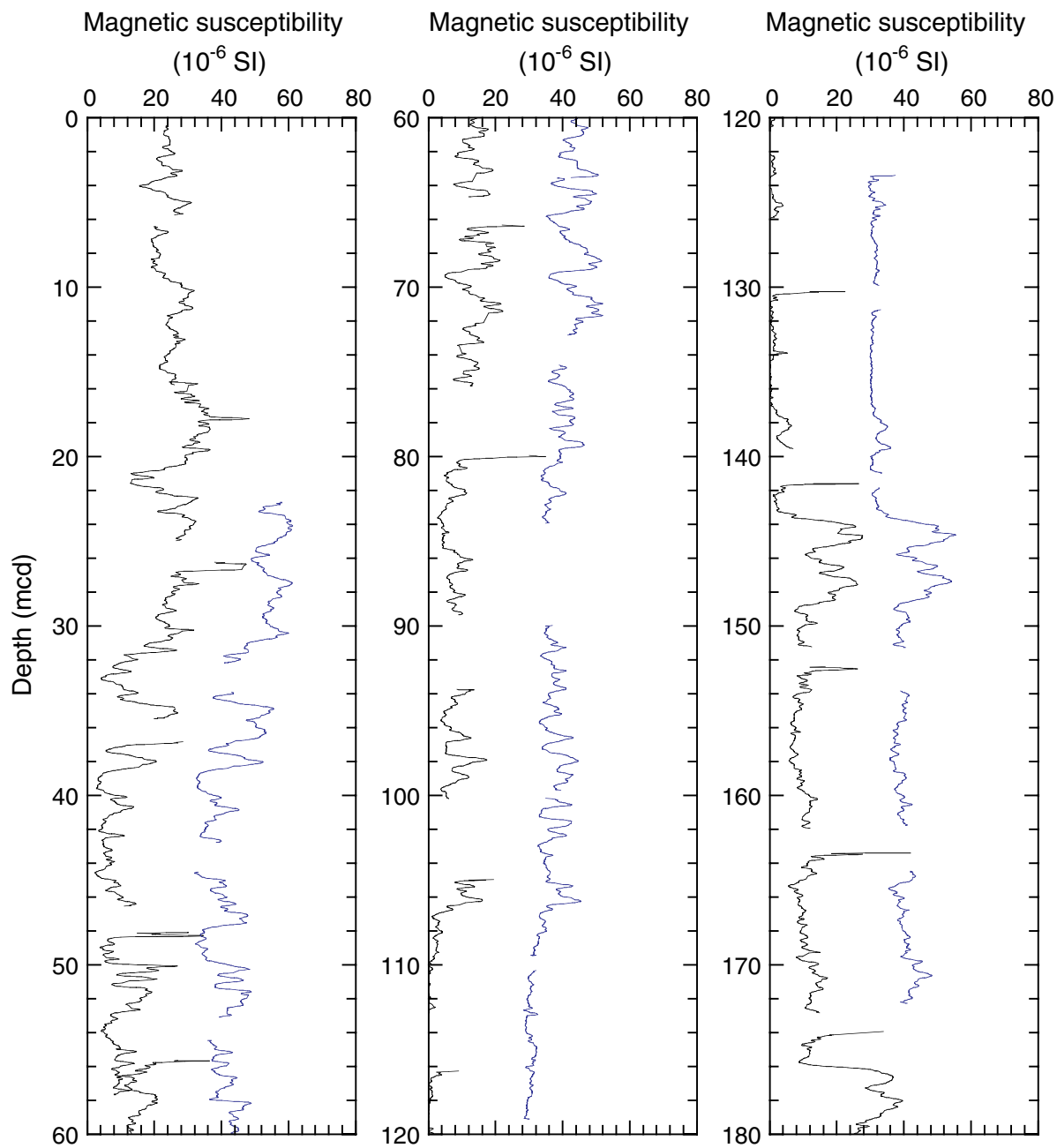


Figure F19. Color reflectance (L^*) data for Holes 1219A (leftmost curve in each panel) and 1219B (rightmost curve in each panel) plotted vs. composite depth. The data from Hole 1219B are offset by a constant for illustration purposes. All data sets are smoothed with a nine-point Gaussian filter. Intervals with obvious flow-in or drilling disturbance are removed from the data sets (see Table T8, p. 107).

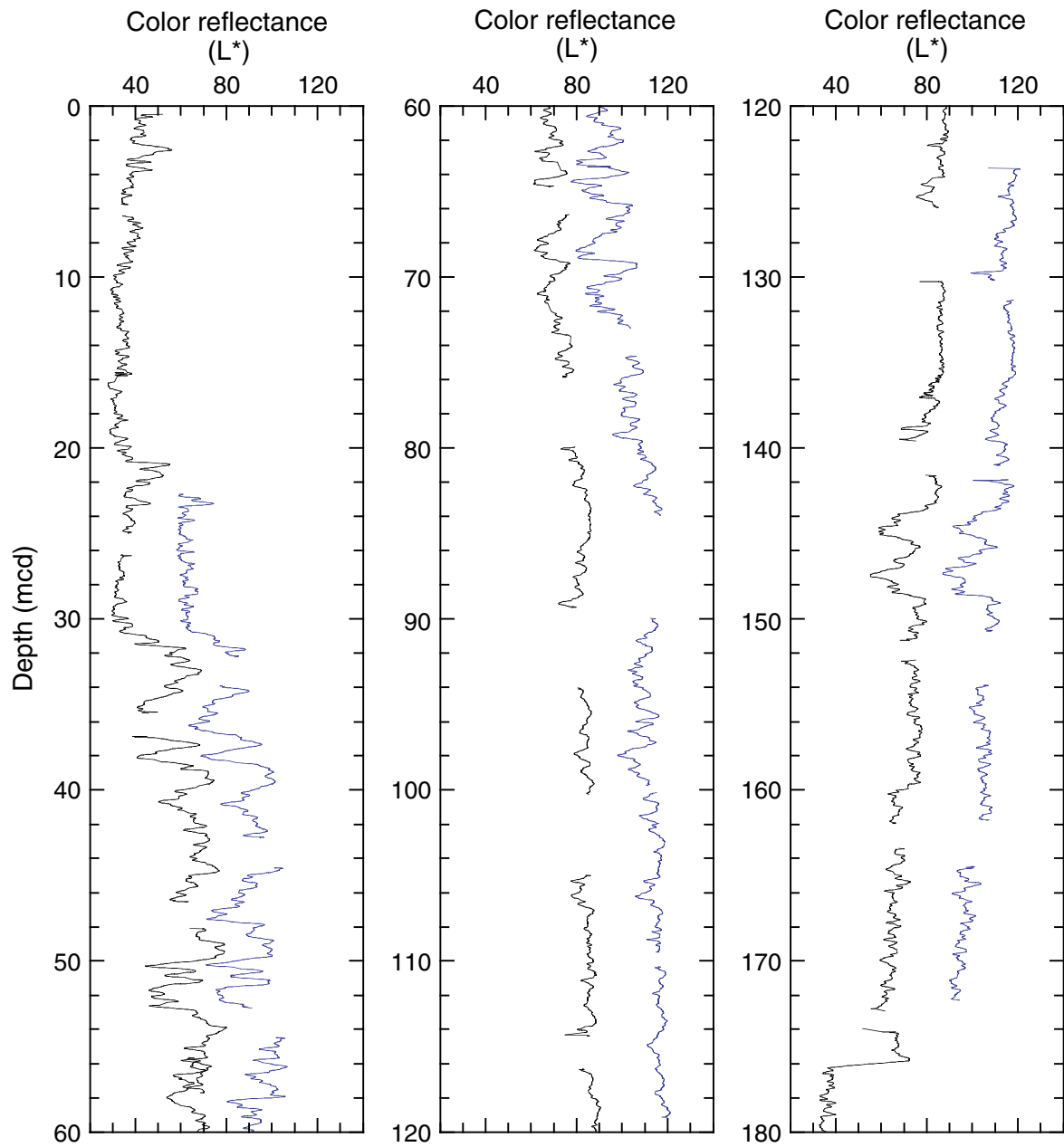


Figure F20. Spliced records of gamma ray attenuation (GRA) bulk density, magnetic susceptibility, and the color reflectance parameter (L^*) shown for the composite section of Site 1219. Lithology changes are clearly visible.

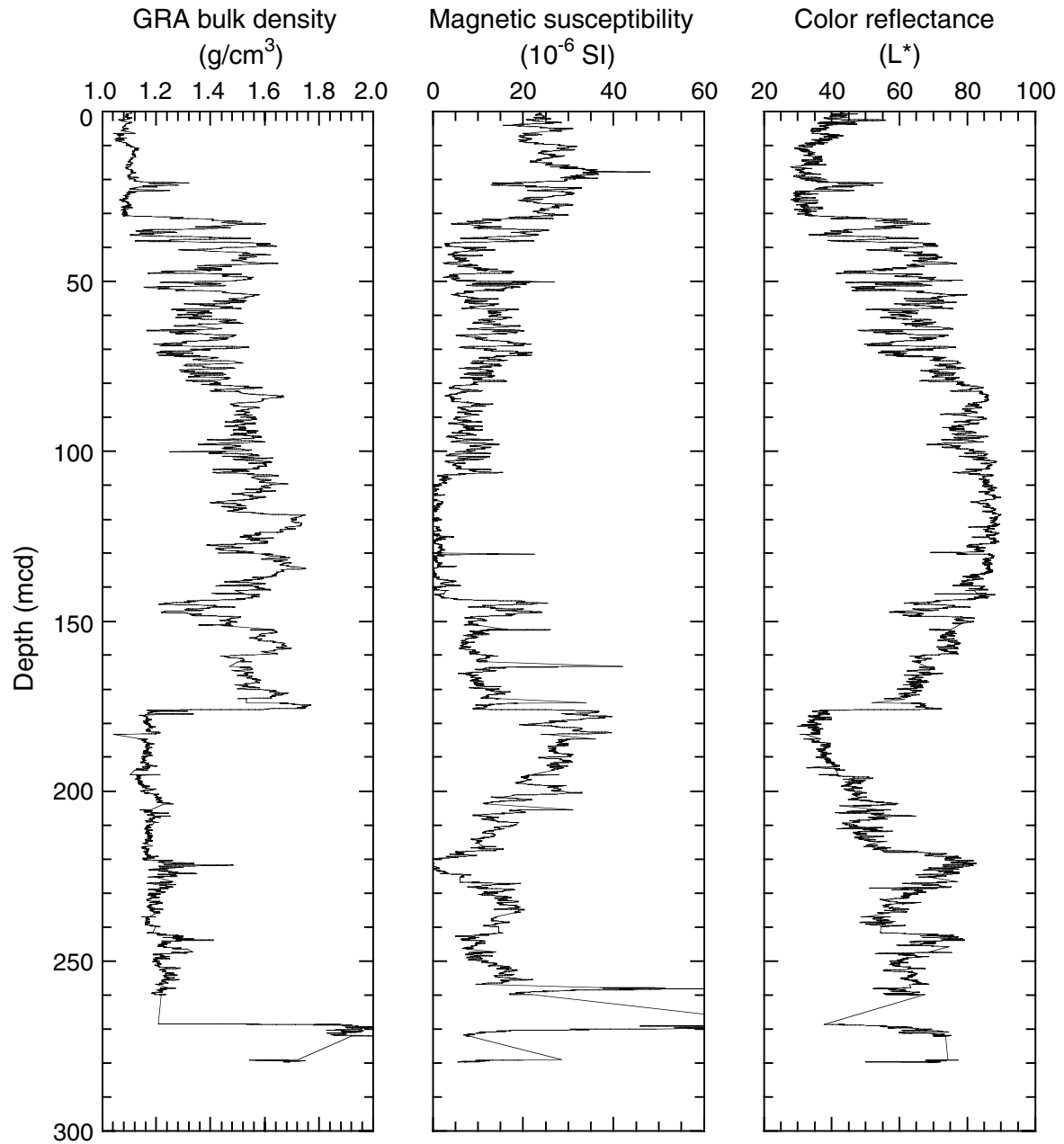


Figure F21. Spliced records of gamma ray attenuation (GRA) bulk density, magnetic susceptibility, and the color reflectance parameter (L^*) compared between Sites 1218 and 1219. The data are plotted on the common depth scale of Site 1218, using the transfer function from Site 1219 mcd to Site 1218 mcd shown at the bottom of the figure. In all three data panels, constant positive offsets were applied to data from Site 1219 (blue) to facilitate visual comparison with data from Site 1218 (black).

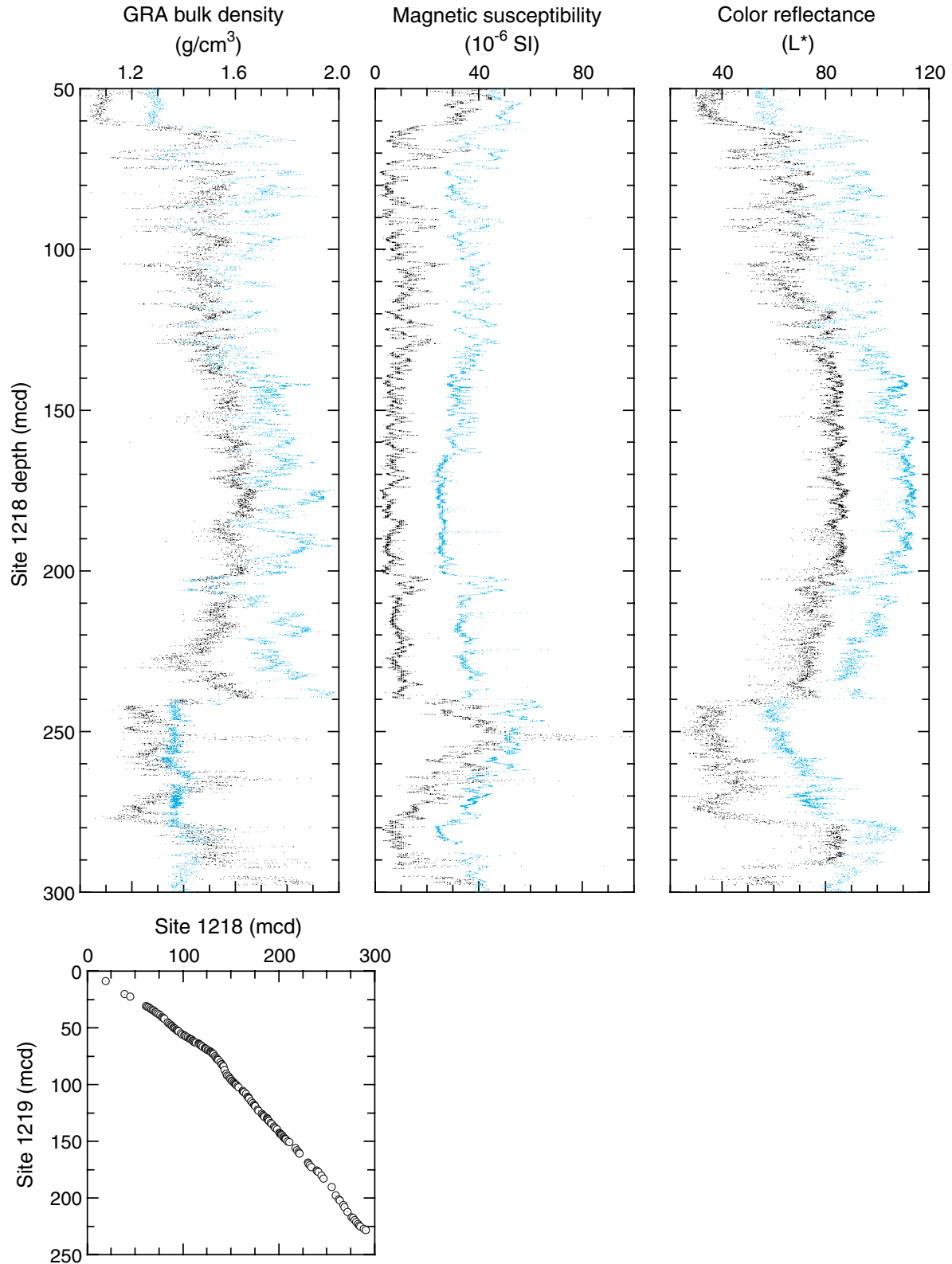


Figure F22. LSRs and chronostratigraphic markers for Site 1219.

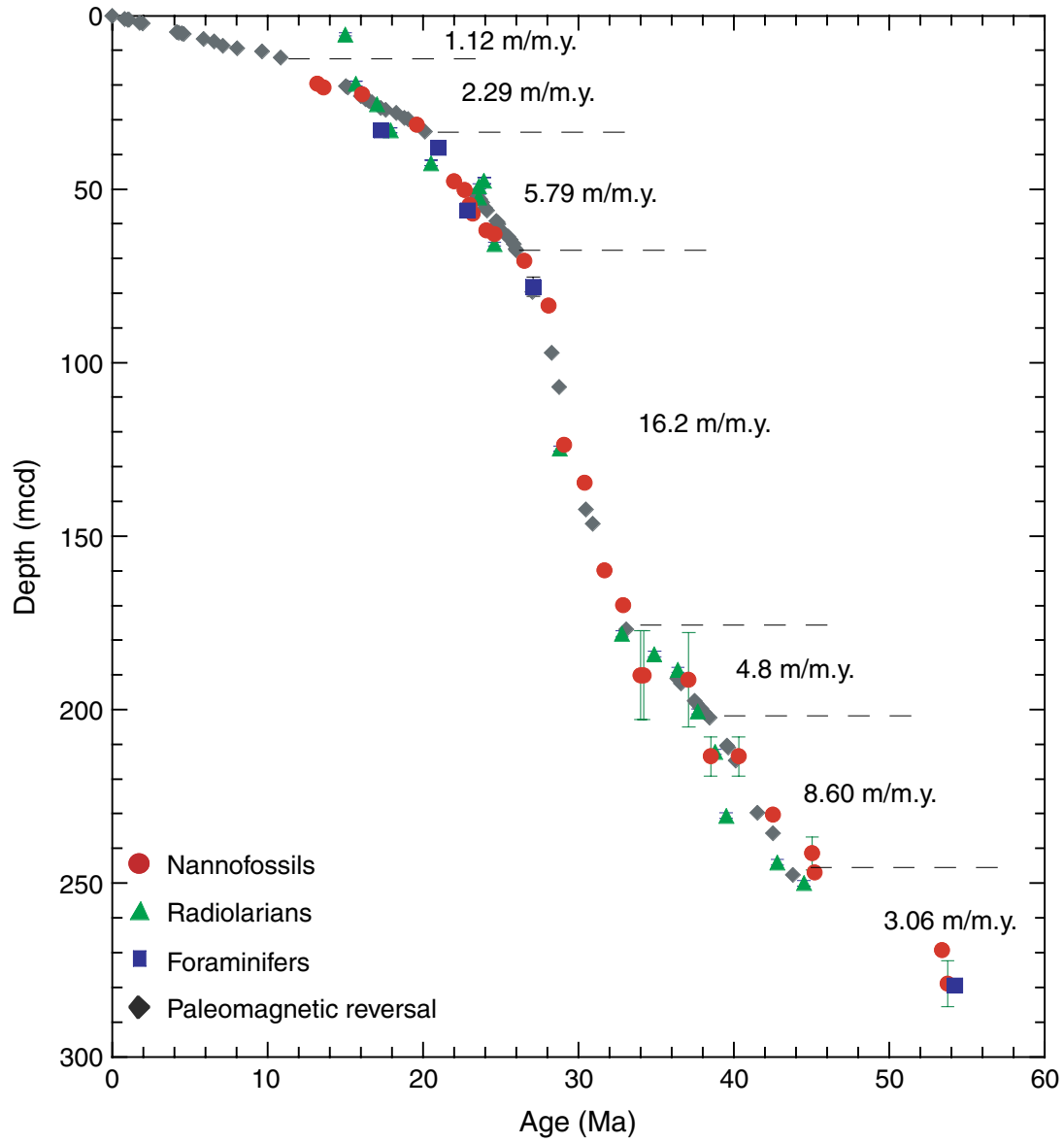


Figure F23. Density record of site survey piston Core EW9709-12P compared to density record of Site 1219.

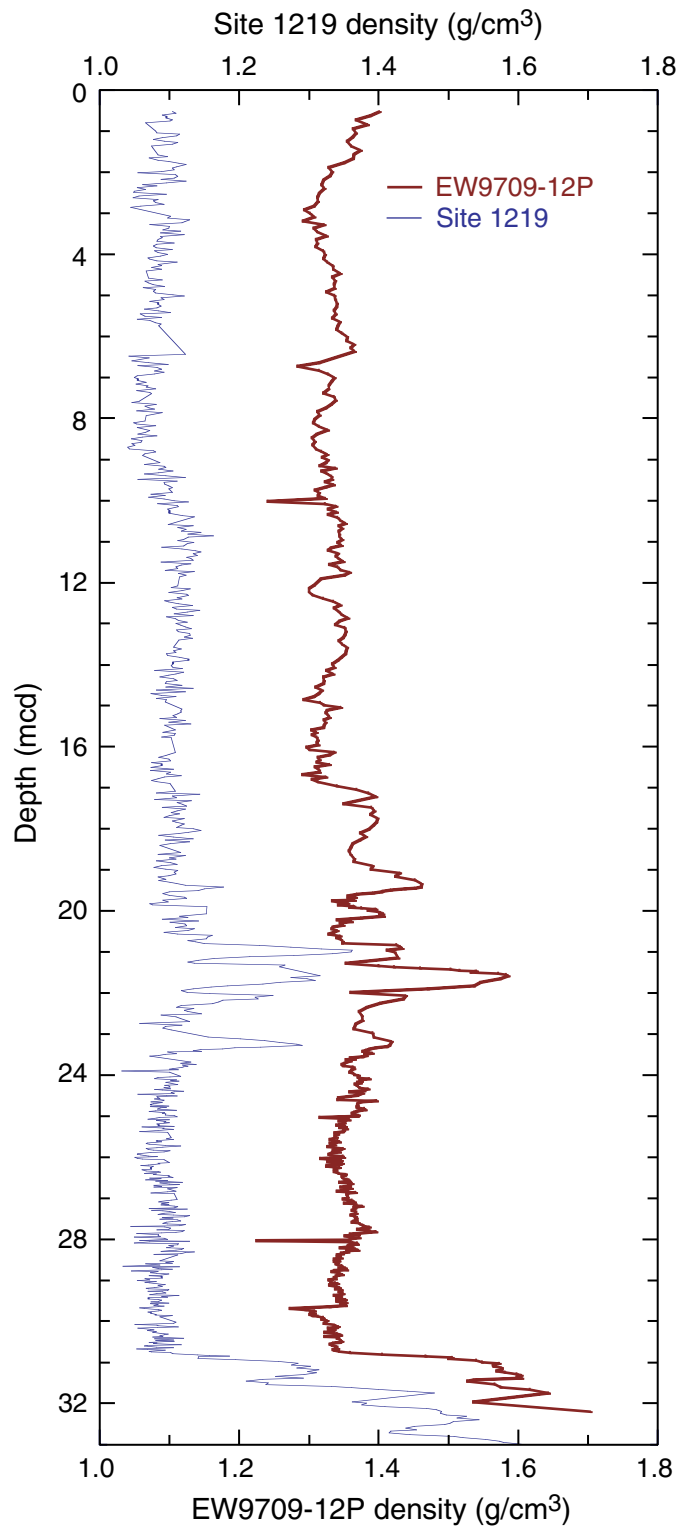


Figure F24. Bulk mass accumulation rates (MARs) for Site 1219.

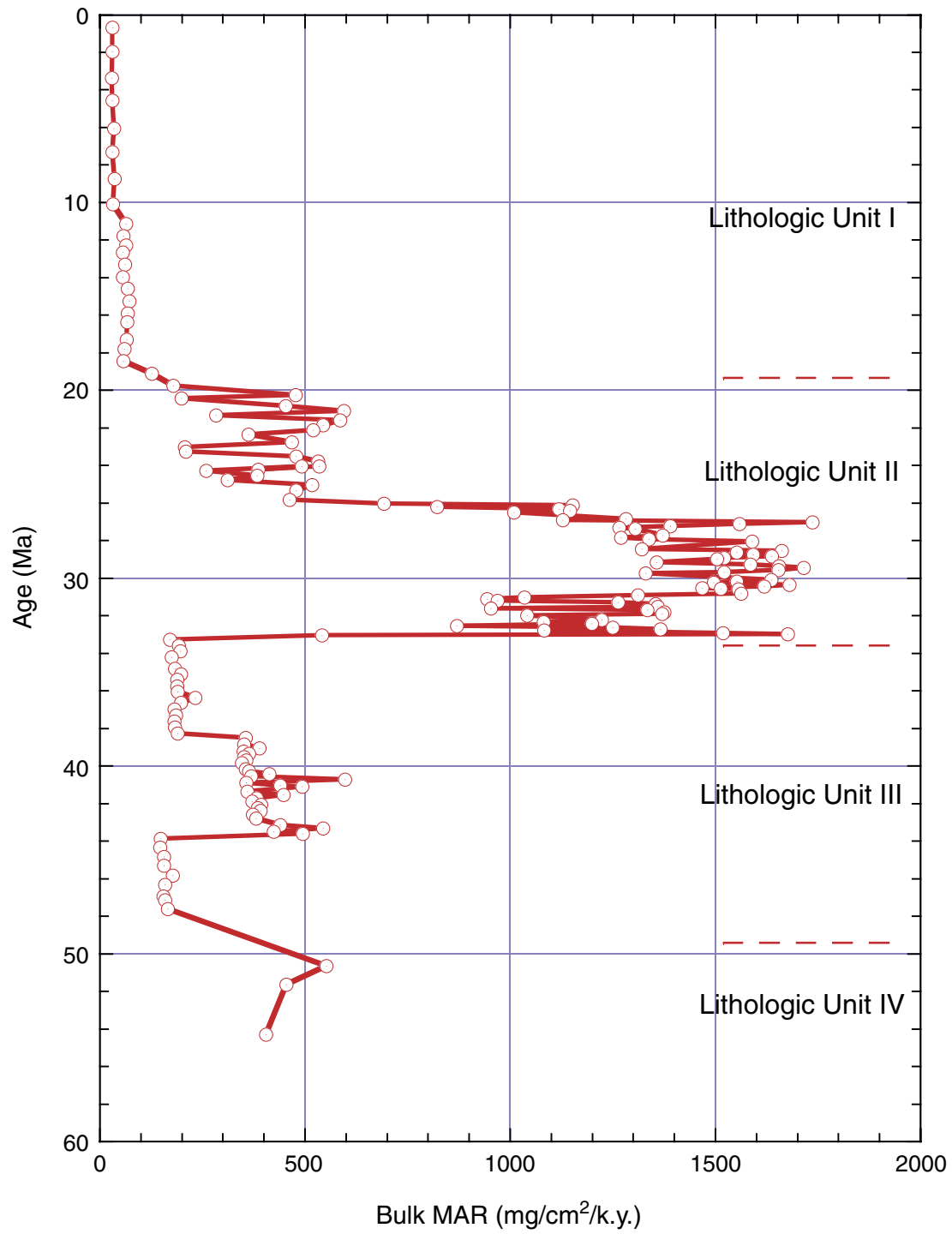


Figure F25. Interstitial water data from Site 1219. Solid circles = Ca, crosses = Mg.

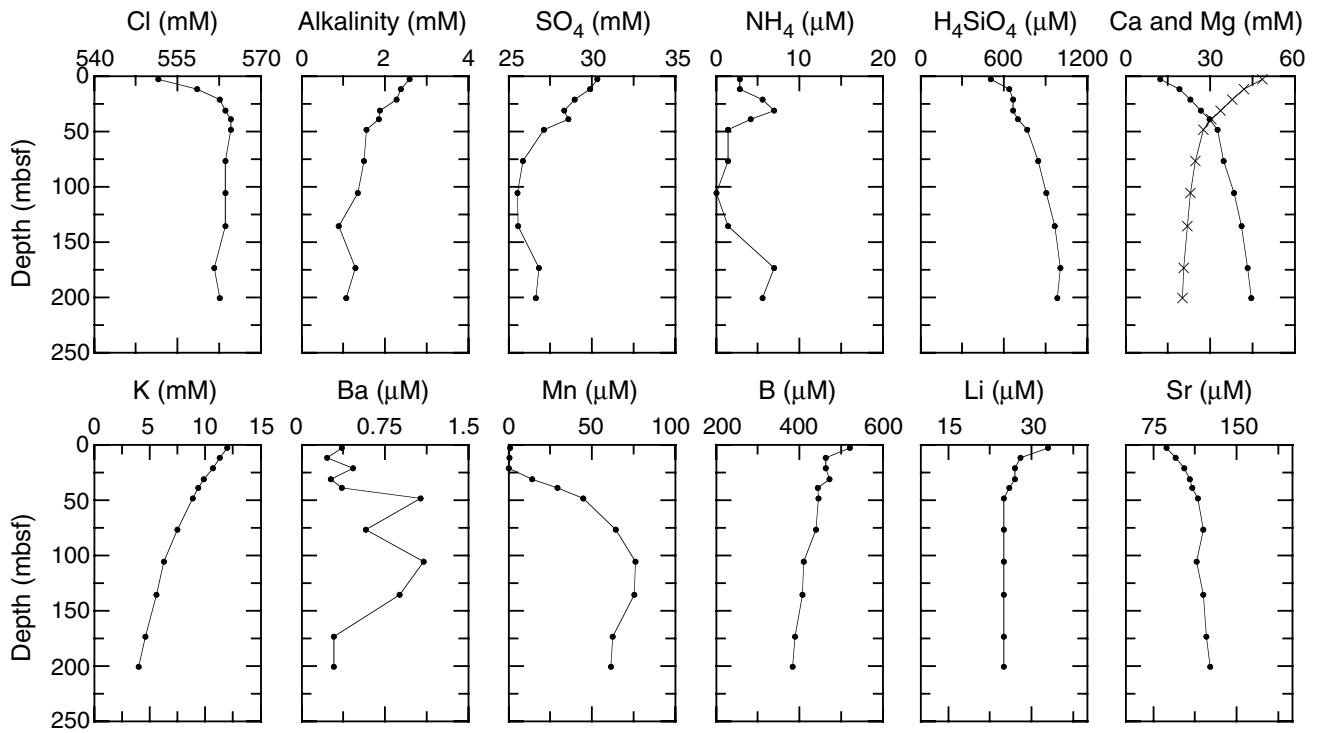


Figure F26. Bulk-sediment data from Site 1219. Ca values higher than 35.9 wt% are out of the range of the standards (see "Geochemistry," p. 20, in the "Explanatory Notes" chapter).

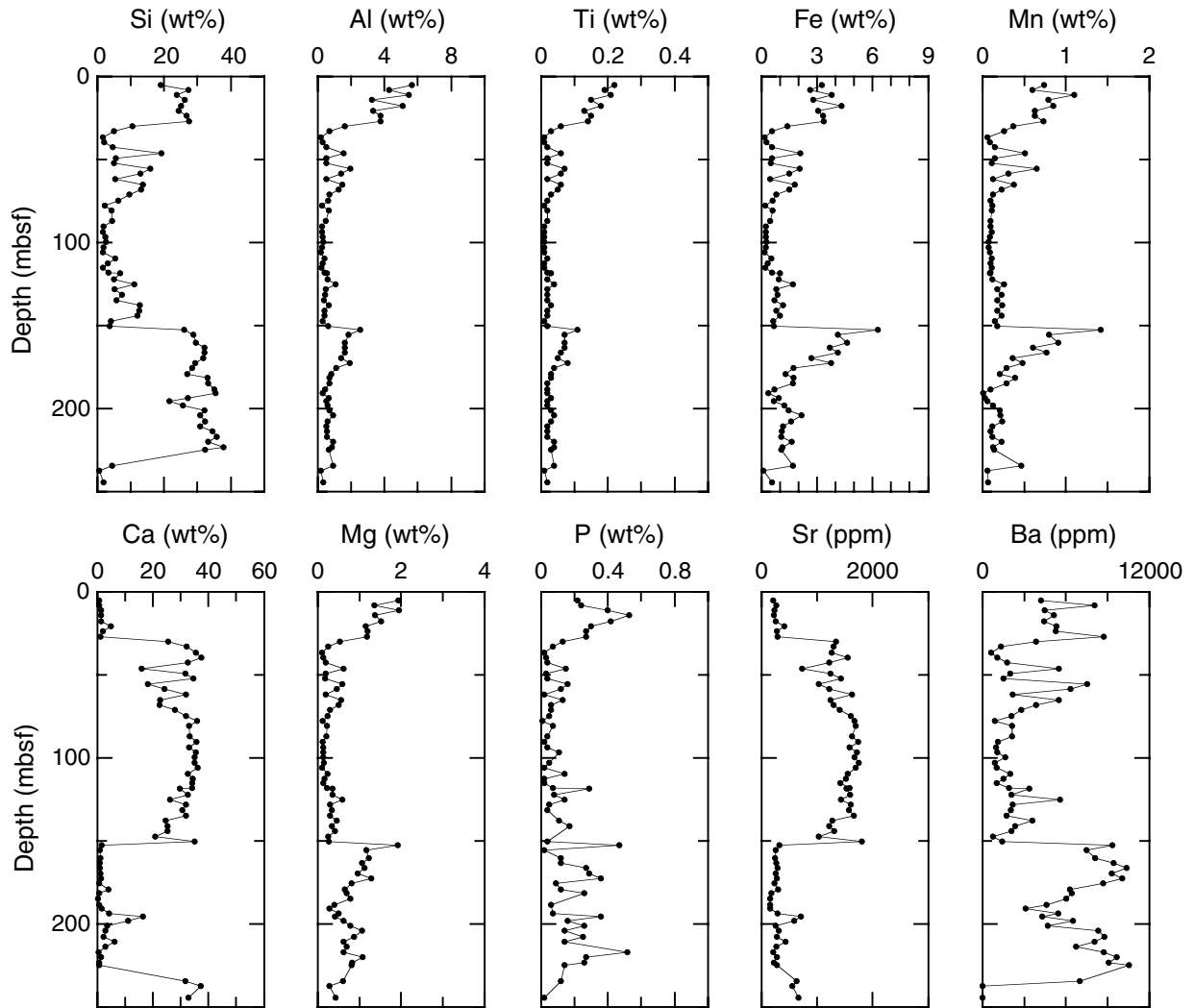


Figure F27. CaCO_3 and Ca data for Site 1219. CaCO_3 values higher than 90 wt% are calculated from Ca values out of the range of the standards (see "Geochemistry," p. 20, in the "Explanatory Notes" chapter).

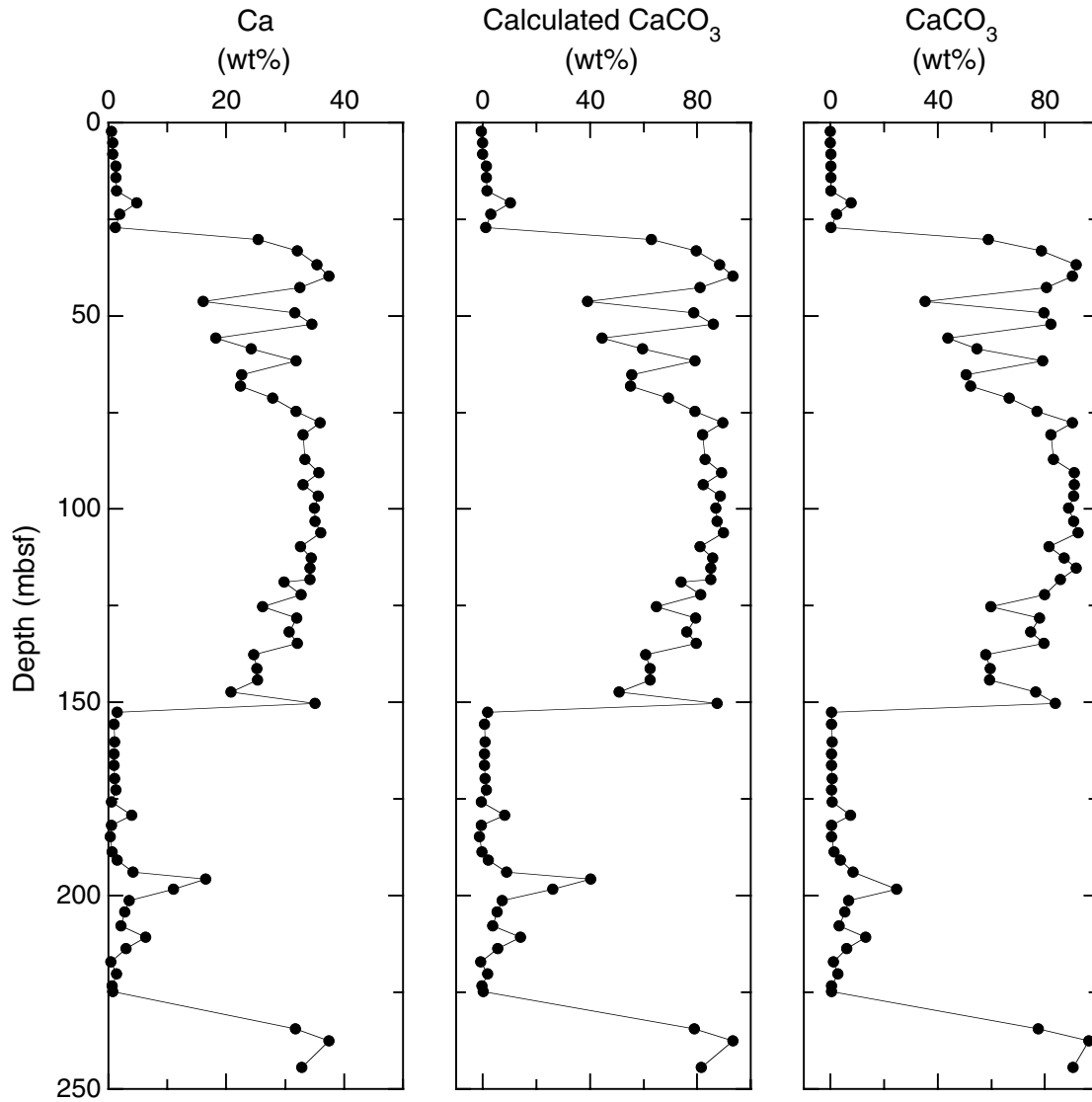


Figure F28. MAD measurements for Hole 1219A. A. Porosity (solid symbols) and water content (open symbols). B. Discrete-sample wet bulk density (open symbols) and gamma ray attenuation (GRA) bulk density (line). C. Grain density. Lithologic Units I–V are noted on the right side of the figure.

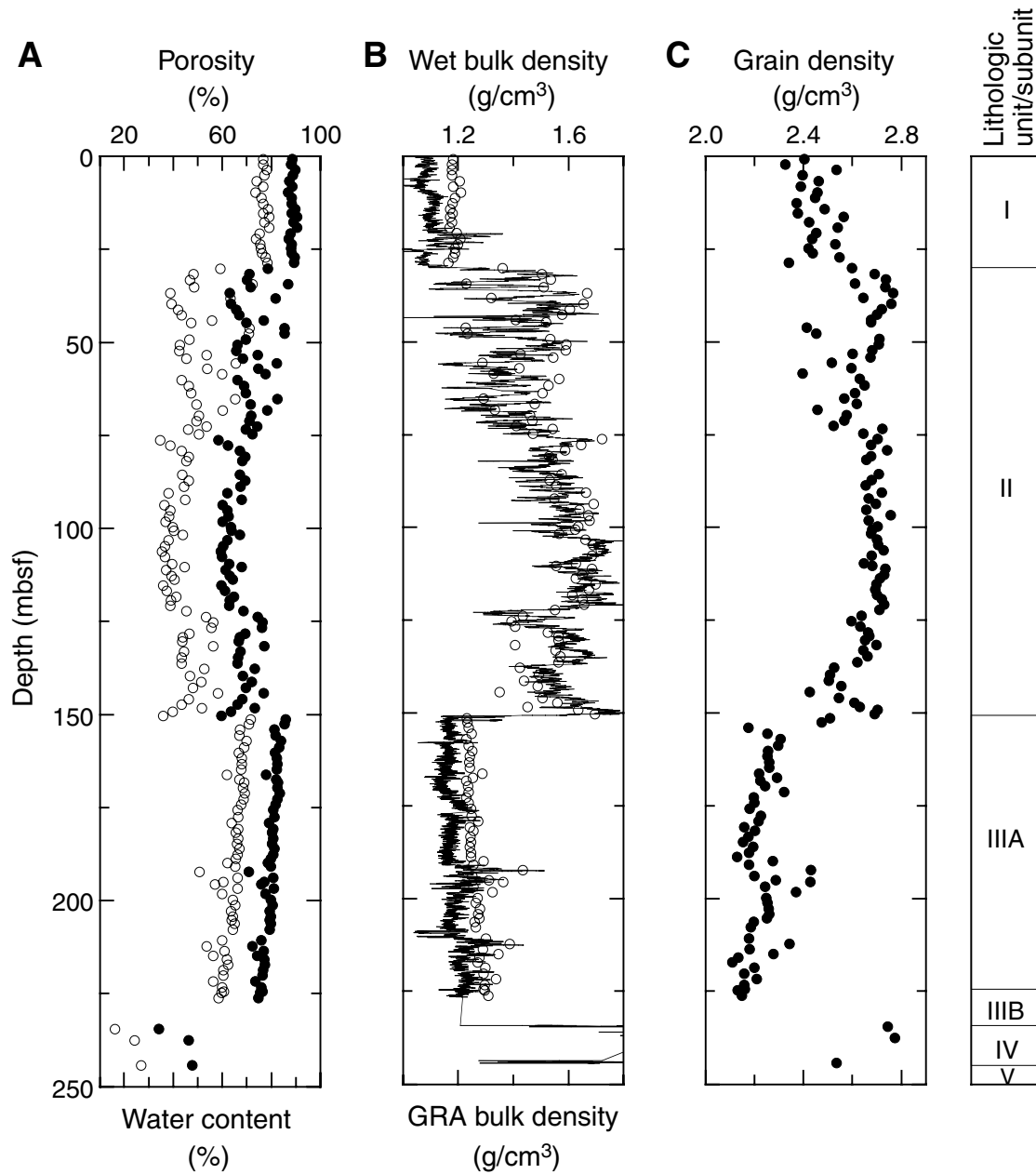


Figure F29. Comparison of MST gamma ray attenuation (GRA) bulk density, PWL velocity, and MS with light-dark cycles found in Sections 199-1219A-6H-2 through 6H-6.

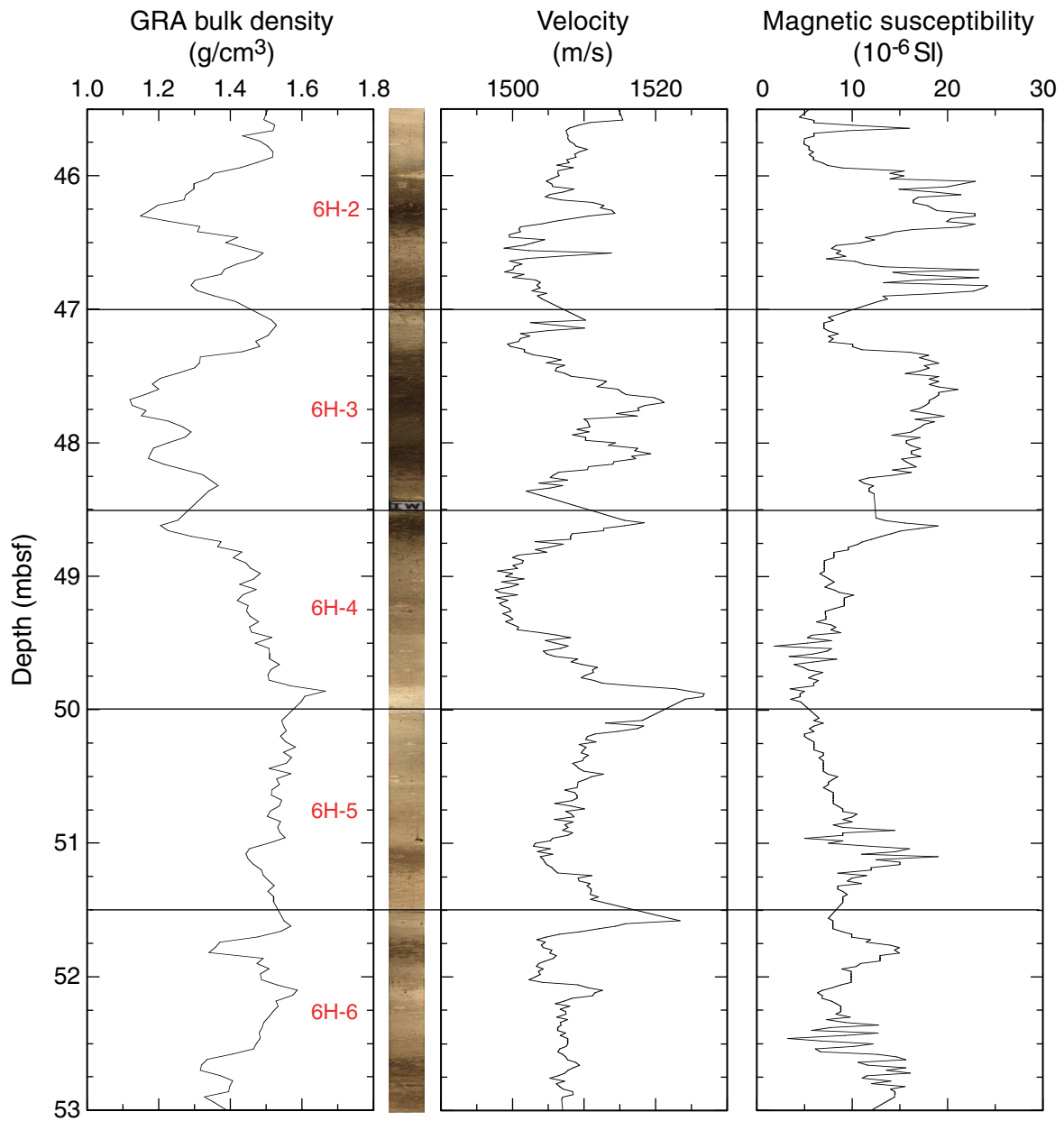


Figure F30. (A) Wet and (B) dry bulk density from discrete samples from Cores 199-1219A-1H through 24H plotted with gamma ray attenuation (GRA) bulk density interpolated with a 20-cm-wide Gaussian window.

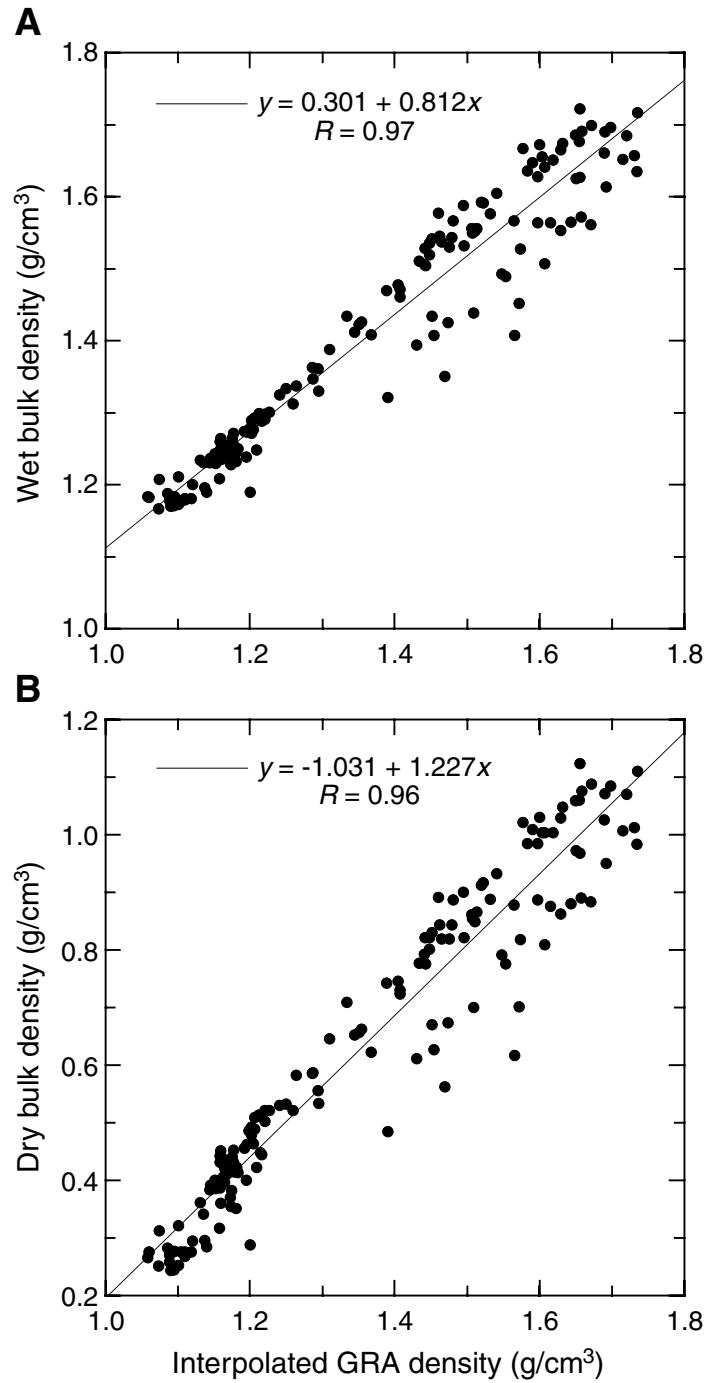


Figure F31. LAS mineralogy determinations for Hole 1219A. Lithologic Units I–V and ages are noted to the left of the figure.

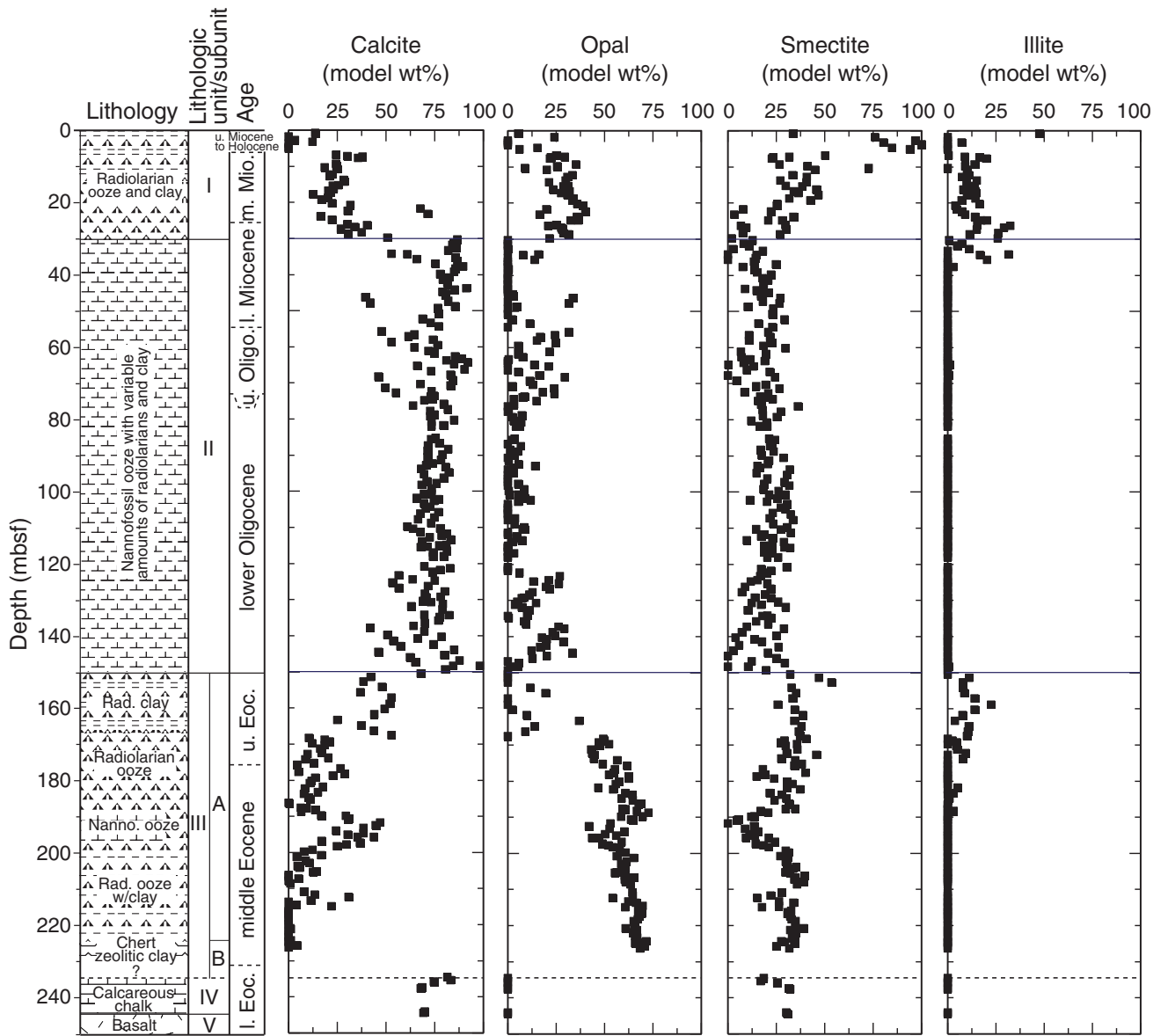


Figure F32. Compressional wave velocity from the PWL (line) and transverse velocity measurements of the insertion (diamonds) and contact probe (circles) systems for Hole 1219A. Velocity measurements from Cores 199-1219A-26X and 27X, which range from 1851 to 2051 m/s, are not shown. Lithologic Units I-IV are noted on the right side of the figure.

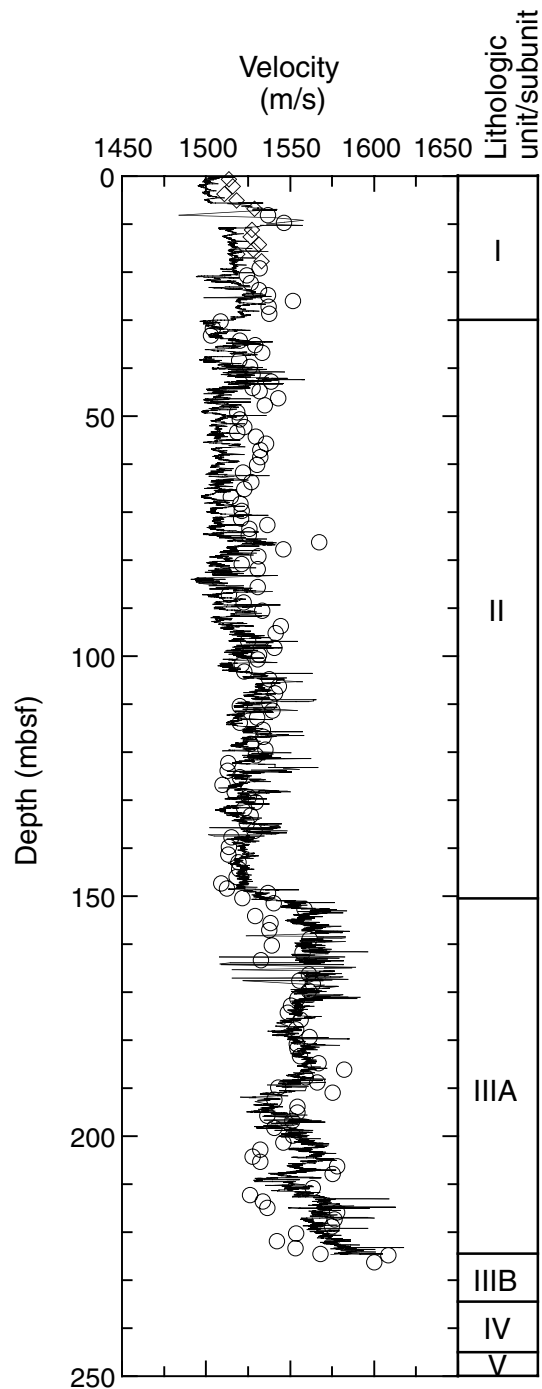


Figure F33. Compressional wave velocity (transverse) plotted with wet bulk density; Unit I radiolarian clay and ooze (open circles), Unit II nannofossil ooze (diamonds), and Unit III radiolarian clay and ooze (solid circles). Data from Unit IV nannofossil chalk are not shown.

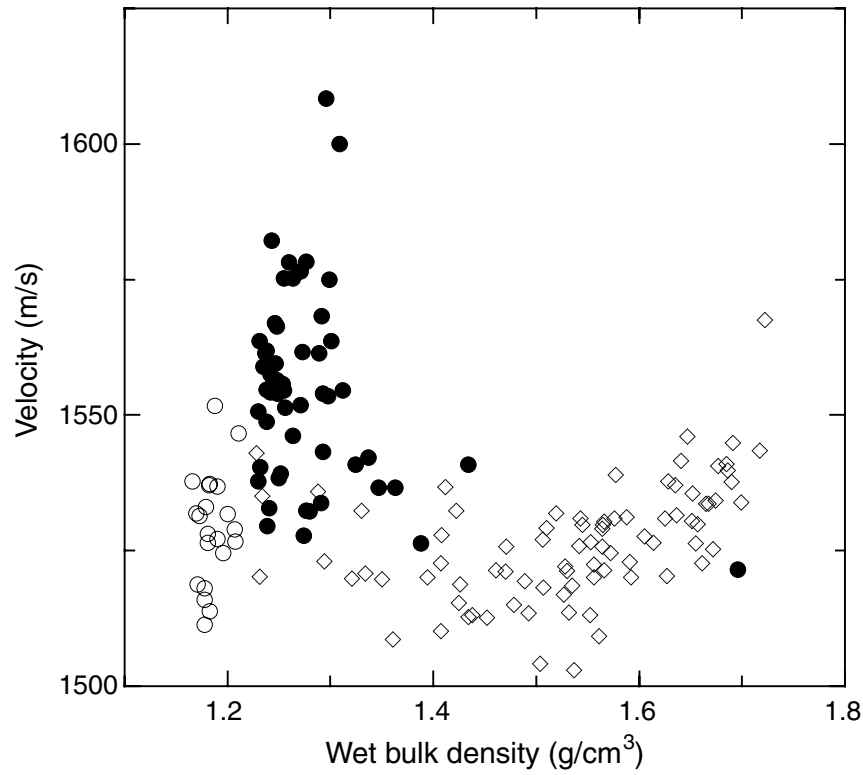


Figure F34. Thermal conductivity for Holes 1219A (solid symbols) and 1219B (open symbols). Lithologic Units I-V are noted on the right side of the figure.

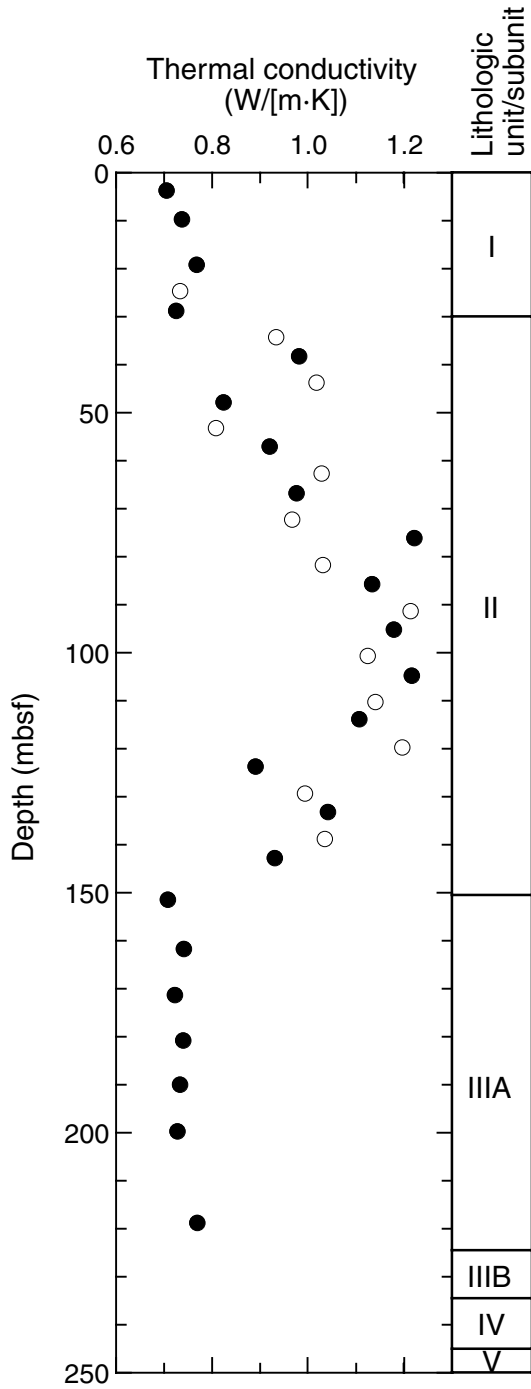


Figure F35. Thermal conductivity plotted with porosity for Holes 1219A (solid symbols) and 1219B (open symbols). An inverse relationship between thermal conductivity and porosity characterizes the nannofossil ooze (squares) but is weakly developed in the radiolarian ooze and clay (circles). Porosity values for Hole 1219B were derived from the GRA bulk density using the regression of porosity with GRA bulk density for APC-recovered sediments in Hole 1219A. Porosity = $132.8 - \text{GRA density} \times 42.9$. $R = 0.93$.

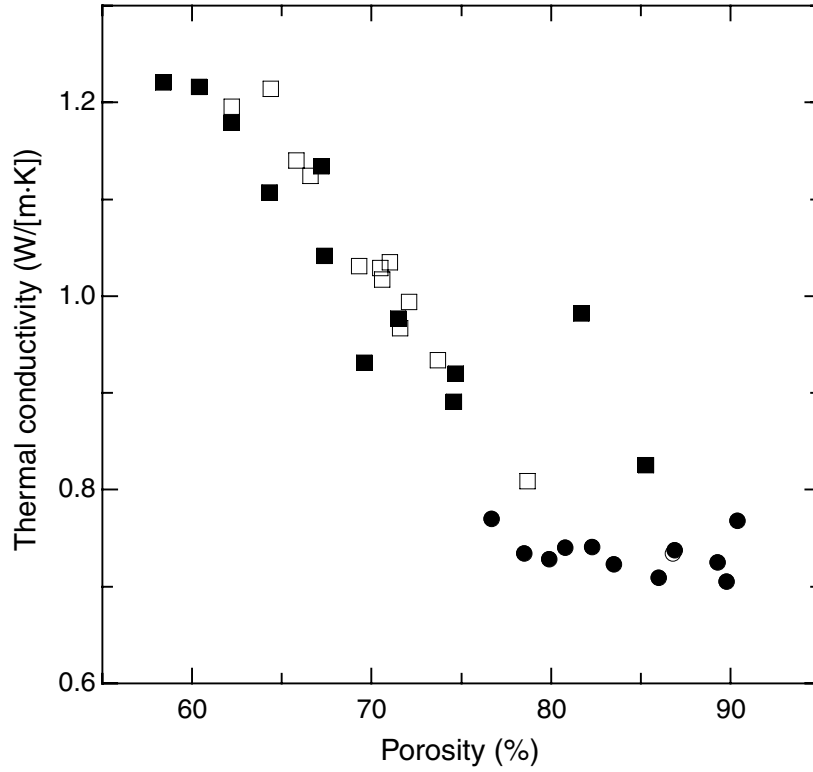


Figure F36. Heat flow calculation for Site 1219. A. Sediment temperatures in Hole 1219B. B. Thermal resistance based on a constant average in situ thermal conductivity of 0.71 W/(m·K) in lithologic Unit I (0–30 mbsf) and a linear increase in thermal conductivity in Unit II (30–125 mbsf). C. Bullard plot where heat flow is calculated from a linear regression of all temperature data.

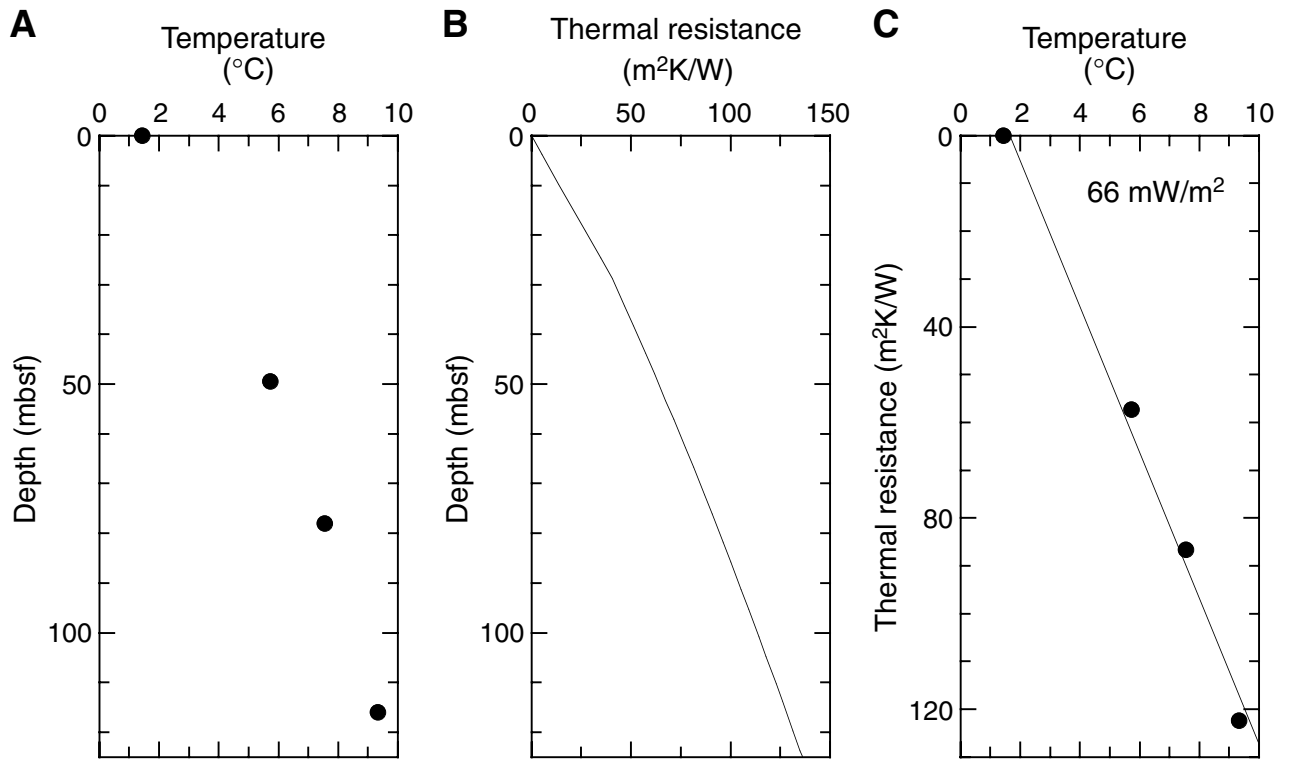


Figure F37. Natural gamma radiation for Hole 1219A. Most data below 30 mbsf are at or near background levels. Lithologic Units I-V are noted on the right side of the figure. cps = counts per second.

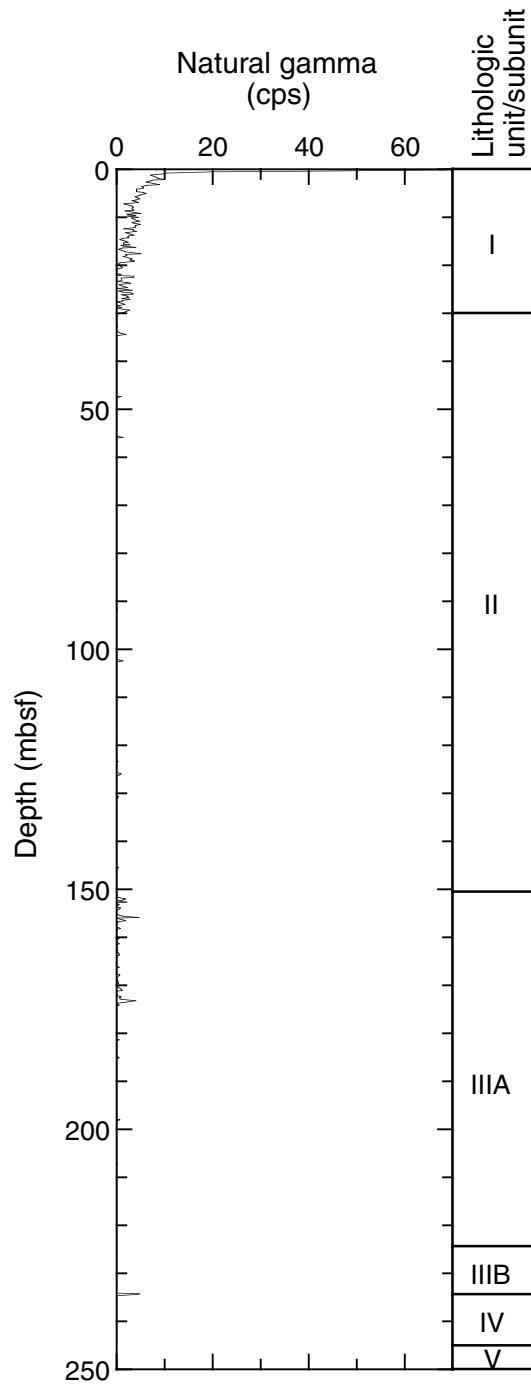


Figure F38. MS for Hole 1219A. Lithologic Units I-V are noted on the right side of the figure.

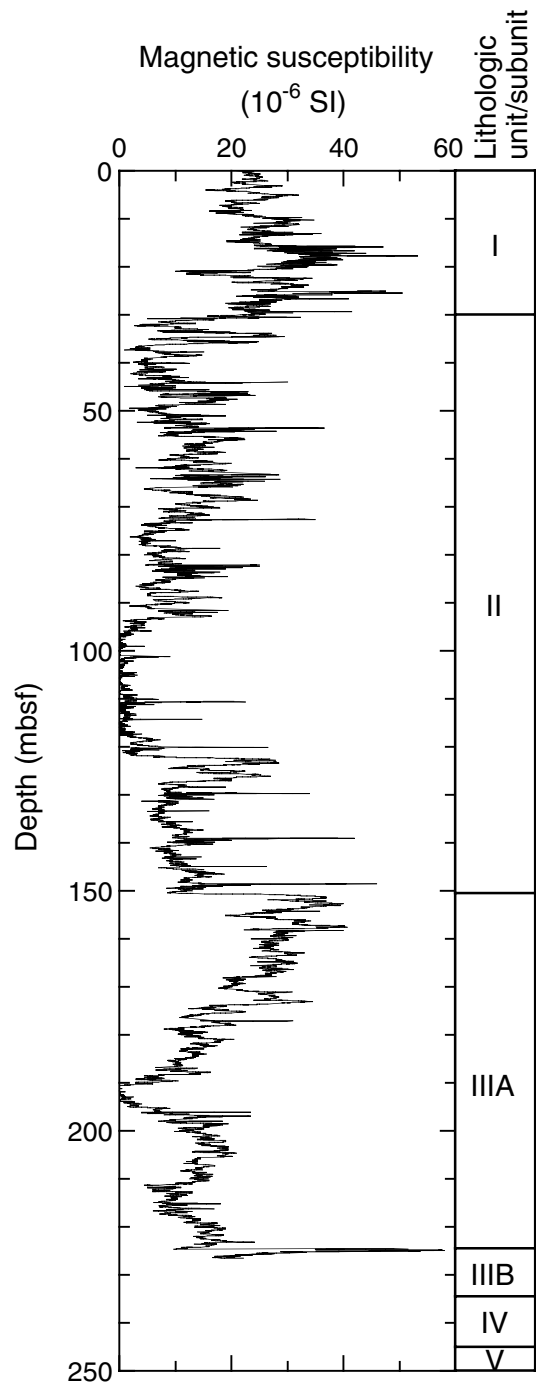


Figure F39. Summary of logging operations at Hole 1219A. MGT = multisensor gamma ray tool, FMS = Formation MicroScanner.

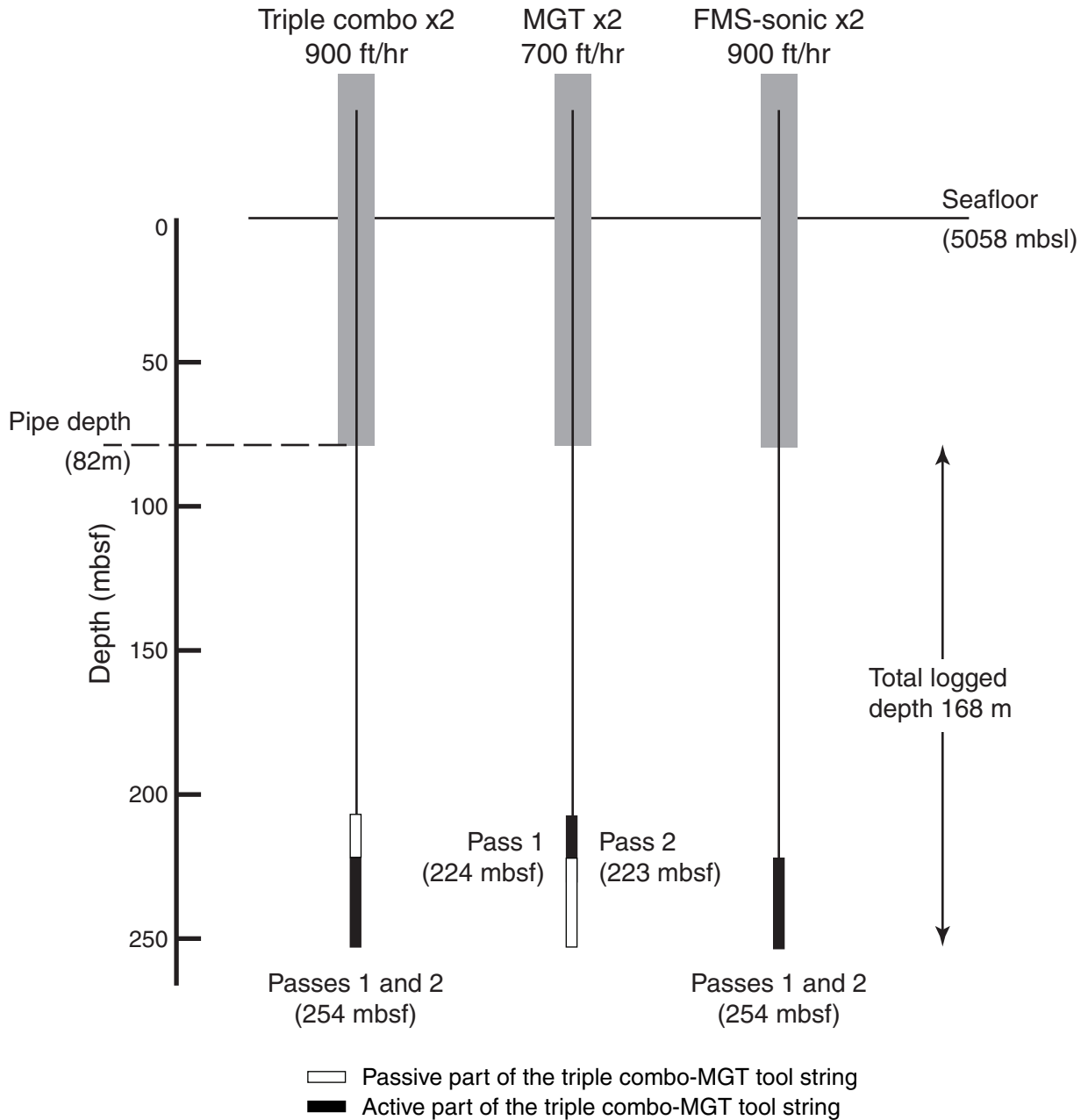


Figure F40. Caliper (C; quality control), tool acceleration (acc.; quality control) and gamma ray logs, Hole 1219A. Note the discrepancy between the triple combo and Formation MicroScanner (FMS) caliper data. T. combo = triple combo, MGT = multisensor gamma ray tool.

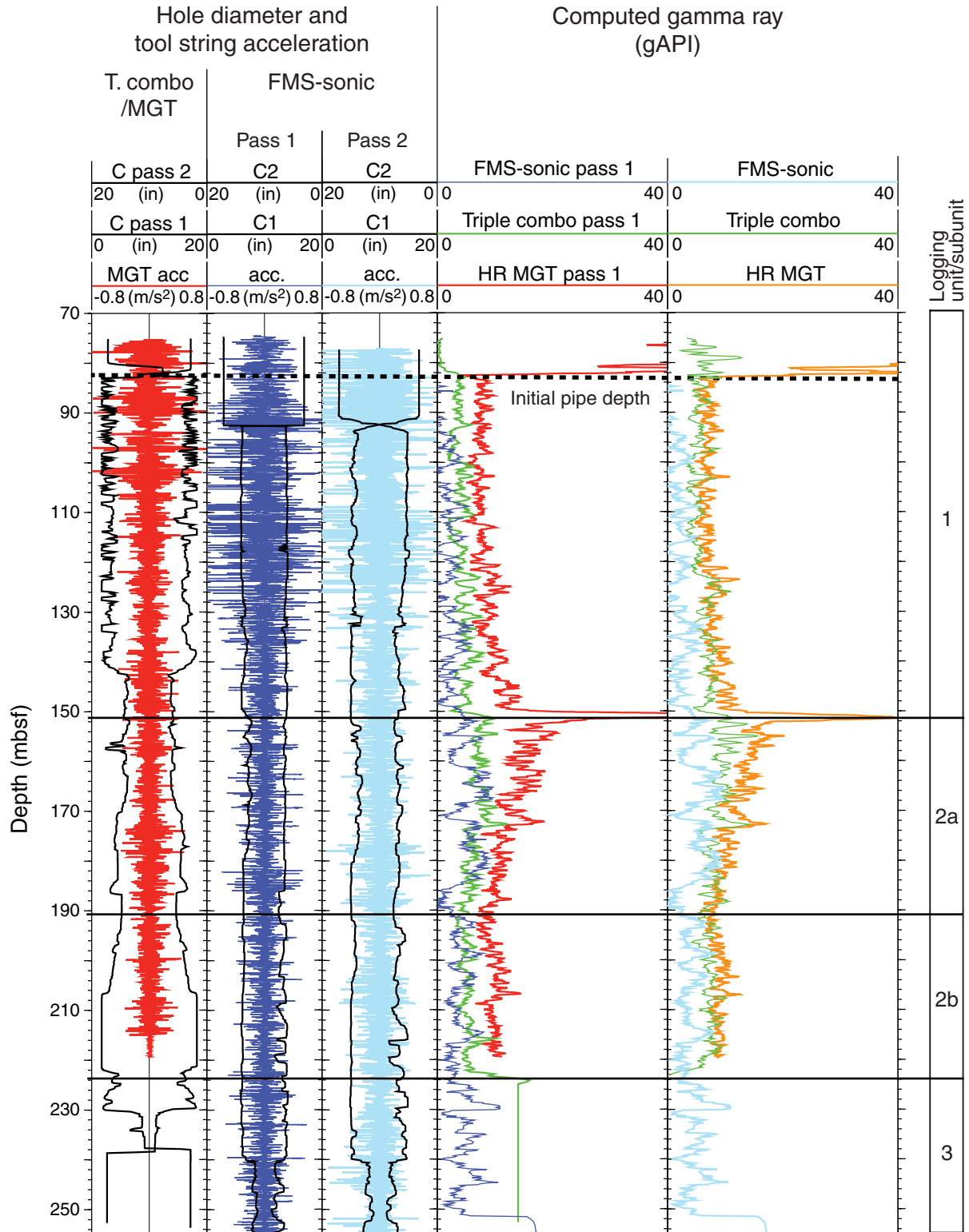


Figure F41. An example of the problem encountered by the *P*-wave labeling algorithm in “slow” sediments, where the formation velocity approaches that of the drilling mud, taken from the coherency plot of FMS–sonic pass 1. The dashed lines represent the results of the *P*-wave labeling algorithm.

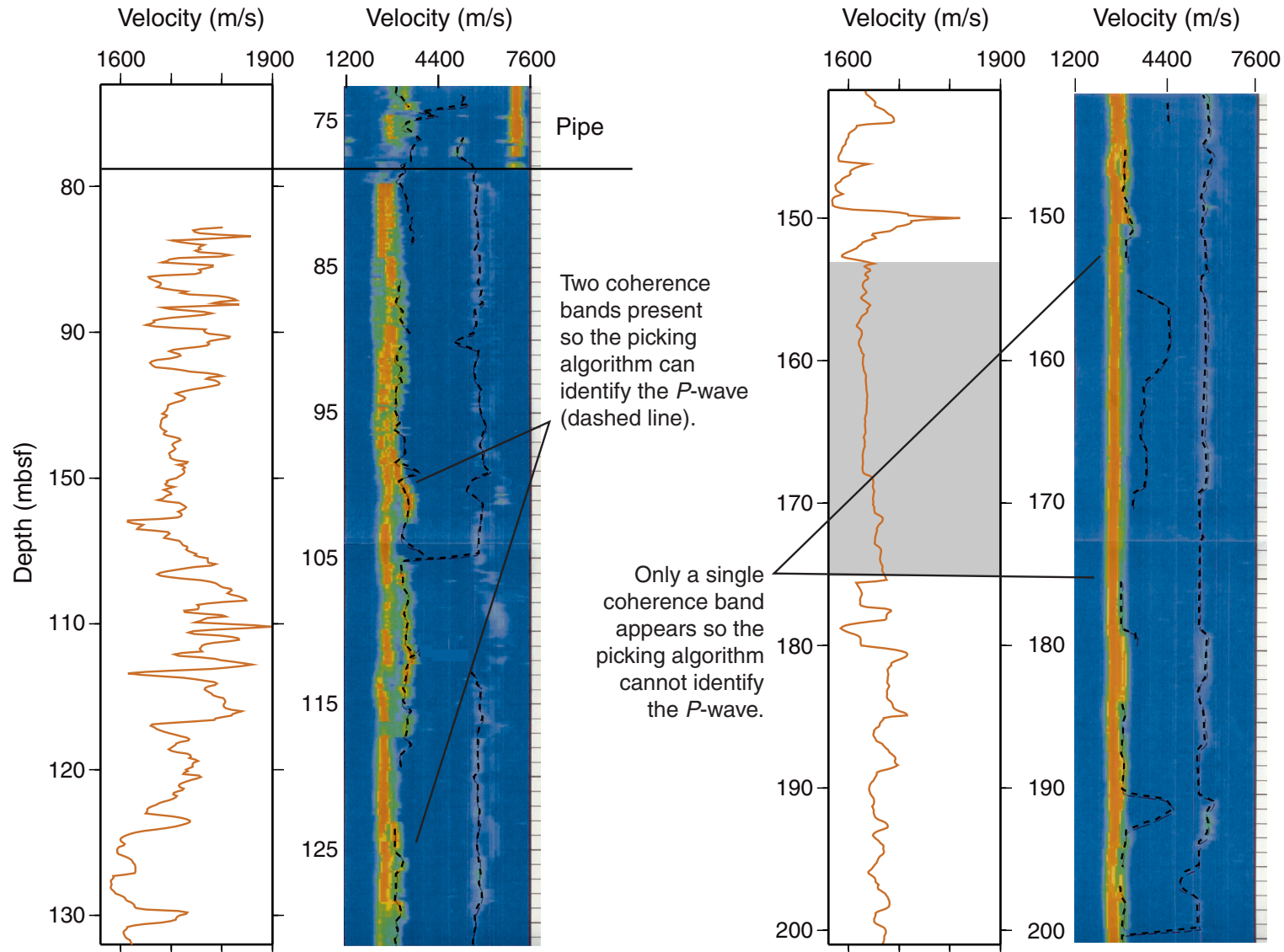


Figure F42. Core recovery and geophysical logs compared with equivalent core physical properties measurements. A Formation MicroScanner (FMS) microresistivity curve is included for comparison with the triple combo resistivity logs. gAPI = American Petroleum Institute gamma ray units.

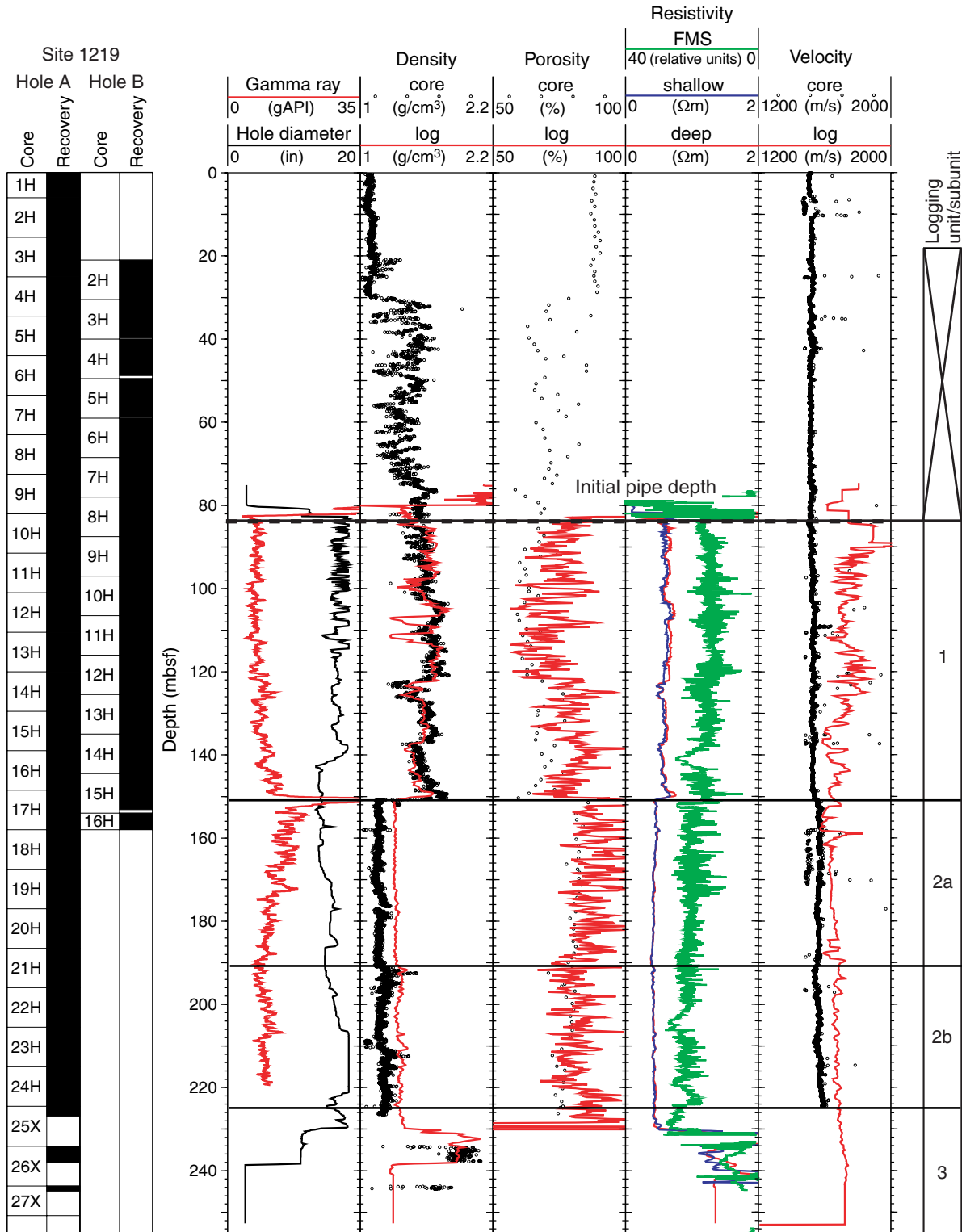


Figure F43. A. Blackman-Tukey spectrum with data quality expressed as tool acceleration, wavelet transform (WT) analysis, and hole diameter caliper logs from multisensor gamma ray tool (MGT) pass 2. (Continued on next page.)

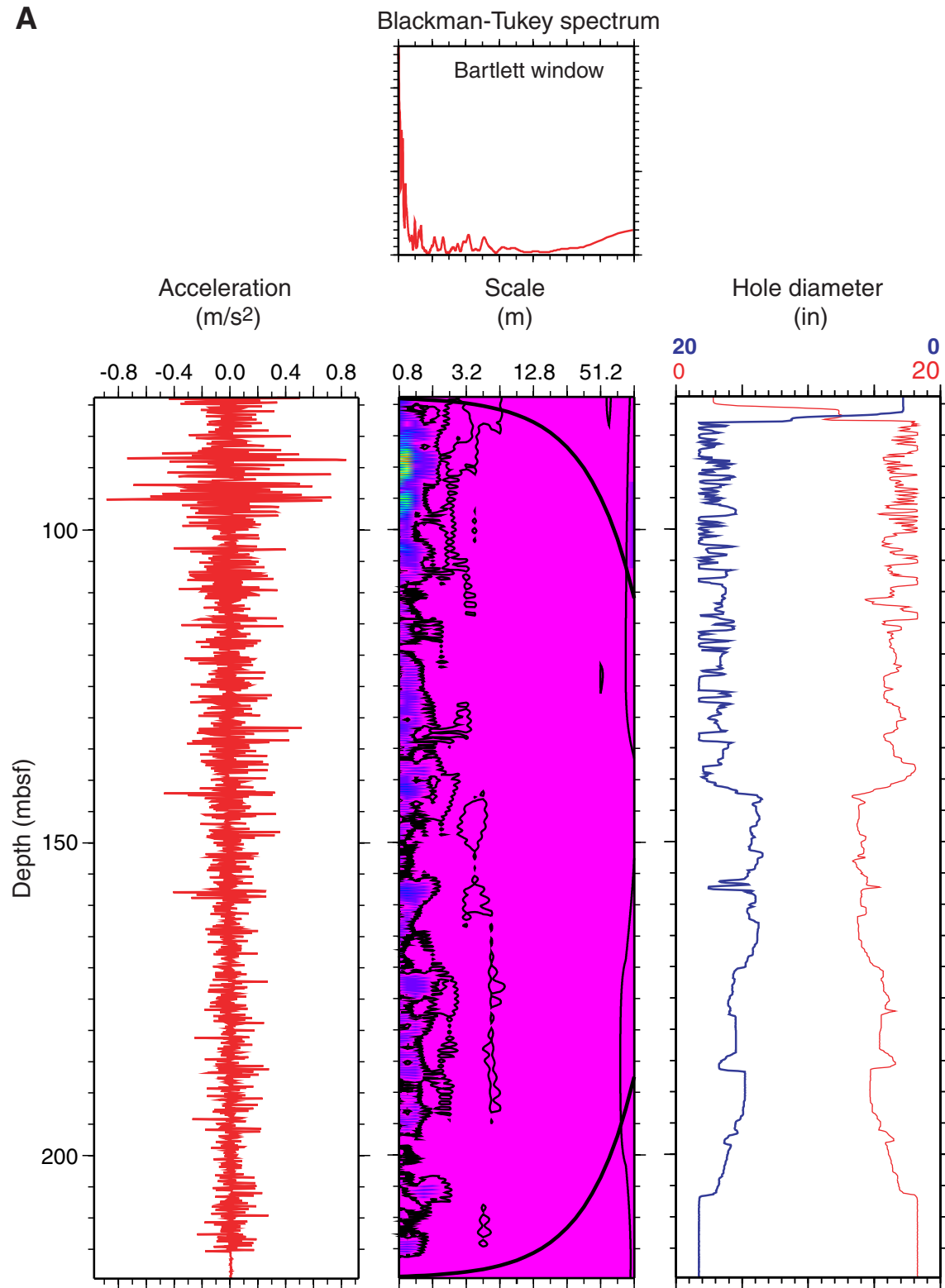


Figure F43 (continued). B. Blackman-Tukey spectrum with data quality expressed as tool acceleration, WT analysis, and hole diameter caliper logs from Formation MicroScanner (FMS)-sonic tool pass 2.

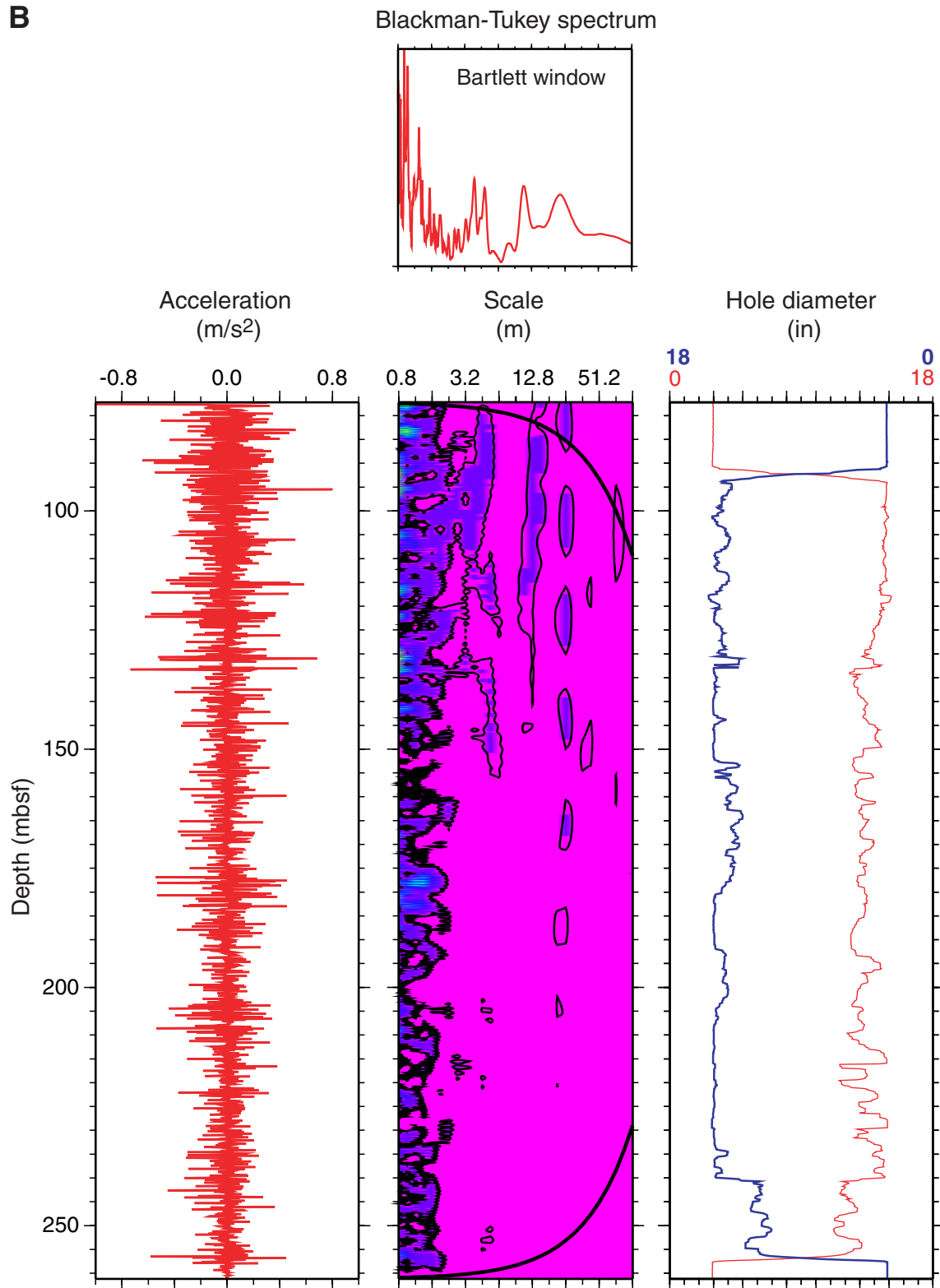


Figure F44. Wavelet transform (WT) analyses of the (A) density log in relation to (C) possible borehole wall rugosity effects from triple combo pass 1. Respective wavelet spectrum diagrams are shown for (B) density and (D) borehole diameter. The cross-wavelet spectrum is presented in the (E) modulus and (F) phase diagrams. Note the high significance region in the density wavelet spectrum at ~100 mbsf (B), which is produced by the density spike at the same depth (A).

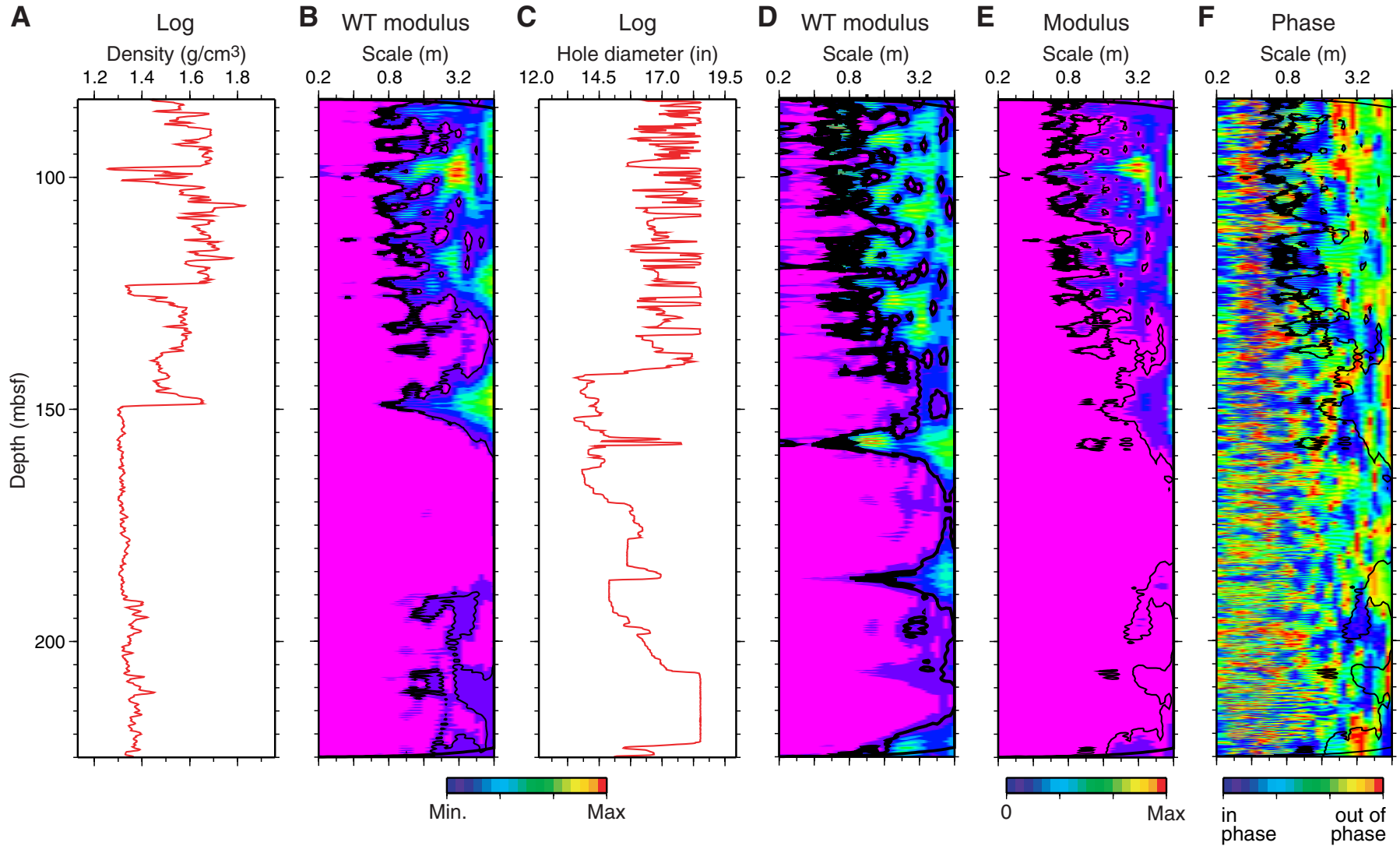


Figure F45. Core recovery, hole diameter log, hostile environment NGR sonde logs, and HLDT photoelectric effect (PEF) log. gAPI = American Petroleum Institute gamma ray units.

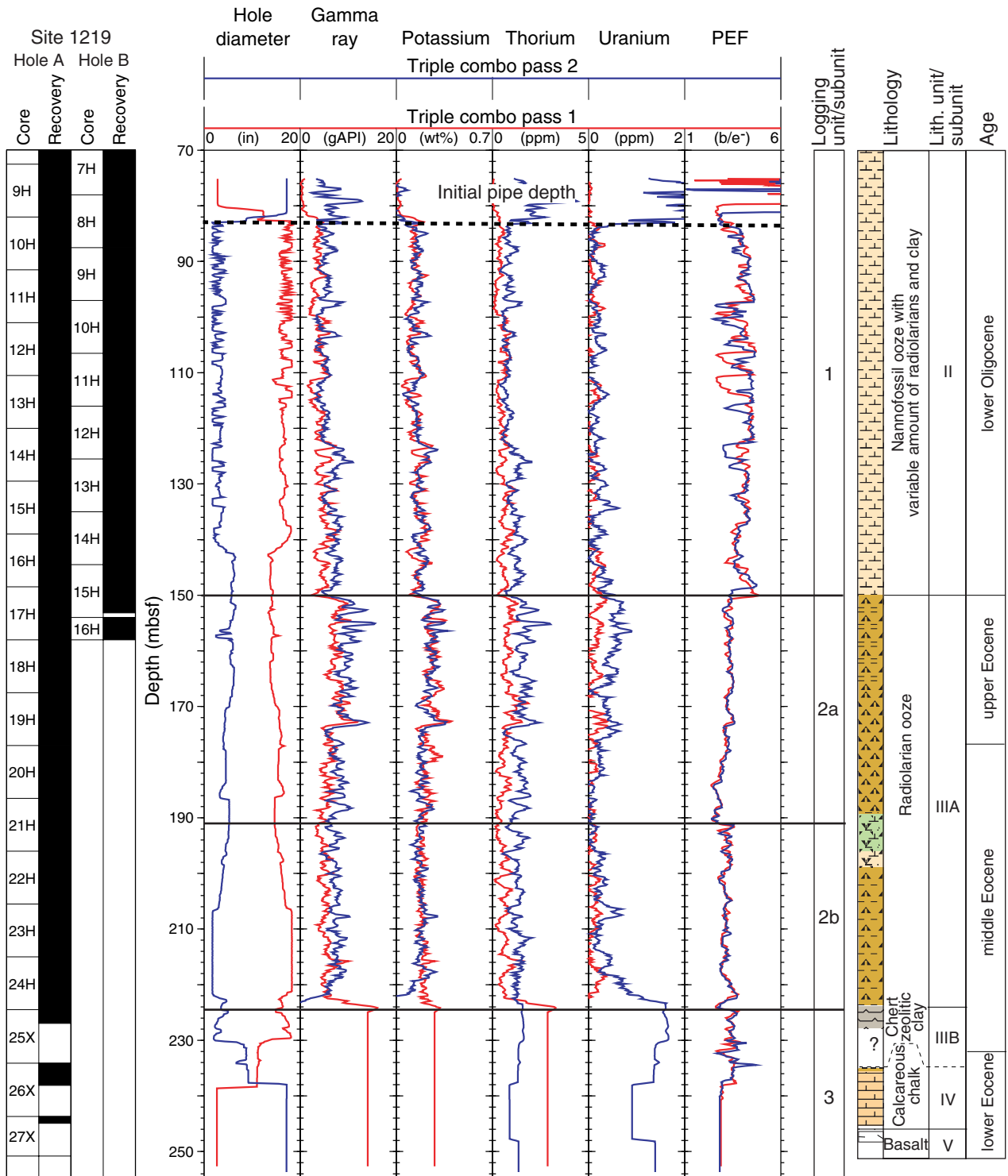


Figure F46. Formation MicroScanner (FMS) images of chert bands in logging Unit 3.

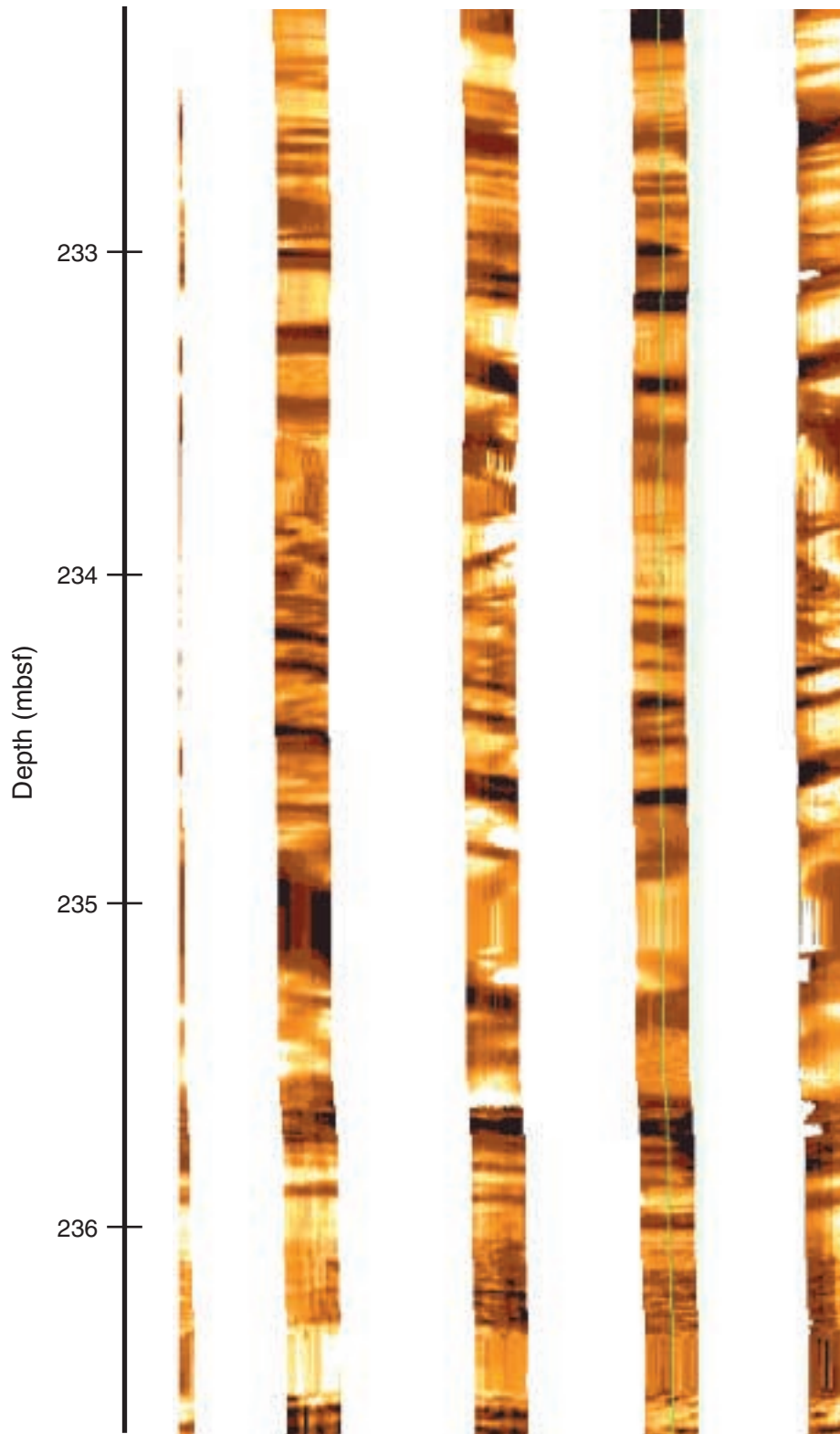


Figure F47. Wavelet transform (WT) analyses of (A) porosity and (C) density logs from pass 1 of the triple combo. The wavelet spectrum diagrams for (B) porosity and (D) density show a dominant depth-scale frequency at ~15 m, with a less significant higher frequency at ~4 m. The same pattern is shown in the (E) cross-wavelet modulus, and the two data sets are (F) out of phase as expected. NB Pass 1 shows the same pattern. NB = nota bene, or note.

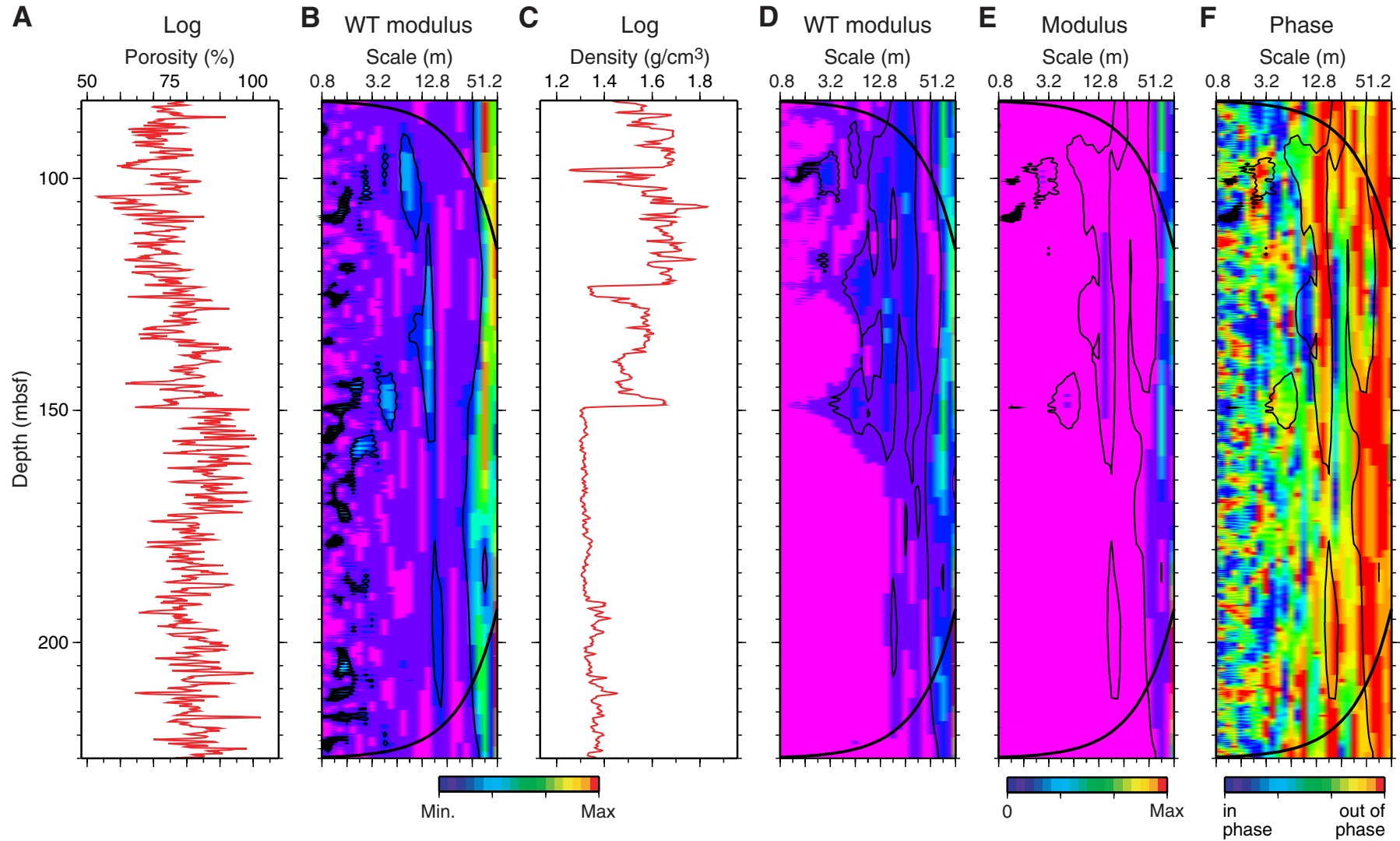


Figure F48. A. Synthetic seismogram derived from velocity (split core) and density (spliced log and corrected GRA core) data for Hole 1219A. Note the depth vs. time difference between the bottom of the hole and the first strong (chert?) reflector below. Depth vs. time relationship, density, velocity, and reflection coefficient curves are also shown. (Continued on next page.)

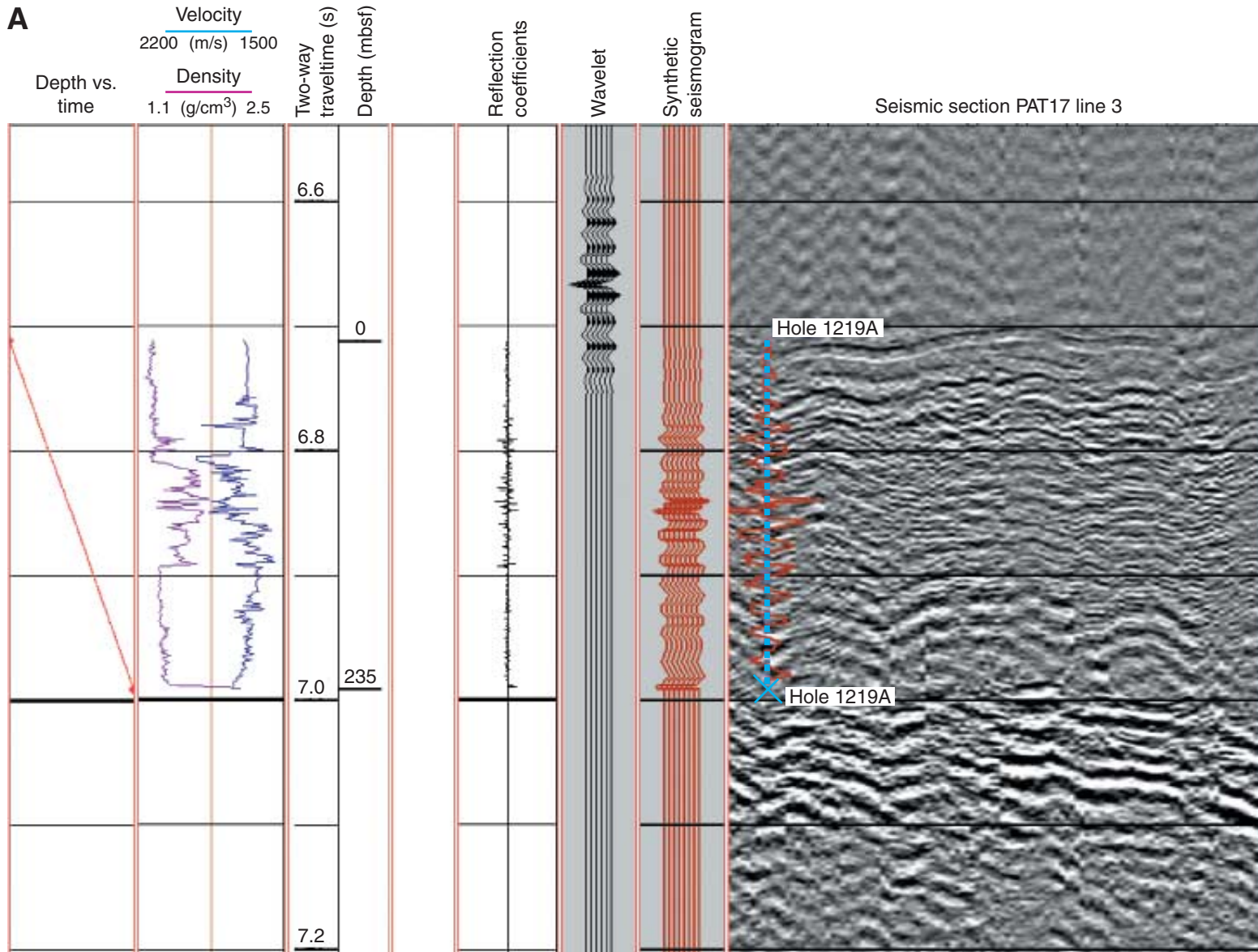


Figure F48 (continued). B. Synthetic seismogram derived from velocity (whole core) and density (spliced log and corrected GRA core) data for Hole 1219A. Note the location of the bottom of the hole on top of the first strong (chert?) reflector. Depth vs. time relationship, density, velocity, and reflection coefficient curves are also shown.

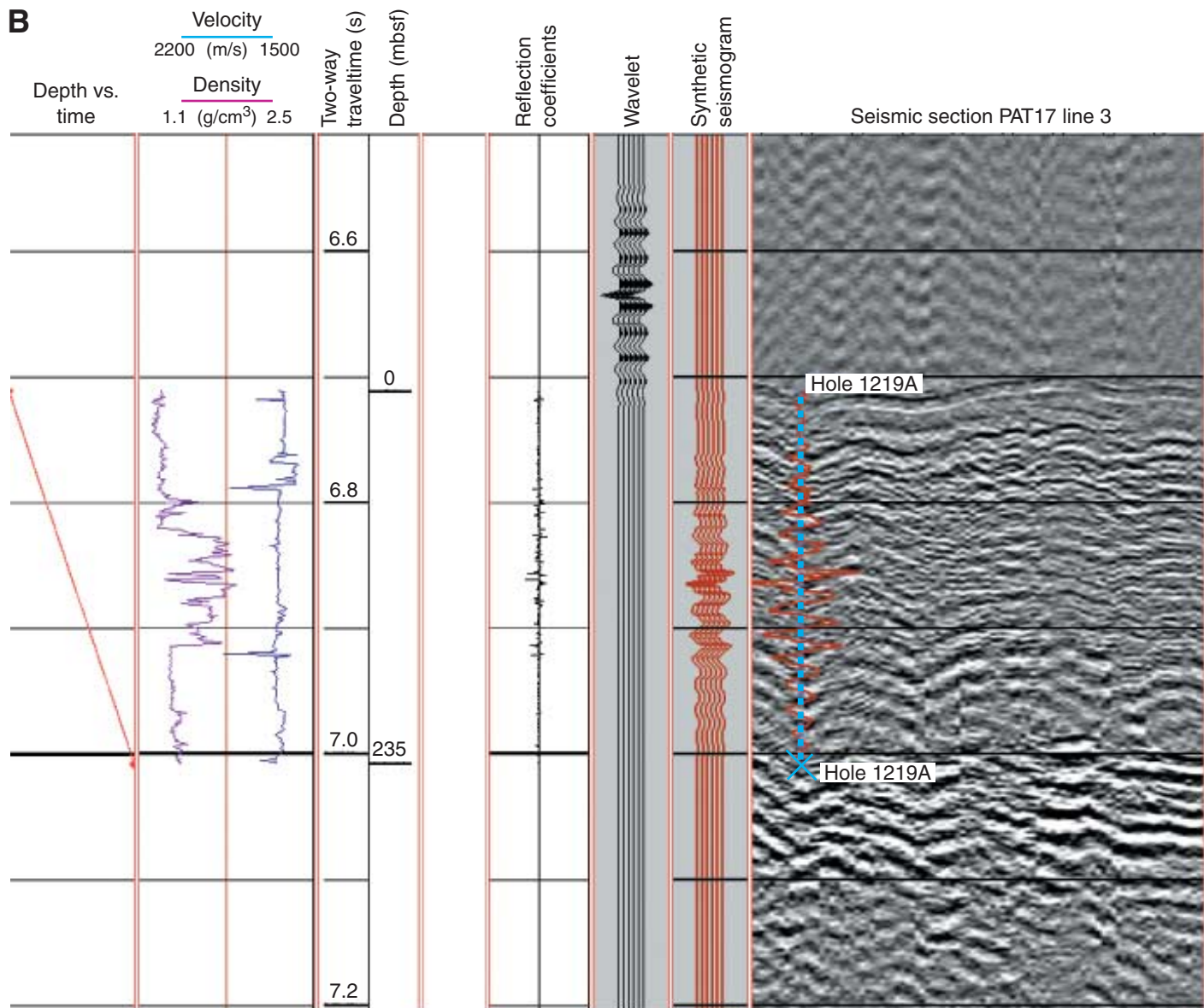


Table T1. Coring summary, Site 1219. (See table note. Continued on next page.)

Hole 1219A

Latitude: 7°48.0097'N
 Longitude: 142°0.9390'W
 Time on site (hr): 122.75 (0200 hr, 23 Nov–0445 hr, 28 Nov 2001)
 Time on hole (hr): 82.42 (0200 hr, 23 Nov–1225 hr, 26 Nov 2001)
 Seafloor (drill pipe measurement from rig floor, mbrf): 5074.5
 Distance between rig floor and sea level (m): 11.2
 Water depth (drill pipe measurement from sea level, m): 5063.3
 Total depth (drill pipe measurement from rig floor, mbrf): 5325.3
 Total penetration (meters below seafloor, mbsf): 250.8
 Total length of cored section (m): 250.8
 Total core recovered (m): 240.41
 Core recovery (%): 95.7
 Total number of cores: 27
 Total number of drilled intervals: 0

Hole 1219B

Latitude: 7°48.0186'N
 Longitude: 142°0.9397'W
 Time on hole (hr): 40.33 (1225 hr, 26 Nov–0445 hr, 28 Nov 2001)
 Seafloor (drill pipe measurement from rig floor, mbrf): 5074.5
 Distance between rig floor and sea level (m): 11.2
 Water depth (drill pipe measurement from sea level, m): 5063.3
 Total depth (drill pipe measurement from rig floor, mbrf): 5232.5
 Total penetration (meters below seafloor, mbsf): 158.0
 Total length of cored section (m): 137.0
 Total length of drilled intervals (m): 21.0
 Total core recovered (m): 138.55
 Core recovery (%): 101.1
 Total number of cores: 15
 Total number of drilled intervals: 1

Core	Date (Nov 2001)	Local time (hr)	Depth (mbsf)		Length (m)		Recovery (%)
			Top	Bottom	Cored	Recovered	
119-1219A-							
1H	23	1230	0.0	6.0	6.0	5.95	99.2
2H	23	1345	6.0	15.5	9.5	10.04	105.7
3H	23	1455	15.5	25.0	9.5	9.85	103.7
4H	23	1620	25.0	34.5	9.5	9.87	103.9
5H	23	1740	34.5	44.0	9.5	9.97	105.0
6H	23	1925	44.0	53.5	9.5	9.95	104.7
7H	23	2035	53.5	63.0	9.5	9.49	99.9
8H	23	2140	63.0	72.5	9.5	10.09	106.2
9H	23	2245	72.5	82.0	9.5	9.89	104.1
10H	24	0010	82.0	91.5	9.5	9.62	101.3
11H	24	0110	91.5	101.0	9.5	9.69	102.0
12H	24	0220	101.0	110.5	9.5	10.14	106.7
13H	24	0320	110.5	120.0	9.5	9.63	101.4
14H	24	0430	120.0	129.5	9.5	10.01	105.4
15H	24	0550	129.5	139.0	9.5	9.77	102.8
16H	24	0800	139.0	148.5	9.5	9.94	104.6
17H	24	0935	148.5	158.0	9.5	9.81	103.3
18H	24	1040	158.0	167.5	9.5	10.02	105.5
19H	24	1200	167.5	177.0	9.5	9.51	100.1
20H	24	1330	177.0	186.5	9.5	9.93	104.5
21H	24	1450	186.5	196.0	9.5	9.85	103.7
22H	24	1615	196.0	205.5	9.5	9.84	103.6
23H	24	1745	205.5	215.0	9.5	9.97	105.0
24H	24	1920	215.0	224.5	9.5	9.91	104.3
25X	24	2200	224.5	234.1	9.6	2.45	25.5
26X	25	0130	234.1	243.7	9.6	4.00	41.7
27X	25	0450	243.7	250.8	7.1	1.22	17.2
Cored totals:					250.8	240.41	95.7
199-1219B-							
***** Drilled from 0.0 to 21.0 mbsf *****							
2H	26	1530	21.0	30.5	9.5	9.95	104.7
3H	26	1655	30.5	40.0	9.5	9.18	96.6
4H	26	1845	40.0	49.5	9.5	8.75	92.1
5H	26	1955	49.5	59.0	9.5	9.29	97.8

Table T1 (continued).

Core	Date (Nov 2001)	Local time (hr)	Depth (mbsf)		Length (m)		Recovery (%)
			Top	Bottom	Cored	Recovered	
6H	26	2105	59.0	68.5	9.5	9.97	105.0
7H	26	2245	68.5	78.0	9.5	9.80	103.2
8H	26	2350	78.0	87.5	9.5	10.10	106.3
9H	27	0100	87.5	97.0	9.5	9.50	100.0
10H	27	0220	97.0	106.5	9.5	9.81	103.3
11H	27	0345	106.5	116.0	9.5	9.88	104.0
12H	27	0500	116.0	125.5	9.5	9.88	104.0
13H	27	0615	125.5	135.0	9.5	9.68	101.9
14H	27	0730	135.0	144.5	9.5	10.13	106.6
15H	27	1020	144.5	154.0	9.5	8.68	91.4
16H	28	0200	154.0	158.0	4.0	3.95	98.8
Cored totals:					137.0	138.55	101.1
Drilled total:					21.0		
Total:					158.0		

Note: The expanded coring summary table is available in ASCII (see the ["Supplementary Material"](#) contents list).

Table T2. Calcareous nannofossil datums, Site 1219.

Core, section, interval (cm)		Marker species	Age (Ma)	Depth (mbsf)		Depth (mcd)	
Top	Bottom			Midpoint	±	Midpoint	±
199-1219A-	199-1219A-						
3H-3, 92	3H-3, 138	T <i>Cyclicargolithus floridanus</i>	13.2	19.65	0.23	19.65	0.23
3H-3, 138	3H-4, 145	T <i>Sphenolithus heteromorphus</i>	13.6	20.67	0.79	20.67	0.79
3H-5, 25	3H-6, 26	T <i>Discoaster deflandrei</i> acme	16.2	22.69	0.94	22.51	0.76
4H-4, 92	4H-4, 140	T <i>Triquetrorhabdulus carinatus</i>	19.6	30.66	0.24	31.54	0.24
5H-CC	6H-1, 90	T <i>Triquetrorhabdulus carinatus</i> acme	22.9	44.69	0.22	47.84	1.08
6H-2, 40	6H-2, 105	B <i>Sphenolithus disbelemnus</i>	23.5	46.23	0.33	50.25	0.33
6H-5, 30	6H-5, 90	T <i>Sphenolithus delphix</i>	23.7	50.60	0.30	54.62	0.30
6H-6, 120	6H-7, 20	B <i>Sphenolithus delphix</i>	24.4	52.95	0.25	56.97	0.25
7H-5, 10	7H-5, 80	T <i>Sphenolithus ciperoensis</i>	24.7	59.79	0.35	61.86	0.35
7H-5, 80	7H-6, 90	T <i>Cyclicargolithus abisectus</i> acme	25.5	60.94	0.80	63.01	0.80
8H-3, 100	8H-4, 100	T <i>Sphenolithus distentus</i>	26.5	67.75	0.75	70.80	0.75
9H-2, 140	9H-3, 140	B <i>Sphenolithus ciperoensis</i>	28.1	76.15	0.75	83.52	0.75
12H-5, 80	12H-6, 80	T <i>Sphenolithus pseudoradians</i>	29.1	108.55	0.75	123.68	0.75
13H-3, 80	13H-4, 80	B <i>Sphenolithus distentus</i>	30.4	115.05	0.75	134.95	0.75
15H-5, 140	15H-6, 10	T <i>Reticulofenestra umbilicus</i> ≥14 µm	31.7	137.00	0.10	159.85	0.10
16H-4, 140	16H-5, 140	T <i>Ericsonia formosa</i>	32.9	145.65	0.75	170.07	0.78
17H-2, 90	19H-7, 5	T <i>Discoaster saipanensis</i>	34.0	163.73	12.83	190.06	13.83
17H-2, 90	19H-7, 5	T <i>Discoaster barbadiensis</i>	34.2	163.73	12.83	190.06	13.83
17H-2, 90	20H-1, 114	T <i>Chiasmolithus grandis</i>	37.1	164.52	13.62	191.35	15.12
20H-2, 52	21H-3, 80	B <i>Dictyococcites bisectus</i>	38.5	184.66	5.64	213.49	6.14
20H-2, 52	21H-3, 80	T <i>Dictyococcites hesslandii</i>	40.3	184.66	5.64	213.49	6.14
22H-3, 49	22H-3, 125	B <i>Reticulofenestra umbilicus</i> ≥14 µm	42.5	199.87	0.38	230.20	0.38
22H-CC	24H-1, 36	P <i>Nannotetrina</i> spp.	45.1	210.60	4.76	241.93	5.76
23H-7, 63	24H-1, 6	P <i>Nannotetrina alata</i>	45.2	215.13	0.00	246.93	0.47
26X-1, 60	26X-1, 107	X <i>Tribrachiatus contortus</i> / <i>Tribrachiatus orthostylus</i>	53.4	234.94	0.24	269.27	0.24
26X-3, 52	27X-CC	T-T <i>Tribrachiatus contortus</i> / <i>F. tympaniformis</i>	53.8	244.21	6.59	279.04	7.09
199-1219B-	199-1219B-						
4H-CC	5H-1, 30	T <i>Sphenolithus delphix</i>	23.7	49.28	0.53	53.93	0.77
5H-2, 80	5H-2, 90	B <i>Sphenolithus delphix</i>	24.4	53.35	0.05	56.75	0.05
5H-CC	6H-1, 60	T <i>Sphenolithus ciperoensis</i>	24.7	59.20	0.41	63.82	0.13
11H-3, 85	11H-3, 120	T <i>Sphenolithus pseudoradians</i>	29.1	110.53	0.18	124.60	0.18
14H-7, 40	14H-7, 70	T <i>Reticulofenestra umbilicus</i> ≥14 µm	31.7	144.55	0.15	161.84	0.15
15H-5, 76	15H-5, 104	T <i>Ericsonia formosa</i>	32.9	150.96	0.14	170.31	0.14

Notes: T = top, B = bottom, P = presence, X = abundance crossover, T-T = between top *Tribrachiatus contortus* and top *Fasciculithus* spp. This table is also available in ASCII. [N1]

Table T3 (continued).

Core, section, interval (cm)	Depth (mbsf)	Zone	Preservation	Group abundance	
25X-CC, 35–40	226.90	Not zoned		B	<i>Catapsydrax dissimilis ciproensis</i> <i>Catapsydrax dissimilis</i> <i>Catapsydrax globiformis</i> <i>Catapsydrax unicavus</i> <i>Cassigerinella chipolensis</i> <i>Dentoglobigerina yeguaensis</i> <i>Dentoglobigerina altispira</i> <i>Dentoglobigerina baroemoensis</i> <i>Dentoglobigerina galavisi</i> <i>Dentoglobigerina globularis</i> <i>Dentoglobigerina pseudociproensis</i> <i>Globigerina anguliofficialis</i> <i>Globigerina ciproensis</i> <i>Globigerina praebulluloides</i> <i>Globigerinoides primordius</i> <i>Globigerinoides trilobus</i> <i>Globoquadrina binatensis</i> <i>Globoquadrina deliscens</i> <i>Globoquadrina praedeheiscens</i> <i>Globoquadrina prasaepis</i> <i>Globoquadrina rohri</i> <i>Globoquadrina sellii</i> <i>Globoquadrina tapuensis</i> <i>Globoquadrina tripartita</i> <i>Globoquadrina venzuelana</i> <i>Globorotaloides sp.</i> <i>Globorotaloides suteri</i> <i>Paragloborotalia acrostoma</i> <i>Paragloborotalia continua</i> <i>Paragloborotalia kugleri</i> <i>Paragloborotalia mayeri</i> <i>Paragloborotalia nana</i> <i>Paragloborotalia opima opima</i> <i>Paragloborotalia pseudokugleri</i> <i>Paragloborotalia siakensis</i> <i>Paragloborotalia sp.</i> <i>Subbotina angiporoides</i> <i>Subbotina euapertura</i> <i>Subbotina gortanii</i> <i>Tenuitella clemenciae</i> <i>Tenuitella gemma</i> <i>Tenuitellinata angustiumbilicata</i> <i>Turborotalia ampliapertura</i>

Notes: Preservation: G = good, M = moderate, P = poor. Group abundance: C = common, R = rare, A = abundant, F = few, T = trace (a single specimen was found), P = Present (indicates the presence of one or two individuals in a given sample), blank = absence of any planktonic foraminifer.

Table T4. Distribution of early Eocene planktonic foraminifers, Hole 1219A.

Core, section, interval (cm)	Depth (mbsf)	Zone/ Subzone	Preservation	Group abundance	<i>Acarinina berggieri</i>	<i>Acarinina coalingensis</i>	<i>Acarinina pseudotapiuensis</i>	<i>Acarinina quetra</i>	<i>Acarinina soiaodoensis</i>	<i>Acarinina wilcoxensis</i>	<i>Chiloguembelina wilcoxensis</i>	<i>Glabanomalina planaconica</i>	<i>Glabanomalina pseudoimitata</i>	<i>Marozovella acuta</i>	<i>Marozovella aequa</i>	<i>Marozovella eagari</i>	<i>Marozovella formosa</i>	<i>Marozovella gracilis</i>	<i>Marozovella marginoventata</i>	<i>Marozovella occiusa</i>	<i>Marozovella subbotinae</i>	<i>Paraglobarctavia opima opima</i>	<i>Paraglobarctavia</i> sp.	<i>Pseudohastigerina wilcoxensis</i>	<i>Subbctina patagonica</i>	<i>Subbctina velascoensis</i>
199-1219A- 26X-1, 72-74	234.82			B																						
26X-2, 18-20	235.78	P6b	M	A	F	A	F	A	R	R								F			A			R		
26X-2, 46-48	236.06		M	A	F	F	F	F	F	F	R	R							F			F		R	R	
26X-CC, 21-24	238.07		P	A	F	F	F	F	F	R								R	F	R		F		R	R	
27X-1, 19-21	243.89	P5	M	A	R	P	R	F	P		P	R	F					F			F	F		R	R	F
27X-CC, 7-8	244.59		M	A	R	F		F	P	P	P	R	P	R	F	F					R			R	R	F
27X-CC, 12-14	244.64																									

Notes: Preservation: M = moderate, P = poor. Group abundance: A = abundant, F = few, R = rare, P = present. See Table T3, p. 98, for like symbols.

Table T5. Planktonic foraminifer datum levels, Hole 1219A.

Marker species	Age (Ma)	Core, section, interval (cm)		Depth (mbsf)		Depth (mcd)	
		Top	Bottom	Midpoint	±	Midpoint	±
		199-1219A-	199-1219A-				
T <i>Catapsydrax dissimilis</i>	17.3	4H-4, 136–140	4H-5, 115–120	31.51	0.65	32.39	0.65
T <i>Paragloborotalia kugleri</i>	21.5 [21.0]	5H-2, 80–85	5H-4, 130–135	38.55	1.75	40.84	1.75
B <i>Paragloborotalia kugleri</i>	23.8 [22.9]	6H-5, 5–7	6H-6, 63–65	51.09	1.04	55.11	1.04
T <i>Paragloborotalia opima opima</i>	27.1	8H-CC	9H-1, 109–114	73.32	0.27	78.53	2.43
B <i>Globorotalia mayeri</i>	—	11H-6, 106–110	12H-2, 17–22	101.37	1.31	115.64	2.17
T <i>Turborotalia ampliapertura</i>	30.3	12H-7, 12–17	12H-CC	110.60	0.50	125.73	0.50
B <i>Paragloborotalia opima opima</i>	30.6	14H-2, 53–58	14H-3, 51–56	122.75	0.75	144.20	0.75
T <i>Morozovella acuta</i>	54.7 [54.25*]	27X-1, 19–21	27X-CC, 7–8	244.24	0.35	279.57	0.35

Notes: T = top or highest occurrence, B = bottom or first occurrence. Ages are those of Berggren et al. (1995); ages in square brackets are those of Shackleton et al. (1999). The well defined, but uncalibrated, *Globorotalia mayeri* datum is also included. * = corrected age estimate for the “*T. M. acuta*” event based on the DSDP Site 550 ash bed calibration of Berggren et al. (1995). They list the last occurrence of this taxon as 54.7 Ma, but the figure caption states that it is present at “the midpoint between ash beds –17 and +19, 54.0–54.5 Ma.” This table is also available in [ASCII](#). [N1]

Table T6 (continued).

Core, section, interval (cm)	Depth (mbsf)	Preservation	Group abundance	Bathymetry	<i>Pullenia subcarinata</i>	<i>Pyulina</i> spp.	<i>Recurvoides</i> sp.	<i>Rhizammima</i> sp.	<i>Siphonodotaria abyssorum</i>	<i>Spiroplectammima spectabilis</i>	<i>Stilostomella lepidula</i>	<i>Stilostomella rugosa</i>	<i>Stilostomella subspinosa</i>	<i>Subreophax</i> sp.	<i>Textularia</i> spp.	Unidentified benthic forams	Unilocular species	<i>Vulvulina spinosa</i>
199-1219A-																		
1H-CC, 12-15	5.92	P	R	LA														
2H-CC, 15-19	16.00	M	R	LA														
3H-CC, 12-16	25.31	P	R	LA			F	F										
4H-CC, 18-21	34.84	M	F	LB-UA	F	R			R		R							
5H-CC, 14-18	44.43	P	F	LB-UA					F			F				R	R	
6H-CC, 18-23	53.90	G	R	LB-UA		R		R		R	R							R
7H-CC, 24-29	62.94	VG	F	LB-UA	R			R		R	F		F	R				R
8H-CC, 20-24	73.05	VG	R	LB-UA	R			R	R	R	R				R			R
9H-CC, 10-14	82.35	VG	R	LB-UA					R		R							R
10H-CC, 27-32	91.57	VG	F	LB-UA	R				R		R		R					F
11H-CC, 11-17	101.13	VG	F	LB-UA		R	R		R	R								R
12H-CC, 24-30	111.08	VG	F	LB-UA	F		R						R					R
13H-CC, 7-12	120.08	VG	F	LB-UA			R		R				R					R
14H-CC, 14-18	129.97	VG	F	LB-UA		R			R	R								R
15H-CC, 6-12	139.21	VG	R	LB-UA				R	R				R					R
16H-CC, 11-16	148.89	VG	F	LB-UA	R				R	R								F
17H-8, 12-17	157.91	P	T	LB-UA						R	A							
18H-CC, 17-22	167.97	P	T	LB-UA						A	A							
19H-CC, 0-3	176.98	P	R	LB-UA					F	F	F							
20H-CC, 31-35	186.89		B															
21H-8, 19-24	195.69	M	R	LB-UA									R					C
22H-CC, 27-31	205.80		B															
23H-CC, 23-27	215.43	P	T	LB-UA						F						R		
24H-4, 150-155	221.00	P	R	LB-UA												F		
24H-CC, 21-24	224.88	P	T	LB-UA						A								
25X-CC, 35-40	226.90		B															
26X-CC, 21-24	238.07	P	T	LB-UA														

Table T7. Distribution of radiolarian datum levels, Site 1219.

Marker species/ Zonal boundaries	Age (Ma)	Hole, core, section, interval (cm)		Depth (mbsf)		Depth (mcd)	
		Top	Bottom	Midpoint	±	Midpoint	±
		199-	199-				
<i>T Calocyclus costata</i>	15.00	1219A-1H-4, 45	1219A-1H-CC, 45	5.44	0.49	5.44	0.49
<i>Dorcadospyrus dentata</i> →	15.68	1219A-3H-3, 45	1219A-3H-4, 45	19.70	0.75	19.70	0.75
<i>Dorcadospyrus alata</i>							
RN5/4	15.70	1219A-3H-3, 45	1219A-3H-4, 45	19.70	0.75	19.70	0.75
RN4/3	17.03	1219A-3H-CC, 45	1219B-2H-3, 45	24.84	0.48	25.62	0.31
RN3/2	17.92	1219A-4H-5, 46	1219A-4H-6, 46	32.21	0.75	33.09	0.75
RN2/1	20.53	1219A-5H-4, 45	1219A-5H-5, 45	40.20	0.75	42.49	0.75
<i>B. E. diaphanes</i>	23.94	1219A-5H-CC	1219A-6H-1, 45	44.44	0.01	47.60	0.88
<i>T. A. gracilis</i>	23.94	1219A-5H-CC	1219A-6H-1, 45	44.44	0.01	47.60	0.88
RN1/RP22	23.62	1219A-6H-1, 45	1219A-6H-2, 45	45.20	0.75	49.22	0.75
RP22/21	24.60	1219B-6H-2, 46	1219A-8H-1, 43	62.20	1.24	65.89	0.59
RP21/20	28.80	1219A-12H-6, 45	1219A-12H-7, 45	109.70	0.75	124.83	0.75
RP20/19	32.80	1219A-17H-4, 15	1219A-17H-5, 32	152.85	0.84	178.18	0.84
RP19/18	34.90	1219A-17H-CC	1219A-18H-1, 45	158.17	0.28	184.00	0.78
RP18/17	36.40	1219A-18H-3, 45	1219A-18H-4, 45	162.20	0.75	188.53	0.75
RP17/16	37.70	1219A-19H-4, 45	1219A-19H-5, 45	173.20	0.75	200.53	0.75
RP16/15	38.80	1219A-20H-5, 45	1219A-20H-6, 45	183.78	0.75	212.11	0.75
RP15/14	39.50	1219A-22H-3, 46	1219A-22H-4, 46	200.21	0.75	230.54	0.75
RP14/13	42.80	1219A-23H-5, 45	1219A-23H-6, 45	212.70	0.75	244.03	0.75
RP13/12	44.50	1219A-24H-2, 45	1219A-24H-3, 45	217.70	0.75	250.03	0.75

Notes: T = top, B = bottom. This table is also available in [ASCII](#). [N1]

Table T8. Core disturbance, Site 1219.

Core, section, interval (cm)	Depth (mbsf)		Comments
	Top	Bottom	
199-1219A-			
1H-1, 0-42	0.00	0.42	Flow-in
1H-1, 42-44	0.42	0.44	Void
1H-1, 92-97	0.92	0.97	Flow-in
1H-CC, 0-13	5.80	5.93	Disturbed
2H-1, 0-40	6.00	6.40	Flow-in
3H-1, 0-7	15.50	15.57	Flow-in
3H-1, 31-39	15.81	15.89	Flow-in
3H-1, 39-62	15.89	16.12	Flow-in
4H-1, 0-90	25.00	25.90	Flow-in
3H-CC, 0-15	25.19	25.34	Very disturbed
4H-1, 55-74	25.55	25.74	Void
7H-1, 0-6	53.50	53.56	Soupy
7H-6, 40-85	61.24	61.69	Soupy
8H-1, 0-29	63.00	63.29	Soupy/downhole debris
8H-4, 99-142	68.49	68.92	Faulted
8H-6, 5-33	70.55	70.83	Faulted
10H-1, 0-150	82.00	83.50	Flow-in
10H-2, 0-125	83.50	84.75	Flow-in
11H-7, 30-40	100.80	100.90	Flow-in
12H-1, 0-14	101.00	101.14	Flow-in
12H-3, 112-114	105.12	105.14	Expansion cracks
12H-6, 60-82	109.10	109.32	Soupy
12H-6, 82-88	109.32	109.38	Disturbed
13H-1, 0-15	110.50	110.65	Flow-in
13H-1, 26-27	110.76	110.77	Void
14H-1, 0-10	120.00	120.10	Flow-in
13H-CC, 0-12	120.01	120.12	Disturbed
17H-1, 0-10	148.50	148.60	Soupy/downhole debris
16H-7, 52-67	148.63	148.78	Crushed liner
18H-1, 0-31	158.00	158.31	Downhole debris
19H-1, 0-32	167.50	167.82	Flow-in
19H-3, 57-58	171.07	171.08	Void
19H-4, 75-105	172.75	173.05	Fault
19H-5, 52-81	174.02	174.31	Fault
20H-1, 0-13	177.00	177.13	Disturbed
20H-4, 148-152	182.51	182.55	Disturbed
20H-CC, 9-35	186.67	186.93	Disturbed

Core, section, interval (cm)	Depth (mbsf)		Comments
	Top	Bottom	
22H-1, 0-35	196.00	196.35	Soupy/downhole debris
22H-2, 84-85	198.34	198.35	Void
23H-1, 0-3	205.50	205.53	Soupy
23H-3, 18-94	208.68	209.44	Soupy
23H-3, 94-149	209.44	209.99	Flow-in
23H-4, 0-20	210.00	210.20	Flow-in
23H-4, 20-29	210.20	210.29	Soupy
25X-CC, 26-33	226.81	226.88	Chert
199-1219B-			
2H-1, 0-10	21.00	21.10	Flow-in
2H-1, 100-110	22.00	22.10	
2H-2, 23-25	22.64	22.66	Crack
3H-CC, 6-15	39.58	39.67	Disturbed
4H-1, 0-10	40.00	40.10	Weakly disturbed
6H-1, 0-19	59.00	59.19	Soupy
7H-1, 0-13	68.50	68.63	Disturbed
10H-1, 0-13	97.00	97.13	Void
10H-1, 70-74	97.70	97.74	Soupy
10H-3, 36-37	100.36	100.37	Void
10H-7, 0-65	106.00	106.65	Collapsed core liner
11H-1, 0-150	106.50	108.00	Flow-in
11H-2, 0-150	108.00	109.50	Flow-in
11H-2, 91-132	108.91	109.32	Void
12H-1, 0-2	116.00	116.02	Disturbed
12H-CC, 0-4	125.76	125.80	Disturbed
14H-1, 0-150	135.00	136.50	Flow-in
14H-2, 40-60	136.90	137.10	Flow-in
15H-1, 0-60	144.50	145.10	Flow-in/void
16H-1, 0-45	154.00	154.45	Disturbed
16H-2, 0-13	154.45	154.58	Disturbed
16H-3, 0-54	154.58	155.12	Disturbed
16H-4, 0-1.5	155.12	156.62	Disturbed
16H-5, 0-1.19	156.62	157.81	Disturbed
16H-6, 0-0.14	157.81	157.95	Disturbed

Notes: Data from these intervals were removed from the GRA bulk density, MS, color reflectance, natural gamma, and *P*-wave velocity data sets. This table is also available in [ASCII](#).

Table T9. Composite depths, Site 1219.

Core	Length (m)	Depth (mbsf)	Offset (m)	Depth (mcd)
199-1219A-				
1H	6.0	0.00	0.00	0.00
2H	9.5	6.00	0.00	6.00
3H	9.5	15.50	0.00	15.50
4H	9.5	25.00	0.88	25.88
5H	9.5	34.50	2.29	36.79
6H	9.5	44.00	4.02	48.02
7H	9.5	53.50	2.07	55.57
8H	9.5	63.00	3.05	66.05
9H	9.5	72.50	7.37	79.87
10H	9.5	82.00	8.97	90.97
11H	9.5	91.50	13.41	104.91
12H	9.5	101.00	15.13	116.13
13H	9.5	110.50	19.59	130.09
14H	9.5	120.00	21.45	141.45
15H	9.5	129.50	22.85	152.35
16H	9.5	139.00	24.33	163.33
17H	9.5	148.50	25.33	173.83
18H	9.5	158.00	26.33	184.33
19H	9.5	167.50	27.33	194.83
20H	9.5	177.00	28.33	205.33
21H	9.5	186.50	29.33	215.83
22H	9.5	196.00	30.33	226.33
23H	9.5	205.50	31.33	236.83
24H	9.5	215.00	32.33	247.33
25X	9.6	224.50	33.33	257.83
26X	9.6	234.10	34.33	268.43
27X	7.1	243.70	35.33	279.03
199-1219B-				
2H	9.5	21.00	1.56	22.56
3H	9.5	30.50	3.35	33.85
4H	9.5	40.00	4.41	44.41
5H	9.5	49.50	4.90	54.40
6H	9.5	59.00	4.34	63.34
7H	9.5	68.50	5.98	74.48
8H	9.5	78.00	11.91	89.91
9H	9.5	87.50	12.61	100.11
10H	9.5	97.00	13.20	110.20
11H	9.5	106.50	14.07	120.57
12H	9.5	116.00	15.29	131.29
13H	9.5	125.50	16.29	141.79
14H	9.5	135.00	17.29	152.29
15H	9.5	144.50	19.35	163.85
16H	4.0	154.00	19.35	173.35

Note: This table is also available in [ASCII](#).

Table T10. Splice tie points, Site 1219.

Hole, core, section, interval (cm)	Depth			Hole, core, section, interval (cm)	Depth	
	(mbsf)	(mcd)			(mbsf)	(mcd)
199-				199-		
1219A-1H-4, 128	5.78	5.78	Append to	1219A-2H-1, 0	6.00	6.00
1219A-2H-7, 78	15.78	15.78	Tie to	1219A-3H-1, 28	15.78	15.78
1219A-3H-6, 32	23.32	23.32	Tie to	1219B-2H-1, 76	21.76	23.32
1219B-2H-6, 88	29.29	30.85	Tie to	1219A-4H-4, 46.5	29.97	30.85
1219A-4H-6, 128	33.78	34.66	Tie to	1219B-3H-1, 80.5	31.31	34.66
1219B-3H-4, 142	36.42	39.77	Tie to	1219A-5H-2, 148	37.48	39.77
1219A-5H-7, 40	43.90	46.19	Tie to	1219B-4H-2, 28	41.78	46.19
1219B-4H-4, 60	45.10	49.51	Tie to	1219A-6H-1, 149	45.49	49.51
1219A-6H-5, 124	51.24	55.26	Tie to	1219B-5H-1, 86	50.36	55.26
1219B-5H-6, 50	57.50	62.40	Tie to	1219A-7H-5, 98.5	60.33	62.40
1219A-7H-6, 128	62.12	64.19	Tie to	1219B-6H-1, 84.5	59.85	64.19
1219B-6H-6, 142	67.92	72.26	Tie to	1219A-8H-5, 19.5	69.21	72.26
1219A-8H-7, 32	72.32	75.37	Tie to	1219B-7H-1, 88.5	69.39	75.37
1219B-7H-6, 40	76.40	82.38	Tie to	1219A-9H-2, 100.5	75.01	82.38
1219A-9H-7, 48	81.98	89.35	Append to	1219B-8H-1, 0	78.00	89.91
1219B-8H-7, 82	87.82	99.73	Append to	1219B-9H-1, 0	87.50	100.11
1219B-9H-5, 28	93.78	106.39	Tie to	1219A-11H-1, 148	92.98	106.39
1219A-11H-5, 8	97.58	110.99	Tie to	1219B-10H-1, 78.5	97.79	110.99
1219B-10H-6, 98	105.48	118.68	Tie to	1219A-12H-2, 103.5	103.55	118.68
1219A-12H-6, 28	108.78	123.91	Tie to	1219B-11H-3, 34	109.84	123.91
1219B-11H-7, 64	116.14	130.21	Append to	1219A-13H-1, 0	110.50	130.09
1219A-13H-5, 124	117.30	136.89	Tie to	1219B-12H-4, 109	121.60	136.89
1219B-12H-7, 74	125.74	141.03	Append to	1219B-13H-1, 0	125.50	141.79
1219B-13H-7, 48	134.98	151.27	Append to	1219A-15H-1, 0	129.50	152.35
1219A-15H-7, 62	139.12	161.97	Append to	1219A-16H-1, 0	139.00	163.33
1219A-16H-7, 50	148.61	172.94	Append to	1219A-17H-1, 0	148.50	173.83
1219A-17H-8, 22	157.99	183.32	Append to	1219A-18H-1, 0	158.00	184.33
1219A-18H-7, 48	167.48	193.81	Append to	1219A-19H-1, 0	167.50	194.83
1219A-19H-7, 46	176.96	204.29	Append to	1219A-20H-1, 0	177.00	205.33
1219A-20H-7, 94	186.99	215.32	Append to	1219A-21H-1, 0	186.50	215.83
1219A-21H-8, 48	195.98	225.31	Append to	1219A-22H-1, 0	196.00	226.33
1219A-22H-7, 48	205.48	235.81	Append to	1219A-23H-1, 0	205.50	236.83
1219A-23H-7, 64	215.14	246.47	Append to	1219A-24H-1, 0	215.00	247.33
1219A-24H-7, 58	224.63	256.96	Append to	1219A-25X-1, 0	224.50	257.83
1219A-25X-2, 52	226.52	259.85	Append to	1219A-26X-1, 0	234.10	268.43
1219A-26X-3, 72	237.82	272.15	Append to	1219A-27X-1, 0	243.70	279.03

Note: This table is also available in [ASCII](#).

Table T11. Paleomagnetic events, Site 1219.

Chron/ Subchron	Age (Ma)	Depth (mcd)
T C1n	0.000	0.00
B C1n	0.780	0.95
T C1r.1n	0.990	1.18
B C1r.1n	1.070	1.26
T C2n	1.770	2.08
B C2n	1.950	2.25
T C3n.1n	4.180	4.73
B C3n.1n	4.290	4.90
T C3n.2n	4.480	5.18
B C3n.2n	4.620	5.35
T C3An.1n	5.875	6.76
B C3An.2n	6.555	7.49
T C4n	7.135	8.73
B C4n	8.027	9.40
T C5n	9.639	10.33
B C5n	10.839	12.08
T C5Bn.2n	15.034	20.39
B C5Bn.2n	15.155	20.72
T C5Cn.1n	16.014	23.22
B C5Cn.1n	16.293	24.01
T C5Cn.2n	16.327	24.14
B C5Cn.2n	16.488	24.41
T C5Cn.3n	16.556	24.67
B C5Cn.3n	16.726	25.06
T C5Dn	17.277	26.64
B C5Dn	17.615	27.17
T C5En	18.281	28.16
B C5En	18.781	29.47
T C6n	19.048	29.93
B C6n	20.131	33.48
T C6Cn.1n	23.353	51.58
B C6Cn.1n	23.535	52.30
T C6Cn.2n	23.677	52.96
B C6Cn.2n	23.800	53.81
T C6Cn.3n	23.999	55.52
B C6Cn.3n	24.118	56.18
T C7n.1n	24.730	59.21
B C7n.1n	24.781	59.54
T C7n.2n	24.835	60.18
B C7n.2n	25.183	62.46
T C7An	25.496	63.65
B C7An	25.648	64.63
T C8n.1n	25.823	65.82
B C8n.1n	25.951	67.34
T C8n.2n	25.992	67.66
T C9n	27.027	79.70
B C9n	27.972	97.24
T C10n.1n	28.283	101.47
B C10n.2n	28.745	107.10
T C12	30.479	142.28
B C12	30.939	146.43
B C13n	33.058	176.92
B C16n.2n	36.341	190.99
T C17n.1n	36.618	192.47
B C17n.1n	37.473	197.50
T C17n.2n	37.604	198.24
B C17n.2n	37.848	199.57
T C17n.3n	37.920	199.87
B C17n.3n	38.113	200.90
T C18n.1n	38.426	202.38
B C18n.1n	39.552	210.38
T C18n.2n	39.631	210.97
B C18n.2n	40.130	214.67
B C19n	41.521	229.70
T C20n	42.536	235.72
B C20n	43.789	247.60

Notes: T = top, B = bottom. This table is also available in [ASCII](#).

Table T12. Nannofossil, foraminifer, and radiolarian events, Site 1219.

Marker species/ Zonal boundaries	Age (Ma)	Depth (mcd)	
		Midpoint	±
Nannofossil events:			
T <i>Cyclicargolithus floridanus</i>	13.20	13.20	0.23
T <i>Sphenolithus heteromorphus</i>	13.60	20.67	0.79
T <i>Discoaster deflandrei acme</i>	16.10	22.69	0.94
T <i>Triquetrorhabdulus carinatus*</i>	19.60	20.48	0.24
T <i>Triquetrorhabdulus carinatus acme*</i>	22.00	4.04	1.08
B <i>Sphenolithus disbelemnos</i>	22.70	26.72	0.32
T <i>Sphenolithus delphix</i>	23.00	27.02	0.30
B <i>Sphenolithus delphix</i>	23.20	27.22	0.25
T <i>Sphenolithus ciperoensis</i>	24.10	26.17	0.35
T <i>Cyclicargolithus abisectus acme*</i>	24.60	26.67	0.80
T <i>Sphenolithus distentus</i>	26.50	29.55	0.75
B <i>Sphenolithus ciperoensis</i>	28.10	35.47	0.75
T <i>Sphenolithus pseudoradians</i>	29.10	44.23	0.75
B <i>Sphenolithus distentus</i>	30.40	49.99	0.75
T <i>Reticulofenestra umbilicus</i> ≥14 μm	31.70	54.55	0.10
T <i>Ericsonia formosa</i>	32.90	57.23	0.75
T <i>Discoaster saipanensis</i>	34.00	33.85	13.83
T <i>Discoaster barbadiensis</i>	34.20	33.91	13.83
T <i>Chiasmolithus grandis</i>	37.10	34.84	15.12
B <i>Dictyococcites bisectus</i>	38.50	36.98	6.14
T <i>Dictyococcites hesslandii</i>	40.30	36.99	6.14
B <i>Reticulofenestra umbilicus</i> ≥14 μm	42.50	72.83	0.38
P <i>Nannotetrina</i> spp.	45.10	39.11	5.76
P <i>Nannotetrina alata</i>	45.20	40.19	0.50
X <i>Tribrachiatus contortus</i> / <i>Tribrachiatus orthostylus</i>	53.40	87.73	0.24
T-T <i>Tribrachiatus contortus</i> / <i>Fasciculithus tympaniformis</i>	53.80	43.64	7.09
Foraminifer events:			
T <i>Catapsydrax dissimilis</i>	17.30	33.06	1.32
T <i>Paragloborotalia kugleri</i>	21.00	38.19	0.90
B <i>Paragloborotalia kugleri</i>	22.90	56.28	0.13
T <i>Paragloborotalia opima opima</i>	27.10	78.18	2.79
B <i>Globorotalia mayeri</i>		115.64	2.16
T <i>Morozovella acuta</i>	54.25	279.57	0.35
Radiolarian events:			
T <i>Calocycletta costata</i>	15.00	5.44	0.49
<i>Dorcadospyrus dentata</i> → <i>Dorcadospyrus alata</i>	15.68	19.70	0.75
RN5/4	15.70	19.70	0.75
B <i>Calocycletta costata</i>	17.03	25.62	0.31
RN4/3	17.03	25.62	0.31
B <i>Stichocorys wolffii</i>	17.92	33.09	0.75
RN3/2	17.92	33.09	0.75
T <i>Theocyrtis annosa</i>	20.53	42.49	0.75
RN2/1	20.53	42.49	0.75
B <i>Eucyrtidium diaphanes</i>	23.94	47.60	0.88
T <i>Artophormis gracilis</i>	23.94	47.60	0.88
B <i>Cyrtocapsella tetrapera</i>	23.62	49.22	0.75
RN1/RP22	23.62	52.36	0.75
RP22/21	24.60	65.89	0.58
RP21/20	28.80	124.83	0.75
RP20/19	32.80	178.16	0.84
RP19/18	34.90	184.00	0.78
RP18/17	36.40	188.53	0.75
RP17/16	37.70	200.53	0.75
RP16/15	38.80	212.11	0.75
RP15/14	39.50	230.54	0.75
RP14/13	42.80	244.03	0.75
RP13/12	44.50	250.03	0.75

Notes: * = on Cande and Kent (1995) timescale, 900 k.y. subtracted from age estimates for *Triquetrorhabdulus carinatus acme* and *Cyclicargolithus abisectus acme*. T = top, B = bottom, P = presence, X = abundance cross-over, T-T = between top *Tribrachiatus contortus* and top *Fasciculithus* spp. This table is also available in ASCII. [N1]

Table T13. Depths, ages, rates, and fluxes of sediments, Hole 1219A. (See table notes. Continued on next two pages.)

Depth (mbsf)	Depth shift (m)	Depth (mcd)	Age (Ma)	LSR (m.m.y.)	DBD (g/cm ³)	MAR (mg/cm ² /k.y.)
0.75	0.00	0.75	0.67	1.1144	0.277	31
2.20	0.00	2.20	1.97	1.1144	0.276	31
3.75	0.00	3.75	3.37	1.1144	0.258	29
5.09	0.00	5.09	4.57	1.1144	0.27	30
6.75	0.00	6.75	6.06	1.1144	0.313	35
8.15	0.00	8.15	7.31	1.1144	0.276	31
9.75	0.00	9.75	8.75	1.1144	0.321	36
11.25	0.00	11.25	10.10	1.1144	0.285	32
12.75	0.00	12.75	11.13	2.3036	0.276	64
14.25	0.00	14.25	11.78	2.3036	0.253	58
15.37	0.00	15.37	12.27	2.3036	0.276	64
16.29	0.00	16.29	12.67	2.3036	0.245	56
17.77	0.00	17.77	13.31	2.3036	0.268	62
19.25	0.00	19.25	13.95	2.3036	0.244	56
20.75	0.00	20.75	14.60	2.3036	0.296	68
22.25	0.00	22.25	15.25	2.3036	0.317	73
23.75	0.00	23.75	15.91	2.3036	0.295	68
24.82	0.00	24.82	16.37	2.3036	0.288	66
26.07	0.88	26.95	17.30	2.3036	0.283	65
27.25	0.88	28.13	17.81	2.3036	0.266	61
28.69	0.88	29.57	18.43	2.3036	0.252	58
30.25	0.88	31.13	19.11	2.3036	0.556	128
31.75	0.88	32.63	19.76	2.3036	0.776	179
33.25	0.88	34.13	20.24	5.8328	0.819	478
34.31	0.88	35.19	20.42	5.8328	0.341	199
35.25	2.29	37.54	20.83	5.8328	0.777	453
36.89	2.29	39.18	21.11	5.8328	1.021	596
38.25	2.29	40.54	21.34	5.8328	0.485	283
39.75	2.29	42.04	21.60	5.8328	1.004	586
41.25	2.29	43.54	21.85	5.8328	0.933	544
42.78	2.29	45.07	22.12	5.8328	0.891	520
44.13	2.29	46.42	22.35	5.8328	0.622	363
44.75	4.02	48.77	22.75	5.8328	0.802	468
46.27	4.02	50.29	23.01	5.8328	0.355	207
47.71	4.02	51.73	23.26	5.8328	0.361	211
49.25	4.02	53.27	23.52	5.8328	0.821	479
50.75	4.02	54.77	23.78	5.8328	0.913	533
52.25	4.02	56.27	24.04	5.8328	0.917	535
53.34	4.02	57.36	24.22	5.8328	0.663	387
54.31	2.07	56.38	24.06	5.8328	0.844	492
55.69	2.07	57.76	24.29	5.8328	0.445	260
57.09	2.07	59.16	24.53	5.8328	0.657	383
58.59	2.07	60.66	24.79	5.8328	0.534	311
60.09	2.07	62.16	25.05	5.8328	0.887	517
61.75	2.07	63.82	25.33	5.8328	0.821	479
63.75	3.05	66.80	25.84	5.8328	0.793	463
65.25	3.05	68.30	26.03	15.4540	0.448	692
66.75	3.05	69.80	26.13	15.4540	0.746	1153
68.25	3.05	71.30	26.23	15.4540	0.532	822
69.75	3.05	72.80	26.32	15.4540	0.724	1119
71.25	3.05	74.30	26.42	15.4540	0.742	1147
72.65	3.05	75.70	26.51	15.4540	0.653	1009
73.49	7.37	80.86	26.84	15.4540	0.83	1283
74.75	7.37	82.12	26.93	15.4540	0.73	1128
76.25	7.37	83.62	27.02	15.4540	1.124	1737
77.75	7.37	85.12	27.12	15.4540	1.009	1559
79.25	7.37	86.62	27.22	15.4540	0.9	1391
80.78	7.37	88.15	27.32	15.4540	0.819	1266
81.82	7.37	89.19	27.38	15.4540	0.844	1304
85.59	8.97	94.56	27.73	15.4540	0.888	1372
87.25	8.97	96.22	27.84	15.4540	0.822	1270
88.75	8.97	97.72	27.94	15.4540	0.866	1338
90.55	8.97	99.52	28.05	15.4540	1.029	1590
92.25	13.41	105.66	28.45	15.4540	0.855	1321
93.75	13.41	107.16	28.55	15.4540	1.076	1663
95.25	13.41	108.66	28.64	15.4540	1.004	1552

Table T13 (continued).

Depth (mbsf)	Depth shift (m)	Depth (mcd)	Age (Ma)	LSR (m.m.y.)	DBD (g/cm ³)	MAR (mg/cm ² /k.y.)
96.75	13.41	110.16	28.74	15.4540	1.031	1593
98.23	13.41	111.64	28.84	15.4540	1.06	1638
99.75	13.41	113.16	28.93	15.4540	0.985	1522
100.65	13.41	114.06	28.99	15.4540	0.973	1504
101.75	15.13	116.88	29.17	15.4540	0.878	1357
103.25	15.13	118.38	29.27	15.4540	1.026	1586
104.76	15.13	119.89	29.37	15.4540	1.071	1655
106.19	15.13	121.32	29.46	15.4540	1.11	1715
107.70	15.13	122.83	29.56	15.4540	1.07	1654
109.69	15.13	124.82	29.69	15.4540	0.985	1522
110.41	15.13	125.54	29.74	15.4540	0.861	1331
111.25	19.59	130.84	30.08	15.4540	1.059	1637
112.75	19.59	132.34	30.18	15.4540	1.004	1552
113.81	19.59	133.40	30.24	15.4540	0.968	1496
115.31	19.59	134.90	30.34	15.4540	1.088	1681
116.81	19.59	136.40	30.44	15.4540	1.048	1620
118.31	19.59	137.90	30.54	15.4540	0.95	1468
118.79	19.59	138.38	30.57	15.4540	0.98	1514
119.40	19.59	138.99	30.61	15.4540	1.007	1556
120.75	21.45	142.20	30.81	15.4540	1.012	1564
122.25	21.45	143.70	30.91	15.4540	0.849	1312
123.87	21.45	145.32	31.02	15.4540	0.67	1035
125.25	21.45	146.70	31.10	15.4540	0.611	944
126.75	21.45	148.20	31.20	15.4540	0.627	969
128.30	21.45	149.75	31.30	15.4540	0.818	1264
129.33	21.45	150.78	31.37	15.4540	0.876	1354
130.37	22.85	153.22	31.53	15.4540	0.88	1360
131.75	22.85	154.60	31.62	15.4540	0.617	954
133.21	22.85	156.06	31.71	15.4540	0.863	1334
134.75	22.85	157.60	31.81	15.4540	0.89	1375
136.37	22.85	159.22	31.91	15.4540	0.887	1371
137.75	22.85	160.60	32.00	15.4540	0.674	1042
139.75	24.33	164.08	32.23	15.4540	0.792	1224
141.31	24.33	165.64	32.33	15.4540	0.7	1082
142.86	24.33	167.19	32.43	15.4540	0.776	1199
144.41	24.33	168.74	32.53	15.4540	0.563	870
145.92	24.33	170.25	32.63	15.4540	0.809	1250
147.36	24.33	171.69	32.72	15.4540	0.884	1366
148.36	24.33	172.69	32.79	15.4540	0.701	1083
149.25	25.33	174.58	32.91	15.4540	0.983	1519
150.35	25.33	175.68	32.98	15.4540	1.085	1677
151.45	25.33	176.78	33.05	15.4540	0.351	542
152.59	25.33	177.92	33.27	4.7412	0.36	171
154.09	25.33	179.42	33.59	4.7412	0.406	192
155.60	25.33	180.93	33.91	4.7412	0.414	196
157.10	25.33	182.43	34.22	4.7412	0.37	175
158.90	26.33	185.23	34.81	4.7412	0.387	183
160.27	26.33	186.60	35.10	4.7412	0.417	198
161.75	26.33	188.08	35.41	4.7412	0.399	189
163.31	26.33	189.64	35.74	4.7412	0.397	188
164.85	26.33	191.18	36.07	4.7412	0.4	190
166.28	26.33	192.61	36.37	4.7412	0.492	233
167.50	26.33	193.83	36.63	4.7412	0.416	197
168.25	27.33	195.58	37.00	4.7412	0.384	182
169.75	27.33	197.08	37.31	4.7412	0.392	186
171.25	27.33	198.58	37.63	4.7412	0.383	182
172.75	27.33	200.08	37.94	4.7412	0.386	183
174.25	27.33	201.58	38.26	4.7412	0.4	190
175.75	27.33	203.08	38.51	8.4366	0.422	356
177.69	28.33	206.02	38.86	8.4366	0.417	352
179.25	28.33	207.58	39.05	8.4366	0.462	390
180.75	28.33	209.08	39.22	8.4366	0.415	350
181.78	28.33	210.11	39.35	8.4366	0.431	364
183.33	28.33	211.66	39.53	8.4366	0.417	352
184.83	28.33	213.16	39.71	8.4366	0.423	357
186.06	28.33	214.39	39.85	8.4366	0.411	347
187.67	29.33	217.00	40.16	8.4366	0.421	355
188.75	29.33	218.08	40.29	8.4366	0.431	364
189.89	29.33	219.22	40.43	8.4366	0.489	413

Table T13 (continued).

Depth (mbsf)	Depth shift (m)	Depth (mcd)	Age (Ma)	LSR (m.m.y.)	DBD (g/cm ³)	MAR (mg/cm ² /k.y.)
190.90	29.33	220.23	40.55	8.4366	0.437	369
192.40	29.33	221.73	40.72	8.4366	0.709	598
193.89	29.33	223.22	40.90	8.4366	0.424	358
195.08	29.33	224.41	41.04	8.4366	0.521	440
195.67	29.33	225.00	41.11	8.4366	0.586	494
196.80	30.33	227.13	41.36	8.4366	0.426	359
198.25	30.33	228.58	41.54	8.4366	0.53	447
199.82	30.33	230.15	41.72	8.4366	0.453	382
201.25	30.33	231.58	41.89	8.4366	0.44	371
202.82	30.33	233.15	42.08	8.4366	0.467	394
204.25	30.33	234.58	42.25	8.4366	0.456	385
205.33	30.33	235.66	42.37	8.4366	0.464	391
206.25	31.33	237.58	42.60	8.4366	0.442	373
207.80	31.33	239.13	42.79	8.4366	0.452	381
210.75	31.33	242.08	43.14	8.4366	0.522	440
212.27	31.33	243.60	43.32	8.4366	0.646	545
213.67	31.33	245.00	43.48	8.4366	0.503	424
214.91	31.33	246.24	43.63	8.4366	0.587	495
215.85	32.33	248.18	43.88	3.0564	0.486	149
217.25	32.33	249.58	44.34	3.0564	0.479	146
218.76	32.33	251.09	44.83	3.0564	0.514	157
220.23	32.33	252.56	45.31	3.0564	0.512	156
221.80	32.33	254.13	45.83	3.0564	0.583	178
223.36	32.33	255.69	46.34	3.0564	0.521	159
224.52	33.02	257.54	46.94	3.0564	0.509	156
224.80	33.33	258.13	47.14	3.0564	0.523	160
226.27	33.33	259.60	47.62	3.0564	0.544	166
234.52	34.33	268.85	50.64	3.0564	1.805	552
237.59	34.33	271.92	51.65	3.0564	1.486	454
244.38	35.33	279.71	54.30	3.0564	1.326	405

Notes: LSR = linear sedimentation rate, DBD = dry bulk density, MAR = mass accumulation rate. This table is also available in [ASCII](#).

Table T14. Interstitial water data, Hole 1219A.

Core, section, interval (cm)	Depth (mbsf)	pH	Alkalinity (mM)	Salinity	Cl (mM)	Na (mM)	K (mM)	Ca (mM)	Mg (mM)	SO ₄ (mM)	NH ₄ (μM)	H ₄ SiO ₄ (μM)	Sr (μM)	Li (μM)	Mn (μM)	Ba (μM)	B (μM)
199-1219A-																	
1H-2, 145-150	2.95	7.16	2.59	35.0	552	481	12.0	12.3	48.6	30.3	2.8	507	87	33	0.81	0.36	521
2H-4, 145-150	11.95	7.19	2.38	35.0	559	488	11.3	19.1	41.9	29.9	2.8	641	95	28	0.35	0.23	463
3H-4, 145-150	21.45	7.11	2.28	35.0	563	490	10.7	23.1	37.9	29.0	5.6	667	103	27	0.23	0.46	463
4H-4, 145-150	30.95	7.09	1.88	35.5	564	492	9.9	26.6	33.6	28.4	7.0	665	108	27	14.2	0.26	472
5H-3, 145-150	38.95	7.04	1.86	35.5	565	494	9.4	29.7	30.4	28.6	4.2	703	110	26	29.2	0.36	445
6H-3, 145-150	48.45	7.04	1.55	35.5	565	491	8.9	32.5	27.5	27.1	1.4	769	115	25	44.8	1.07	446
9H-3, 145-150	76.95	7.02	1.50	35.5	564	491	7.5	34.7	24.7	25.9	1.4	847	120	25	64.2	0.58	440
12H-3, 145-150	105.45	7.04	1.35	35.0	564	487	6.3	38.4	22.9	25.6	0.0	905	114	25	76.3	1.10	411
15H-4, 145-150	135.45	6.82	0.89	35.5	564	484	5.6	41.2	21.8	25.6	1.4	967	120	25	75.6	0.88	407
19H-4, 145-150	173.45	7.18	1.28	35.5	562	484	4.6	43.2	20.7	26.8	7.0	1009	123	25	62.4	0.29	389
22X-3, 145-150	200.45	7.24	1.06	35.5	563	484	4.0	44.6	20.1	26.6	5.6	983	126	25	61.4	0.29	383

Note: This table is also available in [ASCII](#). [N1]

Table T15. Bulk sediment data, Hole 1219A. (See table notes. Continued on next page.)

Core, section, interval (cm)	Depth (mbsf)	Si (wt%)	Al (wt%)	Ti (wt%)	Fe (wt%)	Mn (wt%)	Ca (wt%)	Mg (wt%)	P (wt%)	Sr (ppm)	Ba (ppm)
199-1219A-											
1H-2, 73-74	2.23	19.72	6.10	0.27	3.56	1.10	0.58	2.05	0.15	276.58	7,050.11
1H-4, 73-74	5.23	19.09	5.67	0.22	3.27	0.74	0.81	1.94	0.22	214.87	4,224.00
2H-2, 68-69	8.18	27.41	4.28	0.19	2.64	0.60	0.83	1.36	0.24	263.13	8,072.15
2H-4, 73-74	11.23	23.84	5.49	0.21	3.80	1.10	1.36	1.95	0.40	233.25	4,479.92
2H-6, 73-74	14.23	26.26	3.27	0.15	2.81	0.79	1.36	1.38	0.53	230.10	5,167.71
3H-2, 76-77	17.76	25.12	5.09	0.18	4.33	0.85	1.45	1.53	0.42	252.94	4,455.29
3H-4, 73-74	20.73	24.43	3.34	0.13	3.05	0.63	4.88	1.15	0.30	416.02	5,344.13
3H-6, 73-74	23.73	26.83	3.79	0.15	3.34	0.63	1.96	1.20	0.27	277.19	5,289.09
4H-2, 73-74	27.23	27.63	3.78	0.14	3.36	0.73	1.21	1.18	0.27	293.68	8,719.91
4H-4, 73-74	30.23	10.62	1.62	0.06	1.39	0.37	25.47	0.54	0.13	1,340.88	3,842.57
4H-6, 73-74	33.23	4.95	0.72	0.03	0.57	0.26	32.10	0.25	0.07	1,301.14	1,337.00
5H-2, 74-75	36.74	1.62	0.20	0.01	0.16	0.06	35.47	0.11	0.02	1,260.66	634.39
5H-4, 73-74	39.73	2.10	0.30	0.01	0.28	0.09	37.41*	0.13	0.03	1,556.61	1,062.66
5H-6, 77-78	42.77	4.71	0.52	0.02	0.57	0.15	32.58	0.20	0.04	1,223.84	1,767.46
6H-2, 74-75	46.24	19.27	1.55	0.06	2.10	0.51	16.10	0.63	0.15	733.05	5,524.11
6H-4, 74-75	49.24	5.52	0.51	0.02	0.56	0.15	31.69	0.20	0.03	1,247.00	2,024.86
6H-6, 74-75	52.24	4.96	0.52	0.02	0.50	0.11	34.58	0.18	0.04	1,432.95	1,505.29
7H-2, 84-85	55.68	15.92	1.96	0.07	2.07	0.65	18.27	0.59	0.16	1,035.69	7,534.30
7H-4, 73-74	58.57	13.01	1.42	0.06	1.50	0.31	24.23	0.46	0.12	1,223.41	6,324.10
7H-6, 89-90	61.73	5.45	0.51	0.02	0.46	0.13	31.85	0.20	0.02	1,625.67	2,204.01
8H-2, 73-74	65.23	13.72	1.47	0.06	1.81	0.38	22.65	0.57	0.13	1,238.09	5,490.21
8H-4, 73-74	68.23	13.22	1.27	0.05	1.49	0.23	22.46	0.50	0.06	1,300.88	3,880.03
8H-6, 73-74	71.23	9.72	0.70	0.03	0.80	0.13	27.95	0.30	0.06	1,409.73	2,796.15
9H-2, 73-74	74.73	6.28	0.63	0.02	0.61	0.10	31.85	0.24	0.05	1,609.77	2,096.14
9H-4, 73-74	77.73	2.29	0.27	0.01	0.21	0.12	35.97*	0.12	0.01	1,679.36	901.91
9H-6, 73-74	80.73	4.38	0.67	0.02	0.62	0.11	33.01	0.23	0.07	1,700.19	2,153.45
10H-4, 73-74	87.23	4.39	0.49	0.02	0.49	0.10	33.34	0.21	0.04	1,626.36	2,138.73
10H-6, 104-105	90.54	1.90	0.27	0.01	0.25	0.10	35.77	0.12	0.02	1,738.17	1,121.60
11H-2, 73-74	93.73	1.66	0.25	0.01	0.23	0.11	33.04	0.14	0.04	1,587.60	967.86
11H-4, 72-73	96.72	2.36	0.32	0.01	0.23	0.09	35.62	0.13	0.11	1,722.15	1,068.20
11H-6, 73-74	99.73	2.59	0.33	0.01	0.26	0.08	34.99	0.14	BD	1,673.12	1,666.93
12H-2, 74-75	103.24	1.88	0.26	0.01	0.25	0.08	35.09	0.15	0.05	1,755.72	910.41
12H-4, 67-68	106.17	1.76	0.21	0.01	0.16	0.09	36.05*	0.11	0.02	1,692.45	1,031.22
12H-6, 118-119	109.68	5.32	0.43	0.02	0.54	0.11	32.67	0.24	0.14	1,548.51	1,988.84
13H-2, 73-74	112.73	3.22	0.30	0.01	0.34	0.10	34.45	0.17	0.02	1,524.25	1,530.26
13H-4, 73-74	115.29	1.80	0.23	0.01	0.21	0.11	34.21	0.13	0.02	1,422.92	1,018.10
13H-6, 73-74	118.29	3.46	0.43	0.02	0.56	0.10	34.21	0.23	0.07	1,587.41	1,914.96
13H-6, 123-124	118.79	6.77	0.57	0.03	1.02	0.09	29.82	0.36	0.29	1,530.13	3,384.07
14H-2, 73-74	122.23	5.10	0.59	0.02	0.95	0.12	32.71	0.36	0.08	1,603.69	2,074.10
14H-4, 73-74	125.23	11.21	1.09	0.04	1.69	0.26	26.21	0.60	0.14	1,430.57	5,580.55
14H-6, 79-80	128.29	5.22	0.47	0.02	0.79	0.18	32.01	0.30	0.05	1,605.33	2,204.19
15H-2, 74-75	131.74	7.44	0.46	0.02	0.86	0.23	30.68	0.34	0.04	1,573.18	2,046.20
15H-4, 74-75	134.74	5.81	0.39	0.02	0.70	0.18	32.03	0.30	BD	1,659.70	1,762.29
15H-6, 74-75	137.74	12.79	0.66	0.03	1.19	0.24	24.69	0.46	0.11	1,276.07	3,607.03
16H-2, 73-74	141.29	12.62	0.42	0.02	0.81	0.18	25.28	0.35	0.17	1,220.76	2,380.60
16H-4, 73-74	144.29	12.00	0.42	0.02	1.02	0.23	25.30	0.41	BD	1,308.37	2,090.02
16H-6, 73-74	147.34	4.06	0.29	0.01	0.63	0.15	20.78	0.25	BD	1,030.88	778.70
17H-2, 35-37	150.35	3.69	0.63	0.02	0.67	0.18	35.07	0.27	0.04	1,803.57	1,418.82
17H-4, 75-77	152.59	26.03	2.55	0.11	6.29	1.42	1.51	1.93	0.47	325.50	9,370.44
17H-6, 75-77	155.6	28.78	1.84	0.07	4.13	0.80	1.04	1.17	0.02	258.52	7,504.73
18H-2, 77-79	160.27	29.60	1.64	0.07	4.62	0.91	1.15	1.23	0.12	249.39	8,141.15
18H-4, 81-83	163.31	32.13	1.65	0.07	3.71	0.61	1.01	1.06	0.12	274.54	9,448.09
18H-6, 78-80	166.28	32.17	1.64	0.06	4.12	0.77	1.05	1.13	0.27	294.95	10,365.45
19H-2, 74-75	169.74	31.88	1.42	0.05	2.70	0.36	1.09	0.97	0.29	260.80	9,319.69
19H-4, 74-75	172.74	29.42	1.93	0.08	3.77	0.48	1.30	1.29	0.36	282.23	10,044.75
19H-6, 74-75	175.74	28.47	1.12	0.04	1.73	0.29	0.61	0.81	0.09	232.26	8,710.49
20H-2, 73-74	179.23	27.00	0.83	0.03	1.31	0.21	3.99	0.65	0.12	300.13	6,294.36
20H-4, 73-74	181.76	33.10	0.70	0.03	1.73	0.39	0.60	0.69	0.26	176.58	6,442.12
20H-6, 73-74	184.81	33.21	0.70	0.02	1.69	0.29	0.33	0.79	BD	157.64	6,019.37
21H-2, 72-74	188.72	35.16	0.44	0.02	0.71	0.10	0.65	0.40	0.06	152.93	4,640.43
21H-4, 58-59	190.88	35.55	0.31	0.02	0.36	0.01	1.62	0.28	BD	153.84	3,094.43
21H-6, 88-89	193.88	27.10	0.68	0.03	0.95	0.03	4.23	0.50	0.07	294.19	5,456.54
21H-8, 20-21	195.70	21.55	0.52	0.02	0.68	0.06	16.56	0.41	0.36	709.47	4,320.48
22H-2, 73-74	198.23	25.65	0.61	0.02	1.22	0.13	11.05	0.62	0.16	587.50	6,519.99
22H-4, 73-74	201.23	32.20	0.71	0.03	1.47	0.21	3.65	0.79	0.26	262.92	4,723.24
22H-6, 73-74	204.23	30.84	0.95	0.04	2.16	0.22	2.87	1.06	0.14	315.52	8,332.85
23H-2, 78-79	207.78	32.34	0.61	0.03	1.60	0.24	2.23	0.88	0.25	280.31	8,804.49

Table T15 (continued).

Core, section, interval (cm)	Depth (mbsf)	Si (wt%)	Al (wt%)	Ti (wt%)	Fe (wt%)	Mn (wt%)	Ca (wt%)	Mg (wt%)	P (wt%)	Sr (ppm)	Ba (ppm)
23H-4, 73-74	210.73	30.88	0.54	0.02	1.18	0.12	6.35	0.63	0.14	432.69	8,062.33
23H-6, 65-66	213.65	34.60	0.55	0.02	1.12	0.10	3.02	0.70	BD	265.83	6,754.65
24H-2, 74-75	217.24	35.80	0.57	0.02	1.07	0.12	0.45	0.63	0.52	217.59	8,734.76
24H-4, 75-76	220.25	33.35	0.92	0.04	1.62	0.23	1.45	1.08	0.27	283.75	9,667.70
24H-6, 80-81	223.35	37.92	0.86	0.04	1.15	0.13	0.72	0.83	0.26	224.67	9,089.98
25X-1, 32-33	224.82	32.44	0.68	0.03	1.07	0.14	0.83	0.81	0.14	278.44	10,547.98
26X-1, 42-44	234.52	4.56	0.92	0.04	1.69	0.47	31.74	0.61	0.12	639.19	7,001.32
26X-3, 49-51	237.59	0.59	0.20	0.01	0.11	0.06	37.38*	0.29	BD	553.84	13.30
27X-1, 68-70	244.38	1.83	0.36	0.02	0.57	0.07	32.81	0.43	0.02	665.92	7.14

Notes: BD = below detection limit. * = Ca values higher than 35.9 wt% are out of the range of the standards (see "Geochemistry," p. 20, in the "Explanatory Notes" chapter). This table is also available in [ASCII](#).

Table T16. Calcium carbonate and organic carbon data, Hole 1219A.

Core, section, interval (cm)	Depth (mbsf)	CaCO ₃ (wt%)	Organic C (wt%)	CaCO ₃ (wt%)*	Core, section, interval (cm)	Depth (mbsf)	CaCO ₃ (wt%)	Organic C (wt%)	CaCO ₃ (wt%)*
199-1219A-					14H-6, 79-80	128.29	78.06		79.53
1H-2, 73-74	2.23	0.12	0.14	-0.48	15H-2, 74-75	131.74	74.77		76.15
1H-4, 73-74	5.23	0.13		0.10	15H-4, 74-75	134.74	79.62	0.00	79.59
2H-2, 68-69	8.18	0.19		0.14	15H-6, 74-75	137.74	57.86		60.90
2H-4, 73-74	11.23	0.26	0.05	1.50	16H-2, 73-74	141.29	59.65		62.42
2H-6, 73-74	14.23	0.31		1.48	16H-4, 73-74	144.29	59.48	0.54	62.45
3H-2, 76-77	17.76	0.33		1.72	16H-6, 73-74	147.34	76.67		50.98
3H-4, 73-74	20.73	7.81	0.16	10.46	17H-2, 35-37	150.35	83.88		87.33
3H-6, 73-74	23.73	2.43		3.04	17H-4, 75-77	152.59	0.56	0.00	1.91
4H-2, 73-74	27.23	0.23		1.11	17H-6, 75-77	155.60	0.60		0.72
4H-4, 73-74	30.23	59.04	0.00	62.88	18H-2, 77-79	160.27	0.63		1.01
4H-6, 73-74	33.23	78.73		79.77	18H-4, 81-83	163.31	0.39	0.00	0.65
5H-2, 74-75	36.74	91.61		88.35	18H-6, 78-80	166.28	0.36		0.76
5H-4, 73-74	39.73	90.31	0.00	93.28 [†]	19H-2, 74-75	169.74	0.73		0.85
5H-6, 77-78	42.77	80.57		81.00	19H-4, 74-75	172.74	0.53	0.00	1.38
6H-2, 74-75	46.24	35.49		39.02	19H-6, 74-75	175.74	0.63		-0.38
6H-4, 74-75	49.24	79.65	0.00	78.74	20H-2, 73-74	179.23	7.64		8.23
6H-6, 74-75	52.24	82.32		86.10	20H-4, 73-74	181.76	0.36	0.00	-0.38
7H-2, 84-85	55.68	44.01		44.55	20H-6, 73-74	184.81	0.59		-1.08
7H-4, 73-74	58.57	54.75	0.00	59.73	21H-2, 72-74	188.72	1.36		-0.26
7H-6, 89-90	61.73	79.31		79.14	21H-4, 58-59	190.88	3.82	0.00	2.20
8H-2, 73-74	65.23	50.70		55.69	21H-6, 88-89	193.88	8.56		8.84
8H-4, 73-74	68.23	52.44	0.00	55.21	21H-8, 20-21	195.70			40.22
8H-6, 73-74	71.23	66.70		69.20	22H-2, 73-74	198.23	24.87		26.21
9H-2, 73-74	74.73	77.14		79.13	22H-4, 73-74	201.23	6.79	0.00	7.37
9H-4, 73-74	77.73	90.38	0.00	89.63	22H-6, 73-74	204.23	5.36		5.39
9H-6, 73-74	80.73	82.40		82.07	23H-2, 78-79	207.78	3.48	1.05	3.76
10H-4, 73-74	87.23	83.28	0.00	82.94	23H-4, 73-74	210.73	13.23		14.24
10H-6, 104-105	90.54	91.11		89.11	23H-6, 65-66	213.65	6.22		5.77
11H-2, 73-74	93.73	91.16		82.16	24H-2, 74-75	217.24	1.08		-0.78
11H-4, 72-73	96.72	90.88	0.00	88.74	24H-4, 75-76	220.25	2.78	0.00	1.79
11H-6, 73-74	99.73	88.90		87.14	24H-6, 80-81	223.35	0.61		-0.09
12H-2, 74-75	103.24	90.85		87.39	25X-1, 32-33	224.82	0.52	0.00	0.22
12H-4, 67-68	106.17	92.36	0.00	89.82	26X-1, 42-44	234.52	77.66		78.87
12H-6, 118-119	109.68	81.50		81.22	26X-3, 49-51	237.59	96.42	0.00	93.23 [†]
13H-2, 73-74	112.73	87.22		85.76	27X-1, 68-70	244.38	90.49	0.00	81.60
13H-4, 73-74	115.29	91.62	0.00	85.14					
13H-6, 73-74	118.29	85.79		85.14					
13H-6, 123-124	118.79			74.01					
14H-2, 73-74	122.23	80.00		81.34					
14H-4, 73-74	125.23	59.76	0.00	64.78					

Notes: * = calculated from Ca (wt%). † = CaCO₃ values higher than 90 wt% are calculated from Ca values out of the range of the standards (see "Geochemistry," p. 20, in the "Explanatory Notes" chapter). This table is also available in [ASCII](#).

Table T17. Moisture and density measurements, Hole 1219A. (See table note. Continued on next page.)

Core, section, interval (cm)	Depth (mbsf)	Water content (%)	Density (g/cm ³)				Porosity (%)	Core, section, interval (cm)	Depth (mbsf)	Water content (%)	Density (g/cm ³)			Porosity (%)
			Wet bulk	Dry bulk	Grain	Wet bulk					Dry bulk	Grain		
199-1219A-							11H-5, 73-75	98.23	36.8	1.677	1.060	2.667	60.2	
1H-1, 75-77	0.75	76.6	1.183	0.277	2.404	88.5	11H-6, 75-77	99.75	39.8	1.636	0.985	2.702	63.6	
1H-2, 70-72	2.20	76.6	1.178	0.276	2.328	88.2	11H-7, 15-17	100.65	40.2	1.625	0.973	2.682	63.7	
1H-3, 75-77	3.75	78.1	1.178	0.258	2.536	89.8	12H-1, 75-77	101.75	43.9	1.566	0.878	2.675	67.2	
1H-4, 59-61	5.09	77.1	1.178	0.270	2.397	88.8	12H-2, 75-77	103.25	38.2	1.661	1.026	2.701	62.0	
2H-1, 75-77	6.75	74.0	1.207	0.313	2.463	87.3	12H-3, 76-78	104.76	36.6	1.690	1.071	2.705	60.4	
2H-2, 65-67	8.15	76.6	1.182	0.276	2.390	88.5	12H-4, 69-71	106.19	35.4	1.717	1.110	2.727	59.3	
2H-3, 75-77	9.75	73.5	1.211	0.321	2.458	86.9	12H-5, 70-72	107.70	36.5	1.685	1.070	2.678	60.0	
2H-4, 75-77	11.25	76.0	1.190	0.285	2.448	88.3	12H-6, 119-121	109.69	39.5	1.628	0.985	2.648	62.8	
2H-5, 75-77	12.75	76.7	1.181	0.276	2.374	88.4	12H-7, 41-43	110.41	44.7	1.556	0.861	2.681	67.9	
2H-6, 75-77	14.25	78.5	1.173	0.253	2.487	89.8	13H-1, 75-77	111.25	37.2	1.686	1.059	2.734	61.3	
2H-7, 37-39	15.37	76.6	1.181	0.276	2.377	88.4	13H-2, 75-77	112.75	39.2	1.651	1.004	2.730	63.2	
3H-1, 79-81	16.29	79.1	1.171	0.245	2.566	90.4	13H-3, 75-77	113.81	40.5	1.627	0.968	2.714	64.3	
3H-2, 77-79	17.77	77.2	1.179	0.268	2.424	88.9	13H-4, 75-77	115.31	36.0	1.699	1.088	2.697	59.7	
3H-3, 75-77	19.25	79.1	1.170	0.244	2.541	90.4	13H-5, 75-77	116.81	37.4	1.674	1.048	2.693	61.1	
3H-4, 75-77	20.75	75.3	1.196	0.296	2.453	87.9	13H-6, 75-77	118.31	41.1	1.614	0.950	2.700	64.8	
3H-5, 75-77	22.25	73.8	1.208	0.317	2.437	87.0	13H-7, 34-36	119.40	39.1	1.652	1.007	2.720	63.0	
3H-6, 75-77	23.75	75.4	1.200	0.295	2.532	88.4	14H-1, 75-77	120.75	38.9	1.657	1.012	2.729	62.9	
3H-7, 32-34	24.82	75.8	1.190	0.288	2.421	88.1	14H-2, 75-77	122.25	45.3	1.552	0.849	2.709	68.7	
4H-1, 107-109	26.07	76.2	1.188	0.283	2.438	88.4	14H-3, 87-89	123.87	53.3	1.434	0.670	2.638	74.6	
4H-2, 75-77	27.25	77.5	1.183	0.266	2.548	89.6	14H-4, 75-77	125.25	56.2	1.394	0.611	2.595	76.5	
4H-3, 69-71	28.69	78.4	1.166	0.252	2.342	89.3	14H-5, 75-77	126.75	55.5	1.407	0.627	2.633	76.2	
4H-4, 75-77	30.25	59.2	1.361	0.556	2.600	78.6	14H-6, 80-82	128.30	46.5	1.527	0.818	2.665	69.3	
4H-5, 75-77	31.75	48.4	1.504	0.776	2.690	71.2	14H-7, 33-35	129.33	44.0	1.564	0.876	2.669	67.2	
4H-6, 75-77	33.25	46.7	1.537	0.819	2.738	70.1	15H-1, 87-89	130.37	43.7	1.565	0.880	2.653	66.8	
4H-7, 31-33	34.31	72.3	1.231	0.341	2.610	86.9	15H-2, 75-77	131.75	56.2	1.407	0.617	2.698	77.1	
5H-1, 75-77	35.25	48.5	1.510	0.777	2.734	71.6	15H-3, 71-73	133.21	44.4	1.553	0.863	2.645	67.4	
5H-2, 89-91	36.89	38.8	1.667	1.021	2.765	63.1	15H-4, 75-77	134.75	43.4	1.572	0.890	2.662	66.6	
5H-3, 75-77	38.25	63.3	1.321	0.485	2.644	81.7	15H-5, 87-89	136.37	43.3	1.564	0.887	2.620	66.2	
5H-4, 75-77	39.75	39.3	1.655	1.004	2.759	63.6	15H-6, 75-77	137.75	52.7	1.425	0.674	2.526	73.3	
5H-5, 75-77	41.25	41.9	1.605	0.933	2.720	65.7	16H-1, 75-77	139.75	46.9	1.493	0.792	2.508	68.4	
5H-6, 78-80	42.78	43.5	1.577	0.891	2.700	67.0	16H-2, 75-77	141.31	51.3	1.438	0.700	2.505	72.1	
5H-7, 63-65	44.13	55.8	1.408	0.622	2.675	76.8	16H-3, 80-82	142.86	47.9	1.489	0.776	2.555	69.6	
6H-1, 75-77	44.75	47.2	1.519	0.802	2.676	70.0	16H-4, 85-87	144.41	58.3	1.350	0.563	2.426	76.8	
6H-2, 77-79	46.27	71.1	1.228	0.355	2.414	85.3	16H-5, 81-83	145.92	46.3	1.507	0.809	2.545	68.2	
6H-3, 71-73	47.71	70.8	1.234	0.361	2.454	85.3	16H-6, 75-77	147.36	43.4	1.561	0.884	2.607	66.1	
6H-4, 75-77	49.25	46.5	1.535	0.821	2.709	69.7	16H-7, 25-27	148.36	51.7	1.452	0.701	2.630	73.3	
6H-5, 75-77	50.75	42.6	1.592	0.913	2.707	66.3	17H-1, 75-77	149.25	39.8	1.635	0.983	2.702	63.6	
6H-6, 75-77	52.25	42.4	1.591	0.917	2.682	65.8	17H-2, 35-37	150.35	36.0	1.696	1.085	2.690	59.7	
6H-7, 34-36	53.34	53.5	1.426	0.663	2.602	74.5	17H-3, 45-47	151.45	71.5	1.232	0.351	2.508	86.0	
7H-1, 81-83	54.31	45.4	1.545	0.844	2.674	68.5	17H-4, 75-77	152.61	70.8	1.235	0.360	2.475	85.4	
7H-2, 85-87	55.69	65.4	1.288	0.445	2.517	82.3	17H-5, 75-77	154.11	67.2	1.239	0.406	2.177	81.3	
7H-3, 75-77	57.09	53.8	1.422	0.657	2.596	74.7	17H-6, 75-77	155.62	66.9	1.250	0.414	2.255	81.7	
7H-4, 75-77	58.59	59.9	1.330	0.534	2.397	77.7	17H-7, 75-77	157.12	69.9	1.230	0.370	2.308	84.0	
7H-5, 75-77	60.09	43.3	1.566	0.887	2.630	66.3	18H-1, 90-92	158.90	68.8	1.238	0.387	2.297	83.2	
7H-6, 91-93	61.75	46.3	1.528	0.821	2.650	69.0	18H-2, 77-79	160.27	66.7	1.252	0.417	2.256	81.5	
8H-1, 75-77	63.75	47.3	1.506	0.793	2.612	69.6	18H-3, 75-77	161.75	67.9	1.242	0.399	2.254	82.3	
8H-2, 75-77	65.25	65.3	1.294	0.448	2.568	82.5	18H-4, 81-83	163.31	68.0	1.241	0.397	2.261	82.5	
8H-3, 75-77	66.75	49.5	1.478	0.746	2.617	71.5	18H-5, 85-87	164.85	67.8	1.243	0.400	2.261	82.3	
8H-4, 75-77	68.25	60.1	1.334	0.532	2.457	78.3	18H-6, 78-80	166.28	61.8	1.289	0.492	2.219	77.8	
8H-5, 75-77	69.75	50.4	1.461	0.724	2.577	71.9	18H-7, 50-52	167.50	66.9	1.254	0.416	2.294	81.9	
8H-6, 75-77	71.25	49.5	1.470	0.742	2.568	71.1	19H-1, 75-77	168.25	68.8	1.231	0.384	2.224	82.7	
8H-7, 65-67	72.65	53.7	1.412	0.653	2.524	74.1	19H-2, 75-77	169.75	68.3	1.237	0.392	2.243	82.5	
9H-1, 99-101	73.49	46.2	1.542	0.830	2.723	69.5	19H-3, 75-77	171.25	69.1	1.238	0.383	2.321	83.5	
9H-2, 75-77	74.75	50.4	1.471	0.730	2.645	72.4	19H-4, 75-77	172.75	68.6	1.230	0.386	2.199	82.4	
9H-3, 75-77	76.25	34.7	1.722	1.124	2.702	58.4	19H-5, 75-77	174.25	67.7	1.238	0.400	2.201	81.8	
9H-4, 75-77	77.75	38.7	1.647	1.009	2.676	62.3	19H-6, 75-77	175.75	66.2	1.248	0.422	2.181	80.7	
9H-5, 75-77	79.25	43.3	1.588	0.900	2.742	67.2	20H-1, 69-71	177.69	66.6	1.249	0.417	2.228	81.3	
9H-6, 78-80	80.78	46.4	1.530	0.819	2.676	69.4	20H-2, 75-77	179.25	63.7	1.273	0.462	2.217	79.2	
9H-7, 32-34	81.82	45.3	1.543	0.844	2.657	68.2	20H-3, 75-77	180.75	66.6	1.242	0.415	2.159	80.8	
10H-3, 59-61	85.59	43.7	1.576	0.888	2.708	67.2	20H-4, 75-77	181.78	65.6	1.255	0.431	2.203	80.4	
10H-4, 75-77	87.25	46.3	1.532	0.822	2.680	69.3	20H-5, 75-77	183.33	66.5	1.245	0.417	2.176	80.8	
10H-5, 75-77	88.75	44.3	1.556	0.866	2.655	67.4	20H-6, 75-77	184.83	66.0	1.246	0.423	2.154	80.3	
10H-6, 105-107	90.55	38.2	1.665	1.029	2.720	62.2	20H-7, 48-50	186.06	67.0	1.243	0.411	2.195	81.3	
11H-1, 75-77	92.25	44.9	1.550	0.855	2.667	68.0	21H-1, 117-119	187.67	66.2	1.247	0.421	2.180	80.7	
11H-2, 75-77	93.75	36.4	1.691	1.076	2.695	60.1	21H-2, 75-77	188.75	65.5	1.248	0.431	2.130	79.8	
11H-3, 75-77	95.25	38.8	1.641	1.004	2.656	62.2	21H-3, 39-41	189.89	62.2	1.293	0.489	2.276	78.5	
11H-4, 75-77	96.75	38.3	1.672	1.031	2.756	62.6	21H-4, 60-62	190.90	65.2	1.255	0.437	2.178	79.9	

Table T17 (continued).

Core, section, interval (cm)	Depth (mbsf)	Water content (%)	Density (g/cm ³)			Porosity (%)
			Wet bulk	Dry bulk	Grain	
21H-5, 90-92	192.40	50.6	1.434	0.709	2.432	70.9
21H-6, 89-91	193.89	66.1	1.251	0.424	2.202	80.7
21H-7, 58-60	195.08	60.3	1.312	0.521	2.287	77.2
21H-8, 17-19	195.67	57.0	1.363	0.586	2.429	75.9
22H-1, 80-82	196.80	66.1	1.256	0.426	2.245	81.0
22H-2, 75-77	198.25	60.0	1.325	0.530	2.370	77.6
22H-3, 82-84	199.82	64.3	1.271	0.453	2.250	79.9
22H-4, 75-77	201.25	65.2	1.264	0.440	2.255	80.5
22H-5, 82-84	202.82	63.5	1.280	0.467	2.258	79.3
22H-6, 75-77	204.25	64.2	1.274	0.456	2.262	79.8
22H-7, 33-35	205.33	63.7	1.277	0.464	2.252	79.4
23H-1, 75-77	206.25	64.9	1.260	0.442	2.197	79.9
23H-2, 80-82	207.80	64.2	1.264	0.452	2.185	79.3
23H-4, 75-77	210.75	59.9	1.301	0.522	2.179	76.0
23H-5, 77-79	212.27	53.5	1.388	0.646	2.344	72.4
23H-6, 67-69	213.67	61.0	1.291	0.503	2.181	76.9
23H-7, 41-43	214.91	56.4	1.347	0.587	2.278	74.2
24H-1, 85-87	215.85	61.9	1.277	0.486	2.135	77.2
24H-2, 75-77	217.25	62.3	1.271	0.479	2.111	77.3
24H-3, 76-78	218.76	60.5	1.299	0.514	2.202	76.7
24H-4, 73-75	220.23	60.4	1.293	0.512	2.159	76.3
24H-5, 75-77	221.80	56.4	1.337	0.583	2.210	73.6
24H-6, 81-83	223.36	59.9	1.298	0.521	2.160	75.9
24H-7, 47-49	224.52	60.6	1.292	0.509	2.161	76.5
25X-1, 30-32	224.80	59.7	1.296	0.523	2.133	75.5
25X-2, 27-29	226.27	58.4	1.309	0.544	2.150	74.7
26X-1, 42-44	234.52	16.3	2.155	1.805	2.745	34.2
26X-3, 49-51	237.59	24.2	1.961	1.486	2.773	46.4
27X-1, 68-70	244.38	26.9	1.814	1.326	2.535	47.7

Note: This table is also available in [ASCII](#).

Table T18. LAS-based mineralogy, Hole 1219A. (See table note. Continued on next two pages.)

Core, section, interval (cm)	Depth (mbsf)	Calcite (model wt%)	Opal (model wt%)	Smectite (model wt%)	Illite (model wt%)	Core, section, interval (cm)	Depth (mbsf)	Calcite (model wt%)	Opal (model wt%)	Smectite (model wt%)	Illite (model wt%)
199-1219A-						6H-3, 23-25	47.24	81.93	0.00	18.07	0.00
1H-1, 75-77	0.75	13.68	5.30	33.67	47.35	6H-3, 71-73	47.72	41.83	31.53	26.64	0.00
1H-2, 23-25	1.74	0.00	24.01	75.99	0.00	6H-4, 23-25	48.74	85.47	4.44	10.09	0.00
1H-2, 70-72	2.21	3.28	0.00	96.72	0.00	6H-4, 75-77	49.26	76.63	0.00	23.37	0.00
1H-3, 23-25	3.24	12.34	0.00	80.42	7.24	6H-5, 75-77	50.76	77.06	0.00	22.94	0.00
1H-3, 75-77	3.74	0.00	0.00	100.00	0.00	6H-6, 75-77	52.26	68.85	2.08	29.07	0.00
1H-4, 23-25	4.74	0.00	15.20	84.80	0.00	6H-7, 34-36	53.35	72.96	11.24	15.80	0.00
1H-4, 59-61	5.10	0.00	6.13	93.87	0.00	7H-1, 81-83	54.32	77.09	0.00	22.91	0.00
2H-1, 75-77	6.76	24.30	24.93	50.32	0.45	7H-2, 85-87	55.70	47.61	31.59	20.80	0.00
2H-1, 125-127	7.26	38.00	22.27	23.41	16.32	7H-3, 23-25	56.58	64.69	24.32	10.99	0.00
2H-2, 23-25	7.74	35.62	21.70	22.80	19.88	7H-3, 75-77	57.10	61.59	16.61	21.80	0.00
2H-2, 65-67	8.16	30.16	29.35	31.70	8.79	7H-4, 23-25	58.08	73.99	15.16	10.85	0.00
2H-3, 23-25	9.24	24.27	35.24	26.65	13.84	7H-4, 75-77	58.60	52.83	24.76	22.41	0.00
2H-3, 75-77	9.76	24.44	25.55	41.08	8.93	7H-5, 23-25	59.58	76.33	5.30	18.37	0.00
2H-4, 23-25	10.74	24.84	20.11	45.00	10.05	7H-5, 75-77	60.10	64.62	5.83	29.54	0.00
2H-4, 75-77	11.26	18.46	8.80	72.74	0.00	7H-6, 24-26	61.09	71.76	21.46	6.78	0.00
2H-5, 23-25	12.24	22.28	33.33	33.44	10.96	7H-6, 91-93	61.76	74.83	5.38	19.79	0.00
2H-5, 75-77	12.76	21.04	30.90	40.74	7.32	7H-7, 25-27	62.60	85.39	7.72	6.89	0.00
2H-6, 23-25	13.74	28.21	29.79	26.99	15.01	8H-1, 28-30	63.29	88.37	0.54	11.09	0.00
2H-6, 75-77	14.26	28.58	21.23	40.50	9.69	8H-1, 75-77	63.76	80.91	0.00	19.09	0.00
2H-7, 23-25	15.24	25.54	30.78	29.93	13.75	8H-1, 122-124	64.23	91.86	0.00	8.14	0.00
2H-7, 37-39	15.38	22.63	28.68	38.45	10.24	8H-2, 22-24	64.73	85.06	13.66	0.16	1.11
3H-1, 79-81	16.30	23.12	23.32	45.49	8.07	8H-2, 75-77	65.26	66.01	21.08	12.91	0.00
3H-1, 123-125	16.74	20.38	31.84	33.94	13.84	8H-3, 23-25	66.24	90.24	0.00	9.76	0.00
3H-2, 23-25	17.24	21.58	27.47	36.25	14.70	8H-3, 75-77	66.76	73.23	5.29	21.48	0.00
3H-2, 77-79	17.78	12.44	30.80	46.83	9.92	8H-4, 23-25	67.74	83.10	16.25	0.00	0.65
3H-3, 23-25	18.74	20.21	33.83	31.62	14.34	8H-4, 75-77	68.26	46.13	29.50	24.37	0.00
3H-3, 75-77	19.26	16.92	33.28	42.66	7.14	8H-5, 23-25	69.24	84.15	11.45	4.41	0.00
3H-4, 23-25	20.24	22.26	35.97	25.43	16.34	8H-5, 75-77	69.75	67.67	12.89	19.44	0.00
3H-4, 75-77	20.76	31.79	38.97	25.34	3.91	8H-6, 23-25	70.74	83.01	2.38	14.60	0.00
3H-5, 23-25	21.74	67.64	19.85	7.78	4.72	8H-6, 75-77	71.26	49.52	23.87	26.61	0.00
3H-5, 75-77	22.26	30.35	40.08	22.21	7.36	8H-7, 23-25	72.24	73.44	18.10	8.46	0.00
3H-6, 23-25	23.24	71.27	16.35	3.26	9.11	8H-7, 65-67	72.66	55.08	24.07	20.85	0.00
3H-6, 75-77	23.76	16.38	35.75	33.78	14.08	9H-1, 99-100	73.50	74.60	8.66	16.74	0.00
3H-7, 23-25	24.74	22.39	36.40	20.89	20.33	9H-1, 123-125	73.74	72.93	7.61	19.47	0.00
3H-7, 32-34	24.83	22.17	32.48	28.09	17.27	9H-2, 23-25	74.24	73.84	3.09	23.07	0.00
4H-1, 107-109	26.08	29.98	24.98	29.68	15.35	9H-2, 75-77	74.76	69.60	14.84	15.57	0.00
4H-1, 127-129	26.28	40.16	20.73	6.62	32.48	9H-3, 23-25	75.74	79.57	3.30	17.12	0.00
4H-2, 24-26	26.75	33.80	27.65	9.42	29.13	9H-3, 75-77	76.26	63.88	0.00	36.12	0.00
4H-2, 75-77	27.26	26.93	27.95	30.13	14.99	9H-4, 23-25	77.24	81.66	0.48	17.87	0.00
4H-3, 24-26	28.25	37.45	28.80	7.65	26.10	9H-4, 75-77	77.76	72.66	0.00	27.34	0.00
4H-3, 69-71	28.70	30.58	31.33	26.76	11.32	9H-5, 23-25	78.74	74.65	7.22	18.13	0.00
4H-4, 24-26	29.75	50.78	21.52	1.86	25.84	9H-5, 75-77	79.26	72.67	2.04	25.29	0.00
4H-4, 75-77	30.26	86.66	0.00	12.62	0.72	9H-6, 23-25	80.24	84.90	2.97	12.12	0.00
4H-5, 24-26	31.25	84.61	0.00	8.12	7.26	9H-6, 78-80	80.79	73.29	6.85	19.86	0.00
4H-5, 75-77	31.76	84.07	0.00	10.97	4.95	9H-7, 23-25	81.74	79.30	4.20	16.50	0.00
4H-6, 24-26	32.75	85.96	0.29	2.53	11.23	9H-7, 32-34	81.83	73.45	6.27	20.28	0.00
4H-6, 75-77	33.26	81.88	0.00	18.12	0.00	10H-3, 23-25	85.24	75.38	3.37	21.24	0.00
4H-7, 24-26	34.25	52.85	15.78	0.00	31.37	10H-3, 59-61	85.60	73.21	2.43	24.37	0.00
4H-7, 31-33	34.32	60.85	7.78	14.73	16.64	10H-4, 23-25	86.74	77.32	0.00	22.68	0.00
5H-1, 75-77	35.26	85.61	0.00	14.39	0.00	10H-4, 75-77	87.26	71.57	6.61	21.82	0.00
5H-1, 123-125	35.74	65.70	13.94	0.00	20.36	10H-5, 23-25	88.24	81.86	1.26	16.88	0.00
5H-2, 23-25	36.24	86.53	0.00	13.47	0.00	10H-5, 75-77	88.76	71.38	4.93	23.69	0.00
5H-2, 89-91	36.90	75.15	0.00	24.85	0.00	10H-6, 23-25	89.74	79.03	3.56	17.41	0.00
5H-3, 23-25	37.74	89.51	0.00	7.62	2.87	10H-6, 105-107	90.56	71.27	0.00	28.73	0.00
5H-3, 75-77	38.26	85.74	0.51	13.75	0.00	10H-7, 23-25	91.24	78.30	0.49	21.21	0.00
5H-4, 23-25	39.24	84.92	0.00	15.08	0.00	11H-1, 75-77	92.26	73.83	5.53	20.64	0.00
5H-4, 75-77	39.76	77.79	0.00	22.21	0.00	11H-1, 124-126	92.75	70.66	14.15	15.19	0.00
5H-5, 23-25	40.74	82.16	0.00	17.84	0.00	11H-2, 23-25	93.24	80.58	2.89	16.53	0.00
5H-5, 75-77	41.26	79.11	0.00	20.89	0.00	11H-2, 75-77	93.76	68.01	0.00	31.99	0.00
5H-6, 23-25	42.24	81.38	0.00	18.62	0.00	11H-3, 23-25	94.74	82.23	3.03	14.74	0.00
5H-6, 78-80	42.79	81.78	0.00	18.22	0.00	11H-3, 75-77	95.26	69.44	0.00	30.56	0.00
5H-7, 23-25	43.74	91.29	0.00	8.71	0.00	11H-4, 23-25	96.24	79.64	0.00	20.36	0.00
5H-7, 63-65	44.14	85.15	0.00	14.85	0.00	11H-4, 75-77	97.26	70.76	0.00	29.24	0.00
6H-1, 75-77	44.76	78.89	0.00	21.11	0.00	11H-5, 23-25	97.74	75.97	5.25	18.78	0.00
6H-1, 122-124	45.23	80.83	1.99	17.18	0.00	11H-5, 73-75	98.24	68.38	0.00	31.62	0.00
6H-2, 23-25	45.74	80.48	2.49	17.03	0.00	11H-6, 23-25	99.24	73.47	8.27	18.26	0.00
6H-2, 77-79	46.28	39.34	33.67	26.99	0.00	11H-6, 75-77	99.76	73.37	0.48	26.15	0.00

Table T18 (continued).

Core, section, interval (cm)	Depth (mbsf)	Calcite (model wt%)	Opal (model wt%)	Smectite (model wt%)	Illite (model wt%)	Core, section, interval (cm)	Depth (mbsf)	Calcite (model wt%)	Opal (model wt%)	Smectite (model wt%)	Illite (model wt%)
11H-7, 15-17	100.66	69.43	0.98	29.60	0.00	16H-6, 75-77	147.37	65.16	5.55	29.30	0.00
11H-7, 23-25	100.74	73.31	5.31	21.38	0.00	16H-7, 23-25	148.35	98.26	1.11	0.00	0.63
12H-1, 75-77	101.76	65.78	8.84	25.38	0.00	16H-7, 25-27	148.37	84.53	5.12	10.35	0.00
12H-1, 123-125	102.24	76.76	11.87	11.36	0.00	17H-1, 75-77	149.26	80.24	0.00	19.76	0.00
12H-2, 23-25	102.74	74.62	5.29	20.09	0.00	17H-2, 35-37	150.36	67.90	0.00	32.10	0.00
12H-2, 75-77	103.26	69.41	0.00	30.59	0.00	17H-3, 45-47	151.46	42.07	0.00	46.92	11.00
12H-3, 23-25	104.24	72.73	0.00	27.27	0.00	17H-4, 75-77	152.60	38.49	0.00	53.58	7.93
12H-3, 76-78	104.77	70.27	0.00	29.73	0.00	17H-5, 75-77	154.10	47.85	11.50	32.80	7.85
12H-4, 23-25	105.74	76.75	0.00	23.25	0.00	17H-6, 75-77	155.61	36.88	19.37	35.23	8.51
12H-4, 69-71	106.20	67.58	0.00	32.42	0.00	17H-7, 75-77	157.11	52.77	0.00	33.25	13.97
12H-5, 23-25	107.24	74.85	3.66	21.49	0.00	18H-1, 90-92	158.91	51.76	0.00	25.78	22.45
12H-5, 70-72	107.71	66.51	0.00	33.49	0.00	18H-2, 77-79	160.28	49.33	2.22	34.53	13.93
12H-6, 23-25	108.74	73.16	3.38	23.46	0.00	18H-3, 75-77	161.76	43.89	9.71	38.65	7.75
12H-6, 119-121	109.70	60.93	8.42	30.65	0.00	18H-4, 81-83	163.32	25.05	36.83	34.34	3.78
12H-7, 23-25	110.24	77.70	7.66	14.64	0.00	18H-5, 85-87	164.86	37.27	13.87	38.05	10.80
12H-7, 41-43	110.42	63.96	8.71	27.33	0.00	18H-6, 78-80	166.29	43.86	9.12	36.50	10.52
13H-1, 75-77	111.26	67.58	0.00	32.42	0.00	18H-6, 75-52	167.51	52.77	0.00	37.36	9.88
13H-1, 123-125	111.74	81.36	0.00	18.64	0.00	19H-1, 75-77	168.26	10.51	49.22	40.27	0.00
13H-2, 23-25	112.24	78.47	4.37	17.17	0.00	19H-1, 123-125	168.74	18.51	49.97	29.10	2.41
13H-2, 75-77	112.76	72.54	4.45	23.02	0.00	19H-2, 23-25	169.24	21.18	46.89	27.40	4.53
13H-3, 23-25	113.30	83.21	7.09	9.70	0.00	19H-2, 75-77	169.76	12.08	52.25	35.67	0.00
13H-3, 75-77	113.82	68.62	2.41	28.98	0.00	19H-3, 23-25	170.73	18.44	47.42	29.79	4.35
13H-4, 23-25	114.80	81.04	0.20	18.76	0.00	19H-3, 75-77	171.26	16.22	43.16	35.77	4.85
13H-4, 75-77	115.32	70.87	0.00	29.13	0.00	19H-4, 23-25	172.24	16.98	43.57	30.25	9.20
13H-5, 23-25	116.29	77.34	0.00	22.66	0.00	19H-4, 75-77	172.76	9.83	44.63	45.54	0.00
13H-5, 75-77	116.81	67.76	0.00	32.24	0.00	19H-5, 23-25	173.74	20.30	44.41	27.45	7.85
13H-6, 23-25	117.79	81.34	0.00	18.66	0.00	19H-5, 75-77	174.26	8.65	56.51	34.84	0.00
13H-6, 75-77	118.31	74.13	3.13	22.74	0.00	19H-6, 23-25	175.24	12.91	48.98	38.10	0.00
13H-7, 23-25	119.29	79.69	0.00	20.31	0.00	19H-6, 75-77	175.76	4.30	61.50	34.19	0.00
13H-7, 34-36	119.40	73.97	0.00	26.03	0.00	19H-7, 21-23	176.72	26.61	55.35	18.04	0.00
14H-1, 75-77	120.76	69.70	0.00	30.30	0.00	20H-1, 69-71	177.70	5.17	54.70	40.13	0.00
14H-1, 123-125	121.24	82.91	0.00	17.09	0.00	20H-1, 123-125	178.24	28.75	52.32	18.92	0.00
14H-2, 23-25	121.74	77.74	0.00	22.26	0.00	20H-2, 23-25	178.74	22.71	62.59	14.70	0.00
14H-2, 75-77	122.26	73.92	6.11	19.98	0.00	20H-2, 75-77	179.26	13.69	62.50	23.81	0.00
14H-3, 23-25	123.24	56.54	26.84	16.62	0.00	20H-3, 23-25	180.24	11.91	57.46	30.62	0.01
14H-3, 87-89	124.38	63.66	21.16	15.19	0.00	20H-3, 75-77	180.76	10.98	55.88	33.14	0.00
14H-4, 23-25	124.74	74.99	13.27	11.74	0.00	20H-4, 23-25	181.26	17.68	46.86	30.46	5.01
14H-4, 75-77	125.26	53.28	26.45	20.26	0.00	20H-4, 75-77	181.78	8.36	54.35	37.29	0.00
14H-5, 23-25	126.24	71.54	19.58	8.89	0.00	20H-5, 23-25	182.26	15.03	60.75	21.58	2.64
14H-5, 75-77	126.76	56.49	21.47	22.04	0.00	20H-5, 75-77	183.33	7.94	64.32	27.75	0.00
14H-6, 23-25	127.74	80.14	12.68	7.18	0.00	20H-6, 23-25	184.31	10.10	58.82	30.08	0.99
14H-6, 80-82	128.31	69.89	11.01	19.10	0.00	20H-6, 75-77	184.83	11.15	64.55	24.10	0.20
14H-7, 23-25	129.24	77.90	8.31	13.79	0.00	20H-7, 24-26	185.82	0.00	68.42	31.58	0.00
14H-7, 33-35	129.34	70.67	7.08	22.26	0.00	20H-7, 48-50	186.06	0.48	67.68	31.84	0.00
15H-1, 87-89	130.38	69.07	4.94	25.99	0.00	21H-1, 117-119	187.68	6.19	59.16	34.65	0.00
15H-1, 124-126	130.75	73.21	14.49	12.30	0.00	21H-1, 143-145	187.93	9.18	60.85	29.97	0.00
15H-2, 24-26	131.25	79.18	3.77	17.05	0.00	21H-2, 23-25	188.24	13.59	66.59	16.80	3.02
15H-2, 75-77	131.76	62.87	7.25	29.87	0.00	21H-2, 75-77	188.76	6.51	72.61	20.88	0.00
15H-3, 24-26	132.75	78.92	10.87	10.21	0.00	21H-3, 23-25	189.74	16.61	69.70	13.69	0.00
15H-3, 71-73	134.22	69.69	10.01	20.30	0.00	21H-3, 39-41	189.90	29.30	58.63	12.08	0.00
15H-4, 24-26	134.25	82.13	0.00	17.87	0.00	21H-4, 23-25	190.54	31.06	63.55	5.39	0.00
15H-4, 75-77	134.76	77.60	0.37	22.02	0.00	21H-4, 60-62	190.91	30.56	64.75	4.69	0.00
15H-5, 24-26	135.75	76.91	8.40	14.69	0.00	21H-5, 23-25	191.74	46.88	53.12	0.00	0.00
15H-5, 87-89	136.38	69.86	9.27	20.87	0.00	21H-5, 90-92	192.41	44.60	41.90	13.51	0.00
15H-6, 24-26	137.25	64.21	26.13	9.66	0.00	21H-6, 23-25	193.24	38.50	52.62	8.88	0.00
15H-6, 75-77	137.76	41.86	29.28	28.86	0.00	21H-6, 89-91	193.90	24.25	60.16	15.59	0.00
15H-7, 24-26	138.75	69.74	23.07	7.18	0.00	21H-7, 23-25	194.74	38.48	50.31	11.21	0.00
16H-1, 75-77	139.76	50.75	24.23	25.03	0.00	21H-7, 58-60	195.09	30.40	55.92	13.68	0.00
16H-1, 123-125	140.24	78.55	17.62	3.83	0.00	21H-8, 17-19	195.68	35.42	43.58	21.00	0.00
16H-2, 23-25	140.80	66.21	20.06	13.73	0.00	21H-8, 23-25	195.74	43.65	47.18	9.17	0.00
16H-2, 75-77	141.32	53.65	28.66	17.69	0.00	22H-1, 80-82	196.81	16.89	58.74	24.36	0.00
16H-3, 23-25	142.30	74.38	19.72	5.90	0.00	22H-1, 124-126	197.25	36.68	48.95	14.37	0.00
16H-3, 80-82	142.87	57.29	16.64	26.06	0.00	22H-2, 24-26	197.75	29.66	51.97	18.38	0.00
16H-4, 23-25	143.80	84.93	12.32	2.75	0.00	22H-2, 75-77	198.26	24.72	54.18	21.10	0.00
16H-4, 85-87	144.42	46.04	33.35	20.61	0.00	22H-3, 24-26	199.25	12.36	57.85	29.79	0.00
16H-5, 20-22	145.34	79.98	20.02	0.00	0.00	22H-3, 82-84	199.83	7.94	60.77	31.29	0.00
16H-5, 81-83	145.93	62.24	12.66	25.10	0.00	22H-4, 24-26	200.75	16.74	56.15	27.11	0.00
16H-6, 23-25	146.85	87.84	0.00	12.16	0.00	22H-4, 75-77	201.26	4.07	65.03	30.90	0.00

Table T18 (continued).

Core, section, interval (cm)	Depth (mbsf)	Calcite (model wt%)	Opal (model wt%)	Smectite (model wt%)	Illite (model wt%)
22H-5, 24-26	202.25	8.87	61.37	29.76	0.00
22H-5, 82-84	202.83	10.76	58.58	30.66	0.00
22H-6, 24-26	203.75	4.58	60.34	35.09	0.00
22H-6, 75-77	204.26	5.54	60.93	33.54	0.00
22H-7, 24-26	205.25	14.23	56.18	29.59	0.00
22H-7, 33-36	205.35	12.56	55.28	32.16	0.00
23H-1, 75-77	206.26	0.00	60.35	39.65	0.00
23H-1, 124-126	206.75	0.00	64.95	35.05	0.00
23H-2, 23-25	207.24	5.20	60.47	34.33	0.00
23H-2, 80-82	207.81	0.00	60.79	39.21	0.00
23H-3, 7-9	208.58	0.93	63.38	35.69	0.00
23H-4, 75-77	210.76	7.95	64.26	27.80	0.00
23H-5, 23-25	211.74	13.40	64.67	21.93	0.00
23H-5, 77-79	212.28	30.86	54.20	14.95	0.00
23H-6, 23-25	213.24	11.40	62.20	26.40	0.00
23H-6, 67-69	213.68	0.00	66.29	33.71	0.00
23H-7, 1-3	214.52	3.98	69.62	26.40	0.00
23H-7, 41-43	214.92	21.89	60.63	17.48	0.00
24H-1, 85-87	215.86	0.00	67.36	32.64	0.00
24H-1, 123-125	216.24	0.00	68.89	31.11	0.00
24H-2, 23-25	216.74	0.00	69.31	30.69	0.00
24H-2, 75-77	217.26	0.00	67.83	32.17	0.00
24H-3, 23-25	218.24	0.00	67.08	32.92	0.00
24H-3, 75-77	218.76	0.00	65.13	34.87	0.00
24H-4, 23-25	219.74	0.00	65.28	34.72	0.00
24H-4, 73-75	220.23	0.00	60.94	39.06	0.00
24H-5, 23-25	221.29	1.18	66.65	32.17	0.00
24H-5, 75-77	221.81	0.00	64.83	35.17	0.00
24H-6, 23-25	222.79	0.00	65.77	34.23	0.00
24H-6, 81-83	223.37	0.00	66.93	33.07	0.00
24H-7, 23-25	224.29	1.09	71.43	27.48	0.00
24H-7, 47-49	224.53	0.00	70.60	29.40	0.00
25X-1, 30-32	224.81	0.00	65.82	34.18	0.00
25X-1, 123-125	225.74	4.29	70.62	25.09	0.00
25X-2, 27-29	226.28	0.00	68.18	31.82	0.00
26X-1, 42-44	234.53	81.45	0.00	18.55	0.00
26X-1, 122-124	235.33	83.10	0.00	16.90	0.00
26X-2, 18-20	235.79	74.47	0.00	25.53	0.00
26X-3, 21-23	237.32	68.53	0.00	31.47	0.00
26X-3, 49-51	237.60	67.88	0.00	32.12	0.00
27X-1, 34-36	244.05	69.82	0.00	30.18	0.00
27X-1, 68-70	244.39	69.10	0.00	30.90	0.00

Note: This table is also available in [ASCII](#). [N1]

Table T19. Split-core velocity measurements, Hole 1219A. (See table notes. Continued on next page.)

Core, section, interval (cm)	Depth (mbsf)	Velocity (m/s)			Anisotropy (%)	Core, section, interval (cm)	Depth (mbsf)	Velocity (m/s)			Anisotropy (%)
		z*	y*	x†				z*	y*	x†	
199-1219A-						11H-7, 16	100.66				1531
1H-1, 76	0.76	1493	1514		1.4	12H-1, 76	101.76				1521
1H-2, 71	2.21	1495	1516		1.4	12H-2, 76	103.26				1523
1H-3, 76	3.76	1493	1511		1.2	12H-3, 77	104.77				1538
1H-4, 60	5.10	1495	1518		1.5	12H-4, 70	106.20				1544
2H-1, 76	6.76	1508	1529		1.3	12H-5, 71	107.71				1541
2H-2, 66	8.16			1537		12H-6, 120	109.70				1538
2H-3, 76	9.76			1547		12H-7, 42	110.42				1520
2H-4, 76	11.26	1510	1527		1.2	13H-1, 76	111.26				1540
2H-5, 76	12.76	1510	1526		1.1	13H-2, 76	112.76				1531
2H-6, 76	14.26	1510	1531		1.4	13H-3, 76	113.82				1520
2H-7, 38	15.38	1512	1528		1.1	13H-4, 76	115.32				1534
3H-1, 80	16.30	1504	1519		1.0	13H-5, 76	116.82				1534
3H-2, 78	17.78	1515	1533		1.2	13H-6, 76	118.32				1526
3H-3, 76	19.26			1532		13H-7, 35	119.41				1536
3H-4, 76	20.76			1525		14H-1, 76	120.76				1530
3H-5, 76	22.26			1527		14H-2, 76	122.26				1503
3H-6, 76	23.76			1532		14H-3, 88	123.88				1513
3H-7, 33	24.83			1537		14H-4, 76	125.26				1520
4H-1, 108	26.08			1552		14H-5, 76	126.76				1510
4H-2, 76	27.26			1537		14H-6, 81	128.31				1517
4H-3, 70	28.70			1538		14H-7, 34	129.34				1526
4H-4, 76	30.26			1509		15H-1, 88	130.38				1530
4H-5, 76	31.76			1504		15H-2, 76	131.76				1523
4H-6, 76	33.26			1503		15H-3, 73	133.23				1527
4H-7, 32	34.32			1520		15H-4, 76	134.76				1525
5H-1, 76	35.26			1529		15H-5, 88	136.38				1529
5H-2, 76	36.76			1534		15H-6, 76	137.76				1515
5H-3, 90	38.40			1520		16H-1, 76	139.76				1514
5H-4, 76	39.75			1526		16H-2, 76	141.32				1513
5H-5, 76	41.26			1528		16H-3, 81	142.87				1519
5H-6, 79	42.79			1539		16H-4, 86	144.42				1520
5H-7, 64	44.14			1528		16H-5, 82	145.93				1518
6H-1, 76	44.76			1532		16H-6, 76	147.37				1509
6H-2, 78	46.28			1543		16H-7, 26	148.37				1513
6H-3, 72	47.72			1535		17H-1, 76	149.26				1537
6H-4, 76	49.26			1519		17H-2, 36	150.36				1522
6H-5, 76	50.76			1520		17H-3, 46	151.46				1540
6H-6, 76	52.26			1523		17H-4, 78	152.62				1559
6H-7, 35	53.35			1519		17H-5, 76	154.10				1530
7H-1, 82	54.32			1530		17H-6, 76	155.60				1538
7H-2, 86	55.70			1536		17H-7, 76	157.11				1538
7H-3, 74	57.08			1532		18H-1, 91	158.91				1562
7H-4, 76	58.60			1532		18H-2, 78	160.28				1539
7H-5, 76	60.10			1530		18H-3, 76	161.76				1558
7H-6, 92	61.76			1522		18H-4, 82	163.32				1533
8H-1, 76	63.76			1527		18H-6, 79	166.29				1561
8H-2, 76	65.26			1523		18H-7, 51	167.51				1556
8H-3, 76	66.76			1515		19H-1, 76	168.26				1564
8H-4, 76	68.26			1521		19H-2, 76	169.76				1561
8H-5, 76	69.76			1521		19H-3, 76	171.26				1555
8H-6, 76	71.26			1521		19H-4, 76	172.76				1551
8H-7, 66	72.66			1537		19H-5, 76	174.26				1549
9H-1, 100	73.50			1526		19H-6, 76	175.76				1556
9H-2, 76	74.76			1526		20H-1, 70	177.70				1554
9H-3, 76	76.26			1568		20H-2, 76	179.26				1562
9H-4, 76	77.76			1546		20H-3, 76	180.76				1554
9H-5, 76	79.26			1531		20H-4, 76	181.79				1555
9H-6, 79	80.79			1521		20H-5, 76	183.34				1556
9H-7, 33	81.83			1531		20H-6, 76	184.84				1567
10H-3, 60	85.60			1531		20H-7, 49	186.07				1582
10H-4, 76	87.26			1514		21H-1, 118	187.68				1560
10H-5, 76	88.76			1522		21H-2, 76	188.76				1566
10H-6, 106	90.56			1534		21H-3, 40	189.90				1543
11H-2, 76	93.76			1545		21H-4, 61	190.91				1575
11H-3, 76	95.26			1542		21H-5, 91	192.41				1541
11H-4, 76	96.76			1525		21H-6, 90	193.90				1555
11H-5, 74	98.24			1541		21H-7, 59	195.09				1555
11H-6, 76	99.76			1532		21H-8, 18	195.68				1537

Table T19 (continued).

Core, section, interval (cm)	Depth (mbsf)	Velocity (m/s)			Anisotropy (%)
		z*	y*	x†	
22H-1, 81	196.81			1551	
22H-2, 76	198.26			1541	
22H-3, 83	199.83			1552	
22H-4, 76	201.26			1546	
22H-5, 83	202.83			1532	
22H-6, 77	204.27			1528	
22H-7, 34	205.34			1532	
23H-1, 76	206.25			1578	
23H-2, 81	207.80			1575	
23H-4, 77	210.77			1564	
23H-5, 79	212.29			1526	
23H-6, 68	213.68			1534	
23H-7, 42	214.92			1537	
24H-1, 87	215.87			1578	
24H-2, 76	217.26			1577	
24H-3, 78	218.78			1575	
24H-4, 74	220.24			1554	
24H-5, 76	221.81			1542	
24H-6, 82	223.37			1554	
24H-7, 48	224.53			1568	
25X-1, 31	224.81			1608	
25X-2, 28	226.28			1600	
26X-1, 43	234.53	1854	1895		2.2
26X-3, 50	237.60	2028	2051		1.1
27X-1, 69	244.39	1821	1851		1.6

Notes: * = determined by insertion probe, † = determined by contact probe. This table is also available in [ASCII](#).

Table T20. Thermal conductivity, Site 1219.

Core, section, interval (cm)	Depth (mbsf)	Thermal conductivity (W/[m-K])
199-1219A-		
1H-3, 76	3.76	0.71
2H-3, 76	9.76	0.74
3H-3, 76	19.26	0.77
4H-3, 76	28.76	0.73
5H-3, 76	38.26	0.98
6H-3, 86	47.86	0.83
7H-3, 76	57.10	0.92
8H-3, 76	66.76	0.98
9H-3, 66	76.16	1.22
10H-3, 76	85.76	1.13
11H-3, 76	95.26	1.18
12H-3, 76	104.76	1.22
13H-3, 76	113.82	1.11
14H-3, 76	123.76	0.89
15H-3, 76	133.26	1.04
16H-3, 76	142.82	0.93
17H-3, 44	151.46	0.71
18H-3, 76	161.76	0.74
19H-3, 76	171.26	0.72
20H-3, 76	180.76	0.74
21H-3, 46	189.96	0.73
22H-3, 76	199.76	0.73
24H-3, 76	218.76	0.77
199-1219B-		
2H-3, 76	24.67	0.73
3H-3, 76	34.26	0.93
4H-3, 76	43.76	1.02
5H-3, 76	53.26	0.81
6H-3, 76	62.76	1.03
7H-3, 76	72.26	0.97
8H-3, 76	81.76	1.03
9H-3, 76	91.26	1.21
10H-3, 76	100.76	1.12
11H-3, 76	110.26	1.14
12H-3, 76	119.76	1.20
13H-3, 76	129.26	0.99
14H-3, 77	138.76	1.04

Note: This table is also available in [ASCII](#).

Table T21. In situ temperature, Hole 1219B.

Core	Depth (mbsf)	In situ temperature* (°C)
199-1219B-		
	0.00	1.45
4H	49.50	5.72
7H	78.00	7.55
11H	116.00	9.34

Notes: * = seafloor temperature is the average of the determinations accompanying the three cores. This table is also available in [ASCII](#).

Table T22. Logging operations, Hole 1219A.

Date (Nov 2001)	Local time (hr)	Operations
25	0945	Hole preparation complete, rig up wireline
	1215	Run into hole with triple combo (MGT, HNGS, APS, HLDT, DITE, TAP)
	1530	Uplog with triple combo at 900 ft/hr from total depth (254 mbsf)
	1635	Going down for a second pass
	1645	Uplog with triple combo at 900 ft/hr from total depth (254 mbsf)
	1745	Going down for an MGT pass
	1805	Uplog with MGT at 700 ft/hr from total depth (224 mbsf)
	1850	Going down for second pass
	1900	Uplog with MGT at 700 ft/hr from total depth (223 mbsf)
	2350	Pull tools out of hole and rigdown
26	0000	Rig up FMS-sonic
	0245	Run into hole with FMS-sonic (NGT, DSI, GPIT, FMS)
	0600	Uplog with FMS-sonic at 900 ft/hr from total depth (254 mbsf)
	0645	Going down for a second pass
	0705	Uplog with FMS-sonic at 900 ft/hr from total depth (254 mbsf)
	1200	Pull tools out of hole and rig down
	1200	End of logging operations

Notes: Drillers total depth = 5325 mbsf, water depth = 5074 m, end of pipe = 82.0 mbsf. MGT = multisensor gamma ray tool, HNGS = hostile environment natural gamma ray sonde, APS = accelerator porosity sonde, HLDT = hostile environment lithodensity tool, DITE = dual induction tool, TAP = high-temperature acceleration pressure tool, FMS = Formation MicroScanner, NGT = natural gamma ray tool, DSI = dipole sonic induction tool, GPIT = general purpose inclinometry tool.

CHAPTER NOTE

- N1.** 13 December 2002—After the CD-ROM version of this volume was published, errors were noted in the ASCII versions of Tables T2, T5, T7, T12, T14, and T18. This version contains the corrected ASCII files